MCEER
EARTHQUAKE ENGINEERING TO EXTREME EVENTS

ISSN 1520-295X

Modeling the Effects of Detonations of High Explosives to Inform Blast-Resistant Design

by
Pushkaraj Sherkar, Andrew S. Whittaker and Amjad J. Aref

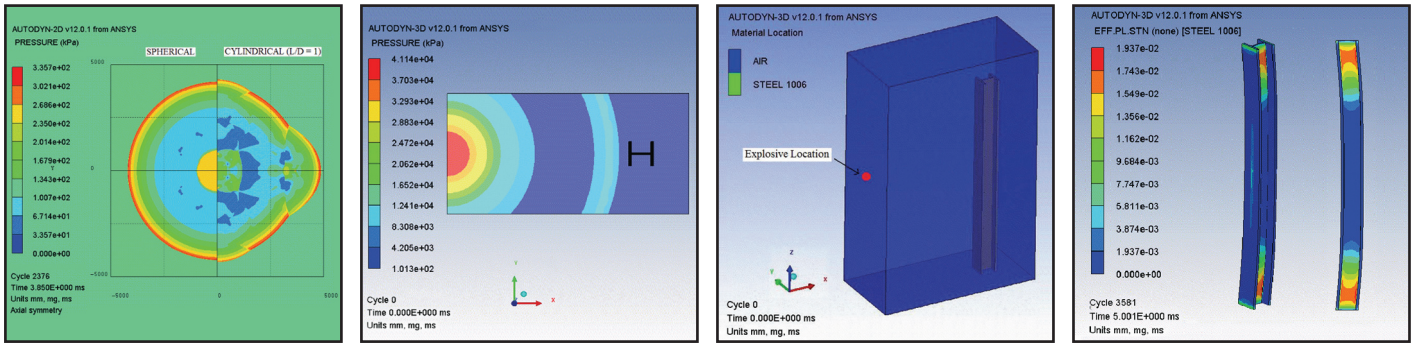

Technical Report MCEER-10-0009

December 1, 2010

This research was conducted at the University at Buffalo, State University of New York and was supported by MCEER Thrust Area 3, Innovative Technologies.

NOTICE

This report was prepared by the University at Buffalo, State University of New York as a result of research sponsored by MCEER. Neither MCEER, associates of MCEER, its sponsors, the University at Buffalo, State University of New York, nor any person acting on their behalf:

a. makes any warranty, express or implied, with respect to the use of any information, apparatus, method, or process disclosed in this report or that such use may not infringe upon privately owned rights; or

b. assumes any liabilities of whatsoever kind with respect to the use of, or the damage resulting from the use of, any information, apparatus, method, or process disclosed in this report.

Any opinions, findings, and conclusions or recommendations expressed in this publication are those of the author(s) and do not necessarily reflect the views of MCEER, the National Science Foundation, or other sponsors.

Modeling the Effects of Detonations of High Explosives to Inform Blast-Resistant Design

by

Pushkaraj Sherkar,[1] Andrew S. Whittaker[2] and Amjad J. Aref[3]

Publication Date: December 1, 2010
Submittal Date: September 14, 2010

Technical Report MCEER-10-0009

MCEER Thrust Area 3, Innovative Technologies

1 M.S. student, Department of Civil, Structural and Environmental Engineering, University at Buffalo, State University of New York
2 Professor and Chair, Department of Civil, Structural and Environmental Engineering, University at Buffalo, State University of New York
3 Professor, Department of Civil, Structural and Environmental Engineering, University at Buffalo, State University of New York

MCEER
University at Buffalo, State University of New York
Red Jacket Quadrangle, Buffalo, NY 14261
Phone: (716) 645-3391; Fax (716) 645-3399
E-mail: *mceer@buffalo.edu*; WWW Site: *http://mceer.buffalo.edu*

Preface

MCEER is a national center of excellence dedicated to the discovery and development of new knowledge, tools and technologies that equip communities to become more disaster resilient in the face of earthquakes and other extreme events. MCEER accomplishes this through a system of multidisciplinary, multi-hazard research, in tandem with complimentary education and outreach initiatives.

Headquartered at the University at Buffalo, The State University of New York, MCEER was originally established by the National Science Foundation in 1986, as the first National Center for Earthquake Engineering Research (NCEER). In 1998, it became known as the Multidisciplinary Center for Earthquake Engineering Research (MCEER), from which the current name, MCEER, evolved.

Comprising a consortium of researchers and industry partners from numerous disciplines and institutions throughout the United States, MCEER's mission has expanded from its original focus on earthquake engineering to one which addresses the technical and socio-economic impacts of a variety of hazards, both natural and man-made, on critical infrastructure, facilities, and society.

The Center derives support from several Federal agencies, including the National Science Foundation, Federal Highway Administration, National Institute of Standards and Technology, Department of Homeland Security / Federal Emergency Management Agency, and the State of New York, other state governments, academic institutions, foreign governments and private industry.

The most common method used in blast-resistant design models structural members as single-degree-of-freedom (SDOF) systems and characterizes the blast loading using a peak reflected overpressure and a reflected impulse calculated from empirical design charts such as those provided in UFC-3-340. In this report, a comprehensive survey of different strategies to model detonations in finite element codes LS-DYNA and AUTODYN and the computational fluid dynamics code Air3D was conducted. Significant differences in results calculated using the three models and between the models and UFC-3-340 were identified. A numerical study was performed using AUTODYN to study the influence of charge shape, charge orientation and point of detonation within the charge on overpressure distributions. Results were compared with those involving a baseline analysis of a spherical charge. A significant dependence on the charge shape and charge orientation was observed. SDOF assumptions are shown to be inappropriate for blast-resistant design against detonations of improvised explosive devices at small standoff distances.

Abstract

Blast-resistant design has traditionally been performed using simplified methods. The most widely used method models structural members such as columns and beams as single-degree-of-freedom (SDOF) systems and characterizes the blast load using a peak reflected overpressure and a reflected impulse, where both are calculated using empirical design charts such as those provided in UFC-3-340. A uniform loading over the height (length) of the component is assumed. Moreover, the empirical design charts assume either a spherical (free-air) burst or a hemispherical (surface) burst and do not consider variations in charge shape, charge orientation and point of detonation within the charge.

A comprehensive survey of different strategies to model detonations in commercially available finite element (FE) codes LS-DYNA and AUTODYN and the computational fluid dynamics (CFD) code Air3D was conducted. A robust modeling strategy capable of modeling different charge shapes and fluid-structure interaction was identified in LS-DYNA and the use of remapping capabilities of AUTODYN and Air3D was demonstrated. A near-field detonation of a spherical charge of TNT and the subsequent fluid-structure interaction with a rigid column was modeled using the three codes. The resulting peak reflected overpressure and impulse monitored on the face of the column were compared with those computed using the empirical design charts in the UFC. There were significant differences between the results of the FE and CFD analysis, and between these results and the predictions of UFC-3-340. The reasons for the differences include the change in the value of the constant specific heat ratio, γ, of air at high temperatures, the effect of afterburning on the reflected impulse, and the effect of blast-wave clearing on both the reflected peak overpressure and impulse.

A numerical study was performed using AUTODYN to study the influence of charge shape, charge orientation and point of detonation within the charge on the overpressure distributions and the response of an A992 Grade 50 $W14\times257$ column. A set of analyses was performed with cylindrical charges with different aspect ratios. Results were compared with those involving a baseline analysis of a spherical

charge. The resulting peak incident overpressure and impulses, and the pressure contours were compared in the near-, mid- and far-fields. In the near-field, $Z < 1.5\ \text{m/kg}^{0.33}$, the overpressure distributions are influenced significantly by charge shape and the point of detonation in the charge. The influence of these variables diminishes with distance. The loading and subsequent response of the $\text{W14} \times 257$ column to a detonation of 1000 kg of TNT at a standoff distance of 3 m showed significant dependence on the charge shape and charge orientation and clearly demonstrated that SDOF assumptions are inappropriate for blast-resistant design against detonations of improvised explosive devices at small standoff distances.

Acknowledgements

Support for this work was provided by MCEER Thrust Area 3, Innovative Technologies. This support is gratefully acknowledged. Any opinions, findings, conclusions or recommendations expressed in this report are those of the authors and do not necessarily reflect those of MCEER, the State of New York, or other sponsors.

The authors would like to express their most sincere gratitude to Messrs. Michael Astrella of Weidlinger Associates in NYC, Michael Willford of ARUP in San Francisco, Dr. Chengqing Wu at the University of Adelaide, Dr. Tuan Ngo and Professor Priyan Mendis at the University of Melbourne for providing information on the Johnson-Cook material model used in the analyses reported herein, and Professor Gary Dargush of the University at Buffalo for his careful review of this report.

Table of Contents

Section	Title	Page
1	**INTRODUCTION**	**1**
1.1	Design of Blast-Resistant Structures	1
1.2	State-of-the-Practice for Computing Blast-Load Effects	2
1.3	Calculation of Blast-Load Effects using Computational Fluid Dynamics	7
1.4	Report Objective and Organization	8
2	**LITERATURE REVIEW**	**9**
2.1	Introduction	9
2.2	Chemistry of Explosives	9
2.2.1	Oxidation	9
2.2.2	Oxygen balance	11
2.3	Classification of Explosives	12
2.3.1	Primary explosives	13
2.3.2	Secondary explosives	14
2.3.3	Propellants	15
2.4	Detonation Physics	15
2.4.1	Introduction	15
2.4.2	Detonation wave profile and the Chapman-Jouget state	17
2.4.3	Rankine-Hugoniot jump equations	18
2.4.4	Afterburning of detonation products	19
2.5	Modeling Detonation	21
2.5.1	Explicit modeling	21
2.5.2	Indirect modeling	22
2.5.3	Modeling afterburn	24
2.6	Modeling Detonations in LS-DYNA, AUTODYN and Air3D	24
2.6.1	Modeling detonations in LS-DYNA	25
2.6.2	Modeling detonations in AUTODYN	27
2.6.3	Modeling detonations in Air3D	27
2.7	Effect of Charge Shape and Orientation on Overpressure Distributions	28
3	**MODELING THE EFFECTS OF DETONATIONS**	**31**
3.1	Introduction	31
3.2	Equations of State for Explosives and Air	32
3.2.1	Equation of State for air	32
3.2.2	Equations of State for explosives	33
3.2.2.1	BKW Equation of State	34
3.2.2.2	JWL Equation of State	34
3.3	Lagrangian Analysis	35
3.4	Eulerian Analysis	37
3.5	Arbitrary Lagrangian-Eulerian Analysis	39
3.6	Coupled Eulerian-Lagrangian Analysis	40
3.7	Sample Problem	42

Table of Contents (Cont'd)

Section	Title	Page
3.8	UFC-3-340-02 Calculations	45
3.9	LS-DYNA Modeling and Pressure Distributions	47
3.9.1	Cuboid-shaped explosive	47
3.9.1.1	Modeling and analysis	47
3.9.1.2	Results and discussion	52
3.9.2	Circular explosive with radial mesh	56
3.9.3	Circular explosive with mesh transition	58
3.9.3.1	Modeling and analysis	58
3.9.3.2	Results and discussion	59
3.9.4	Initial_Volume_Fraction_Geometry option	63
3.9.4.1	Modeling and analysis	63
3.9.4.2	Results and discussion	65
3.9.4.3	Variation in JWL EOS parameters and timesteps between advection cycles	68
3.10	Air3D Modeling and Pressure Distributions	75
3.10.1	Modeling and analysis	75
3.10.2	Results and discussion	77
3.11	AUTODYN Modeling and Pressure Distributions	79
3.11.1	1D analysis	80
3.11.2	3D analysis	84
3.11.3	Results and discussion	86
3.11.4	Afterburning	91
3.11.4.1	Modeling and analysis	91
3.11.4.2	Results and discussion	93
3.11.4.3	Comparison of Euler-FCT and Euler Godunov analysis results	96
3.12	Comparison of Analysis Results Obtained Using LS-DYNA, Air3D, AUTODYN and UFC-3-340	98
3.13	Clearing Effects	103
4	**INFLUENCE OF CHARGE SHAPE, ORIENTATION AND POINT OF DETONATION**	**109**
4.1	Introduction	109
4.2	Influence of Charge Shape on Overpressure Histories	109
4.2.1	Sample problem	109
4.2.2	AUTODYN analyses	110
4.2.2.1	10 kg spherical charge	110
4.2.2.2	10 kg cylindrical charges	111
4.2.3	Results and discussion	113
4.2.4	Effect of charge mass	131
4.3	Influence of Detonation Point on Overpressure Histories	138
4.3.1	Modeling and analysis	138
4.3.2	Results and discussion	139
4.4	Influence of Charge Shape on Structural Response	148

Table of Contents (Cont'd)

Section	Title	Page
4.4.1	Sample problem and numerical models	148
4.4.2	Results and discussion of the baseline analysis using a spherical charge	152
4.4.3	Analysis using cylindrical charges	157
4.4.4	Results and discussions of analysis using cylindrical charges	158
5	**SUMMARY, CONCLUSIONS AND RECOMMENDATIONS**	**169**
5.1	Summary	169
5.2	Conclusions and Recommendations for Modeling and Analysis	170
5.3	Recommendations for Future Research	173
6	**REFERENCES**	**175**
Appendix A	**Supplemental Overpressure Histories**	**183**

List of Figures

Figure	Title	Page
1-1	Blast-wave parameters for a free air spherical TNT burst (from UFC-3-340, (DoD, 2008))	3
1-2	Positive phase blast-wave parameters for a hemispherical TNT surface burst (from UFC-3-340, (DoD, 2008))	4
1-3	Incident pressure history at a point due to a blast (from UFC-3-340, (DoD, 2008))	5
1-4	Reflected pressure coefficients as a function of angle of incidence (from UFC-3-340, (DoD, 2008))	6
1-5	Scaled reflected impulse as a function of angle of incidence (from UFC 3-340, (DoD, 2008))	7
2-1	Classification of explosives according to performance and sensitivity (adapted from Akhavan (2004))	14
2-2	A physical model of a detonation wave depicting the jump-discontinuity, rarefaction wave and the reaction zone (adapted from (Davis, 1982))	16
2-3	The pressure-distance curve showing the profile of a detonation wave (Zukas and Walters, 1998)	17
2-4	Shock wave development due to detonation of a cylindrical charge (Reisler, 1972)	29
3-1	Grid deformation in a Lagrangian analysis (Birnbaum, et al., 1999)	35
3-2	A typical computation step in a Lagrangian analysis (Century Dynamics, 2009a)	36
3-3	A highly distorted mesh due to impact of a projectile (Birnbaum, et al., 1999)	37
3-4	Material flow through a stationary grid in an Eulerian analysis (Birnbaum, et al., 1999)	38
3-5	Optimal mesh rezoning using the ALE formulation (Birnbaum, et al., 1999)	39
3-6	Detonation of a spherical TNT charge in free air with a rigid column at a standoff distance of 3m	42
3-7	Reflection of pressure waves generated by a free-air blast at a rigid surface (Glasstone and Dolan, 1977)	43
3-8	Location of the monitoring points on the face of the column	45
3-9	Symmetric FE model with cuboid-shaped meshes for air (red), explosive (blue) and the rigid column (green); mesh configuration 1	48
3-10	Reflected overpressure histories at point A	54
3-11	Reflected overpressure histories at point B	54
3-12	Reflected overpressure histories at point C	55
3-13	Isosurfaces of pressure showing a non-spherical distribution resulting from the	55
3-14	Radial meshes for the spherical explosive and the air domains	57
3-15	Reduced FE model with fine mesh with elements deleted beyond y = 1m	57
3-16	Finite element models generated using ANSYS preprocessor	58
3-17	Reflected overpressure histories at point A with mesh refinement	60
3-18	Reflected overpressure histories at point B with mesh refinement	60
3-19	Reflected overpressure histories at point C with mesh refinement	61

List of Figures (Cont'd)

Figure	Title	Page
3-20	Contour plot of pressure when the blast wave reaches the column (at t = 0.7 msec)	62
3-21	Contour plot of pressure as the reflected blast wave as it propagates along the height of the column (at t = 1.6 msec)	62
3-22	Pressure contour plot at t = 0; the air is initialized to atmospheric pressure and the explosive is modeled using the option 'INITIAL_VOLUME_FRACTION_ GEOMETRY'	64
3-23	Reflected overpressure histories at point A with mesh refinement	67
3-24	Reflected overpressure histories at point B with mesh refinement	67
3-25	Reflected overpressure histories at point C with mesh refinement	68
3-26	Reflected overpressure histories at point A with updated JWL EOS parameters	70
3-27	Reflected overpressure histories at point B with updated JWL parameters	70
3-28	Reflected overpressure histories at point C with updated JWL parameters	71
3-29	Effect of variation in NADV on the overpressure history at point A	73
3-30	Effect of variation in NADV on the overpressure history at point B	73
3-31	Effect of variation in NADV on the overpressure history at point C	74
3-32	Air3D reflected overpressure histories at point A as a function of cell size	78
3-33	Air3D reflected overpressure histories at point B as a function of cell size	78
3-34	Air3D reflected overpressure histories at point C as a function of cell size	79
3-35	1D wedge filled with TNT and air and modeled with multi-material Eulerian formulation	81
3-36	Incident overpressure histories at a distance of 3.04 m with different EOS used for the detonation products	82
3-37	Incident overpressure histories at a distance of 3.04 m with different cell sizes	83
3-38	Contour plot of pressure at the end (t = 0.6 msec) of the 1D analysis	83
3-39	Pressure contours just after the remapping of 1D output to the 3D air domain	85
3-40	Reflected overpressure histories at point A with mesh refinement	87
3-41	Reflected overpressure histories at point B with mesh refinement	87
3-42	Reflected overpressure histories at point C with mesh refinement	88
3-43	Contour plots of pressure showing the reflection and propagation of the shock wave along the height of the column	90
3-44	Temperature histories at the three monitoring points obtained using AUTODYN	92
3-45	Effect of addition of afterburn energy on the overpressure history at point A	94
3-46	Effect of addition of afterburn energy on the overpressure history at point B	95
3-47	Effect of addition of afterburn energy on the overpressure history at point C	95
3-48	Overpressure histories at Point A obtained using the two Euler solvers	96
3-49	Overpressure histories at Point B obtained using the two Euler solvers	97
3-50	Overpressure histories at Point C obtained using the two Euler solvers	97
3-51	Reflected overpressure histories at point A obtained by numerical analyses	98
3-52	Reflected overpressure histories at point B obtained by numerical analyses	99
3-53	Reflected overpressure histories at point C obtained by numerical analyses	99
3-54	Shock front interaction with a structure of finite dimensions (Norris, et al., 1959)	103

List of Figures (Cont'd)

Figure	Title	Page
3-55	Reflected overpressure histories at point A2 with and without clearing	106
3-56	Reflected overpressure histories at point A1 with and without clearing	107
3-57	Reflected overpressure histories at point A with and without clearing	107
4-1	Pressure contours (kPa) at the beginning of the 2D analysis with the spherical charge	111
4-2	AUTODYN 2D models for the first stage of the analyses	112
4-3	Monitoring gauges in the radial and axial directions of the cylindrical charges (second stage of analysis)	113
4-4	Overpressure histories at an axial distance of 10 charge diameters ($Z = 1.05$ m/kg $^{0.33}$)	116
4-5	Overpressure histories at an axial distance of 20 charge diameters ($Z = 2.10$ m/kg $^{0.33}$)	117
4-6	Overpressure histories at an axial distance of 30 charge diameters ($Z = 3.15$ m/kg $^{0.33}$)	117
4-7	Overpressure histories at an axial distance of 40 charge diameters ($Z = 4.20$ m/kg $^{0.33}$)	118
4-8	Overpressure histories at a radial distance of 10 charge diameters ($Z = 1.05$ m/kg $^{0.33}$)	119
4-9	Overpressure histories at a radial distance of 20 charge diameters ($Z = 2.10$ m/kg $^{0.33}$)	120
4-10	Overpressure histories at a radial distance of 30 charge diameters ($Z = 3.15$ m/kg $^{0.33}$)	120
4-11	Overpressure histories at a radial distance of 40 charge diameters ($Z = 4.20$ m/kg $^{0.33}$)	121
4-12	Peak incident overpressure in the axial direction as a function of normalized distance	122
4-13	Incident impulse in the axial direction as a function of normalized distance	123
4-14	Peak incident overpressure in the radial direction as a function of normalized distance	123
4-15	Incident impulse in the radial direction as a function of normalized distance	124
4-16	Calculation of peak incident overpressure and positive phase incident impulse	124
4-17	Pressure contours (kPa) for the spherical and *Cyl_I* charges	127
4-18	Pressure contours (kPa) for the spherical and *Cyl_III* charges	128
4-19	Pressure contours (kPa) for the spherical and *Cyl_V* charges	129
4-20	Secondary impulse in the axial direction as a function of normalized distance	130
4-21	Secondary impulse in the radial direction as a function of normalized distance	131
4-22	Overpressure histories at an axial distance of 10 charge diameters ($Z = 1.05$ m/kg $^{0.33}$)	132
4-23	Overpressure histories at an axial distance of 30 charge diameters ($Z = 3.15$ m/kg $^{0.33}$)	132

List of Figures (Cont'd)

Figure	Title	Page
4-24	Overpressure histories at a radial distance of 10 charge diameters (Z = 1.05 m/kg $^{0.33}$)	133
4-25	Overpressure histories at a radial distance of 30 charge diameters (Z = 3.15 m/kg $^{0.33}$)	133
4-26	Incident overpressure at a scaled distance of 2.1 m/kg $^{0.33}$ in the axial direction	134
4-27	Incident overpressure at a scaled distance of 2.1 m/kg $^{0.33}$ in the radial direction	135
4-28	Peak incident overpressure in the axial direction as a function of normalized distance	136
4-29	Incident impulse in the axial direction as a function of normalized distance	136
4-30	Peak incident overpressure in the radial direction as a function of normalized distance	137
4-31	Incident impulse in the axial direction as a function of normalized distance	137
4-32	2D axially symmetric model of the end-detonated cylindrical charge, *Cyl_V*	139
4-33	Pressure contours for the Cyl_I_{CD} and Cyl_I_{ED} charges	140
4-34	Pressure contours for the Cyl_III_{CD} and Cyl_III_{ED} charges	142
4-35	Pressure contours for the Cyl_V_{CD} and Cyl_V_{ED} charges	143
4-36	Overpressure history in the +x direction at a normalized distance of 30 charge diameters	144
4-37	Overpressure history in the +x direction at a normalized distance of 40 charge diameters	144
4-38	Overpressure history in the -x direction at a normalized distance of 30 charge diameters	145
4-39	Overpressure history in the -x direction at a normalized distance of 40 charge diameters	145
4-40	Incident impulse as a function of normalized distance in the +x direction	146
4-41	Incident impulse as a function of normalized distance in the -x direction	147
4-42	Incident impulse as a function of normalized distance in the radial direction	147
4-43	AUTODYN numerical models of the sample problem	149
4-44	Stress-strain relationships for AISI 1006 and ASTM A992 steels	151
4-45	Locations of the monitoring gauges	152
4-46	Reflected overpressure and temperature histories at the mid-height of the column on its front face	153
4-47	Reflected overpressure and temperature histories at the quarter height of the column on its front face	154
4-48	Reflected overpressure and temperature histories near the top boundary of the column on its front face	154
4-49	Fringe plots of pressure on a horizontal plane at the mid-height of the column	155
4-50	Shear force history at the top boundary and displacement history at the mid-height of the column for the spherical charge	156
4-51	Fringe plot of effective plastic strain at peak displacement	157
4-52	Two orientations of the cylindrical charges	158

List of Figures (Cont'd)

Figure	Title	Page
4-53	Reflected overpressure histories for the spherical and vertical (A) cylindrical charges	160
4-54	Reflected overpressure histories for the spherical and horizontal (B) cylindrical charges	161
4-55	Shear force histories for the spherical and vertical (A) cylindrical charges	162
4-56	Displacement histories for the spherical and vertical (A) cylindrical charges	163
4-57	Fringe plots of effective plastic strain at peak displacement for the vertical (A) cylindrical charges	163
4-58	Shear force reaction histories for the spherical and horizontal (B) cylindrical charges	165
4-59	Displacement histories for the spherical and horizontal (B) cylindrical charges	165
4-60	Fringe plots of effective plastic strain at peak displacement for the horizontal (B) cylindrical charges	166

List of Tables

Table	Title	Page
1-1	Dynamic Increase Factors (DIFs) for structural steels (adapted from DoD, 2008)	2
2-1	Combustion reactions occurring during afterburning (Donahue, 2009)	20
3-1	Blast-wave parameters at the 3 monitoring points in Figure 3-7 calculated using UFC-3-340	46
3-2	Mesh configurations used in the LS-DYNA cuboid explosive model	49
3-3	Material model parameter values for explosive and air	50
3-4	JWL and ideal gas EOS parameter values for explosive and air	51
3-5	Comparison between results of UFC-3-340 calculations and the cuboid explosive model in DYNA with the very fine mesh	56
3-6	Mesh configurations for the modified spherical explosive FE model	59
3-7	Comparison between results of UFC-3-340 calculations and modified spherical explosive model in LS-DYNA	61
3-8	Mesh details for the 'INITIAL_VOLUME_FRACTION_GEOMETRY' model	65
3-9	Blast-wave parameters calculated using UFC-3-340 and the 'INITIAL_VOLUME_ FRACTION _GEOMETRY' model in LS-DYNA	66
3-10	LNLL JWL EOS parameters (Dobratz and Crawford, 1985)	69
3-11	Blast wave parameters calculated using UFC-3-340 and the 'INITIAL_VOLUME_ FRACTION_GEOMETRY' model in LS-DYNA with updated JWL parameters	71
3-12	Results of UFC-3-340 calculations and the 'INITIAL_VOL….' model in LS-DYNA with different values of NADV	74
3-13	Cell sizes used in 1D, 2D and 3D Air3D calculations	77
3-14	Comparison of Air3D results and UFC-3-340 calculations	77
3-15	Grid details for the AUTODYN analyses	86
3-16	Comparison of blast-wave parameters obtained from AUTODYN and UFC-3-340 calculations	88
3-17	Results of analyses with varying afterburn energies	94
3-18	Blast-wave parameters at point A from numerical analyses and UFC-3-340	100
3-19	Blast-wave parameters at point B from numerical analyses and UFC-3-340	100
3-20	Blast-wave parameters at point C from numerical analyses and UFC-3-340	101
3-21	Comparison of blast-wave parameters at a point of normal reflection (centre of the face of the column)	102
3-22	Effect of clearing on peak reflected overpressure and reflected impulse	104
4-1	Notation for the cylindrical charges	113
4-2	Values of parameters in the J-C model for AISI 1006 steel (Johnson and Cook, 1983)	151
4-3	Peak reflected overpressure and reflected impulse on the W column	162
4-4	Comparison of key response parameters for the spherical and cylindrical charges	167

SECTION 1

INTRODUCTION

1.1 Design of Blast-Resistant Structures

Technical manuals and design standards such as UFC-3-340 (DoD, 2008) and the ASCE Blast Standard (ASCE, forthcoming) can be used to design blast tolerant buildings and other structures. UFC-3-340 includes analysis and design procedures for different types of construction materials and structural framing systems. Guidance is provided for the calculation of the load effects due to internal and external detonations of chemical explosives. Empirical design curves are provided for the calculation of incident overpressure histories for free-air and surface detonations for which the explosive charge shape is assumed to be spherical (free-air detonation) or hemispherical (surface detonation). The empirically derived curves are based on regression analysis of field test data collected by the US Department of Defense over the course of many decades. Load effects (reflected overpressures) on structural components are computed by multiplying incident overpressures (pressure above ambient) by reflection coefficients.

Demands on structural components are generally computed using the load effects and single-degree-of-freedom representations of structural components. Norris et al. (1959), Biggs (1964), Baker (1973), Smith and Hetherington (1994) and other texts provide the technical basis for the calculation of the single-degree-of-freedom properties of a structural component or structural framing system. The resistance of a structural component is computed using materials standards such as the American Institute of Steel Construction, AISC Steel Construction Manual (2005) and the American Concrete Institute, ACI-318-08, Building Code Requirements for Structural Concrete (2008). These materials standards assume quasi-static loading of structural components and framing systems, which is appropriate for gravity, wind and earthquake loading. The rate of loading of components and systems subjected to the effects of detonations of chemical explosives is one or more orders of magnitude greater than that due to more conventional

extreme loadings such as earthquakes and high winds. Materials such as steel and concrete exhibit greater strength when loaded at high rates and standards and manuals for blast-resistant design allow nominal component strengths to be increased by Dynamic Increase Factors to account for rate effects. Table 1-1, which is adapted from UFC-3-340, provides sample information on Dynamic Increase Factors (DIFs) for 3 grades of structural steel. In this table, factors are provided to compute the yield and tensile strength of components subjected to flexure or axial loading. The DIF for yield strength is a function of the loading pressure (high, low) that is assumed to depend on the distance between the target and the point of detonation (near-field, far-field). (Further information is provided in the UFC and Chapter 4 of the *Handbook for Blast Resistant Design of Buildings* (Dusenberry, 2010))

Table 1-1: Dynamic Increase Factors (DIFs) for structural steels (adapted from DoD, 2008)

		Yield strength for flexure		Yield strength for axial load		
ASTM grade	Minimum yield stress (ksi)	Low pressure[1]	High pressure[1]	Low pressure[1]	High pressure[1]	Tensile strength
A36	36	1.29	1.36	1.19	1.24	1.10
A588	50	1.19	1.24	1.12	1.15	1.05
A514	100	1.09	1.12	1.05	1.05	1.00

1. Low and high pressures correspond to far-field and near-field detonations, respectively; see UFC-3-340 (DoD, 2008) or *Handbook for Blast Resistant Design of Buildings* (Dusenberry, 2010) for details.

1.2 State-of-the-Practice for Computing Blast-Load Effects

The state-of-the-practice for computing load effects due to detonations of chemical explosives ranges from the use of the empirical design charts developed by the US Department of Defense (and the UK Ministry of Defense) to calculations using computational fluid dynamics (CFD) codes. Nearly all load-effect calculations are performed using the empirical charts that are presented in a number of resource

documents, including UFC-3-340. Charts are provided to compute key blast wave parameters such as peak incident overpressure, incident impulse, time of arrival, and positive phase duration, for free-air bursts of spherical charges and surface bursts of hemispherical charges. The point of detonation is assumed to be the middle of the sphere. Figure 1-1 and Figure 1-2, which are reproduced from UFC-3-340, present data for (spherical) free-air and (hemispherical) surface bursts, respectively as a function of scaled distance, where the scaled distance Z $(= R / W^{0.33})$ is a function of the mass of the explosive, W, and the distance between the target and the point of detonation, R.

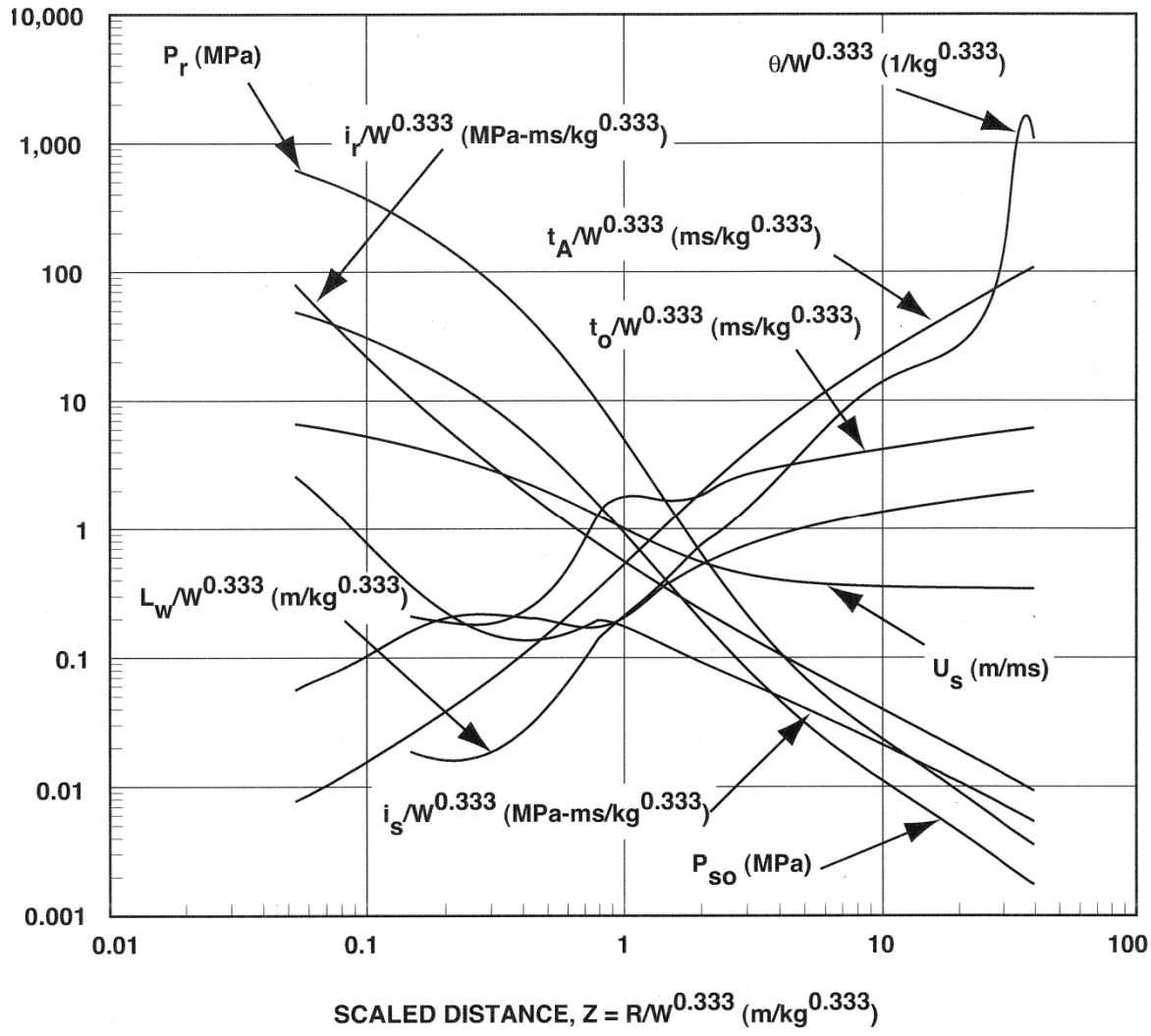

Figure 1-1: Blast-wave parameters for a free air spherical TNT burst (from UFC-3-340, (DoD, 2008))

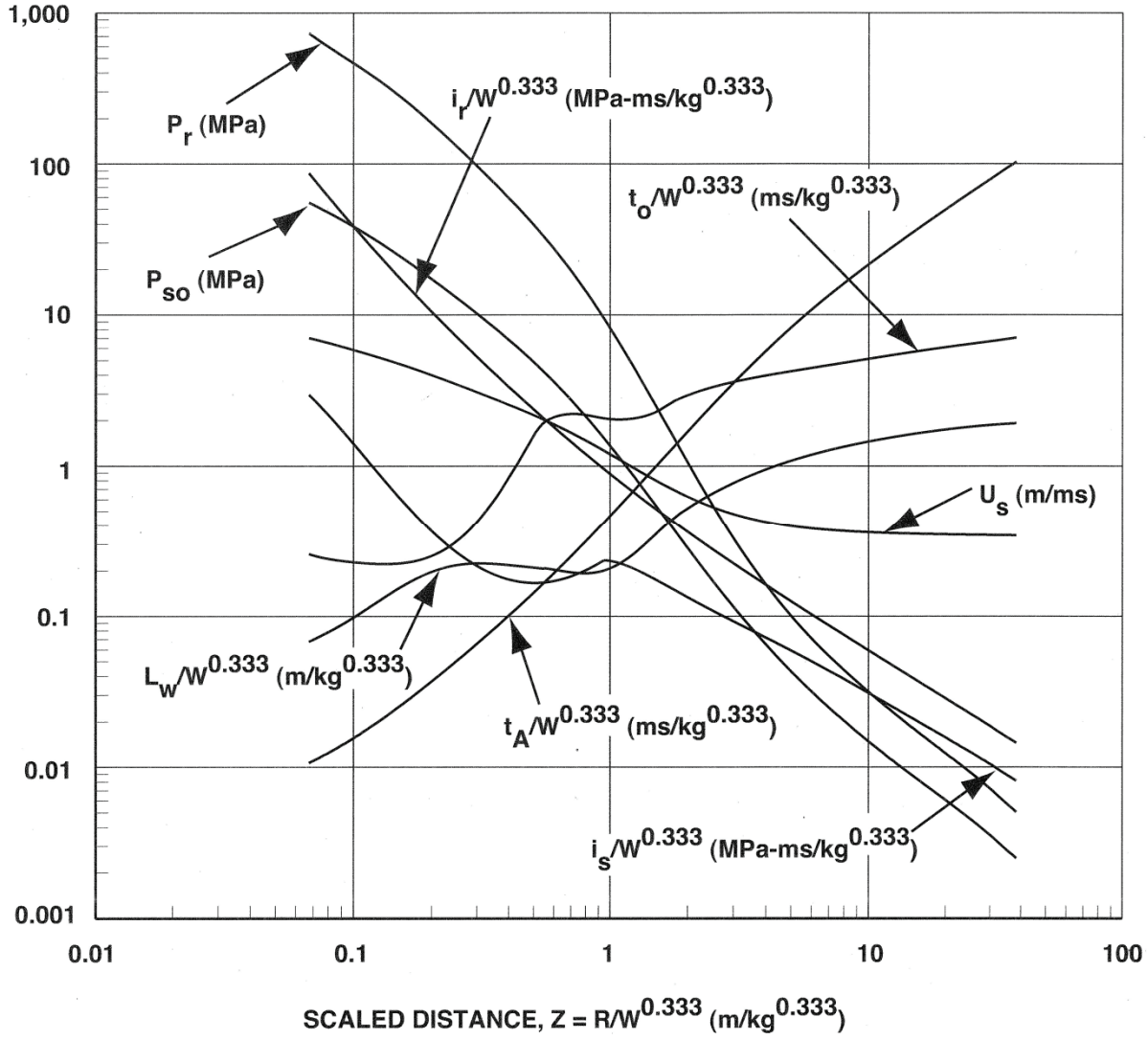

Figure 1-2: Positive phase blast-wave parameters for a hemispherical TNT surface burst (from UFC-3-340, (DoD, 2008))

Figure 1-3, which is also reproduced from the UFC, shows the assumed shape of the pressure history. In these three figures, p_o is the ambient pressure, t_A, is the arrival time of the shock wave, U_s is the shock front velocity, p_{so}, p_{so}^-, i_s, i_s^-, t_o and t_o^- are the positive and negative phase peak overpressures (pressure with respect to ambient), impulses, and durations respectively. The reflected overpressure and impulse at a point of normal incidence are denoted by p_r and i_r, respectively. For design, the true

pressure history that decays exponentially is often replaced by a simplified history that decays linearly from the peak incident overpressure to ambient in a time, t_d, that preserves the incident impulse.

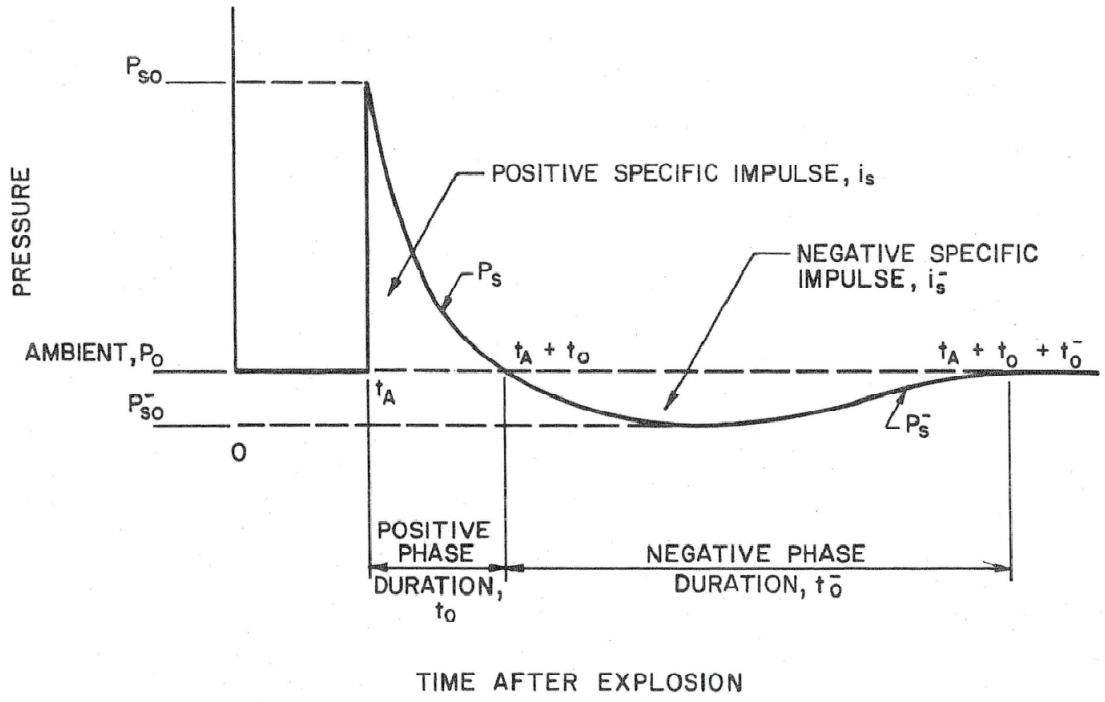

Figure 1-3: Incident pressure history at a point due to a blast (from UFC-3-340, (DoD, 2008))

Blast load effects on structural components and framing systems are generally computed using a peak reflected overpressure (the product of the peak incident overpressure and a reflection coefficient, which varies as a function of the angle of incidence of the blast wave on the component) and a reflected impulse. The angle of incidence α is defined in the inset of Figure 1-4, where an angle of 0 degrees is associated with a normal reflection for which the coefficients are maximized. Peak reflected overpressures and reflected impulses are presented in Figures 1-1 and 1-2 for normal reflections. The coefficients for peak overpressure vary as a function of the peak incident overpressure. Figures 1-4 presents charts for reflection coefficients for peak overpressure and Figure 1-5 presents the scaled reflected impulse as a function of the angle of incidence and peak incident overpressure. The reflected overpressure history is generally assumed to decay linearly from the peak reflected overpressure to ambient in a time to preserve the reflected impulse.

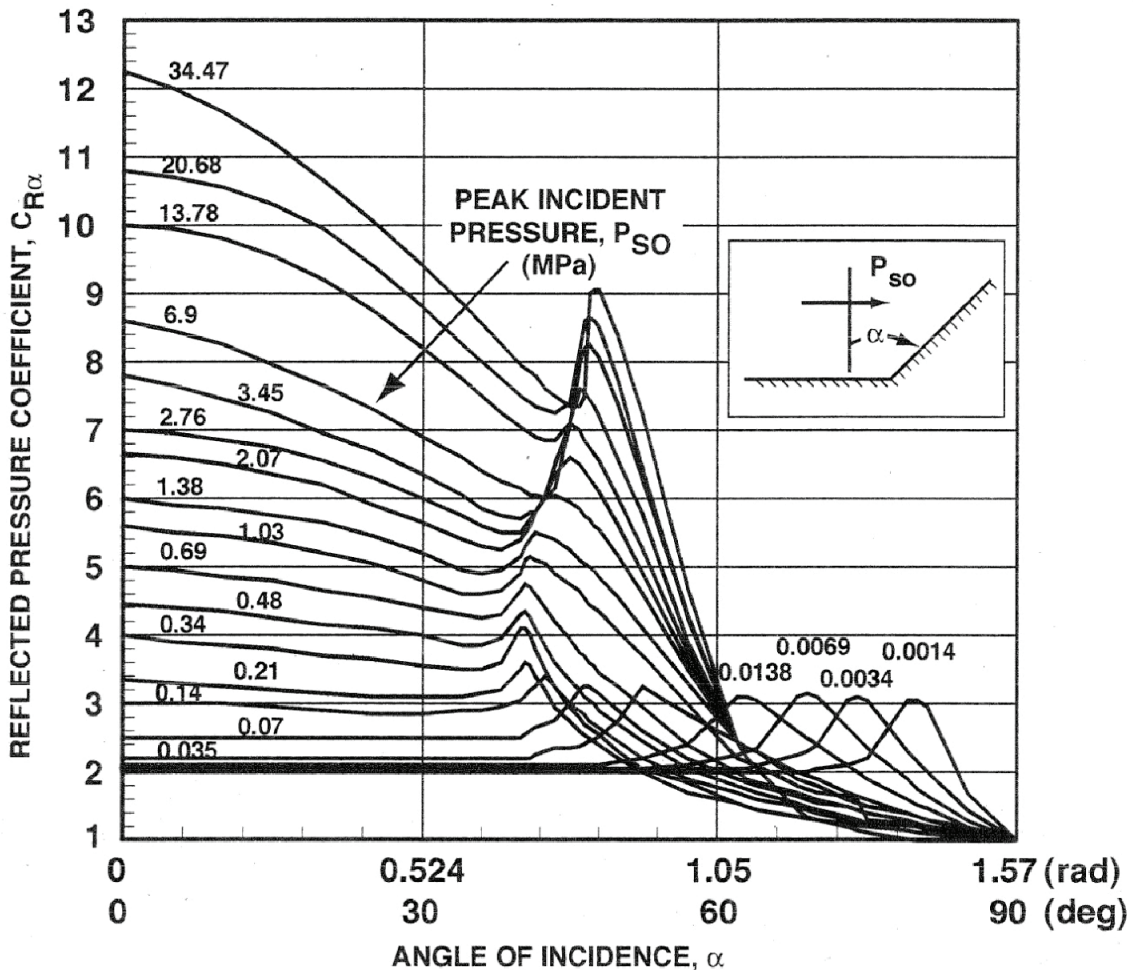

Figure 1-4: Reflected pressure coefficients as a function of angle of incidence (from UFC-3-340, (DoD, 2008))

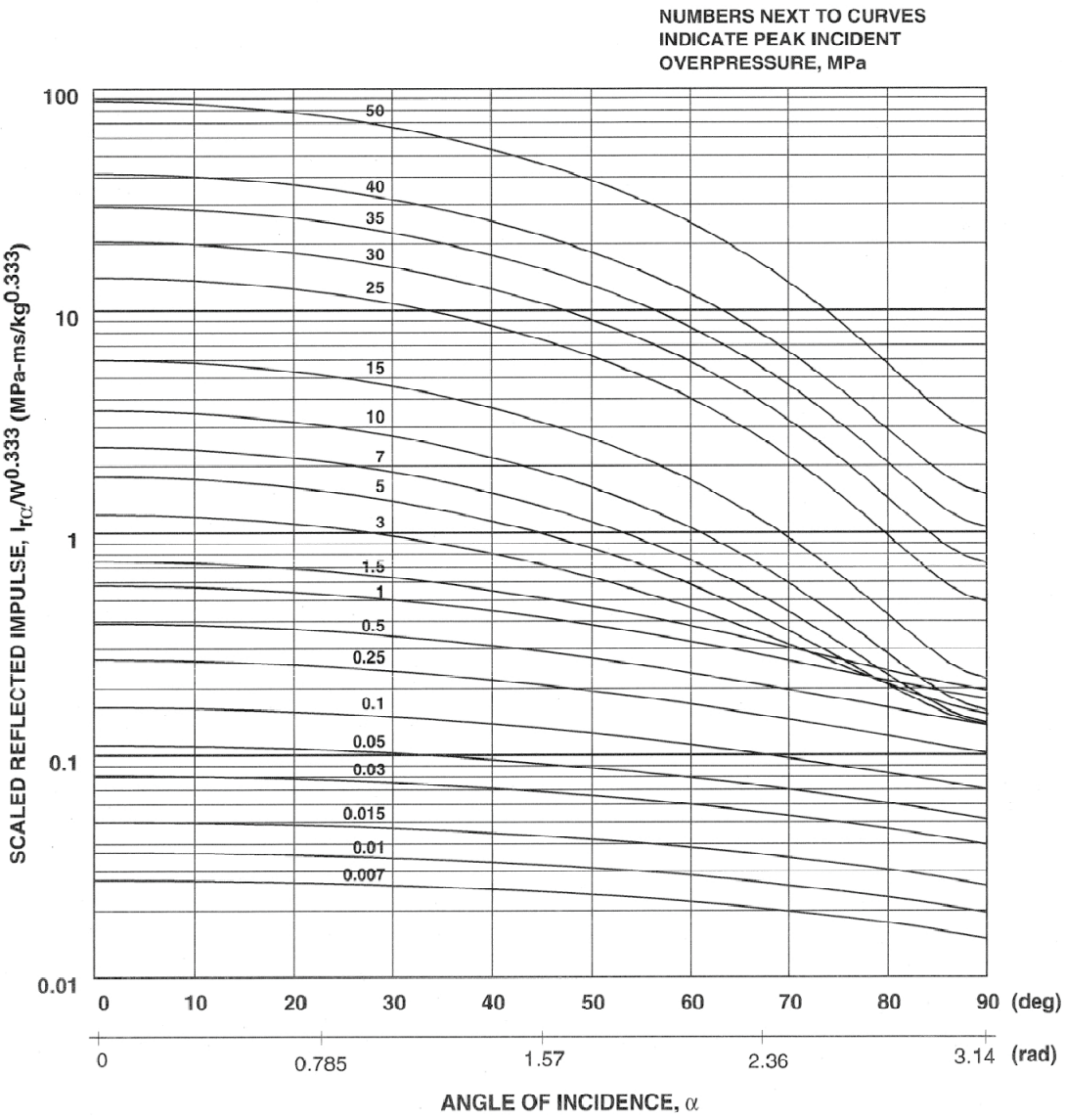

Figure 1-5: Scaled reflected impulse as a function of angle of incidence (from UFC 3-340, (DoD, 2008))

1.3 Calculation of Blast-Load Effects using Computational Fluid Dynamics

There are many computer codes available in the marketplace for calculating fluid loadings on structures. Some of these codes are stand-alone computational fluid dynamics (CFD) codes such as FLUENT (FLUENT Inc., 2003), STAR (CD Adapco Group, 2001) and Air3D (Rose, 2006). Air3D was developed specifically for the calculation of blast load effects. Other CFD codes are embedded in general purpose

finite element (FE) codes (hydrocodes) such as LS-DYNA (LSTC, 2007) and AUTODYN (Century Dynamics, 2009b). Some of these codes (e.g., LS-DYNA and AUTODYN) permit the calculation of pressure fields for the detonation of chemical explosives of arbitrary shapes and sizes, where the point of detonation within the charge can be varied.

1.4 Report Objective and Organization

The key objectives of this report are three-fold, namely, 1) present a comprehensive survey of detonation modeling strategies available in commercially available FE and CFD codes, 2) study the influence of charge shape and the point of detonation in the explosive on the resulting overpressure distributions, 3) investigate the effect of charge shape and orientation on the response of a structural steel column subjected to a near-field blast loading, and 4) provide recommendations for blast-resistant design.

This report consists of 5 chapters including this introduction. Chapter 2 discusses the underlying physical and chemical processes involved in the detonation of chemical explosives and presents a literature review on the numerical modeling of detonations using FE and CFD codes. Chapter 3 presents the results of numerical analyses of a near-field detonation performed using LS-DYNA, AUTODYN and Air3D. Issues related to modeling detonations are discussed. Chapter 4 presents the results of a numerical study on the influence of charge shape, charge orientation and point of detonation in the charge on the overpressure distributions and the response of a structural steel column located in the near-field. Chapter 5 summarizes the studies, lists the key conclusions of the studies and presents recommendations for future research. A list of references follows Chapter 5. Appendix A provides charts that supplement information in Chapter 4.

SECTION 2

LITERATURE REVIEW

2.1 Introduction

The literature review presented in this chapter addresses a number of topics: chemistry of explosives (section 2.2), classification of explosives (section 2.3), detonation physics (section 2.4), techniques for modeling detonations (section 2.5), and the effect of charge shape on the near-field pressure distributions (section 2.7).

2.2 Chemistry of Explosives

Modeling explosive detonations requires a good understanding of chemistry because the chemical composition of an explosive governs its physical properties like detonation velocity (Sundararajan and Jain, 1982). Explosive detonations are products of complex chemical and physical processes within and in the immediate vicinity of the explosive and are accompanied by a near-instantaneous release of a large amount of energy in the form of heat, sound and light. The chemical reactions involved in a detonation are thus exothermic[1] and oxidation reactions because the reactants are oxidized to give a mixture of hot gaseous products.

2.2.1 Oxidation

There are two major types of oxidation reactions involved in a detonation. In the first type, there are two reactants, an oxidizer and a fuel, that react to form the products of the explosion. The second type of reaction, which is more common in explosives, involves a single reactant where the oxidizer and the fuel

[1] A chemical reaction that is accompanied by the release of heat: the energy required for the reaction to proceed is less than the energy released.

are contained in the same molecule, which decomposes during the reaction and is transformed into oxidized products.

The majority of the explosives consist of single molecules made up of Carbon (C), Hydrogen (H), Nitrogen (N) and Oxygen (O). These are called CHNO explosives and can be represented by the general formula $C_cH_hN_nO_o$, where *c*, *h*, *n*, *o* are the number of carbon, hydrogen, nitrogen and oxygen atoms, respectively, contained in one molecule of the explosive. During the decomposition[2] reaction, the reactant molecule breaks down into its individual component atoms as follows

$$C_cH_hN_nO_o \rightarrow cC + h\,H + nN + oO$$

These individual atoms then recombine to form the final products of the reaction. The typical products formed are

$2N \rightarrow N_2$

$2H + O \rightarrow H_2O$

$C + O \rightarrow CO$

$CO + O \rightarrow CO_2$

↓ Order in which the products are formed depending upon the availability of oxygen

If oxygen remains after the formation of carbon dioxide, then the explosive is called over-oxidized. Any oxygen left after the formation of CO_2 forms O_2. However most explosives, with the exception of nitroglycerine and ammonium nitrate, do not have sufficient oxygen to convert all of the carbon to CO_2 and these are called under-oxidized explosives. For such explosives, the products of the reaction extract oxygen from the surrounding air as they expand freely. While doing so, these products mix with oxygen and may burn to form CO_2. These secondary reactions are part of a process known as afterburning.

[2] A decomposition reaction is a chemical reaction in which a compound is separated into individual elements or simpler compounds.

Afterburning is discussed in section 2.4.4. The relative amount of oxygen in an explosive is therefore an important factor in determining the nature and reactivity of the detonation products; it is quantitatively expressed as oxygen balance. The heat generated by an oxygen-deficient explosive (such as trinitrotoluene (TNT)) is less than that generated by an explosive that oxidizes completely.

2.2.2 Oxygen balance

Oxygen Balance (OB) is a method of quantifying how well an explosive provides its own oxidant (Zukas and Walters, 1998). There are various ways to define oxygen balance. Oxygen can be balanced by having one oxygen atom for every carbon atom (balanced for CO) or by having two oxygen atoms for every carbon atom (balanced for CO_2). Generally, the oxygen balance is expressed in terms of the weight percent of excess oxygen compared to the weight of the explosive. Oxygen balance is a useful parameter in many applications and can be correlated to the explosion properties such as gas volume produced and the heat of explosion.

The general formula to calculate the OB for an explosive is (Cooper and Kurowski, 1996);

$$\text{OB} = 100 \frac{AW_o}{MW_{\text{exp}}} \left[o - \left(2c + \frac{h}{2} \right) \right] \tag{2-1}$$

where

AW_o = Atomic weight of oxygen

MW_{exp} = Molecular weight of explosive material

o = Number of oxygen atoms

c = Number of carbon atoms

h = Number of hydrogen atoms

As the atomic weight of oxygen is 16 $\rightarrow$ $$\text{OB (\%)} = \frac{1600}{MW_{\text{exp}}} \left[o - \left(2c + \frac{h}{2} \right) \right] \tag{2-2}$$

Based upon the general formula for a CHNO explosive, $C_cH_hN_nO_o$, the molecular weight of an explosive can be determined as

$$MW_{exp} = 12.01c + 1.008h + 14.008n + 16.000o \quad (2\text{-}3)$$

and the OB for the benchmark explosive, trinitrotoluene or TNT ($C_7H_5N_3O_6$) for which MW_{exp} = 227.13 (from eq. 2-3) is;

$$\text{OB (\%)} = \frac{1600}{227.13}\left[6 - \left(2\,(7) + \frac{5}{2}\right)\right] = -74\ \%$$

A negative sign indicates a deficiency of oxygen. The explosive TNT is therefore highly under-oxidized.

Consider the explosive Nitroglycol, $C_2H_4N_2O_6$, whose molecular weight is 152.07. Its oxygen balance is

$$\text{OB (\%)} = \frac{1600}{152.07}\left[6 - \left(2\,(2) + \frac{4}{2}\right)\right] = 0\ \%$$

which indicates that Nitroglycol is a perfectly-balanced explosive.

Consider a third explosive, Nitroglycerine, $C_3H_5N_3O_9$, for which MW_{exp} = 227.09. Its oxygen balance is

$$\text{OB (\%)} = \frac{1600}{152.07}\left[9 - \left(2\,(3) + \frac{5}{2}\right)\right] = 3.52\ \%$$

which indicates that that it is over-oxidized.

2.3 Classification of Explosives

Explosions can be divided in three major groups; 1) physical explosions such as that of an over-pressurized steam boiler, 2) chemical explosions as described previously, and 3) atomic/nuclear explosions. The focus here is chemical explosions. Explosives are categorized into two groups according to their chemical compositions: substances that are explosive, and substances that are explosive mixtures,

such as blackpowder. In substances that are explosive, it is the molecular groups that have explosive properties. Examples of such molecular groups are (Akhavan, 2004):

1. Nitro compounds
2. Nitric esters
3. Nitramines
4. Derivatives of chloric and perchloric acids
5. Azides
6. Compounds capable of producing an explosion that include fulminates, acetylides, nitrogen-rich compounds such as tetrazene, peroxides and ozonides.

This classification of explosives on the basis of the certain molecular groups is crude and does not provide much information on the likely performance of the explosives. A better way to classify explosives is on the basis of their performance, uses and sensitivity. As shown in Figure 2-1, in this type of classification, explosives are parsed in three classes (Akhavan, 2004);

1. Primary explosives,
2. Secondary explosives and
3. Propellants

2.3.1 Primary explosives

A distinctive feature of primary explosives (also called primary high explosives) is that they undergo a very rapid transition from burning to detonation and can transmit the detonation to less sensitive explosives. They generally detonate when subjected to heat or shock. Detonation of such explosives results in their molecules dissociating and producing tremendous amounts of heat and/or shock, which is why they are often used in initiating devices for secondary explosives. They are very sensitive to initiation by shock, friction, electric spark or high temperatures and their detonation velocities are in the range of 3500-5500 m/s. Examples of primary explosives are lead azide, lead styphante

(trinitroresorcinate), lead mononitroresorcinate (LMNR), potassium dinitrobenzofuran (KDNBF) and barium styphnate.

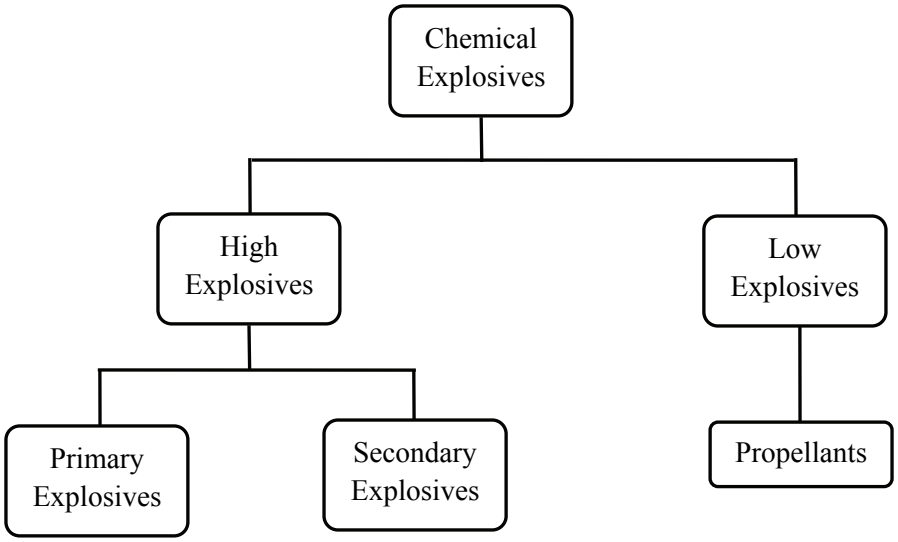

Figure 2-1: Classification of explosives according to performance and sensitivity (adapted from Akhavan (2004))

2.3.2 Secondary explosives

Unlike primary explosives, secondary explosives cannot be detonated easily by heat or shock. They are less sensitive than primary explosives and can only be detonated by a shock produced by a primary explosive. For example, the explosive RDX ($C_3H_6N_6O_6$)[3] explodes violently when triggered by a primary explosive. The intermediate product of the reaction is a disorganized mass of atoms that combine to give predominantly gaseous products in addition to heat. The detonation velocities of secondary explosives range from 5500 to 9000 m/s. Some examples of secondary explosives are TNT (Trinitrotoluene), tetryl, picric acid, nitro-cellulose, nitroglycerine, nitroguanidine, RDX, HMX (octogen), PETN (Pentaerythritoltetranitrate) and TATB (triaminotrinitrobenzene).

[3] RDX forms the basis of a number of military explosives such as Composition A, B and C, Tempex, and the plastic explosives C-4 and Semtex.

2.3.3 Propellants

Propellants are combustible materials containing sufficient oxygen required for their combustion. Propellants burn and do not explode. Their burning is violent, accompanied by flame or sparks and a hissing or crackling sound. They can be initiated by a flame or spark and change from a solid to a gaseous state relatively slowly. Examples of propellants are blackpowder, smokeless propellant, blasting explosives and ammonium nitrate explosives, which do not contain nitro-glycerine or other aromatic nitro compounds.

2.4 Detonation Physics

2.4.1 Introduction

To understand the physics of detonation of an explosive, consider a physical model with the following simplified assumptions (Zukas and Walters, 1998):

1. The model consists of a uniaxial planar wave front with no lateral boundaries that travels in a direction perpendicular to the wave front.
2. The wave front is discontinuous and is handled in a similar way to the jump-discontinuity in simple nonreactive shock waves.
3. The gaseous products behind the detonation front are in chemical and thermodynamic equilibrium and the chemical reaction is complete, that is, the product gases expand as an inert [4] flow.
4. The chemical reaction is completed instantly and the reaction zone length is zero.
5. The detonation process is steady state, that is, the wave velocity is constant and the detonation products are in the same state, regardless of the position of the wave in distance and time.

[4] An inert flow is a flow that is non-reactive, that is, no more reactions can occur within the flow.

The physical model is presented in Figure 2-2. Note that the reaction zone behind the shock front is shown only for explanatory purposes and its length is assumed to be zero. A rarefaction wave is shown behind the shock front reaction zone and represents the expansion of the detonation products from a region of higher density to a region of lower density.

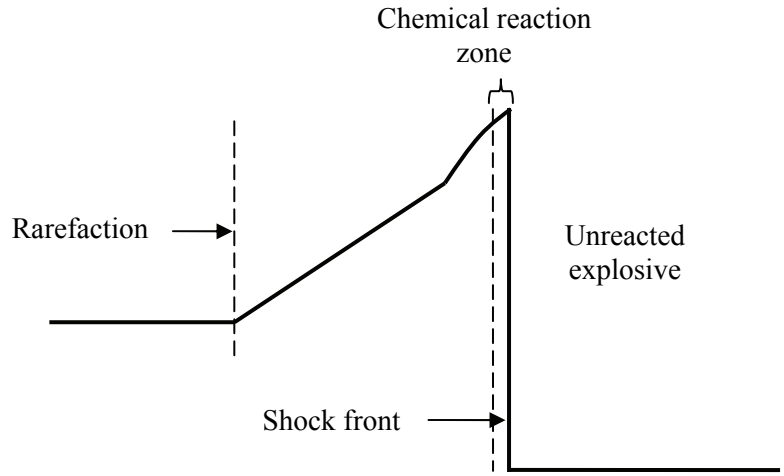

Figure 2-2: A physical model of a detonation wave depicting the jump-discontinuity, rarefaction wave and the reaction zone (adapted from (Davis, 1982))

The detonation process can be viewed as a shock wave moving through an explosive. As the shock front moves ahead, it compresses and thereby raises the temperature of the adjacent unreacted explosive above its ignition point[5]. The heating of the explosive initiates a chemical reaction within a small region just behind the shock front known as the reaction zone. This reaction is exothermic and is completed instantaneously. The energy released by the reaction drives the shock front forward. At the same time the gaseous products of the reaction expand and form a rarefaction wave that moves towards the detonation front. The shock front, chemical reaction and the leading edge of the rarefaction wave are all in equilibrium, and hence are moving at the same speed, which is defined as the detonation velocity.

[5] The ignition point is the minimum temperature at which a substance will spontaneously ignite in a normal atmosphere without an external ignition source

Detonation is a steady-state process and the shock front does not change shape (i.e., pressure remains constant) and the detonation velocity does not change with time. The shock front is basically a discontinuity between moving material and stationary material. Pressure, velocity and density change significantly across a shock front and this phenomenon is known as the detonation jump.

2.4.2 Detonation wave profile and the Chapman-Jouget state

To understand the detonation jump condition from the unreacted explosive to the gaseous products, consider the idealized profile of a detonation wave in Figure 2-3. The spike at the front of the detonation wave is called the Von Neuman spike and is the shock state that initiates the reaction. The thin region behind the Von Neuman spike is the reaction zone where all of the chemical reaction takes place. In the model discussed in section 2.4.1, the Von Neuman spike is ignored and the reaction zone thickness is assumed to be zero (Zukas and Walters, 1998) (In most explosives, the width of the reaction zone is approximately 1 mm (Cooper and Kurowski, 1996)). The tail end of the reaction zone is termed Chapman-Jouget (C-J) plane and its state (pressure, density, shock velocity) is characteristic of an explosive material with given initial density. The rarefaction wave that is responsible for bringing the gaseous products from the C-J state to the fully expanded state at ambient pressure is called the Taylor wave.

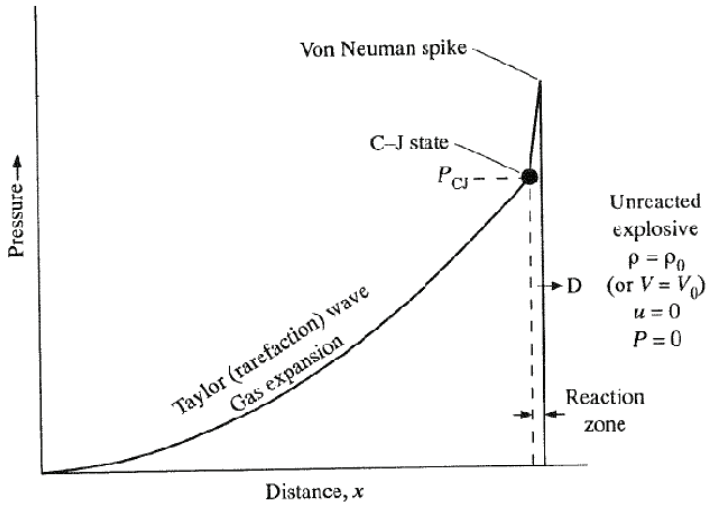

Figure 2-3: The pressure-distance curve showing the profile of a detonation wave (Zukas and Walters, 1998)

2.4.3 Rankine-Hugoniot jump equations

The calculation of the changes (jumps) in pressure, velocity and density across a shock front leads to a set of equations known as the Rankine-Hugoniot jump equations that are based on the conservation of mass, momentum and energy. The Rankine-Hugoniot jump equations are derived below. How these equations are then used to find a solution for a shock problem is then presented.

Consider a moving shock wave. The material in the region in front of the shock is at an initial density ρ_o. As the shock wave moves through this region, the material is compressed and the density increases from ρ_o to ρ. Let a be the area of a region swept by the shock wave. The law of conservation of mass requires that the mass of the material in the region before and after the passage of the shock wave remain the same. This yields the mass balance equation:

$$\rho_o a\ U\ t\ =\ \rho a\ (U - u)\ t \tag{2-4a}$$

$$\frac{\rho}{\rho_o}\ =\ \frac{U}{U\ -\ u} \tag{2-4b}$$

where U is the detonation velocity, and u is the particle velocity.

The passage of the shock wave through a region changes the velocity of the material in the region from 0 to u. This results in a change of momentum of the material equal to $(\rho_o aUt)u$. By definition, the change in momentum is the impulse, namely, the product of force and time. If the pressure generated by the shock-wave compression in the material is p and its initial pressure is p_o, the force exerted on the material is equal to $(p - p_o)a$. The law of conservation of momentum requires the change in momentum to be equal to force multiplied by time, namely,

$$(p\ -p_o)a\ t\ =\ \rho_o aUut \tag{2-5a}$$

$$p\ -p_o = \rho_o Uu \tag{2-5b}$$

The third quantity that is conserved is energy. Energy balance requires that the change in kinetic energy of the material should be equal to the change in its internal energy. The change in kinetic energy of the material is $0.5\rho_o aUtu^2$. If E_o and E are the initial and final specific internal energies[6], the change in internal energy is $(E - E_o)\rho_o aUt$. Conservation of energy yields the third Rankine-Hugoniot equation,

$$(E - E_o)\rho_o aUt = \frac{1}{2}\rho_o aUtu^2 \tag{2-6a}$$

$$E - E_o = \frac{1}{2}u^2\left[\frac{p + p_o}{p - p_o}\right] \tag{2-6b}$$

The Rankine-Hugoniot jump equations, 2-4, 2-5 and 2-6, involve five variables (ρ, p, E, u, U). As the number of equations available is less than the number of unknowns by two, the solution of the problem requires two more equations. A fourth equation can be an Equation of State (EOS) that represents the behavior of the expanding gases generated by the detonation. An EOS relates the pressure p with the density ρ and the specific energy E of the material. An EOS is calibrated based on experimental data and is discussed in section 3.2. The fifth equation is a known value of one of the variables.

2.4.4 Afterburning of detonation products

Section 2.4.2 discussed the process of detonation and the propagation of the detonation wave through an explosive. The discussion assumed that all the energy of the explosive is released upon detonation and used to drive the shock front forward. However, for under-oxidized explosives, this assumption is not necessarily correct. For such explosives there exists an additional energy-release mechanism. This energy-release mechanism becomes clearer by investigation of the chemistry involved after the detonation of an under-oxidized explosive. Consider TNT, an under-oxidized explosive that does not have sufficient

[6] Internal energy is the sum of all forms of energy of a system and is a function of the molecular structure and the degree of molecular activity of the particles of the system.

oxygen to completely oxidize. As the shock wave moves away from the explosive and passes through the surrounding air, the detonation products consume oxygen from the air and oxidize. This process is termed *afterburning* (Donahue, 2009). Afterburning involves combustion reactions that release energy and increase the temperature of the affected region, enhancing the effects of detonation. Unlike detonation, where the release of energy takes place in micro-seconds, afterburning is a process that can last milliseconds to seconds.

There are two requirements essential for afterburning to occur: 1) the temperature in the region should be high enough for combustion reactions to take place, and 2) there must be enough oxygen in the ambient air. TNT is a fuel-rich explosive, with the main fuels being Carbon (C), Carbon Monoxide (CO), Hydrogen (H_2), and Methane (CH_4). These species undergo combustion reactions when the respective ignition temperatures T_{ig} are reached. The combustion reactions with their associated heats of reaction ΔH_r [7] and ignition temperatures T_{ig} are presented in Table 2-1.

Table 2-1: Combustion reactions occurring during afterburning (Donahue, 2009)

Oxidation reaction	Ignition temperature (^oK)	Moles of fuel/moles of TNT	Heat of reaction ΔH_r (kJ/mole of fuel[1])	Afterburn energy ΔH_{ab} (kJ/mol-TNT)
$CO + 0.5O_2 \rightarrow CO_2$	880	2.233	282.80	631.49
$H_2 + 0.5O_2 \rightarrow H_2O$	850	0.3516	241.80	85.02
$C + O_2 \rightarrow CO_2$	975	3.410	393.60	1342.18
$CH_4 + 2O_2 \rightarrow CO_2 + 2H_2O$	850	0.2656	800.00	212.48
Total energy of afterburning combustion:				2271.17 kJ/mol-TNT = 10.01 MJ/kg-TNT

1. Fuel is the species reacting with oxygen

[7] Heat of reaction, ΔH_r, is the amount of heat added or removed during a chemical reaction. A positive value of ΔH_r means that heat is released and a negative value of ΔH_r means heat is absorbed during the reaction.

From the information presented in Table 2-1, if the temperature is around 1000 ^{o}K and sufficient oxygen is present then all the combustion reactions occur and energy is released. If all of the fuel is depleted, the released afterburn energy (10.01 MJ/kg) is more than twice the detonation energy of 4.3 MJ/kg (Donahue, 2009).

2.5 Modeling Detonation

Experimental studies of blast problems require special and expensive instrumentation given the highly dynamic or impulsive nature of the loading. Large-scale blast tests can cost millions of dollars (Zukas, 2004). Numerical simulation of blast experiments can avoid the need to conduct such experiments if the mathematical models are robust. Numerical modeling of detonations includes modeling of the shock-wave propagation through the explosive and its subsequent passage through the surrounding medium. Closed-form solutions of blast wave propagation from a spherical charge were developed by Brode (1959). However, for complex problems involving non-spherical charges, fluid-structure interaction, and multiple reflections of blast waves, analytical solutions are unavailable and numerical simulations are required. Explicit modeling of the detonation process can be undertaken using finite element (FE) codes and hydrocodes[8] such as LS-DYNA (LSTC, 2007) and AUTODYN (Century Dynamics, 2009b). Indirect methods to model detonations, such as the balloon analog of Ritzel and Mathews (1997), have been developed and implemented in some analysis codes.

2.5.1 Explicit modeling

Explicit modeling of the detonation process involves creating a physical finite element (FE) model of the explosive and the surrounding air. The first task involves generating FE meshes for the air and explosive and applying the appropriate boundary conditions. The FE model consists of a Lagrangian mesh for solids and an Eulerian mesh for gases or fluids. The Arbitrary Lagrangian-Eulerian (ALE) formulation, a

[8] A hydrocode is a computer program for the study of very fast, very intense loading on materials and structures (Zukas 2004). For information on the development and theory of hydrocodes, see Zukas (2004).

formulation that combines both the Lagrangian and Eulerian techniques can also be used for modeling detonations and fluid structure interaction (Chafi, et al., 2009). More information on these formulations is presented in sections 3.3, 3.4 and 3.5. The second task is to assign material properties and initial conditions by specifying the initial energy, mass of the explosive and the initial temperature and pressure of the surrounding air. An EOS representing the relation between the pressure p, specific internal energy E and the density ρ is assigned to both the air and the detonation products. Equations of state are discussed in more detail in section 3.2. Using this information (EOS, material properties and initial and boundary conditions) and the conservation laws for mass, momentum and energy, a hydrocode solves the differential equations governing the dynamic problem at hand. Such explicit modeling of the detonation process not only allows detailed modeling of the detonation process and the wave propagation through the explosive but also the subsequent passage of the shock wave through the surrounding air and resultant fluid-structure interactions, if any. The advantage of modeling the detonation event explicitly is that no simplifying assumptions are made and the analyst has complete freedom to model any charge shape, size, geometry and point of detonation within the explosive, which should allow an accurate assessment of the blast overpressures. LS-DYNA and AUTODYN are two non-restricted codes used for modeling detonations. These two codes implement finite element, finite difference and/or finite volume techniques but differ in their solution methodology, modeling options and usability.

2.5.2 Indirect modeling

The calculation of overpressure[9] fields remote from the point of detonation can be accomplished by replacing the explosive with an unconfined balloon or sphere with pressurized gas at high temperature. The blast event is initiated by the rupture of the balloon. This can be seen as a shock-tube problem where the balloon represents the driver gas (Ritzel and Mathews, 1997). The methodology is based on the

[9] Overpressure is pressure above ambient atmospheric pressure (101.3 kPa).

seminal work of Brode (1956). The specific internal energy of a pressurized volume of an ideal gas is given by (Brode, 1956);

$$E = \frac{(p - p_o)\, v}{\gamma - 1} \tag{2-7}$$

where E is the specific internal energy, p is the initial static pressure in the balloon, p_o is the ambient pressure, v is the specific volume of the balloon, and γ [10] is the ratio of specific heats for the balloon gas. The blast waveform can be manipulated by keeping the total energy constant and varying the balloon pressure p, temperature T, γ , and molecular weight M, of the gas. The advantages of this method include (adapted from Ritzel and Mathews, 1997)

1. Simple and adjustable explosion-source models can be used in CFD codes to simulate blast wave flows in the mid- and far-fields from explosive sources.
2. The only assumption required is that of an ideal gas with a constant specific heat ratio, γ.
3. The model can be adjusted to provide a good approximation of blast waves from real explosive sources that cannot be energy-scaled[11].
4. The analog can be used in computer codes that allow prescribed heat flux to materials to simulate explosive afterburning of under-oxidized explosives like TNT.

The balloon analog can also be used to model cylindrical charges by keeping the aspect ratio of the balloon the same as that of the explosive. The shortcoming of the balloon analog, which was identified by its authors, is that it yields good results only in the mid- and far-fields. A comparison of this modeling

---

[10] The specific heat ratio $\gamma = C_p / C_v$, where C_p and C_v are specific heats at constant pressure and constant volume, respectively.

[11] Energy based scaling (also called Sachs blast scaling) is used for scaling blast parameters. The Sachs scaling law states that pressure, time, impulse can be expressed as a function of the scaled distance given by $\overline{R} = R\, p_o^{1/3} / \xi^{1/3}$ where R is the radial distance from the explosive charge, ξ is the total charge energy, and p_o is the ambient pressure.

methodology with field experiments (Anderson, et al., 2002) illustrated the limitation of the balloon analog in the near-field.

2.5.3 Modeling afterburn

As afterburning involves chemical reactions and time-dependent energy release, it is very difficult to include it in the analytical solution of even a simple detonation problem. The modeling of afterburn energy release using CFD codes is also a challenge, but there have been some developments in the past few years. Ritzel and Mathews (1997) demonstrated the effect of afterburning simulation with the IFSAS (Integrated Fluid Structure Analysis Software) CFD code and the balloon analog. Half of the initial total explosive energy was stored as detonation or the balloon energy and half was released as afterburn energy. Their results indicated that the addition of afterburn energy resulted in the gases expanding more rapidly, and to a much higher temperature, compared to the case where afterburn is not considered. Afterburning also had an effect of reducing the near-field peak overpressure and increasing the impulse in the far field.

Other computer codes like CHEETAH (Fried, et al., 1998) and CHINOOK (Martec Limited, 2008) have been used to model phenomena like afterburning and the related chemical reactions but these codes are export-controlled by the US government and are not commercially available. Commercial hydrocodes like LS-DYNA model only the physics of the explosive detonation and not the associated chemistry. Afterburning cannot be modeled using LS-DYNA. There is a provision in AUTODYN to model the release of afterburn energy but not the actual chemical reactions. Given the limited capabilities of the commercially available codes to model afterburning and the uncertainty of its role in enhancing the effects of a detonation, afterburning has generally been ignored.

2.6 Modeling Detonations in LS-DYNA, AUTODYN and Air3D

Detonation of high explosives and the resulting blast waves present a highly complex problem that can be analyzed with hydrocodes or codes that use finite element and finite difference techniques. Hydrocodes

like LS-DYNA (LSTC, 2007) and AUTODYN (Century Dynamics, 2009b) are designed specifically for dynamic and highly non-linear problems like impact, penetration and blast events. Computational fluid dynamics (CFD) codes like Air3D (Rose, 2006) and FLUENT (FLUENT Inc., 2003) are also used for fluid dynamics simulations. Although all these computer codes model detonation and blast wave propagation, their modeling strategies differ and each has its advantages and disadvantages for modeling a particular blast problem. Although LS-DYNA has alternate techniques to model a detonation and is capable of simulating fluid-structure interaction, it is not as user-friendly as AUTODYN. AUTODYN has remapping capabilities with which higher mesh resolution can be achieved without much increase in computational cost. Air3D is a CFD code that is based on the balloon analog of Ritzel and Mathews (1997). To understand and apply the best modeling strategy for a given problem, it is worthwhile to review the different modeling techniques implemented by each code.

2.6.1 Modeling detonations in LS-DYNA

LS-DYNA was developed initially as an explicit[12] numerical analysis code and has since been widely used to solve high strain-rate problems or dynamic and impulsive problems with its advanced Eulerian, Lagrangian and Arbitrary Lagrangian-Eulerian (ALE) solvers. A detonation problem with shock wave propagation can be modeled in a number of ways in LS-DYNA. Three methods are discussed here.

As noted in section 2.5.1, explicit modeling of an air-blast problem requires the generation of two separate meshes, one for the explosive and another for the surrounding air. The first modeling technique involves modeling both the explosive and the air elements using multi-material ALE formulations. The multi-material ALE formulation is appropriate for air-blast simulations as an element can contain two or more different materials, such as the air and gases generated by the explosion. It allows the finite element

[12] Explict refers to the numerical method used to solve the time derivatives in the momentum and energy equations. It is a time step procedure where the unknowns at a timestep are calculated using information at previous steps only. Explicit methods are computationally fast but only conditionally stable.

mesh to move independently of the material flow. The ALE formulation is particularly well suited for problems involving fluid-structure interactions. This modeling strategy has been found to model correctly the blast-structure interaction and wave propagation through a medium such as air (Chafi, et al., 2009).

Another way to model an explosion in LS-DYNA requires only a mesh of the air domain. The explosive can be contained within the air mesh by specifying an initial fraction of the air volume occupied by the explosive through the *INITIAL_VOLUME_FRACTION_GEOMETRY option in LS-DYNA. This option is used in conjunction with the ALE multi-material formulation. The explosive geometry can be specified to be of a sphere, a cylinder or a cube.

The third modeling technique is semi-empirical. This technique uses the CONWEP (Hyde, 1988) algorithm built in LS-DYNA to generate pressure histories that can be imposed on a component of a structure. The CONWEP algorithm is based on the empirical data of Kingery and Bulmash (1984) and predicts incident and reflected pressure histories for a given explosive mass and stand-off. This method can model two types of detonations: 1) free-air blast of a spherical charge, and 2) surface blast of a hemispherical charge. This modeling technique reduces substantially the computational cost for blast analyses in the mid and far-field by avoiding the explicit modeling of the detonation process. Another modification to this modeling technique involves the application of pressure histories computed by CONWEP algorithm on the ALE air domain surrounding the structure instead of directly imposing it on the structure (Slavik, 2009). Although this modeling technique reduces the computational cost significantly, empirical expressions cannot be applied with confidence for near field problems because of the complexity of the flow processes involved in the formation of a blast wave (Luccioni, et al., 2006). As CONWEP is based on empirical data, it should be applied to near-field problems with caution because the code has likely not been validated by pressure readings from field experiments involving small scaled ranges and charges of tens to hundreds of kg of TNT-equivalent explosive.

2.6.2 Modeling detonations in AUTODYN

AUTODYN is an explicit analysis program designed for highly nonlinear dynamic problems. Alternate solvers can be used to model different regions of a problem. These solvers include a Lagrangian solver, used for solid continua and structures and the Eulerian solver for modeling gases, fluids and solids that undergo large deformations. AUTODYN also has an efficient and fast single material high resolution Euler Flux Corrected Transport processor for 2D and 3D blast problems. A feature of AUTODYN is its remapping technique where the output of a high resolution initial detonation stage is remapped as initial conditions for the subsequent calculation stage. This allows modeling of the detonation process with very high grid resolution without increasing the computational demand. Similar to LS-DYNA, a large library of material models with different Equations of State is available in AUTODYN to model a wide range of blast problems (Fairlie, 1998).

2.6.3 Modeling detonations in Air3D

Air3D is a CFD Eulerian code that uses the balloon analog of Ritzel and Mathews (1997) to model detonations. It is based on the Advection Upstream Splitting Method (Wada and Liou, 1997) and uses the MUSCL-Hancock time integration method (Toro, 1997) to solve the Euler equations and provide a solution that is second-order[13] accurate in space and time. The input needed for the program is the mass, initial energy and density of the explosive. Using this information and equation 2-7, Air3D models the explosive as a balloon with high pressure and temperature. Applying this bursting sphere analog as discussed in section 2.5.2, Air3D calculates the pressure histories at locations specified by the user. It can model 1D (radial symmetry), 2D (cartesian coordinates) and 3D problems and has remapping capabilities. The key advantages of modeling detonations in Air3D are that it requires limited input and is user friendly. The disadvantages of the code are its inability to model blast-structure interaction and that it

[13] The approximation to a solution is second order accurate if the term ∂t^2 in the Taylor series expansion of the solution is correctly reproduced http://www.ipp.mpg.de/~rfs/comas/Helsinki/helsinki04/compphys/node5.html).

should not be used to characterize overpressures in the immediate vicinity of the explosive: issues clearly identified by the author of the code. Air3D models structures as rigid blocks that function as perfect reflectors, which is a reasonable assumption in many instances (e.g., Ballantyne, et al., 2010).

2.7 Effect of Charge Shape and Orientation on Overpressure Distributions

Design manuals and guidelines such as UFC-3-340-02 (DoD, 2008) and the ASCE Blast Standard (ASCE, forthcoming) compute incident and reflected overpressure histories as a function of the scaled distance, Z $(= R / W^{0.33})$, and the angle of incidence. They typically assume either a spherical free air burst or hemispherical surface burst. The assumption of spherical or hemispherical charge shape is consistent with a point source detonation and was the basis of early calculations of pressure histories from blast loading (e.g., Brode, 1959). Experimental and numerical studies in recent years have explored the influence of charge shape, charge orientation and the point of detonation within the charge on the overpressure distributions. All have been shown to have a significant effect, especially in the near-field. Blast waves generated from a cylindrical charge are very complex compared with a spherical charge and multiple shocks are evident from the resulting pressure histories (Ismail and Murray, 1993). The complex interaction of shock waves generated from a cylindrical charge is shown in Figure 2-4. Spherical waves are generated in both radial and axial directions upon detonation of the cylindrical charge and are denoted as primary waves in the figure. The waves emanating in the radial direction of the cylindrical charge are denoted as primary side waves while those in the axial direction are denoted as primary end waves. As the waves propagate they overlap resulting in "bridging" of the waves that distorts their spherical shape. The bridging here represents the constructive interference between the primary waves resulting in the formation of new reinforced wave denoted as the bridge wave in the figure. The resultant shock waves are non-spherical with geometry that depends upon the orientation of the charge and the point of detonation within the charge.

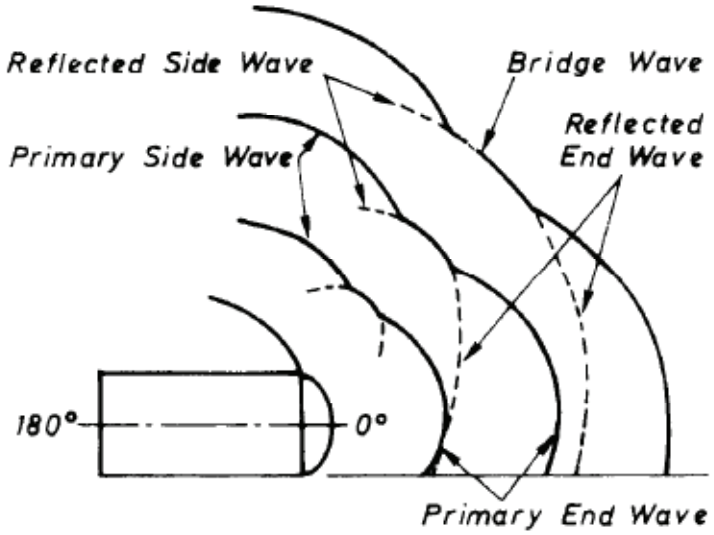

Figure 2-4: Shock wave development due to detonation of a cylindrical charge (Reisler, 1972)

The peak overpressure and overpressure histories depend on the aspect ratio (L/D) of the cylinder where L is length and D is diameter. Numerical studies validated with experimental results by Zimmerman et al. (1999) and Wu et al. (2010) have shown that the aspect ratio governs the amount of energy directed in the radial and axial directions. For larger aspect ratios, more energy is directed in the radial direction whereas for smaller aspect ratios, more energy is directed in the axial direction. The differences increase with increasing aspect ratio. The pressure distributions in the near field are affected by the shape of the charge, the orientation of the charge, horizontal or vertical (Adamik, et al., 2004), and the point of detonation within the charge.

SECTION 3

MODELING THE EFFECTS OF DETONATIONS

3.1 Introduction

This chapter discusses finite element modeling of detonations with an emphasis on modeling tools available in the finite element codes LS-DYNA (LSTC, 2007) and AUTODYN (Century Dynamics, 2009b), and the computational fluid dynamics (CFD) code Air3D (Rose, 2006). Section 3.2 introduces Equations of State and their application to analysis of detonations. Sections 3.3, 3.4, 3.5 and 3.6 introduce the theory and solution algorithms in LS-DYNA, AUTODYN and Air3D for modeling detonations. The advantages and disadvantages of the solution algorithms (or formulations) for applications to detonation problems are identified.

Each of these codes requires the user to select material properties and Equations of State (EOS) to solve the following conservation equations (e.g., Baker, 1973; Aquelet and Souli, 2006)

Conservation of mass:
$$\frac{\partial \rho}{\partial t} + \rho \mathrm{div}(\vec{u}) + (\vec{u} - \vec{w}).\mathrm{grad}(\rho) = 0 \tag{3-1}$$

Conservation of momentum:
$$\rho \frac{\partial \vec{u}}{\partial t} + \overline{\overline{\mathrm{grad}}}(\vec{u})\rho(\vec{u} - \vec{w}) = \mathrm{div}(\overline{\overline{\sigma}}) + \vec{\mathrm{b}} \tag{3-2}$$

Conservation of energy:
$$\rho \frac{\partial E}{\partial t} + \rho(\vec{u} - \vec{w}).\mathrm{grad}(E) = \overline{\overline{\sigma}}.\overline{\overline{\mathrm{grad}}}(\vec{u}) + \vec{\mathrm{b}}.\vec{\mathrm{u}} \tag{3-3}$$

where b, ρ, u, w, σ and E are the body forces, density, particle velocity, mesh velocity, stress, and specific internal energy, respectively. (In these equations, "." denotes an inner product that produces a scalar quantity; the gradient [grad] of a vector field is a tensor field; the divergence [div] of a tensor field is a vector field; and the double overbar implies a tensor.)

An understanding of the analysis strategies in each code is important because their incorrect application to a particular detonation problem could lead to significant errors. Section 3.7 presents a sample problem that is used as the basis for comparing results of CFD analysis. Benchmark data from UFC-3-340, *Design of Structures to Resist the Effects of Accidental Explosions* (DoD, 2008) are presented in section 3.8. Sections 3.9, 3.10 and 3.11 present results of the analyses of the sample problem of section 3.7, using LS-DYNA, Air3D, and AUTODYN, respectively. Mesh sensitivity studies are performed. Results obtained in sections 3.8, 3.9, 3.10 and 3.11 are compared and discussed in section 3.12. The effects of clearing are discussed in section 3.13.

3.2 Equations of State for Explosives and Air

The Rankine-Hugoniot equations represent equilibrium among the state variables across the detonation front as discussed in Chapter 2. The Taylor wave shown in Figure 2-3 represents the isentropic[14] expansion of the detonation product gases from the Chapman-Jouget (C-J) state. The Taylor wave cannot be constructed from the C-J parameters alone. An Equation of State (EOS) or empirical data for the expansion of gases is required for a solution. For detonation problems, the EOS is a thermodynamic relation between the state variables of pressure p, density ρ and the specific internal energy E of the material. The EOS must be specified together with the material properties of the explosive and the surrounding air to model blast wave propagation through air.

3.2.1 Equation of State for air

Unlike nuclear explosions for which the air surrounding the explosive and detonation products is heated to extremely high temperatures (of the order of 1,000,000 ^{o}K) (Glasstone and Dolan, 1977), chemical explosions generally only heat the surrounding air to much lower temperatures (of the order of 3000 ^{o}K) and hence the dissociation of O_2 and N_2 molecules in air does not occur. It is therefore customary in

[14] In an isentropic process, the entropy of the system remains constant.

numerical analyses to treat the air surrounding a chemical explosion as an ideal gas with a constant specific heat ratio γ. The polytropic EOS is a generalized EOS with a linear variation in the specific internal energy E and is given by (Woodruff, 1973).

$$p = C_0 + C_1\mu + C_2\mu^2 + C_3\mu^3 + E\left(C_4 + C_5\mu + C_6\mu^2\right) \tag{3-4}$$

where $C_0, C_1, C_2, C_3, C_4, C_5, C_6$ are constants and $\mu = \rho / \rho_o - 1$, where ρ and ρ_o are the current and initial densities of air. The polytropic EOS can be used to represent an ideal gas EOS by setting $C_0 = C_1 = C_2 = C_3 = C_6 = 0$ and $C_4 = C_5 = \gamma - 1$. Substituting these values in equation 3-4, the EOS for an ideal gas is:

$$p = \left(\gamma - 1\right) \frac{\rho}{\rho_o} E \tag{3-5}$$

Note that the implementation of the polytropic EOS as an ideal gas EOS presented here is that used in LS-DYNA. In AUTODYN, an ideal gas EOS can be specified directly using equation 3-5 and nominating the values of E and γ.

3.2.2 Equations of State for explosives

A number of empirical EOS have been developed for high explosives, including BKW (Becker-Kistiakowski-Wilson) (Mader, 1963, 1967), JCZ (Jacobs-Cowperthwaite-Zwisler) (Cowperthwaite and Zwisler, 1972), LJD (Lennard-Jones-Devonshire) (Fickett, 1962) and JWL (Jones-Wilkin-Lee) (Kury, et al., 1965). The use of each EOS is limited to the range of the experimental data from which it was constructed (Zukas and Walters, 1998). It is therefore essential that an EOS be chosen carefully and calibrated appropriately. Of the EOS identified above, JWL is the most popular and is easily calibrated. Most explosives can be modeled using this EOS (e.g., Alia and Souli, 2006; Mader, 2007).

3.2.2.1 BKW Equation of State

The Becker-Kistiakowski-Wilson EOS is similar to an ideal gas EOS ($p\,v = \mathbb{R}\,T$) except that it has a dominant imperfection term added to it that denotes its deviation from the ideal gas EOS. The BKW EOS is (Zukas, 2004):

$$\frac{p\,v}{\mathbb{R}\,T} = 1 + Xe^{\beta X} \tag{3-6}$$

where $X = b / v\,(T+\theta)^{\alpha}$, v is the specific volume, T is the temperature in ^{o}K, p is the pressure, and $\mathbb{R}$ is the universal gas constant (= 8.314 J/^{o}K-mol). The constants α (exponent), b (covolume) and θ (temperature correction term) are adjusted to match the experimental data. The term $Xe^{\beta X}$ is the imperfection term and has a value between 10 and 15 for most explosives (Zukas, 2004). It is to be noted that the BKW EOS is used for explosives and not air, which explains the magnitude of the imperfection term and the large deviation from the ideal gas EOS. The derivation of this EOS is presented by Mader (2007) with a detailed discussion of its implementation in computer codes. The BKW EOS is convenient in the sense that it can calculate the state of detonation products (C-J pressure, detonation velocity and temperature) once the chemical composition of the explosive, density and heat of formation are known but its use in hydrocodes can be computationally expensive (Hamashima, et al., 2003).

3.2.2.2 JWL Equation of State

The JWL equation is the pressure-volume relationship on the expansion isentrope (the Taylor wave in Figure 2-3) and is given by

$$p = A\left(1 - \frac{\omega}{R_1 V}\right)e^{-R_1 V} + B\left(1 - \frac{\omega}{R_2 V}\right)e^{-R_2 V} + \frac{\omega}{V}E \tag{3-7}$$

where p is the pressure, V is the relative volume, E is the specific internal energy and A, B, R_1, R_2, and ω are constants obtained by calibration of test data. These parameters are determined from the detonation of a cylinder of explosives confined by copper-like metal (Mader, 2007).The C-J pressure is a function of

the kinetic energy and hence velocity of the expanding copper cylinder. The velocity of the expanding copper is measured until the wall of the copper cylinder fractures. Its correlation with the C-J pressure is then used to determine the constants. For a complete derivation of the JWL EOS, the reader is directed to Zukas and Walters (1998) and Alia and Souli (2006), among others. A table of constants for the JWL EOS for many explosives is available in the LLNL Explosives Handbook (Dobratz and Crawford, 1985).

3.3 Lagrangian Analysis

Most of the structural dynamics codes used nowadays perform Lagrangian analyses to develop a solution. In a Lagrangian analysis, the material in an element remains in the element and does not flow in or out of it. The numerical mesh deforms according to the material flow such that no material transport takes place between two elements as shown in Figure 3-1. The coordinates x, velocities u, forces F, and masses m in a mesh are associated with the corner nodes, while stresses σ, strains ε, pressures p, energies e and densities ρ are centered within the cells (Birnbaum, et al., 1999). In a Lagrangian analysis, the mesh velocity is equal to particle velocity ($w = u$) in the conservation equations 3-1 to 3-3. A schematic representation of a calculation step in a Lagrangian analysis is shown in Figure 3-2.

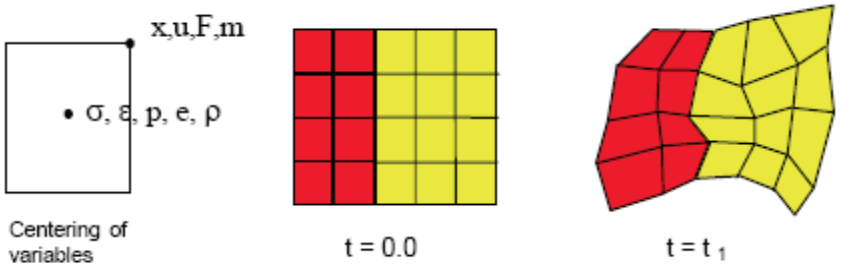

Figure 3-1: Grid deformation in a Lagrangian analysis (Birnbaum, et al., 1999)

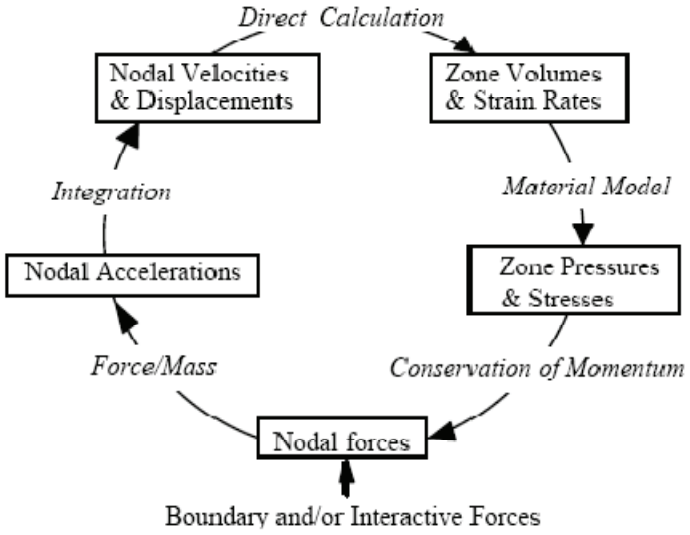

Figure 3-2: A typical computation step in a Lagrangian analysis (Century Dynamics, 2009a)

A distinguishing feature of a Lagrangian analysis is that free surfaces and material interfaces occur at cell boundaries in the numerical mesh and remain so throughout the analysis. Fine details of material flow can be tracked and time series of material properties (e.g., velocity and pressure) can be obtained easily as the material remains in the original element. Lagrangian analysis is well suited for computing the response of solids.

The main disadvantage of a Lagrangian analysis is that its use in problems involving large angular distortions such as those shown in Figure 3-3 can lead to erroneous results or termination of an analysis. As element size is one of the criteria for determining the timestep in an explicit analysis, very small element sizes lead to very small timesteps. This can even lead to termination of the analyses if the timestep drops below a specified minimum value. This problem can be overcome by a technique called *rezoning* where the variables of a highly distorted mesh are conservatively remapped into an undistorted mesh, repairing the mesh and allowing the analysis to continue. Such techniques are described by Zukas (2004). As this process is manual, the user must determine where and when rezoning should be applied.

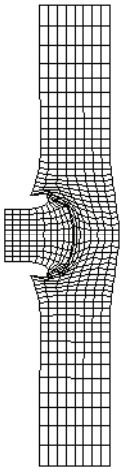

Figure 3-3: A highly distorted mesh due to impact of a projectile (Birnbaum, et al., 1999)

Another shortcoming of Lagrangian analysis is the computational cost associated with the solutions of contact and impact problems. Often complex logic is applied to detect void opening and closing, material interactions and sliding contacts and these processes tend to use most of the CPU time (Zukas, 2004). Given the two shortcomings of Lagrangian analyses described here, their applicability to blast problems involving large mass flow and fluid-structure interaction is limited. However, Lagrangian solvers can be used with Eulerian solvers or Arbitrary Lagrangian-Eulerian (ALE) solvers to analyze fluid-structure interaction: see Section 3.4.

3.4 Eulerian Analysis

In contrast to a Lagrangian analysis where the mesh deforms as the material flows, an Eulerian analysis involves material flow through a stationary mesh as shown in Figure 3-4. As the material moves from one element to the other, the time series of material properties, material interfaces and free surfaces cannnot be tracked as accurately as in a Lagrangian analysis. The material flow also necessitates the use of advection[15] algorithms in Eulerian solvers, thus making them more complex and more computationally

[15] In fluid flow, the term 'advection' means transportation of fluid material

expensive than Lagrangian solvers. An Eulerian solver is well suited for modeling the behavior of fluids and gases, because the mesh remains fixed in space. In an Eulerian solver, all variables are cell centered in a mesh, which facilitates coupling with other solvers required to address fluid-structure interaction problems.

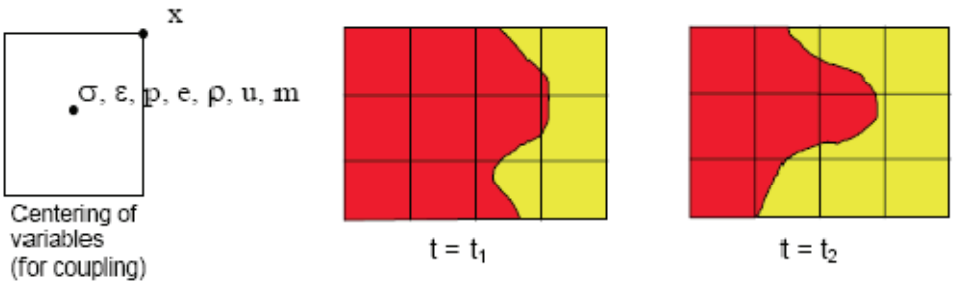

Figure 3-4: Material flow through a stationary grid in an Eulerian analysis (Birnbaum, et al., 1999)

Most Eulerian solvers use a control volume method to solve the governing conservative equations of mass, momentum and energy. The mesh velocity is set to zero ($w = 0$) in equations 3-1 to 3-3. Eulerian solvers tend to use a two-step procedure for every calculation timestep. The first step is a Lagrangian computational step in which the mesh moves with the fluid thereby conserving mass. The mesh velocities and displacements are calculated and nodal characteristics are updated. This process continues until the mesh deformation is acceptable or the mesh is not too distorted, after which a rezoning step is performed resulting in an undistorted mesh. Material is then advected from one element to another, which is determined by the amount of mesh rezoning. At the end of each calculation timestep of an Eulerian analysis, only the material moves from one location to another while the mesh remains stationary.

In some situations, such as the air and detonation product gases generated by an explosion, an element can have more than one material in it at the same time. In such cases, multiple materials are handled by Eulerian solvers by either using the volume fraction technique or the interface technique developed originally by Youngs (1982). Consider a material interface that cuts through an Eulerian cell. The interface is constructed by using the information on volume fractions in the neighboring cells and performing a series of geometry-related tasks. These tasks include detection of line intersections, creation

of a polygon containing one of the fluids, and determining its area and volume. A number of volume-tracking methods have been developed. The simple linear interface calculation (SLIC), volume of fluid (VOF) and piecewise linear interface calculation (PLIC) methods have been implemented in many finite element and CFD codes. More information on these methods is available in Rider et al. (1998).

3.5 Arbitrary Lagrangian-Eulerian Analysis

Numerical modeling of detonations involves both fluid and structural dynamics; shock wave propagation through the air being the fluid part, and interaction with a structure and its response being the structural part. As seen in sections 3.3 and 3.4, Lagrangian and Eulerian solvers are suitable for modeling solid and fluid behavior, respectively. In recent years, a new solver has been developed that combines the features of Lagrangian and Eulerian solvers: the Arbitrary Lagrangian-Eulerian (ALE) solver. It is capable of addressing both the structural and fluid dynamics aspects of a detonation problem. Unlike a purely Eulerian solver, where the nodes are rezoned to their original location in a mesh, the ALE solver rezones the nodes to an optimal position. An advection step is much more computationally expensive than a Lagrangian calculation step and most of the time is spent in calculating the material to be transported between elements. An optimum is sought by the rezoning algorithm of the ALE solver between the mesh distortion and the computational expense needed for the material advection calculation (Kim and Shin, 2008). The ALE solver handles large distortions (a shortcoming of the Lagrangian solvers) but preserves the ability to clearly identify interfaces (a shortcoming of the Eulerian solvers).

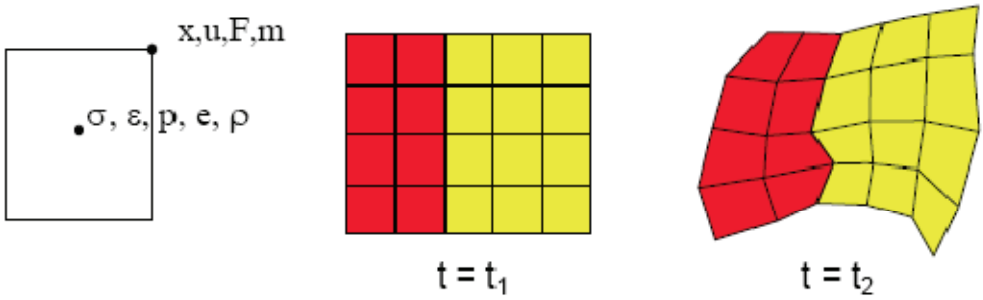

Figure 3-5: Optimal mesh rezoning using the ALE formulation (Birnbaum, et al., 1999)

The ALE solver can behave more like a Lagrangian or an Eulerian solver during a computational step, depending upon the user input and the physics of the problem. Different mesh rezoning and advection algorithms are used by different codes. The advection algorithms track the material flow from one element to the other and are usually stable, monotonic and conservative. Mass, momentum and energy are advected in fluid elements. More information on the ALE mesh rezoning and advection algorithms implemented in LS-DYNA can be obtained from Webster (2007) and the LS-DYNA Theory Manual (LSTC, 2006).

Another feature of the ALE solver is that it can handle multiple materials in an element. In the vicinity of the detonation of an explosive, an element can contain multiple materials such as air and the gaseous products of the detonation. The multi-material ALE solver solves the same governing equations as that of the single material ALE solver except that they are solved iteratively for each material group. However, this increases the computational cost of an ALE calculation timestep as additional data is needed to specify the presence of multiple materials in a single element that should be updated in the rezoning algorithm.

3.6 Coupled Eulerian-Lagrangian Analysis

When a blast wave that is propagating through a medium such as air or water reaches a solid surface, it is reflected, resulting in fluid-structure interaction and a transfer of energy from the wave to the surface. To properly model this behavior, the solvers must be coupled to capture the fluid and structure responses. In the coupling methods, mass, energy and momentum are transferred from the Eulerian grid to Lagrangian grid and vice-versa, in the form of boundary conditions. In LS-DYNA, fluid-structure interaction (FSI) is handled using an ALE solver for the fluid and a Lagrangian solver for the structure. The fluid mesh with the ALE solver is termed the master mesh and the structure mesh with the Lagrangian solver is termed the slave mesh. Two coupling algorithms are available in LS-DYNA: constrained-based and penalty-based. These two algorithms are well established for applications to impact and blast problems. The constrained-based algorithm modifies the velocities and/or accelerations of the solid element nodes and forces them to

follow each other. This coupling method conserves mass and momentum but not energy (LSTC, 2006). The more popular penalty–based algorithm tracks the relative motion between the nodes of the fluid (ALE) and structure (Lagrangian) meshes and applies penalty forces that resist the penetration of the ALE material through the Lagrangian mesh. If d is the relative displacement between a Lagrangian node and the ALE material location, the coupling force:

$$F = -K d \tag{3-8}$$

is applied where K is the spring constant that is based on the constitutive material properties of the model (Webster, 2007). This force is applied to both the slave nodes and the master segment to satisfy equilibrium. It is important to note that for fluid-structure interaction to take place, the structure (Lagrangian) mesh should spatially overlap the fluid (ALE) mesh. Guidelines on coupling input parameters, relative resolution between the ALE and Lagrangian meshes and other related issues can be obtained from the LS-DYNA Keyword User's Manual (LSTC, 2007).

Euler-Lagrange coupling is simpler to implement in AUTODYN than in LS-DYNA. Consider a structure (Lagrangian) interface that "cuts" through a fixed fluid (Eulerian) mesh in an arbitrary manner. In AUTODYN, the Eulerian cells intersected by the Lagrangian interface act as a pressure boundary for the Lagrangian grid while the Lagrangian grid acts a geometric boundary on the material flow in the Eulerian mesh. The Eulerian cells adjacent to the Lagrangian interface boundary may be partially covered by the Lagrangian grid and their control volumes and face areas change continuously. In a large-displacement problem, as the Lagrangian grid distorts, it might cover an Eulerian cell that was not covered initially. Similarly a cell that was initially covered can become uncovered. As the Lagrangian mesh distorts and some Eulerian cells are covered, their control volumes can become very small and disappear when fully covered. AUTODYN tackles this problem dynamically by combining the small control volume of an almost-covered cell to the control volume of the adjacent cell to form a single large control volume (Century Dynamics, 2009a).

3.7 Sample Problem

To demonstrate the different detonation modeling techniques available in LS-DYNA, AUTODYN, and the CFD code Air3D, a sample problem involving a detonation of 1000 kg of TNT interacting with a rigid element of finite width is analyzed with each of these codes. The problem consists of 3 parts: 1) detonation of a spherical explosive and wave propagation through the explosive, 2) subsequent propagation of the detonation wave through the air, and 3) interaction with a rigid column and the propagation of the reflected wave along the height of the column. The problem geometry is presented in Figure 3-6.

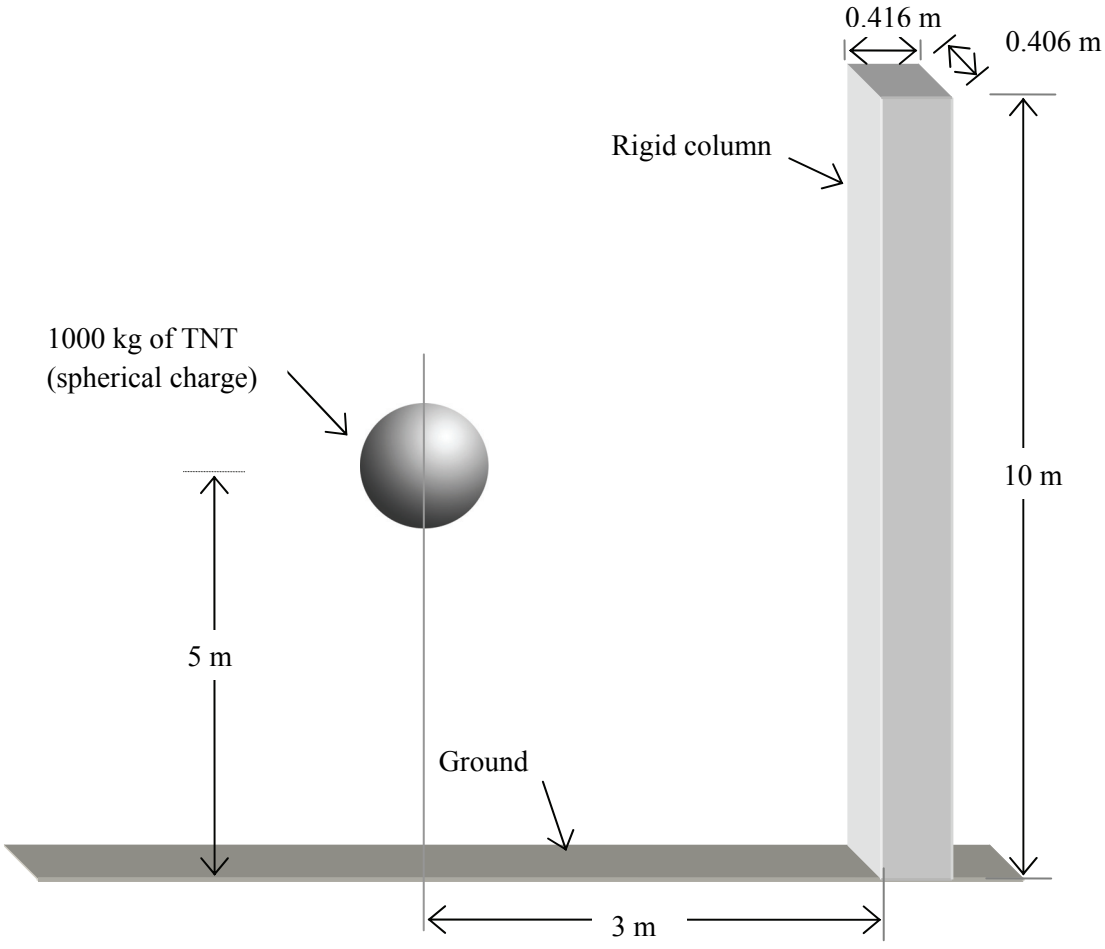

Figure 3-6: Detonation of a spherical TNT charge in free air with a rigid column at a standoff distance of 3m

For the 1000 kg of TNT-equivalent explosive and the stand-off distance of 3m, the scaled distance, Z $(= R / W^{0.33})$ is 0.3. Although there is no consensus in the blast community on what constitutes a near-field detonation, detonations involving scaled distances less than 0.5 m/kg$^{0.33}$are near-field. After the explosive is detonated, the shock wave propagates first through the explosive and then into the surrounding air, which is initially at atmospheric pressure (101.3 kPa). The wave is reflected when it strikes the face of the column. A normal (0^o) reflection is shown in Figure 3-7. The incident pressure waves are reinforced giving rise to peak reflected overpressures that can be an order of magnitude higher than the peak incident overpressures.

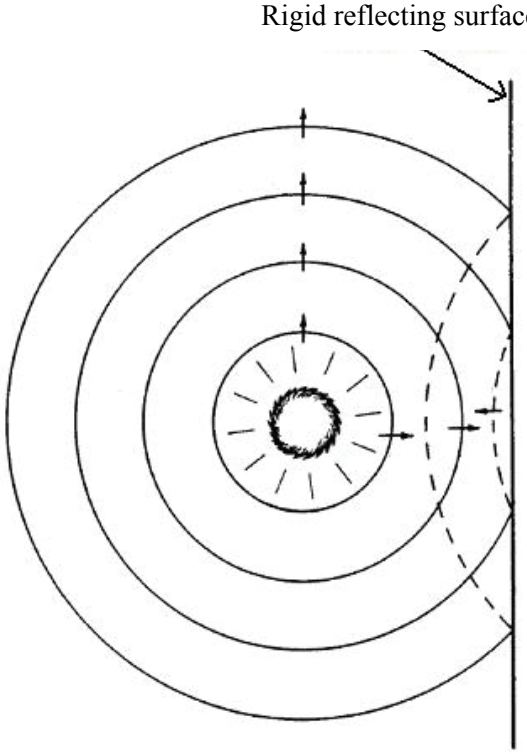

Figure 3-7: Reflection of pressure waves generated by a free-air blast at a rigid surface (Glasstone and Dolan, 1977)

In this problem, the column is assumed to be rigid, resulting in a perfect reflection and instant reinforcement of the incident wave. Although this assumption is reasonable in many cases, (e.g. Ballantyne, et al., 2010) for a detonation of thousands of kilograms of an explosive, the peak reflected

overpressures on a target located in the near-field can exceed the failure strength of most structural materials. Such high pressures can deform or damage the target and lead to non-perfect reflections. In such a scenario, correct material modeling of the target structure is necessary to obtain the correct overpressure distributions on the target. Given that the only consequence of assuming a rigid target in such situations is conservative estimates of peak reflected overpressure and reflected impulse, and that the primary objective here is to analyze pressure distributions in the near-field and not structural response, the column in Figure 3-6 is assumed to be rigid. The results of the analysis are presented in terms of reflected overpressure histories at three monitoring points on the vertical centre-line of the front face of the rigid column: near the middle (point A), quarter section (point B) and near the top boundary (point C). The locations of the three monitoring points are shown in Figure 3-8.

Note that even though the ground is shown at the bottom of the column in Figure 3-6, it was modeled as a transmitting surface in these numerical analyses since the objective was to monitor the reflected pressure distributions along the height of the column due to reflection from the column alone. The inclusion of the ground as a reflecting surface in the numerical models would have complicated interpretation of results. The column can therefore be considered to be suspended in midair and the detonation problem characterized as a free-air burst.

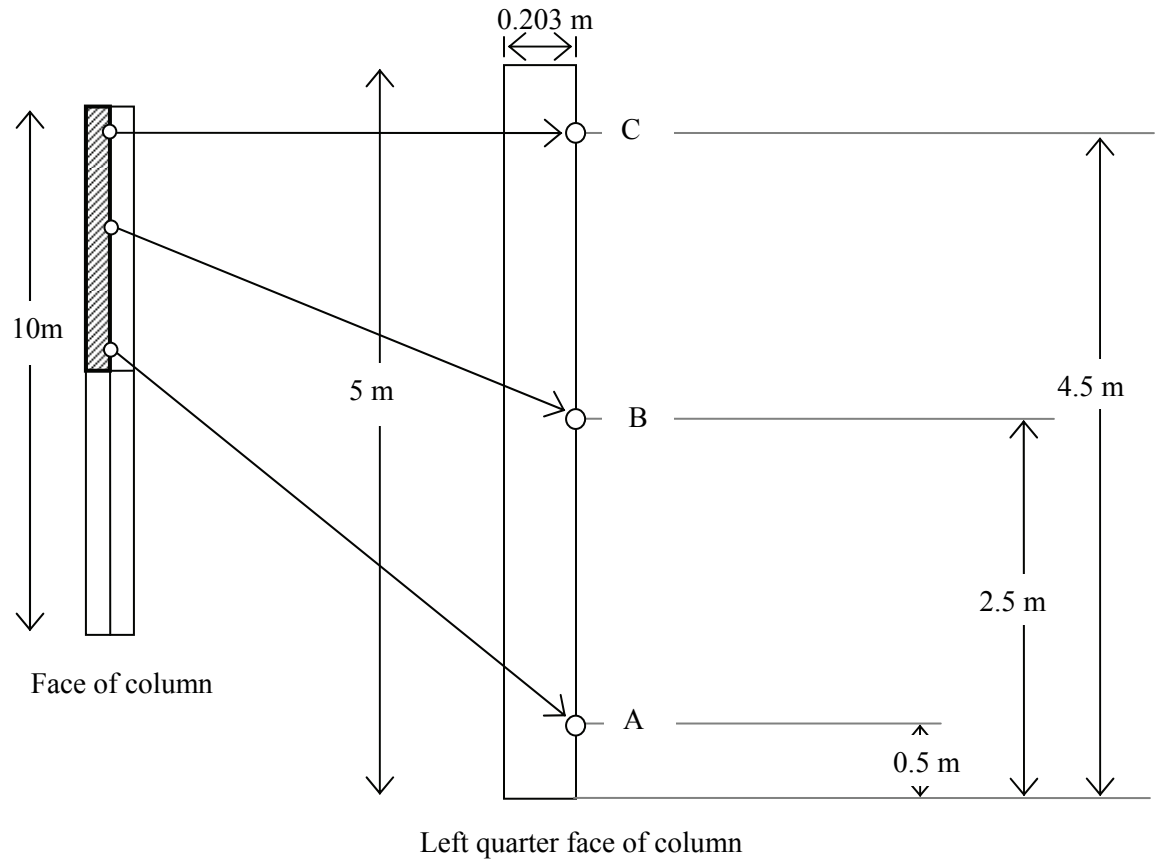

Figure 3-8: Location of the monitoring points on the face of the column

3.8 UFC-3-340-02 Calculations

Before discussing the LS-DYNA, Air3D and AUTODYN numerical models of the detonation problem introduced in section 3.7 and presenting key results, it is worthwhile to benchmark results against those computed using the industry-standard procedures presented in UFC-3-340 (DoD, 2008). The values of peak incident overpressure, peak incident impulse, arrival time, peak reflected overpressure and the reflected impulse at the three monitoring points are used for this purpose. Note that the scaled distance, angle of incidence and the standoff at the three monitoring points are different. The UFC-3-340 charts for these blast-wave parameters are based on the empirical relations of Kingery and Bulmash (1984) and were presented previously in Figures 1-1, 1-4 and 1-5.

Figure 1-1 is used for calculating the peak incident overpressure, peak incident impulse, peak reflected overpressure and other blast-wave parameters at a point whose scaled distance, *Z*, is known. A straight

line is drawn on the x-axis corresponding to the Z value. Wherever the straight line intersects a curve, another straight line is drawn from the point of intersection to the y-axis. The corresponding value on the y-axis is the value of the blast parameter at that point. Except for the incident and reflected overpressures, all other blast-wave parameters need to be scaled, that is, the value of the blast parameter obtained from the y-axis must be multiplied by $W^{0.33}$, where W is the mass of the explosive.

Figure 1-1 can only be used for calculating reflected overpressures and reflected impulses at points that experience normal reflection (0^o). For points where the angle of incidence is greater than 0^o, Figures 1-4 and 1-5 are used to calculate the reflected values. The values above each curve in the figures are the incident overpressure. The reflected overpressure coefficient is obtained from Figure 1-4 for values of the angle of incidence and the incident overpressure. The reflected overpressure is then obtained by multiplying the reflected pressure coefficient by the incident overpressure. The values of blast-wave parameters at the three monitoring points obtained using the charts in Figures 1-1, 1-4 and 1-5 are presented in Table 3-1.

Table 3-1: Blast-wave parameters at the 3 monitoring points in Fig 3-7 calculated using UFC-3-340

	Point A	Point B	Point C
Height (m)	0.50	2.50	4.50
Standoff distance, R (m)	3.04	3.91	5.41
Scaled distance, Z $(= R / W^{0.33})$ $(m/kg^{0.33})$	0.30	0.39	0.54
Angle of incidence (degrees)	9.46	39.8	56.3
Peak incident overpressure (MPa)	9.0	6.0	3.0
C_r (from Figure 3-10)	8.80	6.0	3.70
Peak reflected overpressure (MPa)	79.2	36.0	11.1
Incident impulse (MPa-msec)	1.70	1.50	1.70
Reflected impulse (MPa-msec)	32.0	14.0	5.40
Time of arrival (msec)	0.65	1.0	1.90

3.9 LS-DYNA Modeling and Pressure Distributions

Different finite element (FE) models of the problem described in the section 3.7 were created and analyzed using the general purpose non-linear finite element analysis code LS-DYNA. These FE models used different modeling strategies. The following sections address the associated numerical modeling issues and present the results from analyses performed with each model. Preprocessing of the FE models, including mesh generation and application of boundary conditions, was performed using PATRAN (MSC Software Corporation, 1999) and the preprocessor in ANSYS (ANSYS Academic Research, 2009).

3.9.1 Cuboid-shaped explosive

3.9.1.1 Modeling and analysis

A FE model of the sample problem was generated using cuboid-shaped meshes for the air domain and the explosive. Although charge shape can have a significant effect on the overpressure distributions in the near-field, this analysis was preliminary in nature and the generation of cuboid meshes for both the air and explosive was much simpler than generating a spherical mesh for the explosive and a cuboid-shaped mesh for the air. A one-to-one mapping of the mesh nodes at the explosive-to-air boundary was used. The implications of choosing such a mesh configuration are discussed later. In LS-DYNA, different parts of a FE model are defined by the '*PART' keyword and each part can be assigned different materials, Equation of States, and solution formulations. Three parts were defined in this FE model: air, explosive and the rigid column. Eight-noded solid elements (HEX-8) were used for all parts. The 1-point multi-material Arbitrary Lagrangian-Eulerian (ALE) solver (ELFORM = 11) that is available in LS-DYNA was used for both the air and the explosive, while the default constant-stress solid formulation was used for the column elements.

To reduce the size of the FE model, symmetry was applied in *x*, *y* and *z* directions and only 1/8 of the air domain and explosive and 1/4 of the column were modeled. The FE model is presented in Figure 3-9. The size of the FE model was $4\text{m} \times 1.5\text{m} \times 6\text{m}$ and it was assumed that the boundaries of the air domain were sufficiently far removed so as to not affect the results of the analysis. No boundary conditions were

applied at these boundaries (referred to as upper *xy*-, *xz*- and *yz*- planes henceforth). The default 'off' option was used for Euler boundary condition (EBC) under the 'Control_ALE' keyword. The 'off' option allows unconstrained velocities at the Eulerian mesh boundaries. The consequences of not using boundaries conditions at the upper planes of the air domain are discussed in the following section. The use of symmetry requires applying boundary conditions to the lower *xy*-, *xz*- and *yz*- planes. The translational degrees-of-freedom of all the nodes in these planes were constrained in their normal directions. Three meshes with decreasing element size were analyzed and the details of each mesh configuration are shown in Table 3-2. The mesh for the air domain was created such that the element size increased gradually away from the explosive.

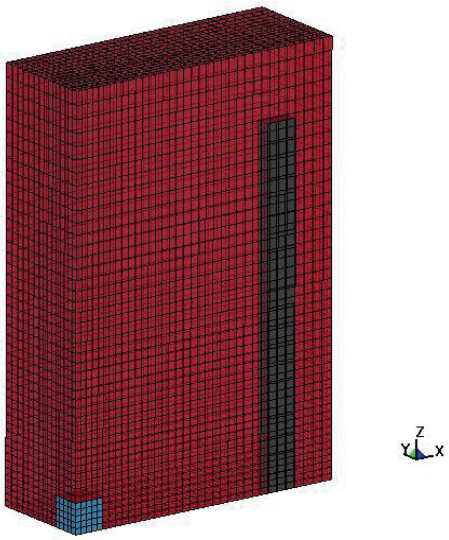

Figure 3-9: Symmetric FE model with cuboid-shaped meshes for air (red), explosive (blue) and the rigid column (green); mesh configuration 1

Table 3-2: Mesh configurations used in the LS-DYNA cuboid explosive model

Mesh configuration	Number of elements				Element size (mm)	
	Total	Explosive	Air	Column	Explosive	Air
1 (Coarse)	23,985	125	23,500	360	85	90-130
2 (Fine)	361,256	4,096	353,000	4,160	27	30-75
3 (Very fine)	504,000	10,000	474,000	20,000	17	43-58*

* Element aspect ratio was approximately varied from 1 to 2

The 'high-explosive-burn' material model available in LS-DYNA was used for the explosive along with the JWL EOS presented in equation 3-5. The 'BETA' flag was set to the default 'beta + programmed burn' option. This option calculates the burn fraction F using equations 3-10a, 3-10b and 3-10c and multiplies it by the pressure calculated by the EOS, p_{eos}, to give the effective pressure in the explosive; see equation 3-9. This option controls the release of chemical energy in the detonation (LSTC, 2007). (Different hydrocodes apply alternate burn models like the LUND model (Mandell, et al., 1998) used in the Lagrangian code FLAG (Burton, 1992, 1994).)

$$p = F\, p_{eos} \tag{3-9}$$

$$F = \max(F_1, F_2) \tag{3-10a}$$

$$F_1 = \begin{cases} \dfrac{2(t-t_l)UA_{\mathrm{e\,max}}}{3v_e} & t > t_l \\ 0 & t < t_l \end{cases} \tag{3-10b}$$

$$F_2 = \beta = \frac{1-V}{1-V_{CJ}} \tag{3-10c}$$

where

U = Detonation velocity

t_l = Lightning or ignition time of an element (distance of the element from the initiation point divided by the detonation velocity)

V = Relative volume

v_e = Element volume

A_{emax} = Area of the largest side of an element

The air was modeled as an ideal gas using the 'NULL' material model and the 'Linear Polynomial' EOS presented in equation 3-6. The air domain was initialized to atmospheric pressure by specifying the initial energy of air in the 'NULL' material model (LSTC, 2007). The material constants and the EOS parameters used in the analysis are listed in Tables 3-3 and 3-4. The initiation point was the center of the explosive (the origin of the FE model) and was specified through the '*Initial_Detonation' keyword.

The advection method used in the analyses was the 2nd order Van-Leer algorithm (LSTC, 2006) and is preferred over the donor cell algorithm (1st order accurate) for blast problems for its higher order accuracy. The advection method is selected under the '*Control_ALE' keyword. The number of time steps between advection cycles (NADV) was set equal to 1 as recommended in LS-DYNA Keyword User's Manual (LSTC, 2007). The value of NADV determines how frequently the advection calculations are performed. The higher the value of NADV, the smaller the number of advection calculations performed.

Table 3-3: Material model parameter values for explosive and air

High explosive burn material model for explosive		**NULL material model for air**	
Parameter	Value	Parameter	Value
Density (kg/m^3)	1600	Density (kg/m^3)	1.225
CJ pressure (GPa)	21	CJ pressure (GPa)	0
Detonation velocity (m/s)	6730		

Table 3-4: JWL and ideal gas EOS parameter values for explosive and air

JWL EOS for explosive		**Linear polynomial EOS for air**	
Parameter	Value	Parameter	Value
A (GPa)	373.8	C_0	0
B (GPa)	3.747	C_1	0
R_1	4.15	C_2	0
R_2	0.90	$C_3 = C_6$	0
ω	0.35	$C_4 = C_5$	0.4
E_o (GPa)	7	E_o (GPa)	0.00025

The termination time for the analysis was determined by trial and error. It was found that a time of 4 msec was sufficient to completely capture the overpressure histories at the three monitoring points. The initial timestep for the analysis was set arbitrarily to 1×10^{-4} sec (0.1 msec). If the initial timestep is not specified, LS-DYNA calculates the timestep on the basis of the smallest element size in the FE model. As the analysis proceeds the timestep is calculated such that the stability criterion, also known as the Courant condition, is satisfied (LSTC, 2006). To avoid numerical instabilities, the Courant condition restricts the timestep, Δt, to a value calculated by equation 3-11a, where c is speed of sound and Δx is the characteristic length of the element. The characteristic length is calculated using equation 3-11b where v_e is the volume of the element and A_{emax} is the area of the largest face of the element. The timestep is calculated for each element using equations 3-11a and 3-11b. The minimum value of all these timesteps is then multiplied by a safety factor, *SF,* to produce the timestep for the next calculation as presented in equation 3-11c, where N is the number of elements. Although the safety factor has a default value of 0.9, its value is generally reduced to 0.67 for analyses involving high explosives (LSTC, 2007).

$$\Delta t \leq \frac{\Delta x}{c} \tag{3-11a}$$

$$\Delta x = \frac{v_e}{A_{\mathrm{e\,max}}} \tag{3-11b}$$

$$\Delta t^{N+1} = SF * \min(\Delta t^1, \Delta t^2, \Delta t^3 .....\Delta t^N) \tag{3-11c}$$

Fluid-structure interaction is modeled in LS-DYNA using the '*CONSTRAINED_LAGRANGE_IN_SOLID' option. Using this option, the column mesh (the Lagrangian part) is specified as the slave and the air mesh (ALE part) is the master. Note that the column mesh and the air mesh overlap and the relative resolution of the meshes decides the value of the coupling points (NQUAD) between them. The LS-DYNA Keyword User's Manual (LSTC, 2007) recommends at least 2 or 3 coupling points (2 or 3 Lagrange nodes) per ALE element length. The mesh configurations were generated accordingly. However, the results with this type of coupling were not promising as shown in section 3.9.1.1. From the contour plots of pressure it was clear that leakage occurred, where leakage is defined here as non-complete reflection of the pressure wave, that is, the coupling between the ALE and Lagrangian parts of the model was not perfect. A different coupling approach was therefore used in the models with finer meshes. A merged-nodes contact was defined between the column and air domains. The nodes at the air-column interface were merged. This type of contact is the most economical and efficient way of coupling the air (fluid) and column (solid) meshes. The results obtained from both coupling methods are presented in the following section.

3.9.1.2 Results and discussion

The reflected overpressure distributions at the 3 monitoring points are presented in Figures 3-10 to 3-12. The pressure contours for the very fine mesh at a time of 0.6 msec are shown in Figure 3-13. There are two important observations to be made from these overpressure distributions. First, the results of the LS-DYNA analysis are highly mesh-dependent. The peak values of reflected overpressure for the very fine mesh increased by a factor of 2 at points A and C compared with the fine mesh. Both analyses used the merged-nodes contact between the air and the column. The variation in peak reflected overpressure at

point B with mesh refinement is small. Second, the pressure contours of Figure 3-13 clearly show that non-spherical pressure waves are generated by the cuboid explosive. The pressure wave is not uniform and is rather concentrated along the principal axes (*x* and *z* directions) of the explosive: the incident overpressures are higher at 0^o and 90^o than at 45^o. The comparison between peak reflected overpressures and reflected impulses at the three monitoring points obtained from the analysis and those calculated using UFC-3-340 is presented in Table 3-5. It is clear from the overpressure histories that the overpressure distributions were not affected by the absence of boundary conditions at the *xz*-, *xy*- and *yz*-upper planes as no reflections were observed from these boundaries during the analysis runtime of 4 msec.

The coupling algorithm used for the analysis with the coarse mesh was not able to correctly model the fluid-structure interaction because perfect coupling was not achieved between the ALE (fluid) and Lagrangian (structure) meshes. The contour plots of pressure, not presented here, showed that a percentage of the pressure wave passed through the column instead of being reflected. As a result, the input parameters used in the '*CONSTRAINED_LAGRANGE_IN_SOLID' keyword and the mesh resolutions were reviewed for the purpose of improving the coupling. The second method used to implement ALE-Lagrangian coupling, namely, merging the nodes at the air-column boundary, was a better choice for coupling. The pressure contours showed that no part of the pressure wave passed through the column indicating perfect coupling between the pressure waves. The air and column domains were meshed with cuboid-shaped elements with common nodes at the interface. However, this is not always possible as will be seen in section 3.9.3, and in such situations, the coupling algorithm is the only available option for treating Eulerian-Lagrangian interaction.

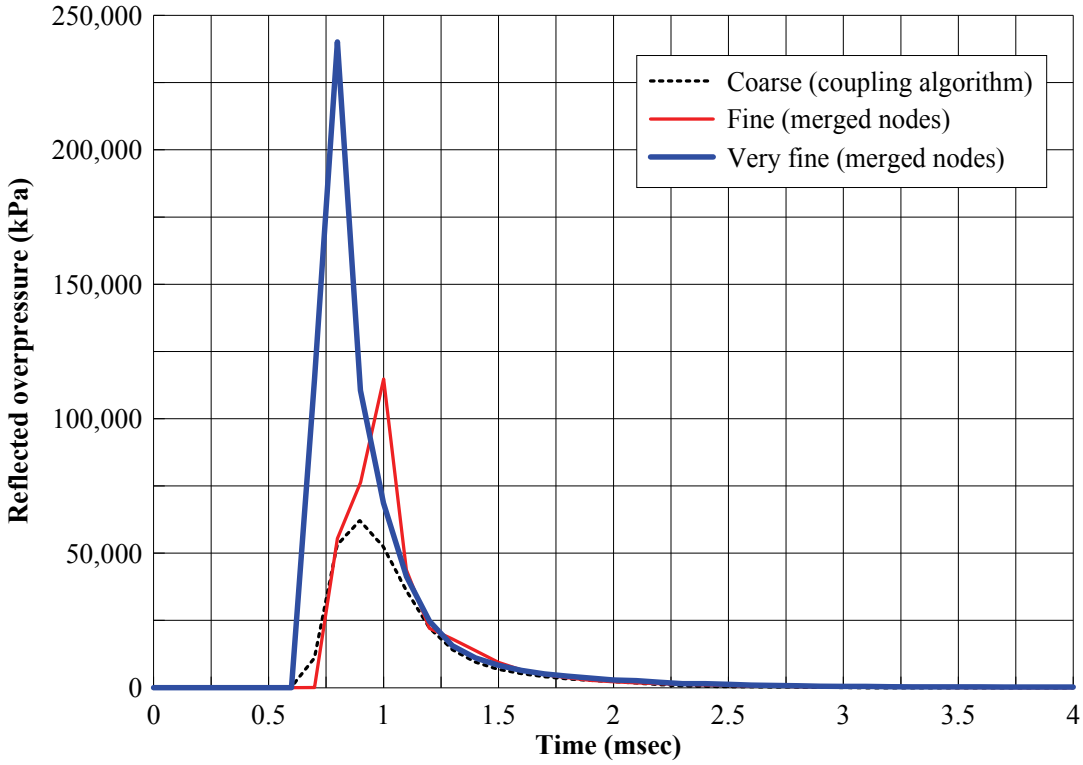

Figure 3-10: Reflected overpressure histories at point A

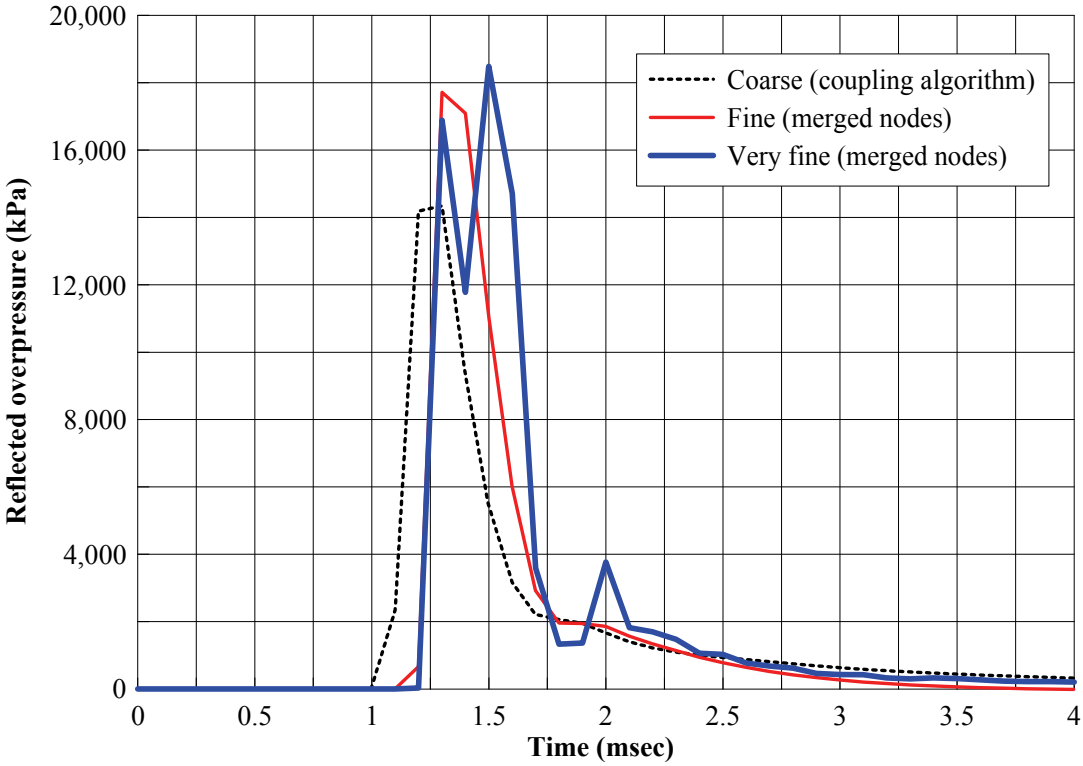

Figure 3-11: Reflected overpressure histories at point B

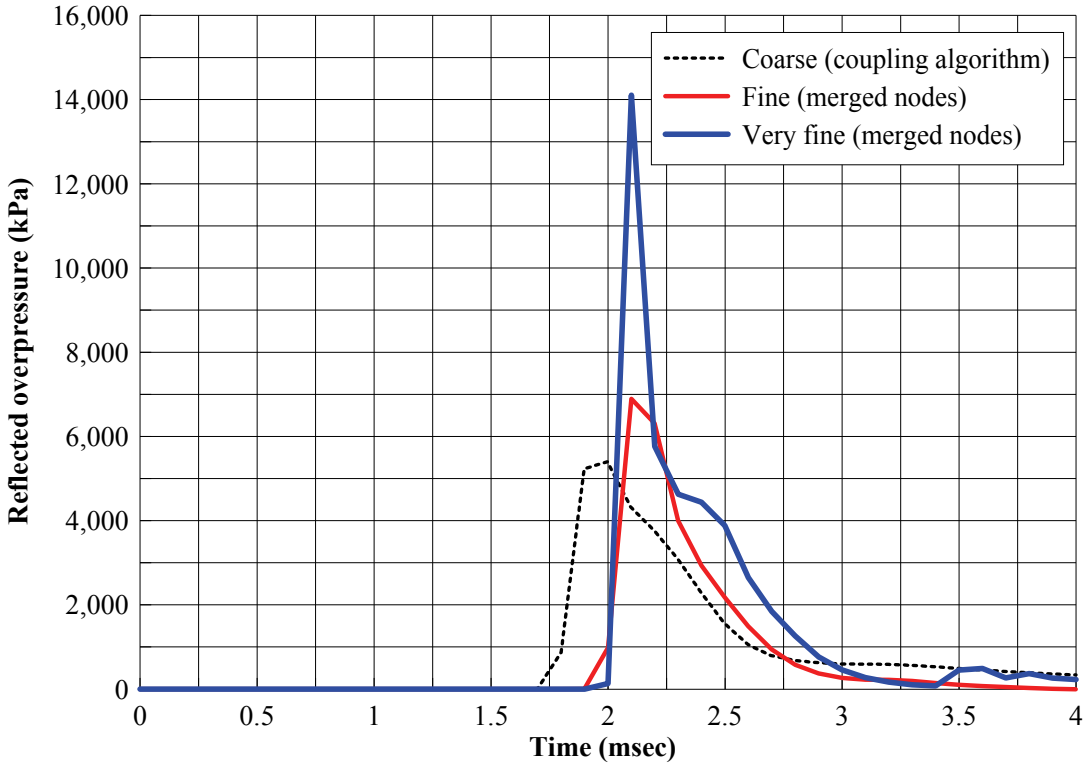

Figure 3-12: Reflected overpressure histories at point C

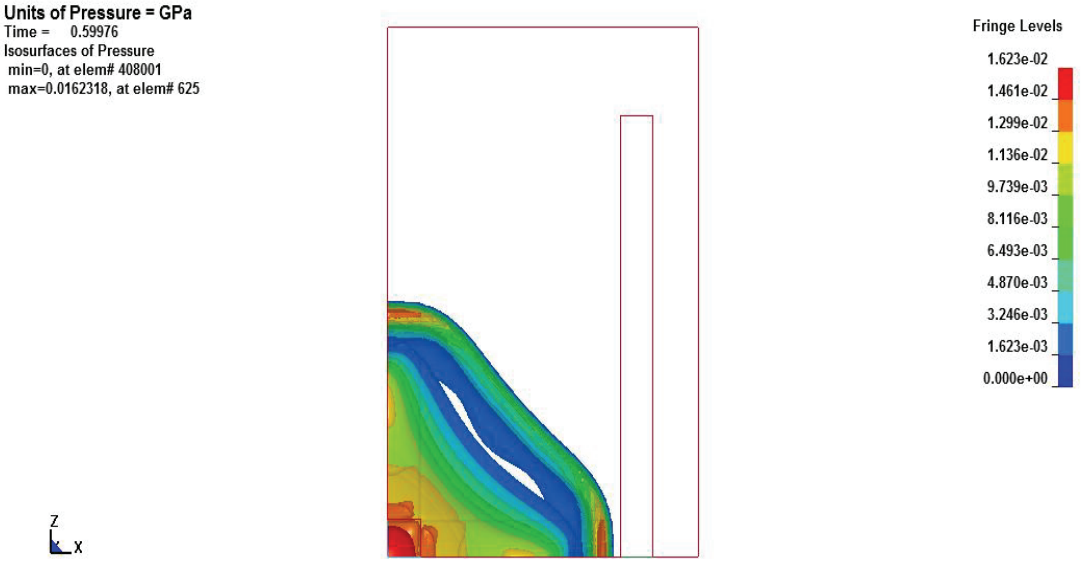

Figure 3-13: Isosurfaces of pressure showing a non-spherical distribution resulting from the cuboid shape of the explosive.

Table 3-5: Comparison between results of UFC-3-340 calculations and the cuboid explosive model in DYNA with the very fine mesh

Monitoring location	Blast-wave parameter	LS-DYNA	UFC-3-340
Point A	Peak reflected overpressure (MPa)	240.1	79.2
	Reflected impulse (MPa -msec)	67.2	32.0
	Time of arrival (msec)	0.80	0.65
Point B	Peak reflected overpressure (MPa)	18.5	36.0
	Reflected impulse (MPa -msec)	8.47	14.0
	Time of arrival (msec)	1.50	1.0
Point C	Peak reflected overpressure (MPa)	14.1	11.1
	Reflected impulse (MPa -msec)	4.25	5.4
	Time of arrival (msec)	2.10	1.90

3.9.2 Circular explosive with radial mesh

The results of the analysis of the cuboid explosive model showed that the shape of the explosive had a significant effect on the overpressure distributions. A model consisting of a spherical explosive mesh was generated to further study the effect of explosive geometry. The air domain was also spherical and is shown in Figure 3.14a. A radial mesh was generated using PATRAN (MSC Software Corporation, 1999) such that it became coarser further away from the origin. The nodes at the air-explosive boundary were merged. A radial mesh is suitable for simulating the detonation of spherical explosive but creates problems near the origin. The element aspect ratio increases substantially and tends to infinity as the mesh collapses near the origin. This problem was tackled by beginning the mesh a small distance (1 mm) from the origin as shown in Figure 3-14b. The resultant loss of explosive mass is negligible. However, this solution does not solve the problem completely as the element aspect ratios near the origin are still great, which can result in very small timesteps because LS-DYNA calculates the initial timestep on the basis of the smallest element size. To check the computational efficiency of this model, a trial run was conducted

with a coarse mesh of 54,000 elements. The rigid column was not modeled for this trial. The materials and EOS used for the explosive and air and the boundary conditions were the same as those of the cuboid explosive model.

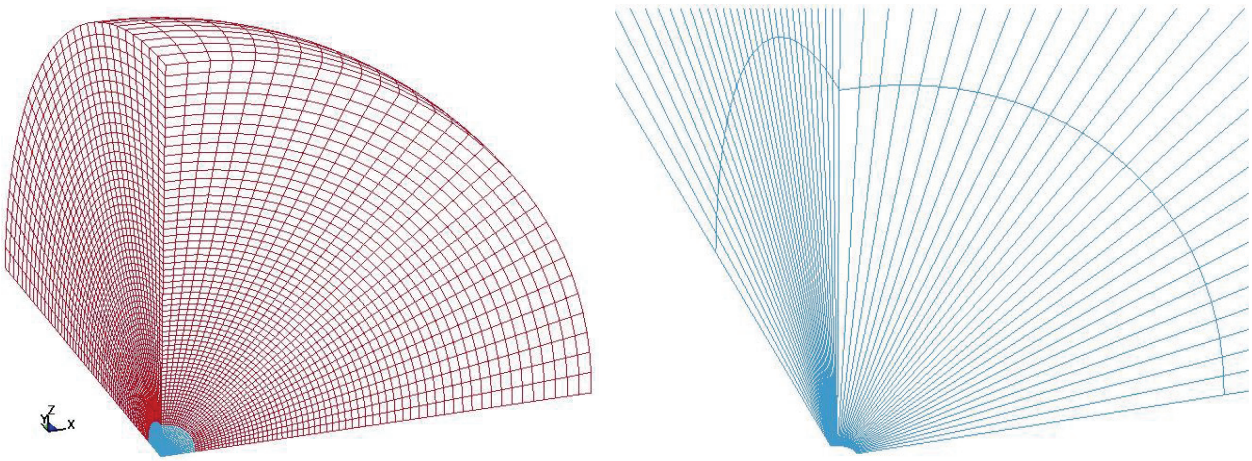

a) Explosive (blue) and air (red) domains b) Explosive mesh near the origin

Figure 3-14: Radial meshes for the spherical explosive and the air domains

The analysis runtime for this model was long. Another analysis was then performed with a fine mesh but with the elements beyond y = 1m deleted. The modified model, shown in Figure 3-15, had approximately 65,000 elements.

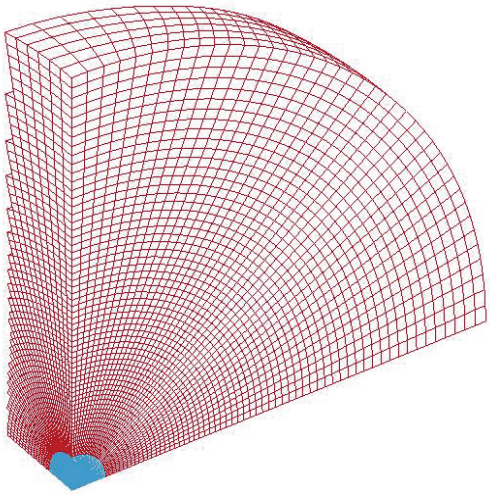

Figure 3-15: Reduced FE model with fine mesh with elements deleted beyond y = 1m

3.9.3 Circular explosive with mesh transition

3.9.3.1 Modeling and analysis

To reduce the computational cost of the FE model used in section 3.9.2, it was necessary to reduce the aspect ratio of the elements near the origin. This was achieved by using rectangular elements near the origin for the explosive and transitioning to a radial mesh within the explosive. Such a mesh configuration was created using the preprocessor in ANSYS (ANSYS Academic Research, 2009) and then using the element and node definitions in the LS-DYNA input file. The modified FE model is shown in Figure 3.16a with elements beyond y = 1m deleted to reduce the size of the model. In the modified FE model, the use of a radial mesh for the air domain put a constraint on the type of coupling method that could be used between the ALE-Lagrangian meshes. With a radial mesh for the air domain and cuboid elements for the column, the nodes at the air-column boundary could not be merged. This necessitated the use of the coupling algorithm (CONSTRAINED_LAGRANGE_IN_SOLID). Improved computational efficiency and better accuracy was anticipated with this mesh as the explosive was now modeled with a large number of elements with aspect ratios of approximately 1. The boundary conditions and material properties in this model were the same as those used previously. Two mesh configurations were used, the second being a refined version of the first. See Table 3-6 for details.

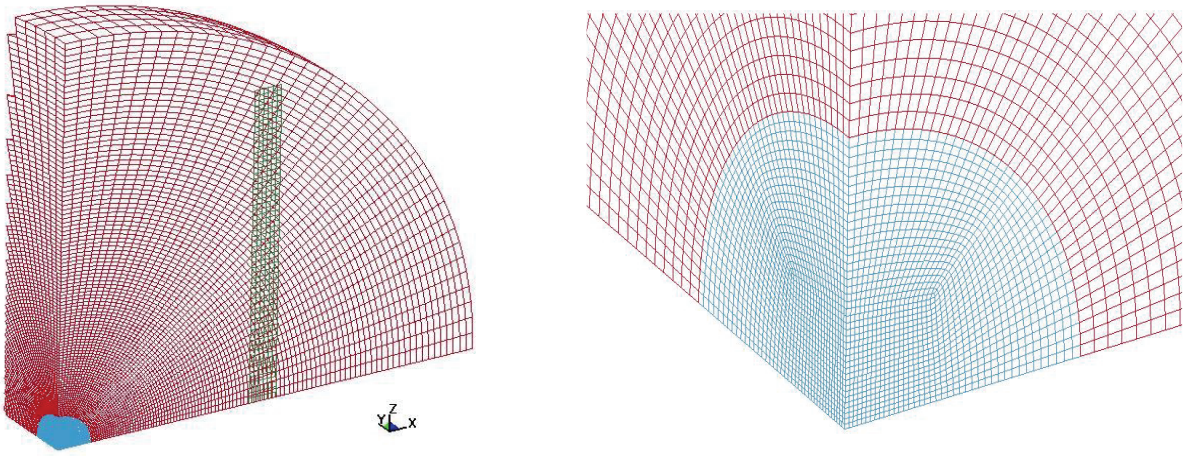

a) Explosive, column and air meshes b) Transition from cuboid to radial mesh

Figure 3-16: Finite element models generated using ANSYS preprocessor

Table 3-6: Mesh configurations for the modified spherical explosive FE model

Mesh configuration	Number of elements				Approximate element sizes (mm)	
	Total	Explosive	Air	Column	Explosive	Air
1 (Coarse)	104,236	32,000	70,796	1,440	10 to 18	31 to 103
2 (Fine)	521,426	171,500	329,962	20,000	8	25[1]

1. Aspect ratios ranged from 1 to 3.

3.9.3.2 Results and discussion

The reflected overpressure distributions obtained at the three monitoring points for the modified spherical explosive model are shown for both mesh configurations in Figures 3-17 to 3-19. There is a 25% to 30% increase in the peak reflected overpressures at monitoring points A and B if the finer mesh is used. The peak reflected overpressure at point C does not change. The critical blast wave parameters obtained from the analysis and those calculated using UFC-3-340 are presented in Table 3-7. The peak reflected overpressure at points B and C obtained from LS-DYNA are less than 50% of the UFC-3-340 values. The contour plots of pressure showing the incident pressure wave (at t = 0.7 msec) and the reflected pressure wave (at t = 1.6 msec) are shown in Figures 3-20 and 3-21, respectively. From Figure 3-21 it can be seen that a part of the pressure wave passes through the column, especially in the upper half of the column, which indicates incomplete reflection or leakage. Perfect coupling cannot be achieved when a radial mesh is coupled with a rectangular mesh because there are always some elements at the boundary that are partially within the column and partially outside in the air domain. By adjusting the coupling input parameters in the 'CONSTRAINED_LAGRANGE_IN_SOLID' option and the relative mesh resolutions of the air and column, the coupling can be improved to an acceptable level.

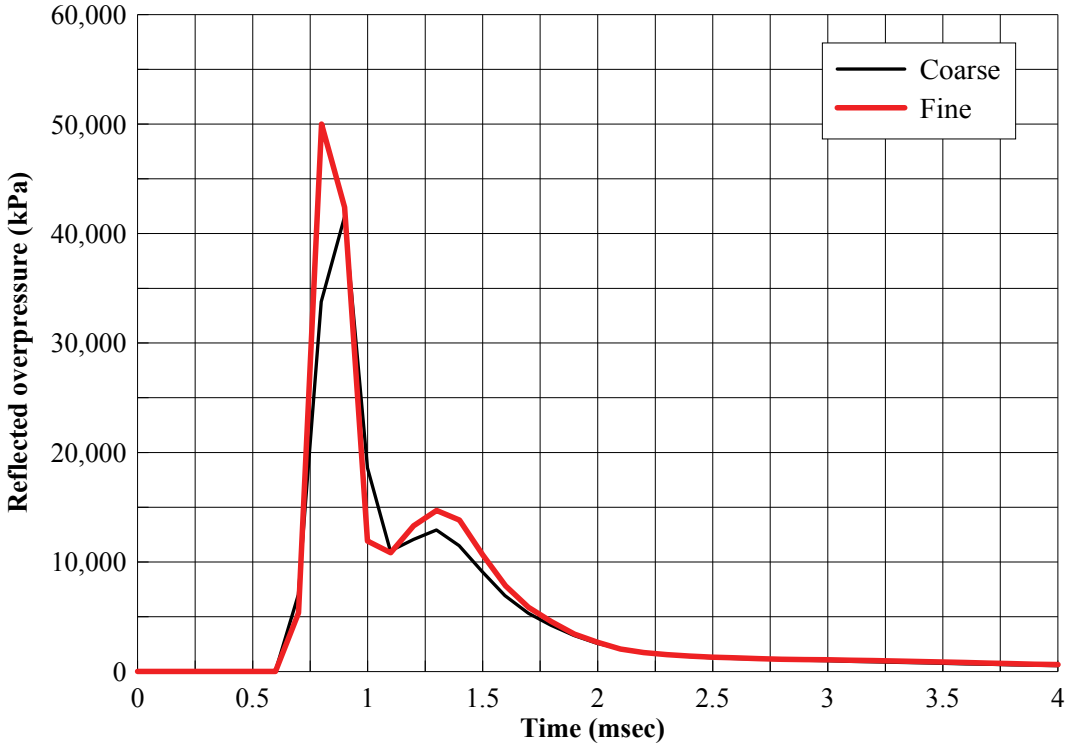

Figure 3-17: Reflected overpressure histories at point A with mesh refinement

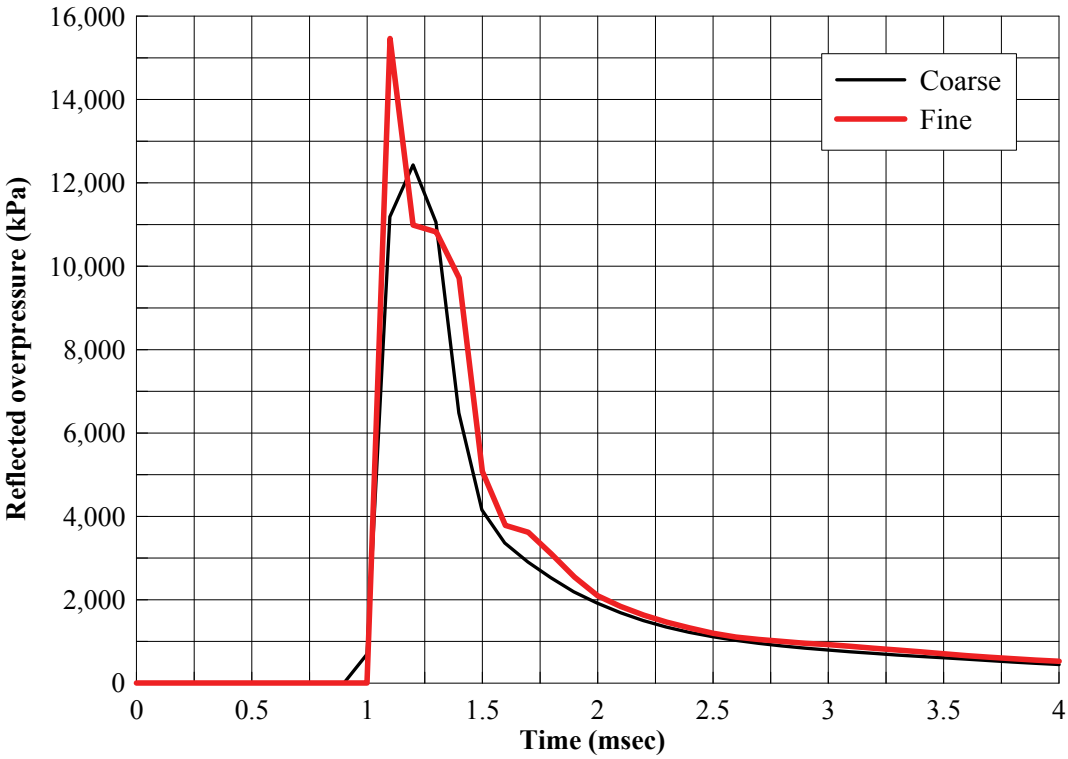

Figure 3-18: Reflected overpressure histories at point B with mesh refinement

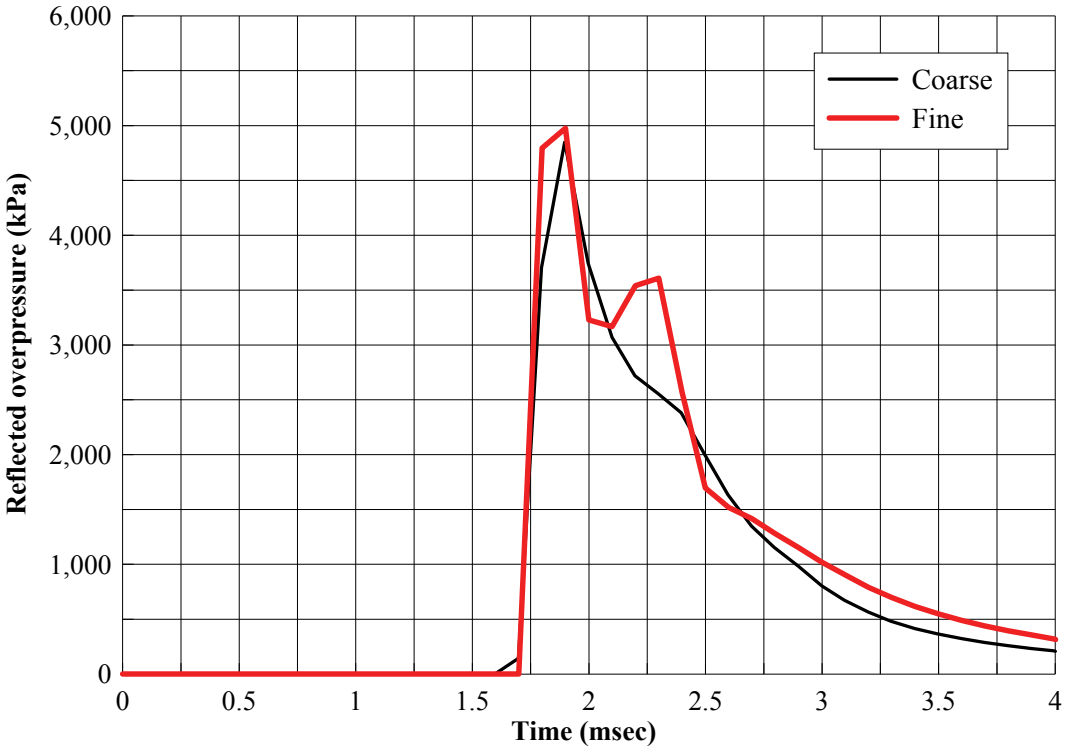

Figure 3-19: Reflected overpressure histories at point C with mesh refinement

Table 3-7: Comparison between results of UFC-3-340 calculations and modified spherical explosive model in LS-DYNA

Monitoring location	Blast-wave parameter	LS-DYNA	UFC-3-340
Point A	Peak reflected overpressure (MPa)	50.0	79.2
	Reflected impulse (MPa -msec)	21.9	32.0
	Time of arrival (msec)	0.70	0.65
Point B	Peak reflected overpressure (MPa)	15.5	36.0
	Reflected impulse (MPa -msec)	8.63	14.0
	Time of arrival (msec)	1.10	1.0
Point C	Peak reflected overpressure (MPa)	4.98	11.1
	Reflected impulse (MPa -msec)	3.94	5.40
	Time of arrival (msec)	1.80	1.90

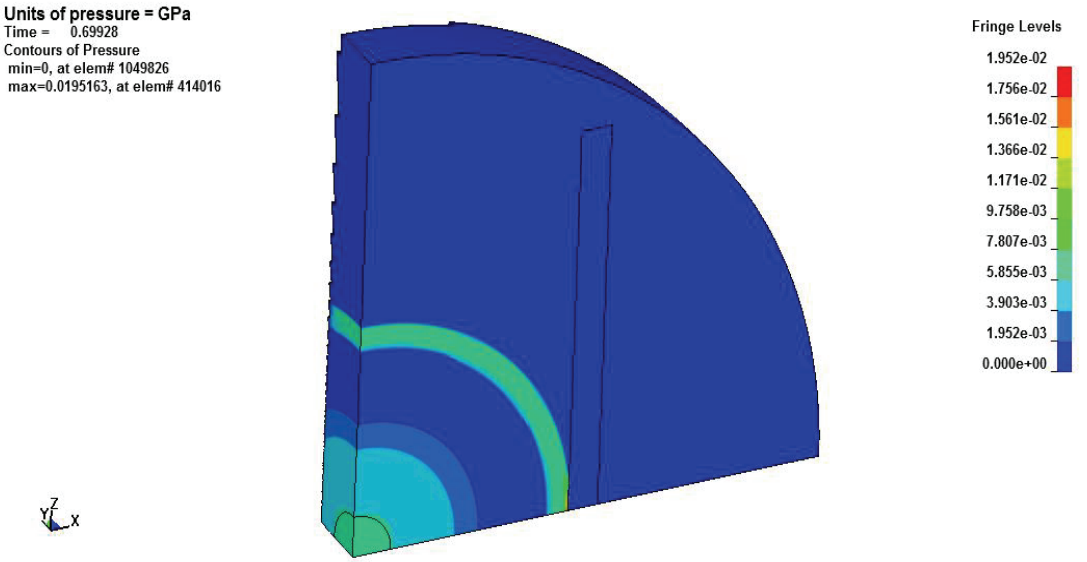

Figure 3-20: Contour plot of pressure when the blast wave reaches the column (at t = 0.7 msec)

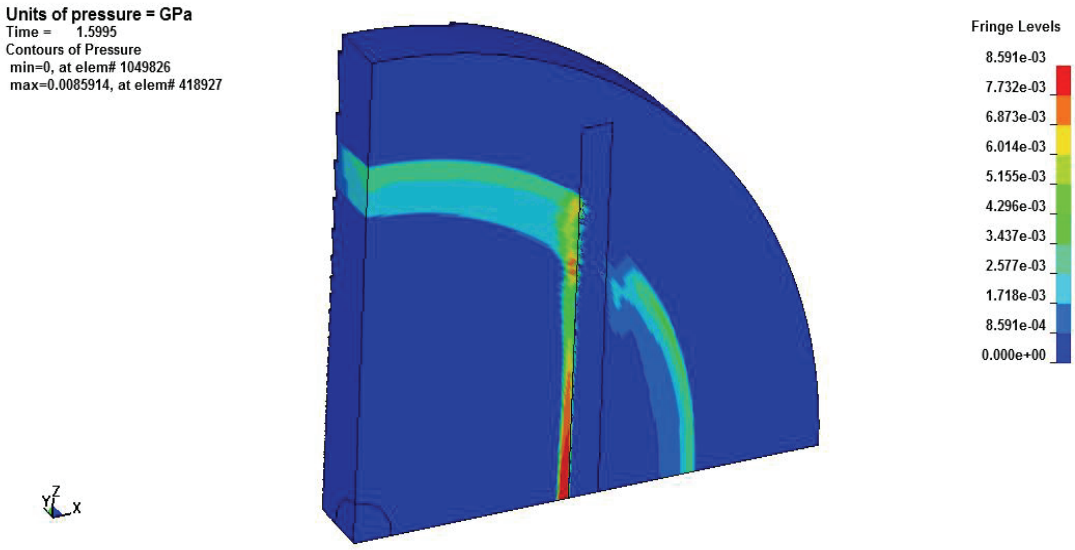

Figure 3-21: Contour plot of pressure as the reflected blast wave as it propagates along the height of the column (at t = 1.6 msec)

Based on the analyses presented in sections 3.9.1, 3.9.2 and 3.9.3, it can be concluded that the two most important requirements for modeling the sample problem are 1) an ability to model a spherical explosive, and 2) a robust coupling method. The cuboid explosive model had nodes merged at the air-column boundary that provided excellent coupling between the ALE and Lagrangian meshes but the resulting pressure waveforms were non-spherical. Conversely, the modified spherical explosive model did not enable good coupling. There was a need to combine the best features of both FE models.

3.9.4 Initial_Volume_Fraction_Geometry option

3.9.4.1 Modeling and analysis

To have a one-to-one connection between the nodes at the air-explosive boundary, the shape of the elements in the meshes of the explosive and air domains have to be similar: see sections 3.9.1 and 3.9.3. If the shape of the explosive is cuboid, the shape of the air domain has to be cuboid or if the explosive is spherical, the air domain has to be spherical. This section discusses a modeling technique that removes this constraint. With this modeling technique, the shape of the air domain is independent of the shape of the explosive. Moreover, perfect coupling can be achieved using a cuboid-shaped mesh for both the air and the column and merging the nodes at the common boundary.

A new model was generated using PATRAN, consisting of two cuboid-shaped meshes: one for the air, and one for the rigid column. The explosive was initialized using the option 'INITIAL_VOLUME_FRACTION_GEOMETRY', in which the explosive was specified to occupy initially a certain volume or portion of the air mesh. A spherical explosive was defined by specifying its origin and radius. Shapes other than a sphere (cylinder, box or a plane) can also be modeled using this option. This method is powerful as it allows the user to model different shapes for the explosive without changing the air mesh. In the FE models of sections 3.9.1, 3.9.2 and 3.9.3, if the shape or radius of the explosive was changed, new meshes had to be generated. However, with the option 'INITIAL_VOLUME_FRACTION_GEOMETRY', only the radius or the shape has to be redefined. Additionally, with this option, a cuboid-shaped mesh can be used for the air and the nodes can be merged

at the air-column boundary, thereby providing perfect coupling. The resulting FE model is shown in Figure 3-22.

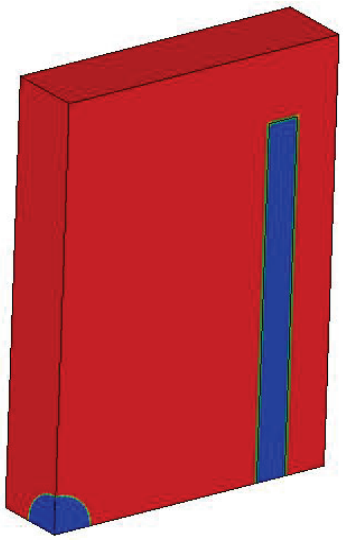

Figure 3-22: Pressure contour plot at $t = 0$; the air is initialized to atmospheric pressure and the explosive is modeled using the option 'INITIAL_VOLUME_FRACTION_ GEOMETRY'

The material models, EOS and boundary conditions for the model shown in Figure 3-22 are the same as those used in the prior FE models except for the addition of non-reflecting boundaries at the outer planes of the air domain. The non-reflecting boundaries prevent reflections of shock waves back into the air domain. In LS-DYNA, this is achieved by computing an impedance matching function for all the non-reflecting boundary segments assuming linear material behavior. Viscous normal and shear stresses are applied to these boundary segments internally and are given by equations 3-11 and 3-12.

$$\sigma_{normal} = - \rho \, c_d \, u_{normal} \tag{3-11}$$

$$\sigma_{shear} = - \rho \, c_s \, u_{tan} \tag{3-12}$$

where

ρ = Material density

c_d, c_s = Dilatational and shear wave speed of the transmitting media

u_{normal} , u_{tan} = Particle velocities in the normal and tangential directions

The analysis was run for 4 msec. A mesh sensitivity analysis was also performed. The mesh configuration details are shown in Table 3-8 and the results are presented in the following section.

Table 3-8: Mesh details for the 'INITIAL_VOLUME_FRACTION_GEOMETRY' model

Mesh configuration	Number of elements			Approximate element sizes for air (mm)
	Total	Air	Column	
1 (Coarse)	71,680	70,240	1,440	48-97[1]
2 (Fine)	147,000	143,850	3,150	39-84[1]
3 (Very fine)	762,272	747,672	14,600	21-59[1]

1. Aspect ratio ranged from 1 to 2.

3.9.4.2 Results and discussion

The reflected overpressure distributions at the three monitoring points are shown in Figures 3-23 to 3-25. As the mesh was refined, the peak reflected overpressures at points A and B increased monotonically. No such trend was observed at point C. The peak reflected overpressure at point B increased gradually whereas the increase was sudden at point A with the peak reflected overpressure rising sharply with the 2nd refinement. There are two plausible reasons for such a sudden increase: 1) the mesh refinements were not uniform (the percent change in the element size was greater in the 2nd refinement); and 2) the peak reflected overpressures at point A are more sensitive to changes in peak incident overpressures than at points B and C because of the smaller scaled distance and the angle of incidence (almost normal reflection). The values of the blast-wave parameters obtained from the FE analysis together with those calculated using UFC-3-340 are presented in Table 3-9. The peak reflected overpressures, reflected impulses and the times of arrival from LS-DYNA and UFC-3-340 are in good agreement. The reflected impulses at points B and C obtained from the LS-DYNA analysis are slightly greater than those

calculated using UFC-3-340. The introduction of the non-reflecting boundary conditions had no impact on the results. Regardless, such boundary conditions were adopted for all subsequent analyses.

Table 3-9: Blast-wave parameters calculated using UFC-3-340 and the 'INITIAL_VOLUME_ FRACTION _GEOMETRY' model in LS-DYNA

Monitoring location	Blast-wave parameter	LS-DYNA	UFC-3-340
Point A	Peak reflected overpressure (MPa)	78.1	79.2
	Reflected impulse (MPa -msec)	28.1	32.0
	Time of arrival (msec)	0.72	0.65
Point B	Peak reflected overpressure (MPa)	37.7	36.0
	Reflected impulse (MPa -msec)	15.6	14.0
	Time of arrival (msec)	1.05	1.0
Point C	Peak reflected overpressure (MPa)	9.41	11.1
	Reflected impulse (MPa -msec)	6.18	5.40
	Time of arrival (msec)	1.70	1.90

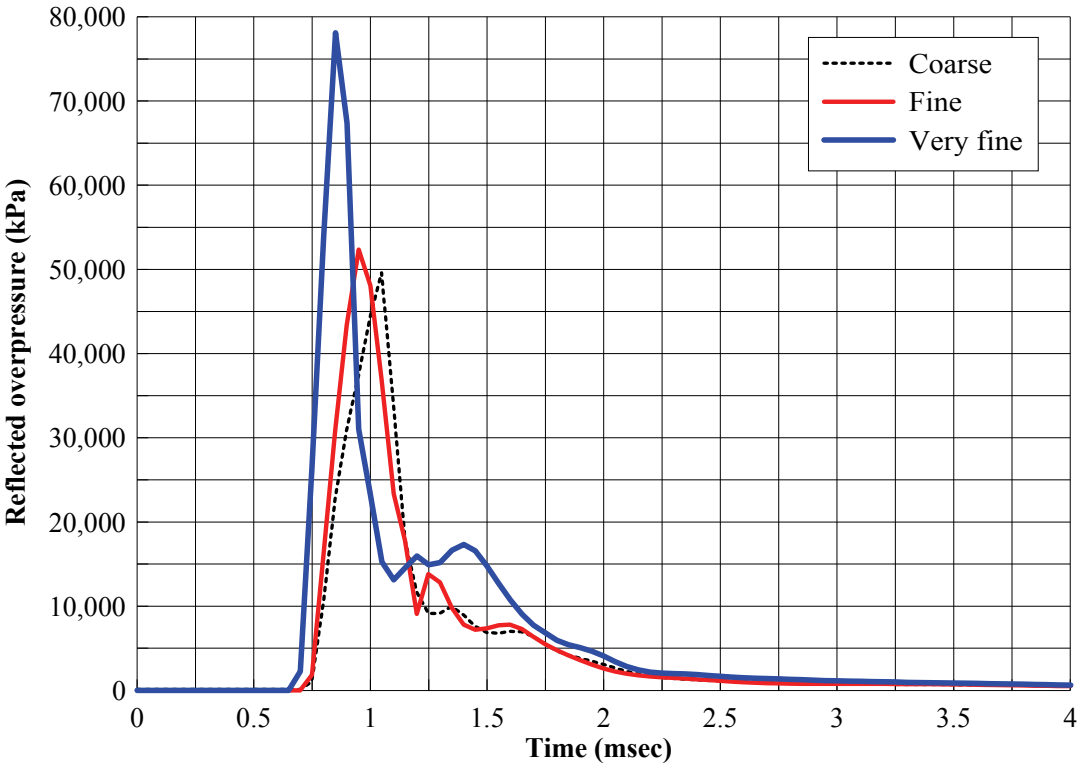

Figure 3-23: Reflected overpressure histories at point A with mesh refinement

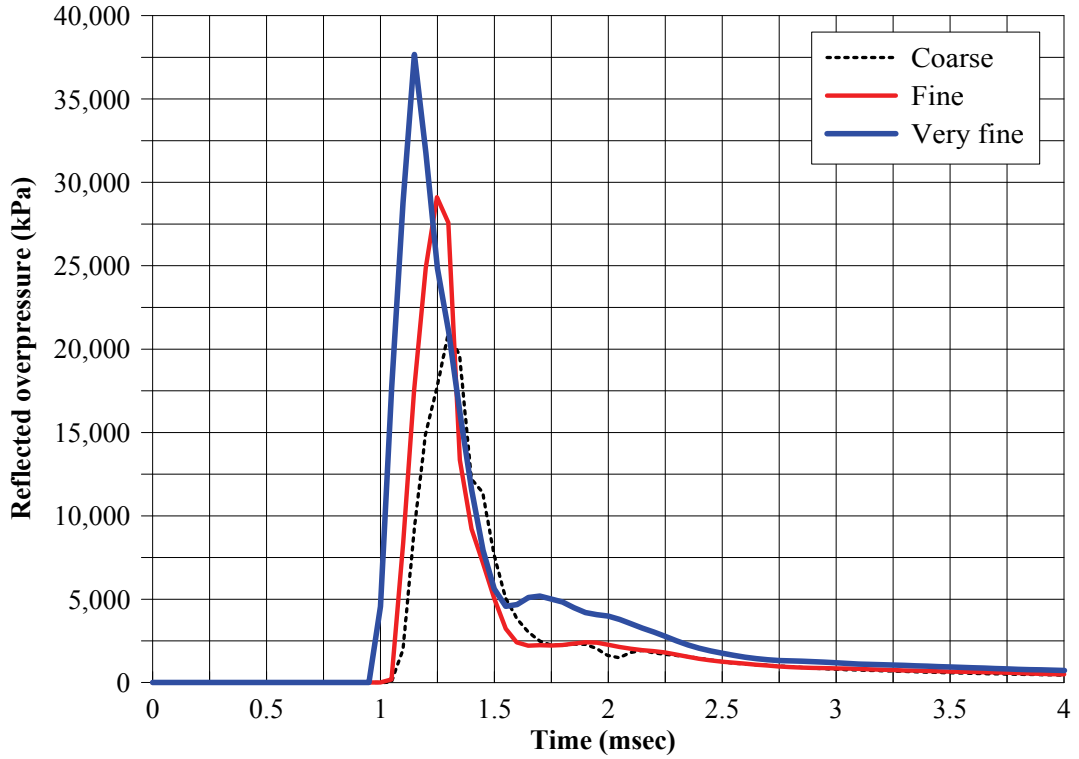

Figure 3-24: Reflected overpressure histories at point B with mesh refinement

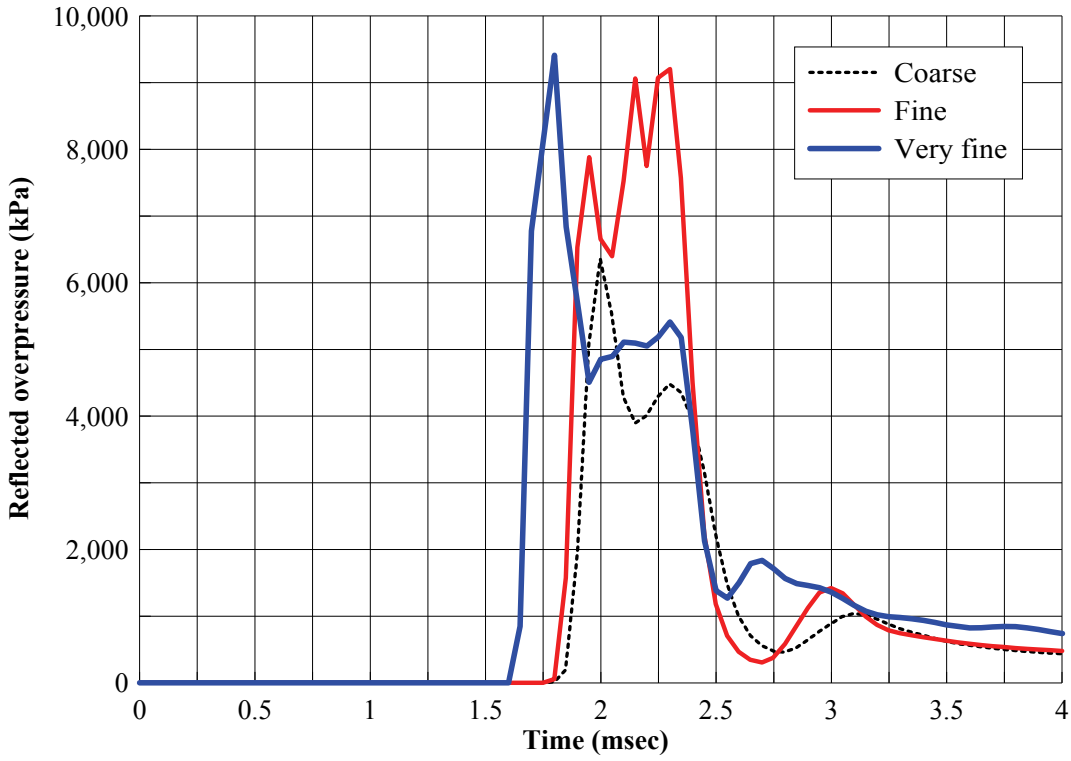

Figure 3-25: Reflected overpressure histories at point C with mesh refinement

3.9.4.3 Variation in JWL EOS parameters and timesteps between advection cycles

Of all the finite element (FE) models considered so far in LS-DYNA, the model using the option 'INITIAL_VOLUME_FRACTION_GEOMETRY' provided the best results as judged by comparison with those values calculated using UFC-3-340. In this section the effect of varying the values of the constants used in the JWL EOS on the results is studied. The JWL EOS, presented by equation 3-7, consists of a number of constants whose values are determined by the copper cylinder test described in section 3.2.2.2. The values of these constants were changed to those reported in the LNLL Explosives Handbook (Dobratz and Crawford, 1985) because this source is commonly cited in the literature. The values of the updated JWL parameters are presented in Table 3-10 and differ from those presented in Tables 3-3 and 3-4. The updated values are used in all subsequent analyses with LS-DYNA, Air3D (density, energy and detonation velocity only) and AUTODYN.

The radius of the spherical explosive was changed in the FE model as the density of the explosive changed slightly. The material properties and the EOS for air were not changed. The overpressure distributions with the altered JWL EOS parameters are shown in Figures 3-26 to 3-28 and a comparison with UFC-3-340 values is enabled by Table 3-11. It is clear that minor changes in the JWL parameters do not significantly affect the results except for the peak overpressures at point A (reduced by 23%) and at point C (increased by 30%).

Table 3-10: LNLL JWL EOS parameters (Dobratz and Crawford, 1985)

JWL EOS parameter	Value
A (GPa)	371.2
B (GPa)	3.231
R_1	4.15
R_2	0.95
ω	0.30
E_o (GPa)	7.0
ρ (kg/m^3)	1630
U (m/s)	6930

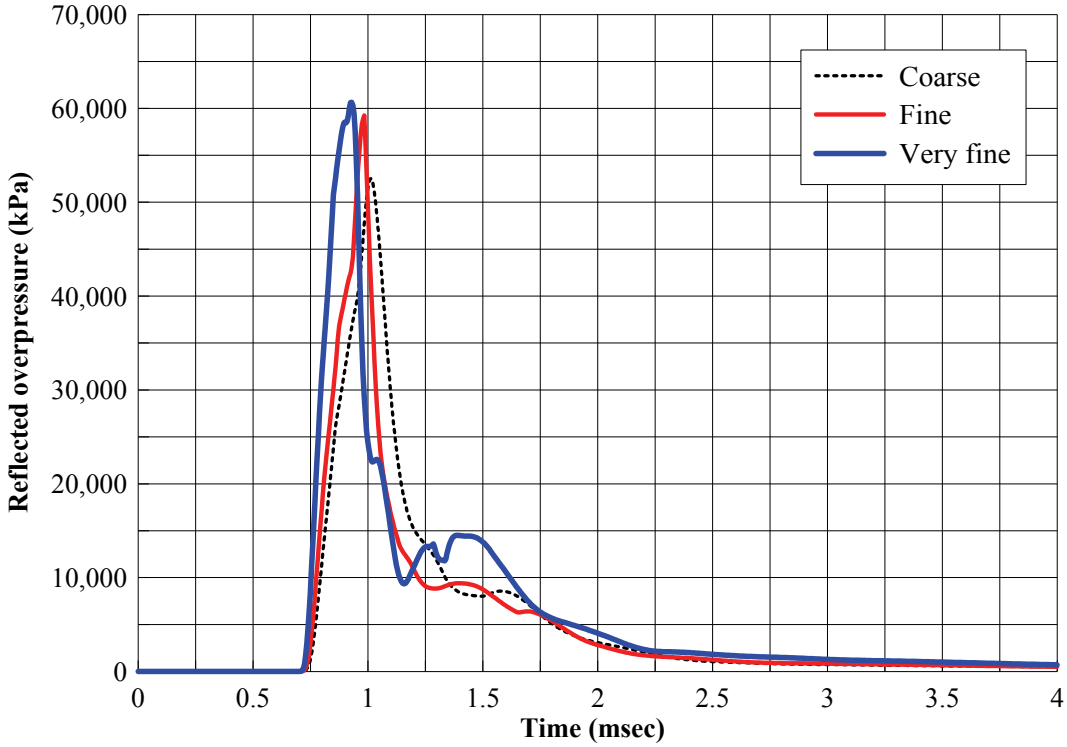

Figure 3-26: Reflected overpressure histories at point A with updated JWL EOS parameters

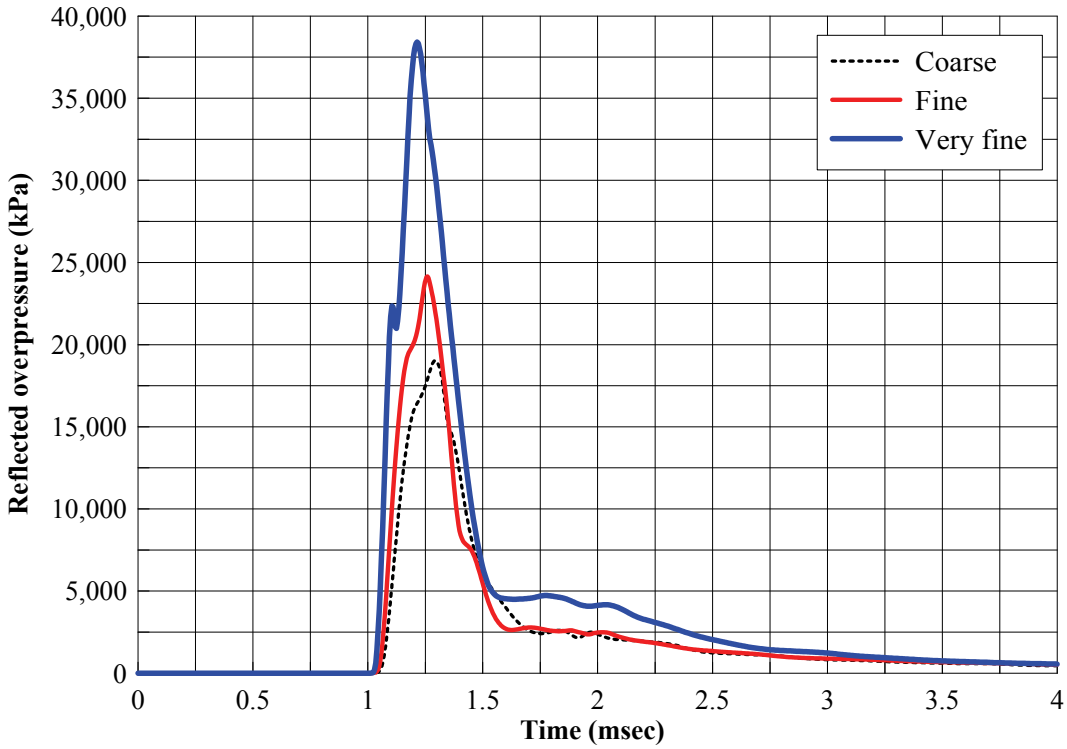

Figure 3-27: Reflected overpressure histories at point B with updated JWL parameters

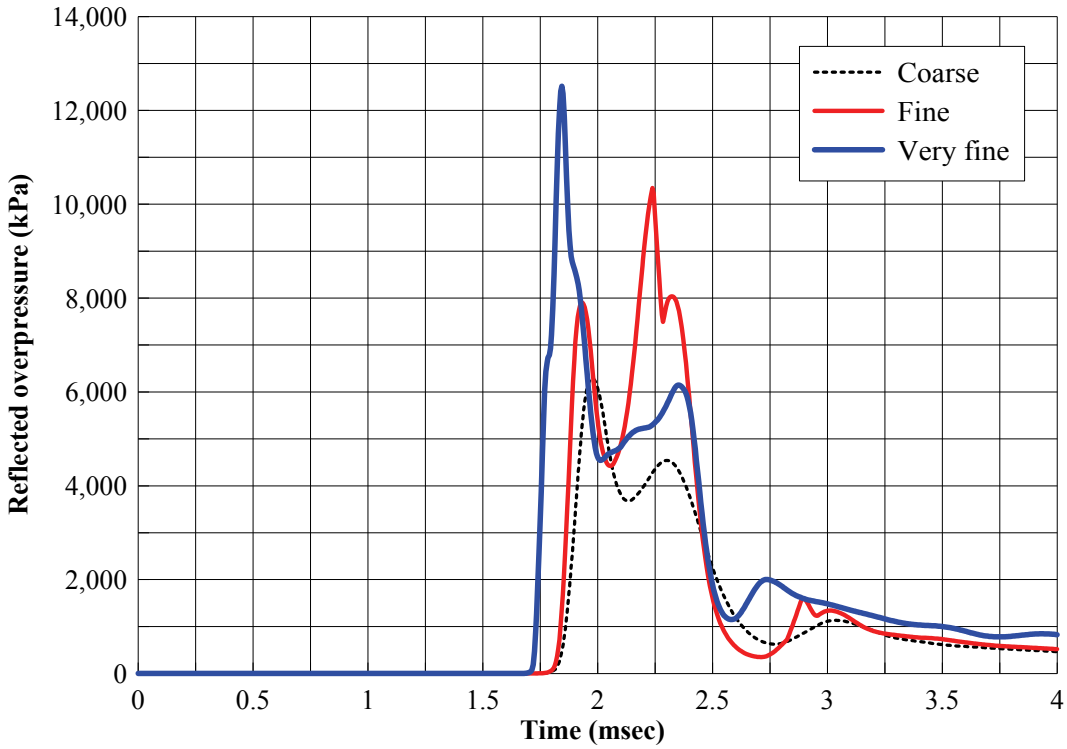

Figure 3-28: Reflected overpressure histories at point C with updated JWL parameters

Table 3-11: Blast wave parameters calculated using UFC-3-340 and the 'INITIAL_VOLUME_FRACTION_GEOMETRY' model in LS-DYNA with updated JWL parameters

Monitoring location	Blast-wave parameter	LS-DYNA	UFC-3-340
Point A	Peak reflected overpressure (MPa)	60.7	79.2
	Reflected impulse (MPa -msec)	24.7	32.0
	Time of arrival (msec)	0.81	0.65
Point B	Peak reflected overpressure (MPa)	38.4	36.0
	Reflected impulse (MPa -msec)	15.6	14.0
	Time of arrival (msec)	1.10	1.0
Point C	Peak reflected overpressure (MPa)	12.5	11.1
	Reflected impulse (MPa -msec)	6.33	5.40
	Time of arrival (msec)	1.77	1.90

A parametric study was conducted to observe the effect of variation in timesteps between advection cycles (NADV) under the 'CONTROL_ALE' keyword. The finest mesh configuration was used for these analyses. The parameter NADV determines the amount of material advected between adjacent elements. In finer meshes, using a small number of timesteps between advection cycles results in a higher peak pressure than using a lower NADV. By decreasing the number of timesteps between advection cycles (i.e., by increasing the advection calculations), a relatively large amount of material is advected through the fine mesh in a given timestep. A greater number of advection calculations are required to properly capture the amount of material transported from one element to another (Webster, 2007).

The number of timesteps between advections cycles was increased from 1 to 5 to 10. The results of the analysis are shown in Figures 3-29 to 3-31. As NADV was increased from 1 to 5, the peak reflected overpressure at point A increased by 10% but did not increase further when the number of advection cycles was increased to 10. At point B, there was almost no change in the peak reflected overpressure or the overpressure history with a change in advection cycles. At point C, the peak reflected overpressures decreased gradually with increase in NADV. There was little change in overpressure history as NADV was increased from 5 to 10. However, an irregular (and unexpected) pressure distribution was observed with NADV = 10. These results do not show a definite dependence on NADV, which is contrary to the observation of Webster (2007). The values of the blast-wave parameters are presented in Table 3-12.

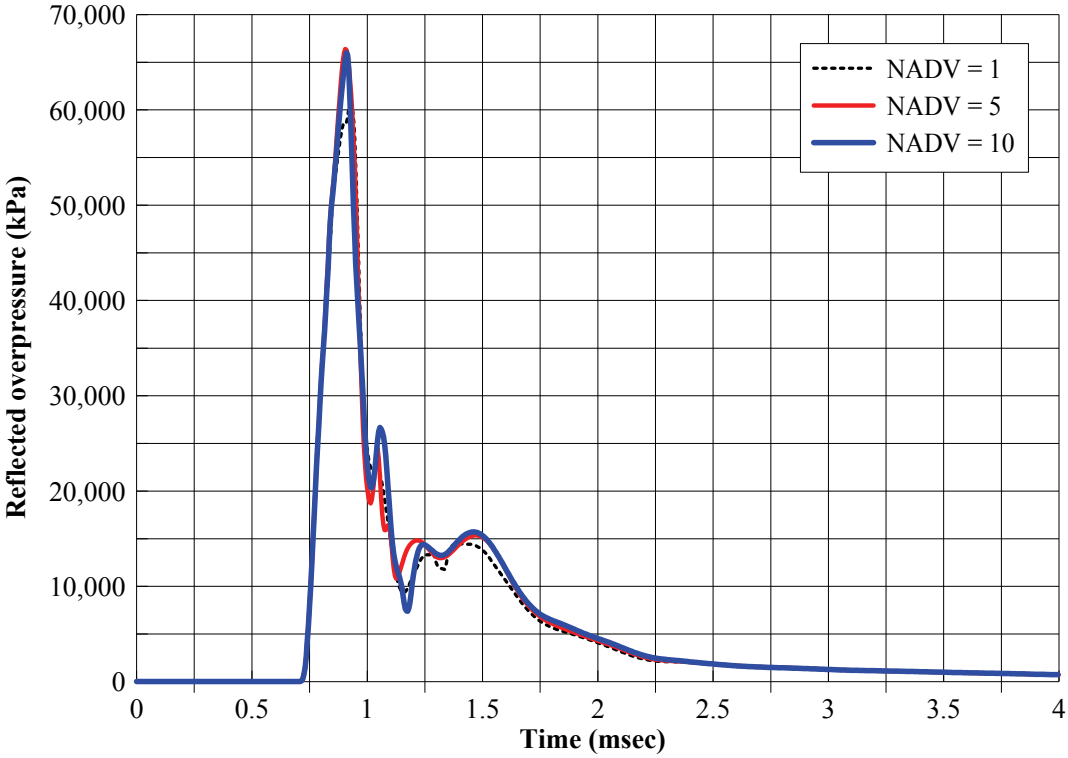

Figure 3-29: Effect of variation in NADV on the overpressure history at point A

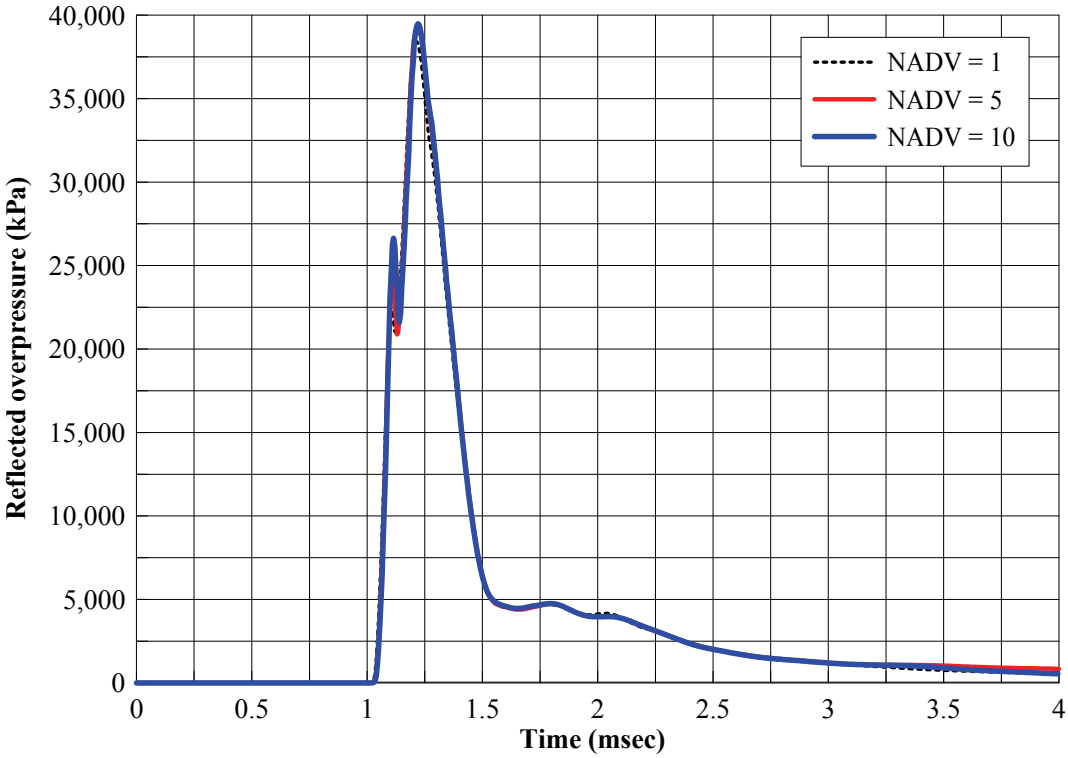

Figure 3-30: Effect of variation in NADV on the overpressure history at point B

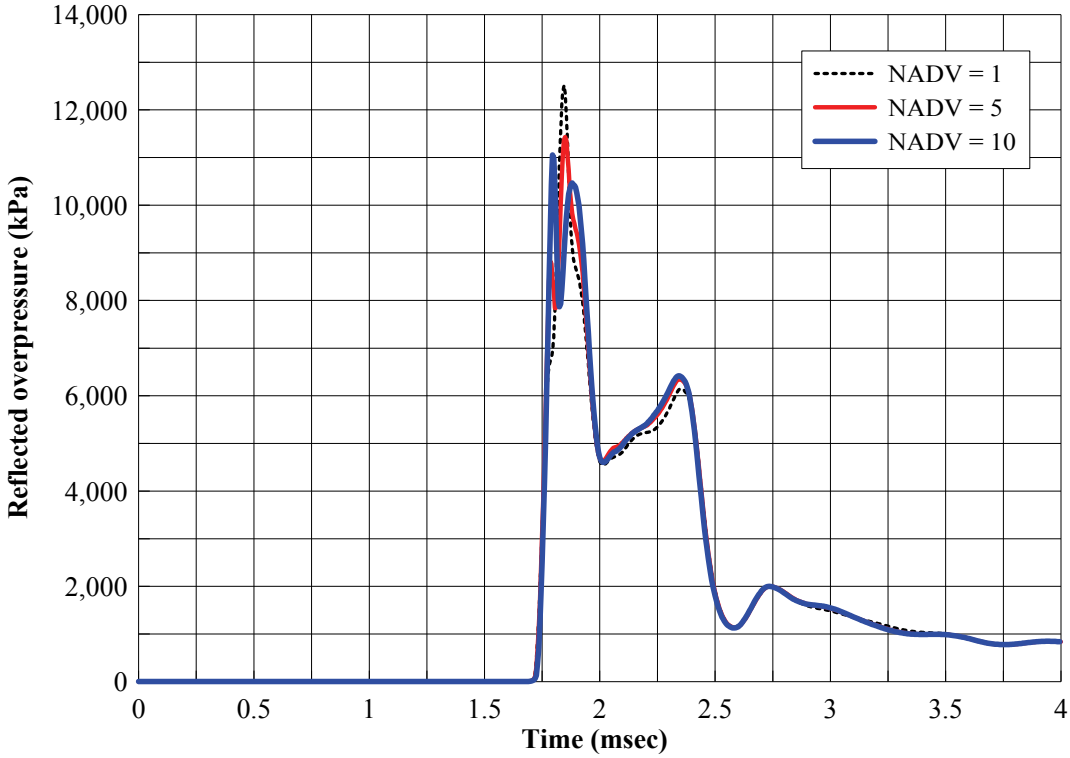

Figure 3-31: Effect of variation in NADV on the overpressure history at point C

Table 3-12: Results of UFC-3-340 calculations and the 'INITIAL_VOL….' model in LS-DYNA with different values of NADV

Monitoring location	Blast-wave parameter	LS-DYNA			UFC-3-340
		NADV			
		1	5	10	
Point A	Peak reflected overpressure (MPa)	60.7	66.4	66.0	79.2
	Reflected impulse (MPa -msec)	24.7	25.5	24.1	32.0
	Time of arrival (msec)	0.81	0.80	0.80	0.65
Point B	Peak reflected overpressure (MPa)	38.4	39.2	39.5	36.0
	Reflected impulse (MPa -msec)	15.6	16.0	14.7	14.0
	Time of arrival (msec)	1.10	1.10	1.11	1.0
Point C	Peak reflected overpressure (MPa)	12.5	11.4	11.1	11.1
	Reflected impulse (MPa -msec)	6.33	6.44	4.77	5.4
	Time of arrival (msec)	1.77	1.77	1.75	1.90

3.10 Air3D Modeling and Pressure Distributions

Air3D (Rose, 2006) is a computational fluid dynamics (CFD) code developed specifically for blast applications. The input data is specified via a text file, which is then run in batch mode. In a 3D analysis, there are 3 sections of the input file that are executed sequentially: spherical (1D), radial (2D) and main (3D). When the spherical input section is executed, the calculations proceed with spherical symmetry until the blast wave reaches a reflecting surface. The output of the 1D analysis is then remapped into 2D (the x, y domain) and then to a 3D domain.

3.10.1 Modeling and analysis

As described in section 2.6.3, Air3D uses the balloon analog of (Ritzel and Mathews, 1997) and assumes a constant γ for air. Air3D was used to model the problem described in section 3.7. The input needed for the 1D section of the input file is initial mass (1000 kg), density (1630 kg/m^3) and energy (4.3 J/kg)[16] of the explosive, the cell size for the 1D calculations and the radius for the 1D calculations (3m in the problem). In the 2D input section, the radial and axial boundaries for the 2D domain are specified by 'rmax' (= 3 m) and 'hmax' (= 3 m). The boundary conditions are specified by 'bru' (-1) and 'hru' (+1) in the input file; '-1' represents a 'stop' boundary and '+1' represents a 'transmit' boundary. For modeling the detonation problem described in section 3.7, there is no need to execute of the radial (2D) input because the output of the spherical (1D) calculations can be directly remapped to the 3D domain. However, remapping to the radial (2D) domain is usually necessary for height-of-burst problems. As the additional computational cost of remapping output from 1D to 2D to 3D was negligible, this sequence was used.

In the 3D section of the input file, the origin of the remapping was the origin of the problem domain

[16] Energy used in Air3D is the same as that used in the LS-DYNA analyses: 7 GPa = (4.3 J/kg) * (1630 kg/m^3)

(0, 0, 0). The size of the 3D domain was specified to be $4\text{m} \times 1.5\text{m} \times 6\text{m}$. The symmetry conditions in the 3D domain were similar to those used in the LS-DYNA analyses. The lower *x*, *y*, and *z* boundaries of the air domain were set to reflect to represent 3D symmetry whereas the upper *x*, *y*, and *z* boundaries were set to transmit. The rigid column was specified through the 'obstacle definition'. Obstacles are defined in Air3D by declaring the cells to be either 'true' (air) or 'false' (solid). The types of obstacles that can be defined in Air3D are cuboids, spheres, cylinders, and extruded triangles (wedges). A three-dimensional array of logical variables is used by Air3D to determine if a cell is 'unused', that is, occupied by a solid, or 'used' if occupied by air. The 'unused' cells act as reflecting boundaries and are not included in the numerical flux calculations (Rose, 2006).

Three analyses were performed with mesh refinements (or cell-size reduction). The cell sizes used in these analyses are given in Table 3-13. The Air3D User Guide (Rose, 2006) recommends a maximum cell size based on scaled distance: the cell size should represent roughly a scaled radial distance of 1 $\text{m/kg}^{0.33}$. If the mass of the explosive is 1000 kg, the cell size should be no greater than 10 mm:

$$\text{Maximum cell size} = 1 \times (1000)^{0.33} = 10 \text{ mm}$$

The cell size could be reduced further in the spherical and radial calculations without a huge increase in computational cost. However, the recommended cell size of 10 mm could not be achieved in the 3D calculations due to computational constraints, but this cell size is needed only at small scaled ranges. At large distances from the point of detonation, there is an increase in the wavelength of the shock wave and the cell size required to produce accurate results increases accordingly. The reflected overpressure history data is obtained at monitoring points on the face of the column by specifying their co-ordinates in the Air3D input file.

Table 3-13: Cell sizes used in 1D, 2D and 3D Air3D calculations

	Element size in the each section of the input file (mm)			Approximate number of cells
Analysis	Spherical	Radial	Main	
1 (Coarse)	2	10	40	570,000
2 (Fine)	1	5	20	4,500,000
3 (Very fine)	0.5	2	15	10,680,000

3.10.2 Results and discussion

The Air3D overpressure histories at the three monitoring points are presented in Figures 3-32 to 3-34. Although the peak reflected overpressures increase moderately, there is no significant change in the reflected overpressure histories with mesh refinement. The cell sizes used in the analyses are less than or equal to the required cell size recommended by the Air3D User Guide (Rose, 2006). A comparison of the Air3D and the UFC-3-340 calculations presented in Table 3-14 show that the peak overpressures are much less than those of the UFC-3-340, especially at point B (by 44%). A similar trend is seen in the reflected impulse. The Air3D arrival times differ slightly from those calculated using UFC-3-340.

An advantage of Air3D is its computational efficiency. Unlike LS-DYNA, the inbuilt parallel processing capability in Air3D allows use of multiple processors resulting in lower runtimes, even for very high resolution analyses.

Table 3-14: Comparison of Air3D results and UFC-3-340 calculations

	Point A		Point B		Point C	
	Air3D	UFC-3-340	Air3D	UFC-3-340	Air3D	UFC-3-340
Peak reflected overpressure (MPa)	65.2	79.2	25.4	36.0	7.13	11.1
Reflected impulse (MPa-msec)	23.4	32.0	9.24	14.0	3.41	5.40
Time of arrival (msec)	0.86	0.65	1.21	1.0	1.83	1.90

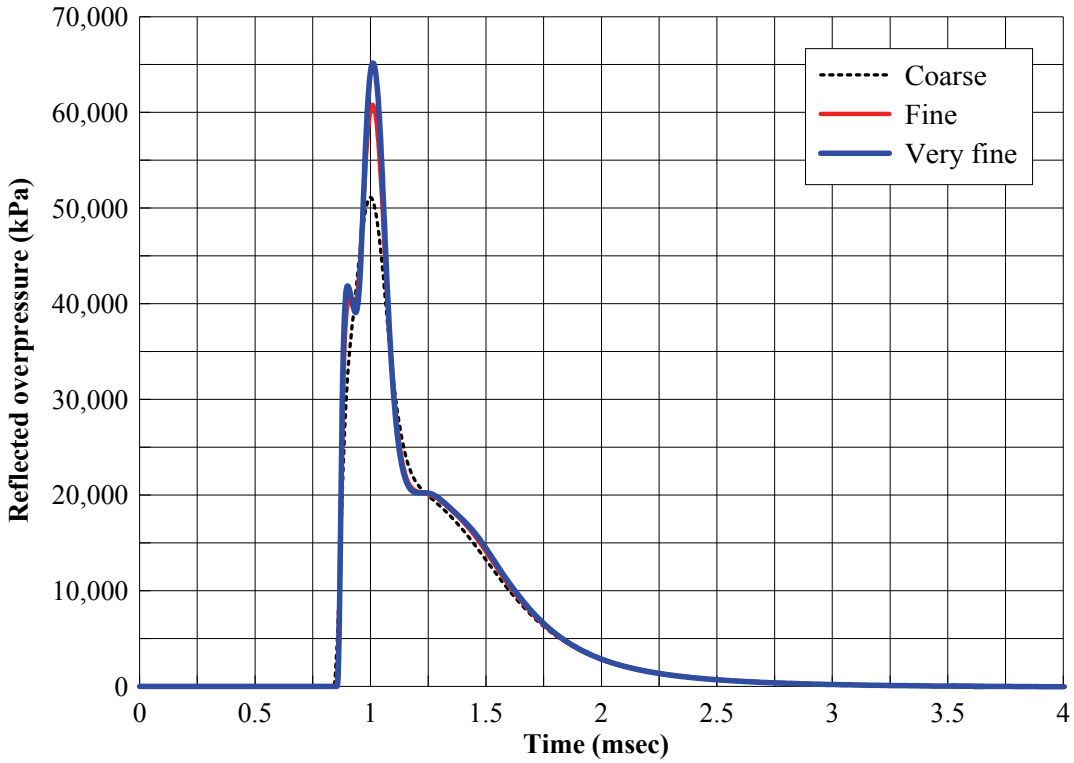

Figure 3-32: Air3D reflected overpressure histories at point A as a function of cell size

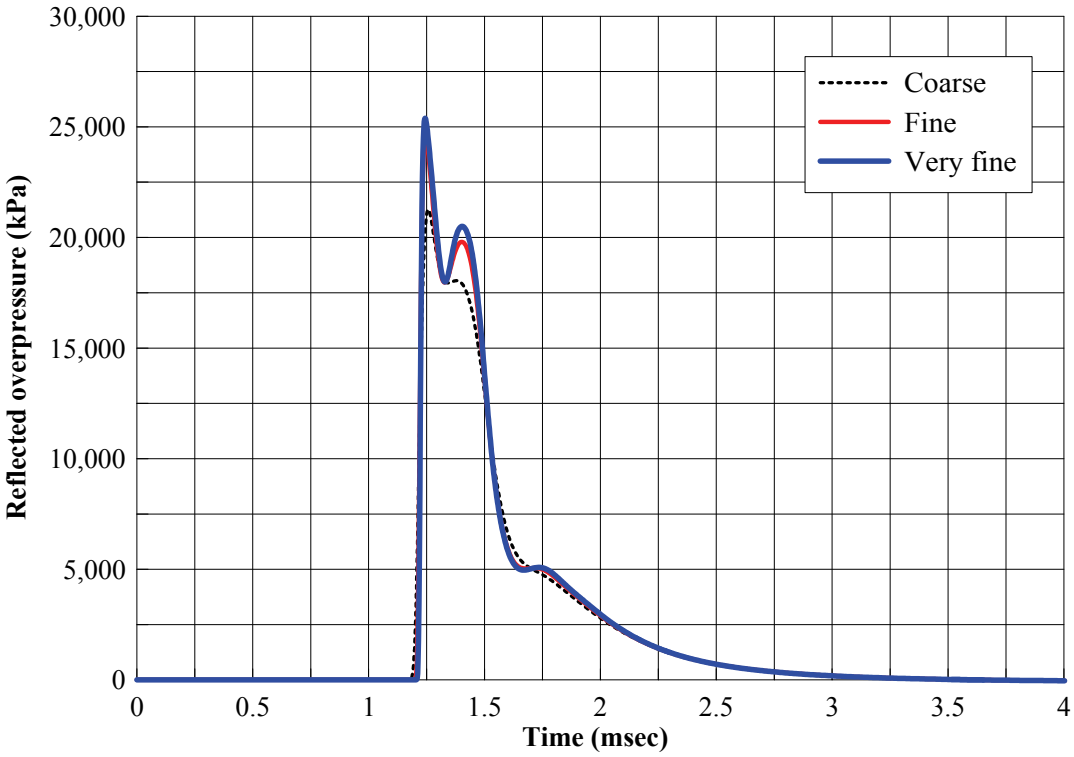

Figure 3-33: Air3D reflected overpressure histories at point B as a function of cell size

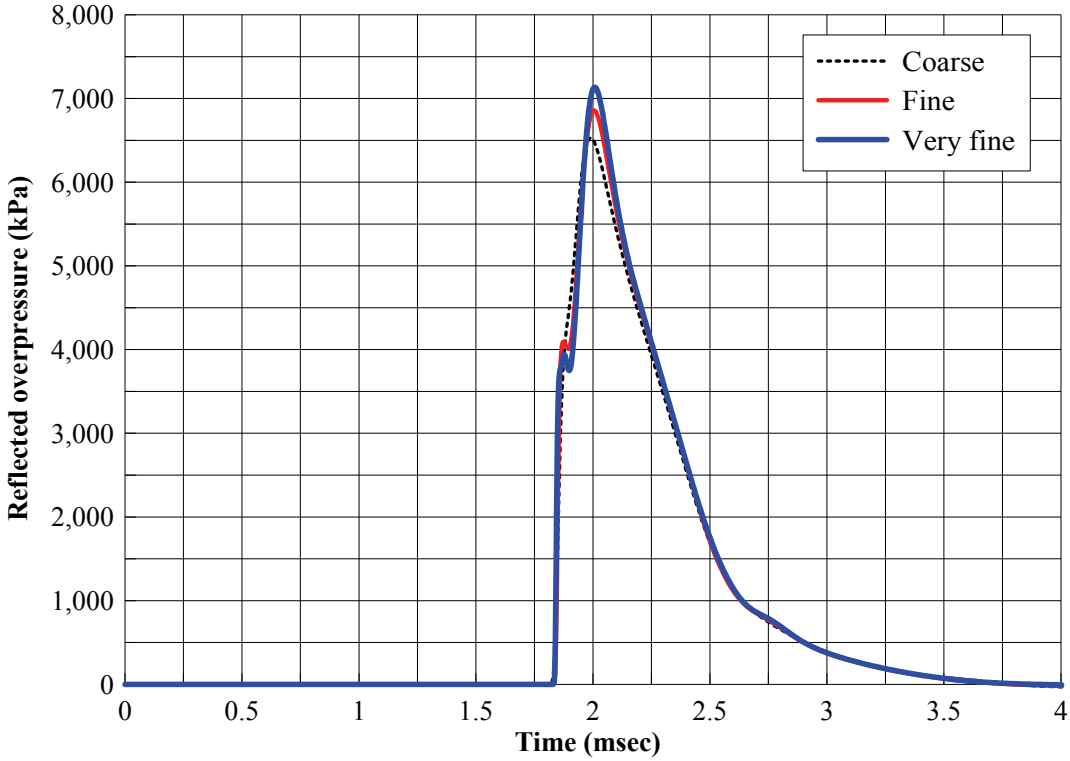

Figure 3-34: Air3D reflected overpressure histories at point C as a function of cell size

3.11 AUTODYN Modeling and Pressure Distributions

Modeling detonations in AUTODYN is different than from LS-DYNA but similar to Air3D. AUTODYN uses finite volume and finite element methods to solve the governing equations presented in equations 3-1 to 3-3. Similar to Air3D, AUTODYN remaps output from 1D/2D to 3D. The remapping feature allows use of higher resolution grid in the analysis of the initial stages of the shock wave expansion. However, remapping in AUTODYN is manual and requires user intervention. Detonation modeling in AUTODYN is two-step process. The first step involves the early time expansion of the explosive products in 1D using radial symmetry, which continues until a reflecting surface is reached. The output of the 1D analysis is then transmitted to the 3D domain that is generated separately. The analysis is the run until the termination time. Although this process is very similar to that used in Air3D, the AUTODYN and Air3D solution methodologies and capabilities differ. AUTODYN is a general purpose hydrocode used for a wide variety of applications but Air3D addresses air-blast only.

3.11.1 1D analysis

The input required in AUTODYN to model the problem described in section 3.7 is similar to that required in LS-DYNA. The explosive was modeled using the JWL EOS and the air was modeled as an ideal gas. Although AUTODYN has its own material library with default values for the various EOS parameters, the values of the JWL EOS parameters listed in Table 3-10 were used for analysis. The air was modeled as an ideal gas with an initial pressure of 101.3 kPa by specifying an initial energy of 2.068×10^5 mJ/mm^3. The initial temperature, density and adiabatic constant (specific heat ratio) γ were set to 288 ^{o}K (15 ^{o}C), 1.225 mg/cm^3, and 1.4, respectively. The multi-material Eulerian solver was used for both the explosive and the air. For the 1D analysis, a 'wedge' of length approximately equal to 3 m (2.990 m) was defined with radial symmetry (AUTODYN-2D); see Figure 3-35. The wedge was filled with explosive and air. The radius of the explosive was 0.527 m. The start point for the wedge was 5 mm from the origin to avoid a zero thickness element at the origin. Although this correction reduced the volume of the explosive, the percent reduction was negligible.

One dimensional analysis was performed until the blast wave reached the end of the 1D domain. However, the analysis was interrupted when the explosive expanded to approximately 10 times its original volume. At this stage the value of the compression ratio, μ presented in equation 3-13a is approximately -0.99. AUTODYN uses the compression ratio to calculate the density of the detonation products; see equation 3-13b. If the value of μ decreases below -0.99, the density of the detonation products can become very small and lead to numerical difficulties.

$$\mu = \frac{\rho}{\rho_o} - 1 \tag{3-13a}$$

$$\rho = \rho_o\ (1 + \mu) \tag{3-13b}$$

Moreover, at large volumetric ratios, the first two terms of the JWL EOS (eq. 3-14) become negligible and the EOS collapses to that of an ideal gas EOS, namely

$$p = A\left(1 - \frac{\omega}{R_1 V}\right)e^{-R_1 V} + B\left(1 - \frac{\omega}{R_2 V}\right)e^{-R_2 V} + \frac{\omega}{V}E \qquad (3\text{-}14)$$

Equating equation 3-14 with equation 3-7, $\gamma = 1 + \omega = 1 + 0.3 = 1.3$ for large volumetric ratios. When the compression ratio reached a value of -0.99, the JWL EOS was changed to an ideal gas EOS with $\gamma = 1.3$ and $\rho = 1 \times 10^{-4}$ gm/cm^3 (Century Dynamics, 2005). The 1D analysis was then continued until the blast wave reached the boundary at 3 m. The termination time for the 1D analysis was specified as 0.6 msec and was determined by trial and error. The results of the 1D analysis were then stored in a '.fil' file.

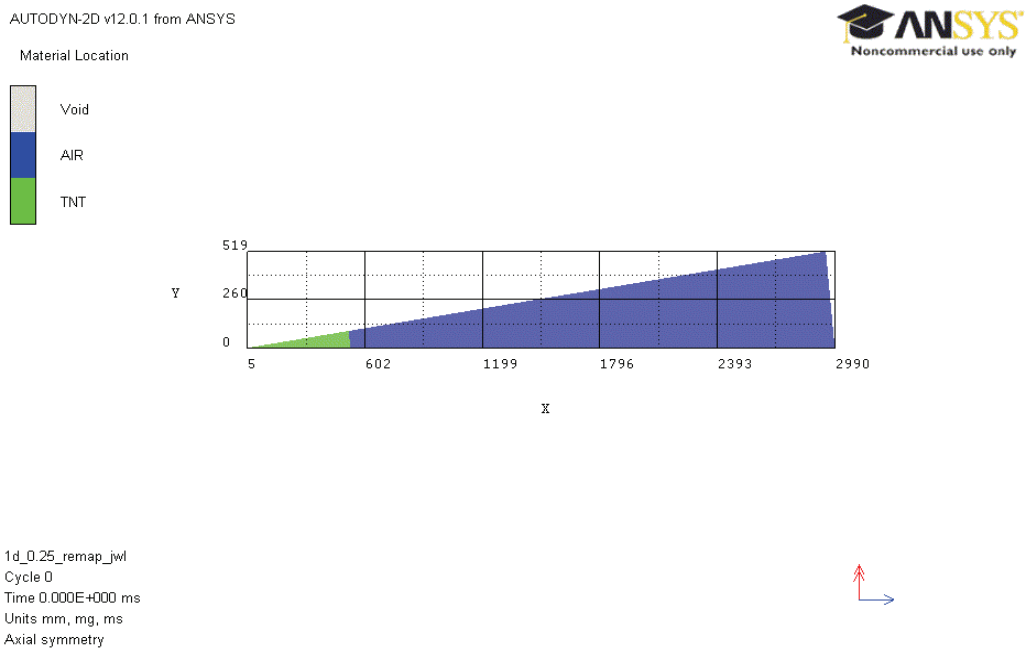

Figure 3-35: 1D wedge filled with TNT and air and modeled with multi-material Eulerian formulation

To verify that changing the JWL EOS to the ideal gas EOS after the explosive had expanded to 10 times its initial volume did not change the overpressure distribution, two trial 1D analyses were performed: one in which the JWL EOS was changed to the ideal gas EOS and the other in which the JWL EOS was retained. The incident overpressure histories at a standoff of 3.04 m were computed. It can be seen from Figure 3-36 that the two methods provide almost identical overpressure histories.

Before proceeding to the 3D analyses, a grid sensitivity analyses was performed in the 1D domain by reducing the cell sizes and monitoring the peak overpressures at a radial distance of 3.04 m (distance to point A). Three cell sizes were used: 1 mm, 0.5 mm, and 0.25 mm. The peak overpressure converged with a cell size of 0.25 mm. The results of the 1D analysis with a cell size of 0.25 mm were remapped to the 3D domain. The overpressure histories for the three cell sizes and the pressure contour plot at the end of the 1D analysis are shown in Figure 3-37 and Figure 3-38, respectively.

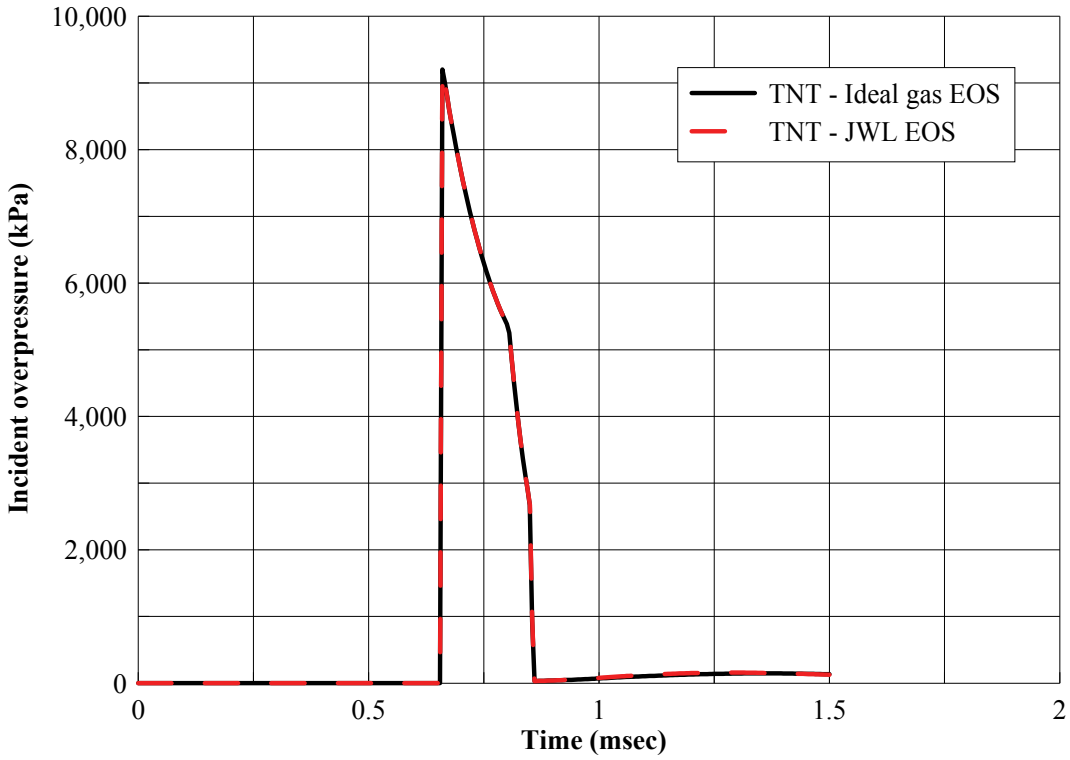

Figure 3-36: Incident overpressure histories at a distance of 3.04 m with different EOS used for the detonation products

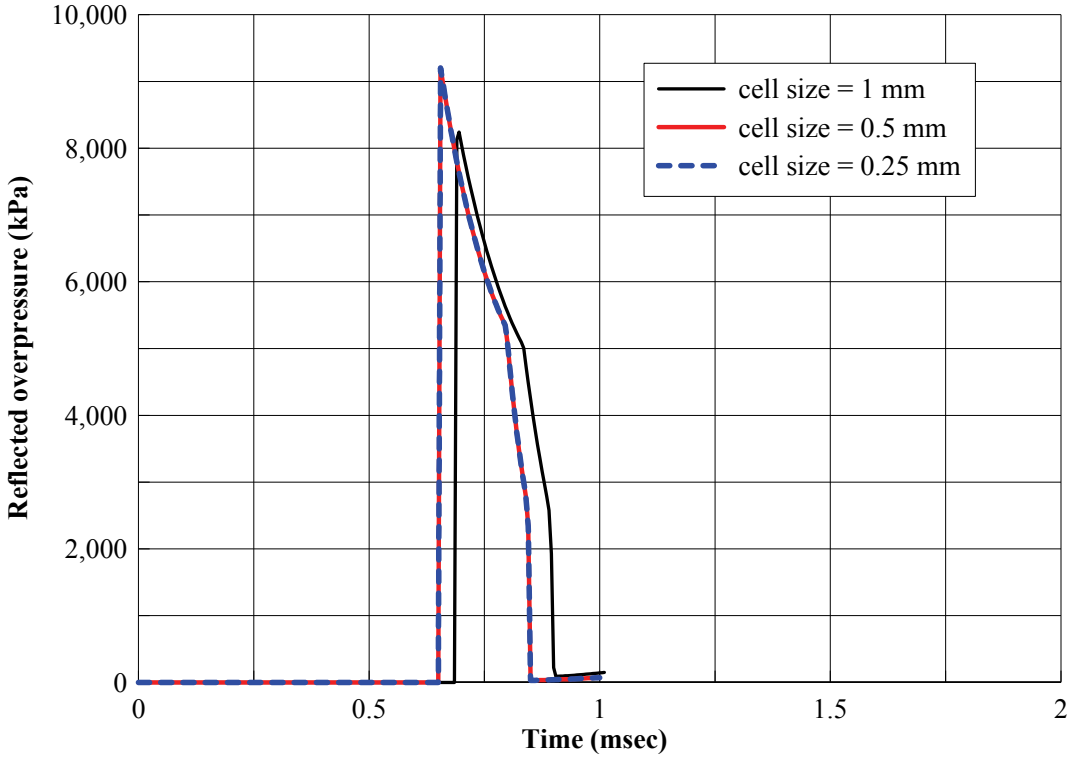

Figure 3-37: Incident overpressure histories at a distance of 3.04 m with different cell sizes

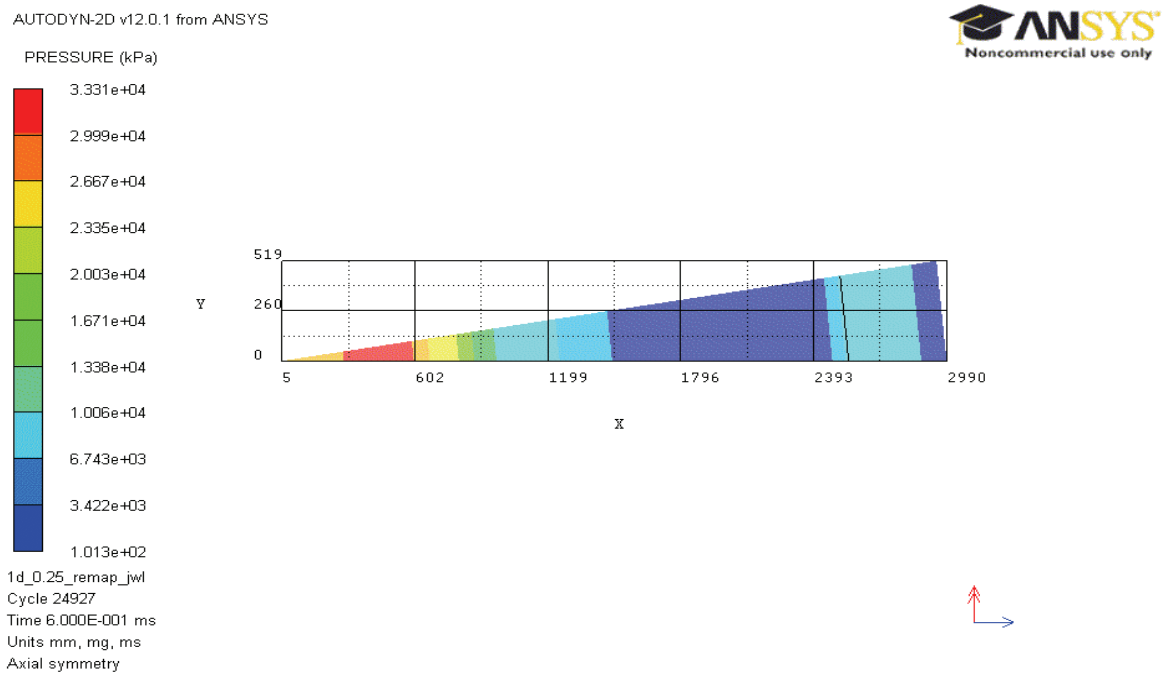

Figure 3-38: Contour plot of pressure at the end (t = 0.6 msec) of the 1D analysis

3.11.2 3D analysis

For the 3D analysis, a 3D cuboid-shaped air domain was created in another AUTODYN file. Air was modeled as an ideal gas. The air domain had dimensions of $4\text{m} \times 0.6\text{m} \times 6\text{m}$. The range of the air domain in the *y*-direction was reduced from that of the LS-DYNA and Air3D models so that finer meshes could be used. This reduction in the *y*-range of the air-domain should not have any effect on the results if appropriate boundary conditions are applied. Similar to LS-DYNA, symmetry in 3 directions was considered and only 1/8 of the air domain and 1/4 of the column were modeled. AUTODYN has a fast and efficient Euler Flux Corrected Transport (FCT) solver that was developed for blast applications (Fairlie, 1998). AUTODYN also offers a multi-material Euler-Godunov solver that can be used for solving fluid and gas dynamics problems but it is generally used for blast-wave modeling because it computes lower peak overpressures and less accurate solutions than the Euler-FCT solver (see Borve, et al., 2008 for details).

The output of the 1D analysis was transformed into the 3D domain and the start time of the 3D analysis was set equal to the end time of the 1D analysis. The pressure contours at the beginning of the 3D analysis are shown in Figure 3-39; the monitoring points are also shown. The output of 1D analysis included multiple materials: air and explosion product gases. When the output was remapped to the single material 3D Euler-FCT domain, the explosion gases had to be converted to air defined in the 3D domain.

As the column was to be defined as rigid, there were three ways of coupling the pressure wave and the column. Similar to Air3D, 'unused' cells can be defined in AUTODYN, thereby eliminating the cells occupied by the column geometry. In AUTODYN, Eulerian boundaries are set to reflect by default unless a boundary condition is specified. Thus the 'unused' cells created reflecting boundaries at the column surfaces for the air domain. Another method by which coupling can be achieved is to model the column with a Lagrangian mesh as a rigid material, and define 'Fully Coupled' coupling, making the Lagrangian mesh interact dynamically with the Eulerian mesh. The column could also be defined as a 'Fill' part and 'RIGID' coupling could be used that automatically defines rigid boundaries for the Eulerian mesh.

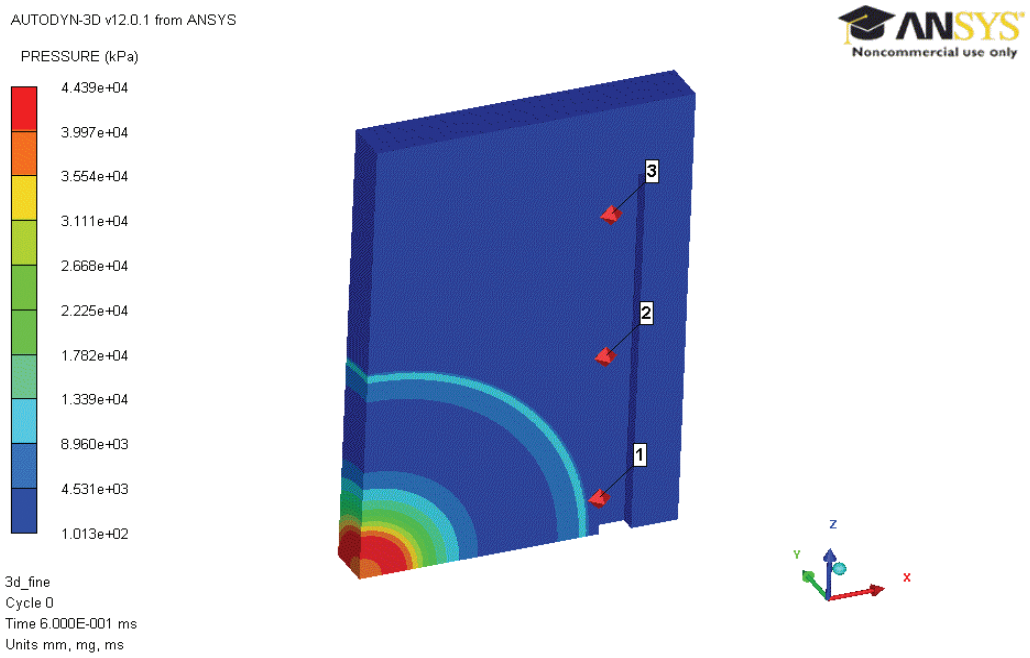

Figure 3-39: Pressure contours just after the remapping of 1D output to the 3D air domain

The first method was used to define the rigid column (i.e., by defining 'unused' cells) for its simplicity and efficiency. In AUTODYN, the cell grid is defined in *I-J-K* format. The 'flow out' boundary conditions are applied at the upper *I*, *J*, *K* boundaries so that the pressure waves do not renter the air domain due to reflection. It should be noted that 'flow out' or 'transmit' boundaries don't transmit all the waves and there can be some reflection back into the domain. These boundaries should not be assigned close to the regions of interest.

Similar to the 1D analyses, the effect of grid refinement on the 3D analysis results was studied. Four grid configurations were considered. Each time the 1D analysis results with 0.25 mm cell size were remapped to the 3D grid and the analysis was run until the termination time of 4 msec. In the initial analyses, the default timestep in the analyses was used. The analysis results with the default timestep showed that instead of a single peak overpressure at monitoring point A, two peaks were observed, clearly indicating the possibility of numerical errors in the analyses. AUTODYN uses the Courant condition and two other stability criteria to determine the timesteps of an analysis. Even though the calculated timestep guarantees stability of the solution, it does not guarantee accuracy. To improve the accuracy, smaller timesteps

should be considered. Moreover, if the grid size is reduced, the timestep must also be reduced. The timesteps required for the grid configurations were determined by trial-and-error and are presented in Table 3-15.

Table 3-15: Grid details for the AUTODYN analyses

Grid configuration	Total number of cells	Approximate cell size (mm)	Timestep required to maintain accuracy[1] (msec)
1 (Coarse)	115,200	50	7.5×10^{-4}
2 (Fine)	571,200	30	1×10^{-4}
3 (Very fine)	1,490,400	20	5×10^{-5}
4 (Finest)	2,954,880	15	2.5×10^{-5}

1. Accuracy is defined here by the disappearance of the second peak in the overpressure distributions.

3.11.3 Results and discussion

The overpressure histories at the three monitoring points obtained from AUTODYN are presented in Figures 3-40 to 3-42. As the cell size is reduced from 50 mm (coarse) to 20 mm (very fine) the peak reflected overpressures at points A and B increased by 19% and 12%, respectively. The peak reflected overpressure at point C decreased by 15%. A comparison of peak reflected overpressures obtained from AUTODYN with the results from UFC-3-340 that are presented in Table 3-16 shows that the AUTODYN-computed values are significantly less. The arrival times of the blast waves are similar to those calculated using UFC-3-340 except at point C where the blast wave arrived earlier in the AUTODYN analysis.

The analysis for the finest grid was not run for the complete problem time of 4 msec. The peak reflected overpressures at points A and B did not increase significantly from those obtained using the coarser grids. The analysis was terminated at about 1.1 msec and results are not presented here.

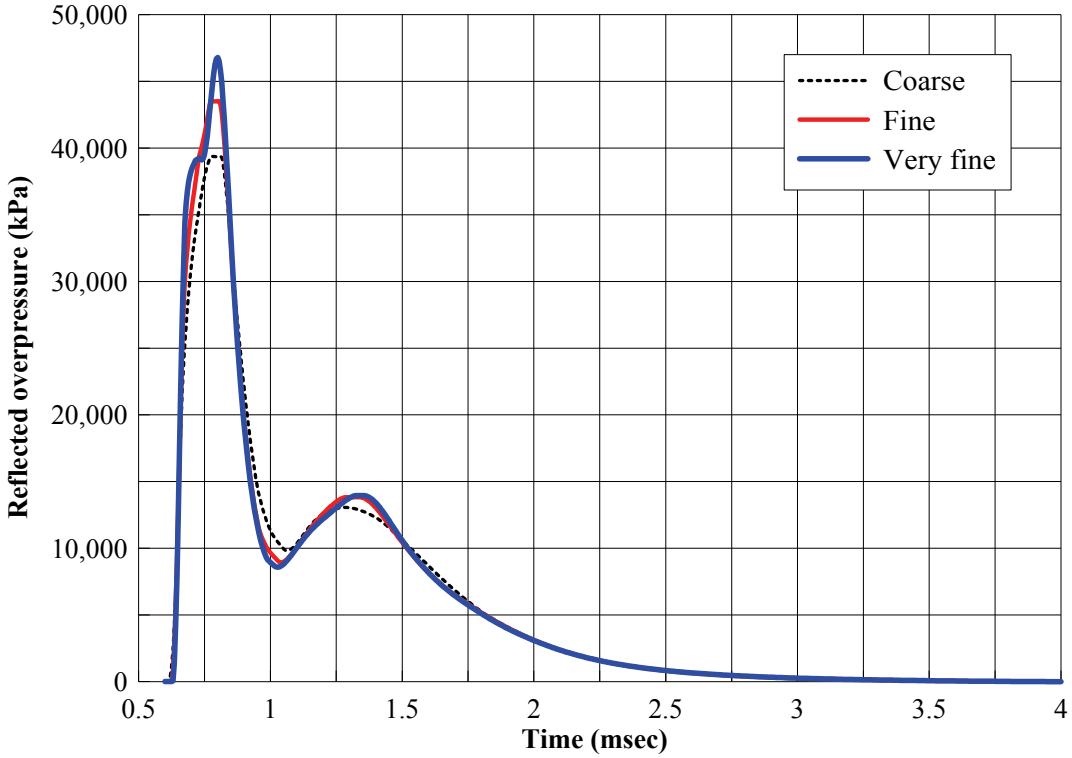

Figure 3-40: Reflected overpressure histories at point A with mesh refinement

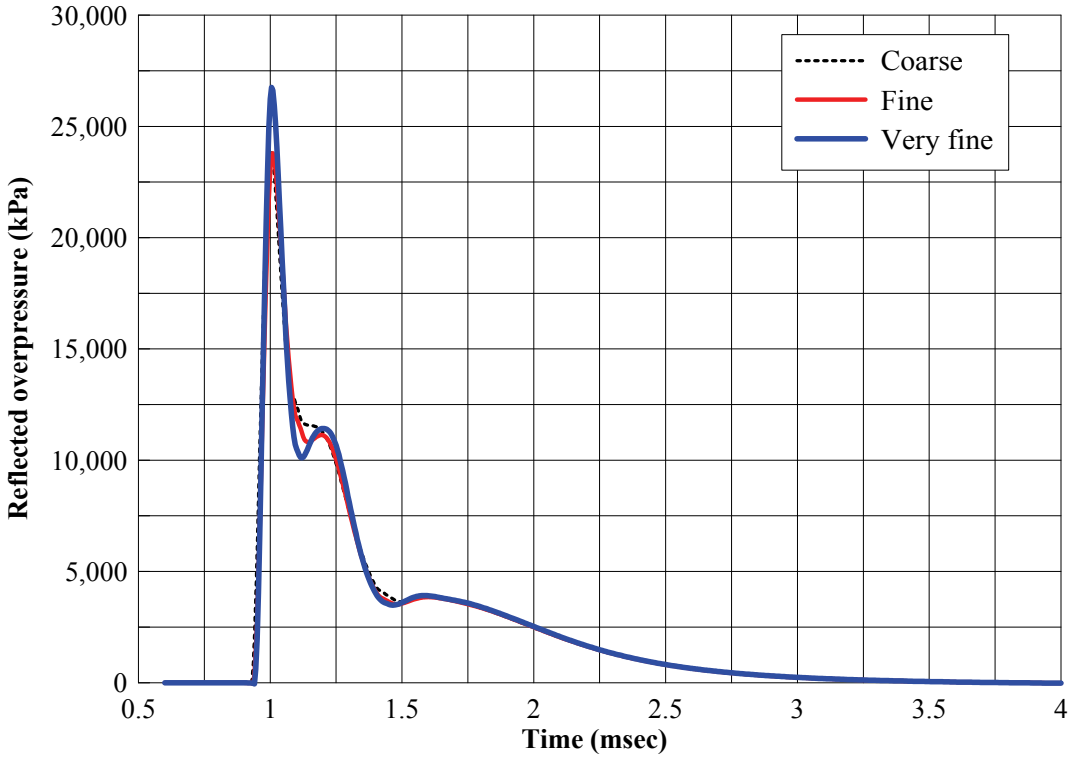

Figure 3-41: Reflected overpressure histories at point B with mesh refinement

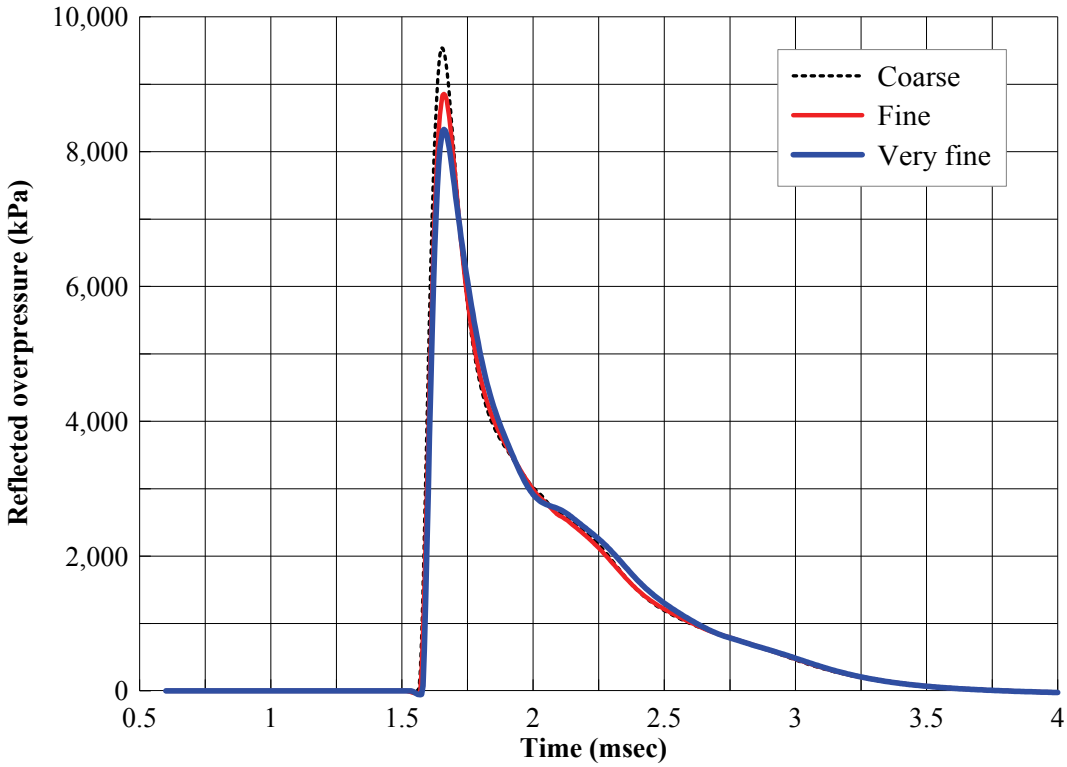

Figure 3-42: Reflected overpressure histories at point C with mesh refinement

Table 3-16: Comparison of blast-wave parameters obtained from AUTODYN and UFC-3-340 calculations

Monitoring location	Blast-wave parameter	AUTODYN	UFC-3-340
Point A	Peak reflected overpressure (MPa)	46.8	79.2
	Reflected impulse (MPa -msec)	20.5	32.0
	Time of arrival (msec)	0.70	0.65
Point B	Peak reflected overpressure (MPa)	26.8	36.0
	Reflected impulse (MPa -msec)	8.43	14.0
	Time of arrival (msec)	0.95	1.0
Point C	Peak reflected overpressure (MPa)	8.33	11.1
	Reflected impulse (MPa -msec)	3.73	5.40
	Time of arrival (msec)	1.61	1.90

The process of propagation of the spherical detonation wave in air, its reflection from the column and the subsequent propagation of the reflected wave along the height of the column can be seen in the contour plots of Figure 3-43. The rigid column and the location of the three monitoring points are shown in the figure. The 3D analysis began at t = 0.6 msec when the spherical detonation wave front was still propagating through the air, immediately before striking the column. At t = 0.6 msec, the shock front pressure is much smaller (9 to 13 MPa) than the pressures near the point of initial detonation (40 to 44 MPa), which was of the order of 18 GPa (see section 3.11.4) as the reaction front was advancing through the explosive. In panel b), the shock wave has struck the wall and is reflected, increasing the pressures in that region to about 37 MPa. In the following four panels, the reflected wave propagates up the height of the column. At t = 1 msec the pressure wave has reached the 2nd monitoring point (B).

The shape of the reflected wave is worthy of note. As shown in Figure 3-7, upon reflection from a rigid surface, the reflected wave retains its hemispherical shape. In the contour plots presented in Figure 3-43, the shape of the reflected wave is not hemispherical but rather that of a flattened curve.

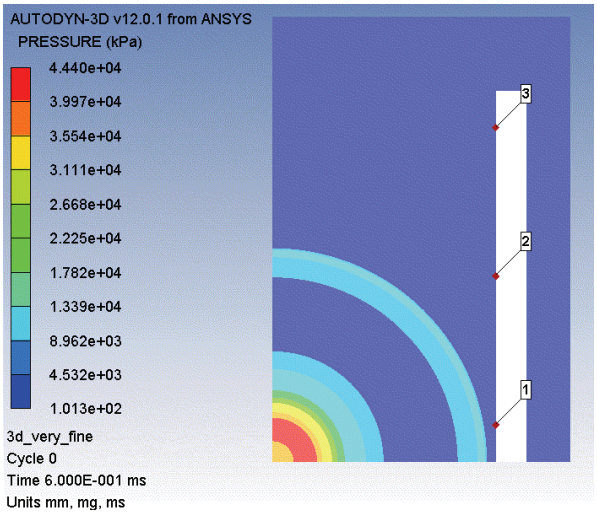

a) t = 0.6 msec

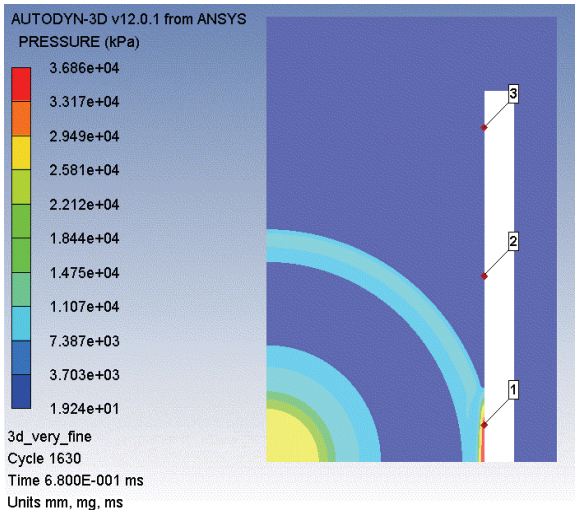

b) t = 0.68 msec

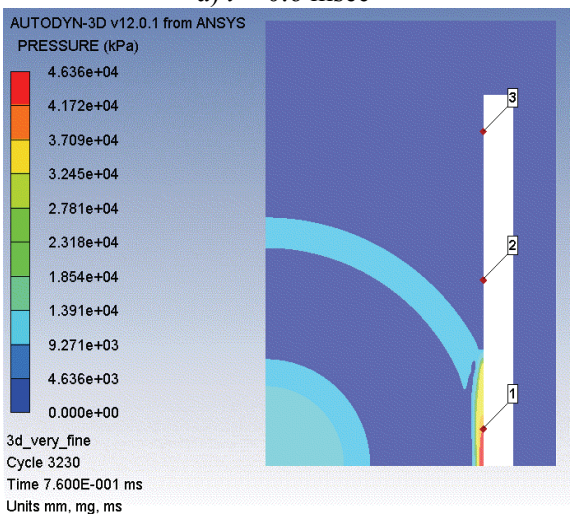

c) t = 0.76 msec

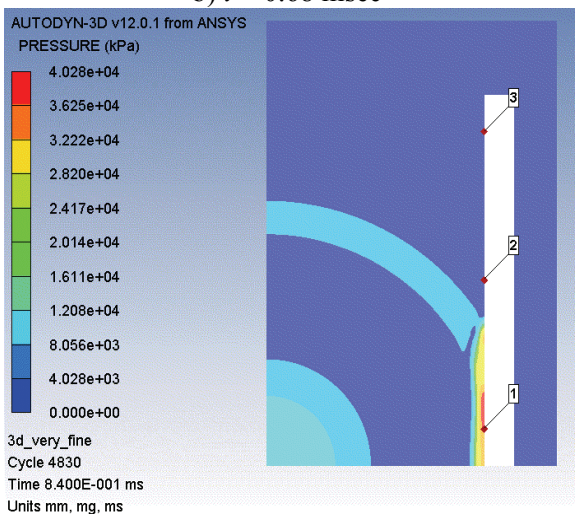

d) t = 0.84 msec

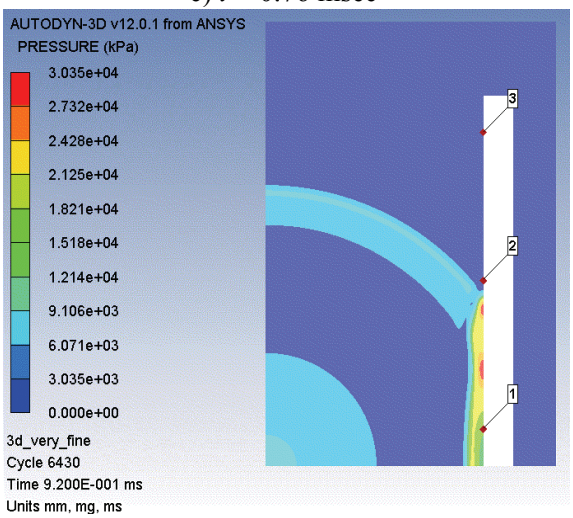

e) t = 0.92 msec

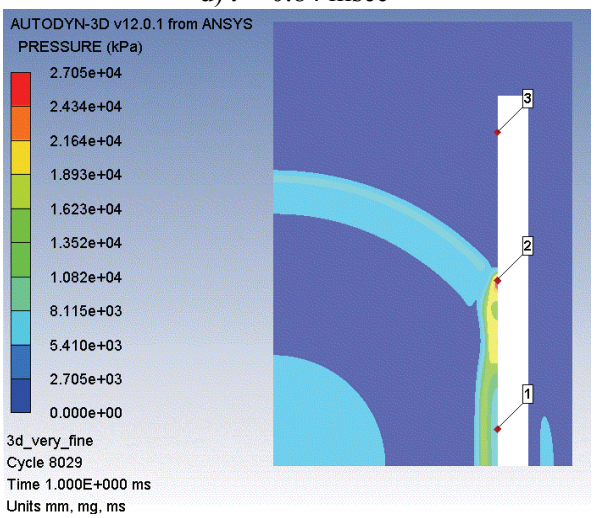

f) t = 1.0 msec

Figure 3-43: Contour plots of pressure showing the reflection and propagation of the shock wave along the height of the column

3.11.4 Afterburning

3.11.4.1 Modeling and analysis

The temperatures in the AUTODYN analyses were monitored to consider the possibility of afterburning in the problem described in section 3.7. The temperatures reached as high as 18,000 ^{o}K at the shock front during the initial expansion. However, it is important to note that most of the afterburning occurs at lower pressures than the detonation pressure (18 GPa) (Donahue, 2009) and so the temperatures must be computed after the initial stages of the expansion. Therefore temperature at the shock front was monitored just before it struck the column and was found to be approximately 4000 ^{o}K. This temperature is higher than that required for the afterburning reactions to occur given sufficient amount of oxygen; see Table 2-1. Donahue (2009) and Ripley et al. (2009) note that as the shock waves reflect from a rigid surface (a column in this case), the shape of the fireball is distorted, reheating the detonation products and promoting their mixing with the surrounding air. Favorable conditions are therefore created for afterburning near the surface of the column. The temperature histories at the three monitoring points are shown in Figure 3-44 and indicate that the peak temperatures are well above the temperatures required for the combustion reactions to take place.

Given that afterburning should occur, AUTODYN was used to model the afterburn energy. The additional energy to be released due to afterburning and the duration of the release can be specified in AUTODYN in the JWL EOS definition. However, in the AUTODYN 1D model discussed in section 3.11.1, the JWL EOS was replaced with an ideal gas EOS after the explosive had expanded to approximately 10 times its initial volume. This modeling methodology therefore restricts the addition of afterburn energy release to the initial stages of the detonation-product expansion where the afterburn process does not occur in practice. The detonation products and air were modeled using an ideal gas EOS in the 3D model and the effect of afterburning on the reflection of the pressure wave at the surface of the column could not be modeled using this method. The only strategy to model afterburning was to replace the single material Euler-FCT solver with the multi-material Euler-Godunov solver.

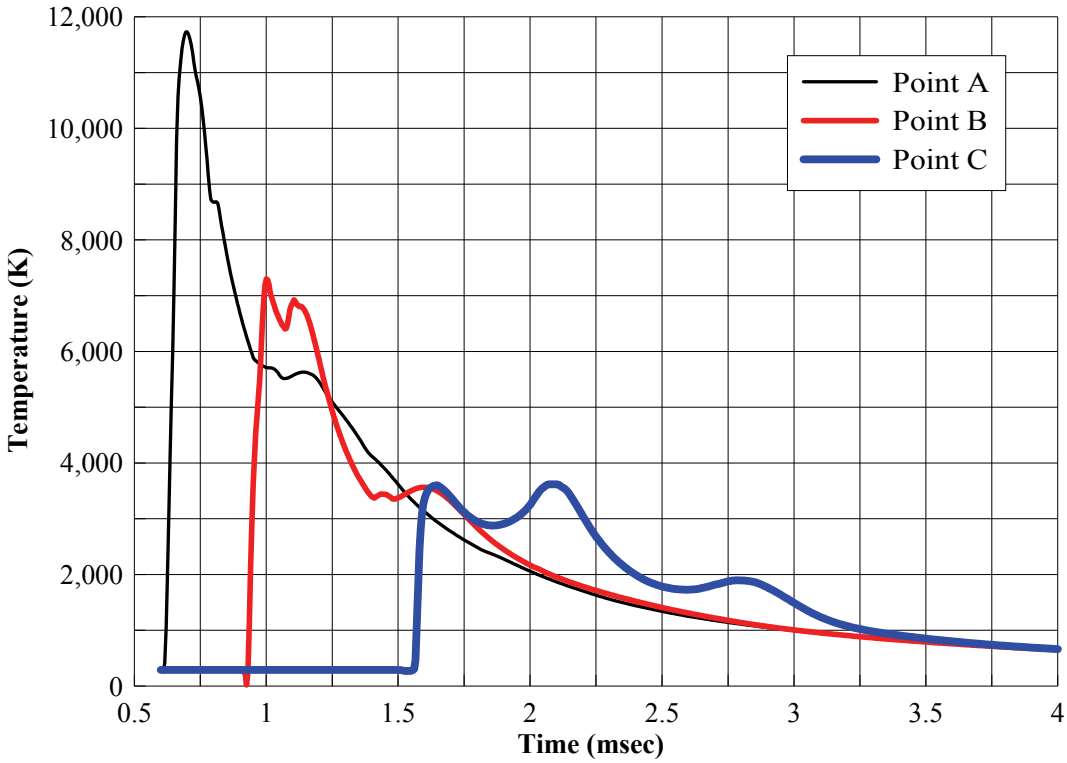

Figure 3-44: Temperature histories at the three monitoring points obtained using AUTODYN

It was necessary to retain the JWL EOS throughout the 1D and 3D analyses to model afterburning with the Euler-Godunov solver. The numerical model used in section 3.11.2 was used for this analysis with the solver changed from Euler-FCT to Euler-Godunov. The JWL EOS was retained and the additional energy due to afterburning was specified. The coarse mesh in Table 3-15 was adopted for the analysis. With the Euler-FCT solver, the analysis with the coarse mesh produced lower peak overpressures than the analyses using the finer meshes. Assuming a similar trend with the Euler-Godunov solver, a coarse mesh was chosen to minimize the computational effort but understanding that the peak reflected overpressures would be underestimated. Four analyses were performed with varying amounts of afterburn energy release: 0%, 25%, 50%, and 100% of the detonation energy. (Fifty percent afterburn is afterburn energy equal to 50% of the initial explosive energy.) The afterburn energy was released from a problem time of 0.3 msec to 3 msec. This release time was chosen keeping in mind that most of the afterburn occurs after the initial stages of expansion of the detonation products and that the positive phase durations of the reflected pressure waves were within this interval.

3.11.4.2 Results and discussion

The overpressure histories at the three monitoring points are summarized in Table 3-17 and presented in Figures 3-45 to 3-47. It is evident from the overpressure histories that the addition of afterburn energy has little effect on the peak reflected overpressures except at point C where the peak reflected overpressure increased by 26% with addition of afterburn energy equal to 100% of the detonation energy. However, there is a significant increase in the reflected impulses at the three points with increasing afterburn energy with a 46% increase at point C. From the last column in Table 3-17, it is clear that the percentage increase in peak reflected overpressures and reflected impulse are greater at Point C than at Point A. This observation can be explained on the basis of the varying amount of afterburn energy added to the incident pressure wave before it reaches each of the three points. In the JWL EOS (eq. 3-7) the last term dominates at large volumetric ratios, where the incident overpressure becomes directly proportional to the internal energy E. The additional afterburn energy (ΔE) is added uniformly during the release interval (0.3 to 3 msec). The incident pressure wave reaches point A at 0.7 msec and point C at 1.7 msec. More energy is added to the incident wave before it reaches point C than at point A. Therefore, the percentage change in the incident overpressure due to the addition of afterburn energy at point C is more than that at point A. A higher peak incident overpressure results in a higher peak reflected overpressure. Greater differences are seen in the peak reflected overpressures and reflected impulses at point C with the addition of afterburn energy than at the other two monitoring points.

Each of the overpressure histories presented in Figures 3-45 and 3-46 includes a hump after the peak reflected overpressure is reached. Similar humps were observed in the analyses with the Euler-FCT solver. These humps are timestep related and disappeared when the timestep was reduced to the values presented in Table 3-15. However, with the Euler-Godunov solver, these humps did not disappear with a reduction in the timestep.

Table 3-17: Results of analyses with varying afterburn energies

Monitoring point	Blast-wave parameter	Afterburn energy as a % of the detonation energy				% increase from 0% afterburn to 100% afterburn
		0	25	50	100	
Point A	Peak reflected overpressure (MPa)	32.2	32.6	33.1	33.9	5
	Reflected impulse (MPa-msec)	18.2	19.0	19.8	21.2	16
Point B	Peak reflected overpressure (MPa)	16.9	17.3	17.8	18.6	10
	Reflected impulse (MPa-msec)	7.95	8.47	8.95	9.84	24
Point C	Peak reflected overpressure (MPa)	5.55	5.91	6.27	7.0	26
	Reflected impulse (MPa-msec)	3.30	3.68	4.04	4.83	46

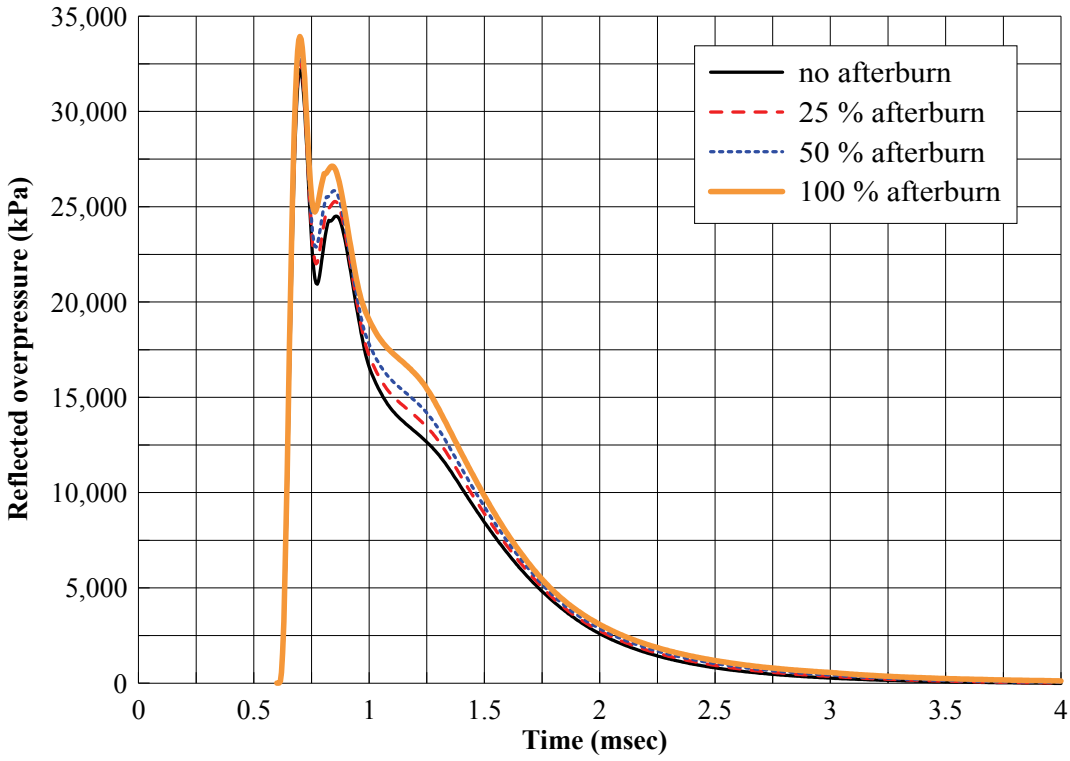

Figure 3-45: Effect of addition of afterburn energy on the overpressure history at point A

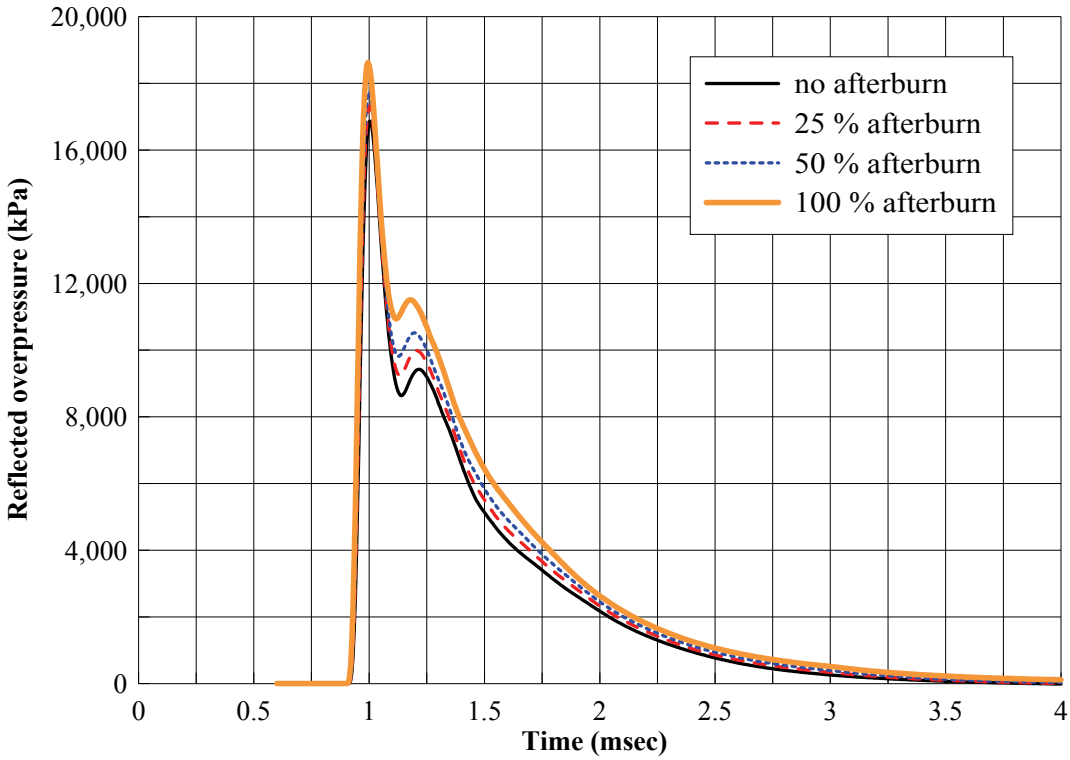

Figure 3-46: Effect of addition of afterburn energy on the overpressure history at point B

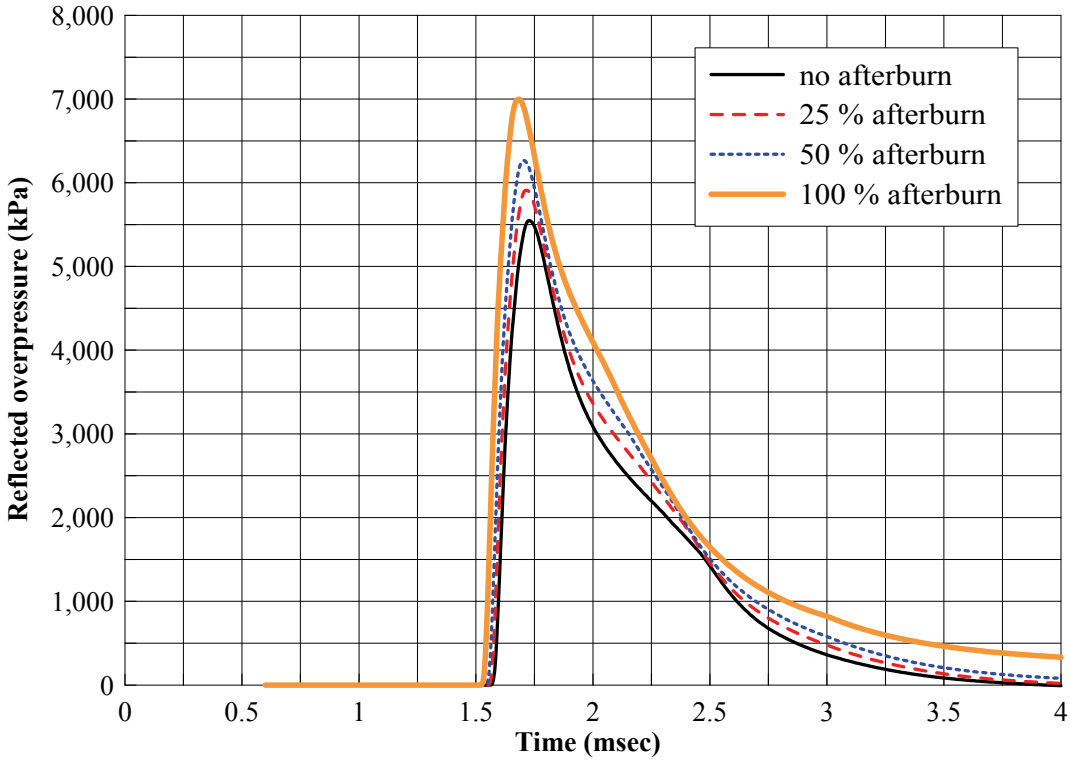

Figure 3-47: Effect of addition of afterburn energy on the overpressure history at point C

3.11.4.3 Comparison of Euler-FCT and Euler Godunov analysis results

A comparison of the Euler-FCT and Euler-Godunov analyses with the coarse mesh are presented in Figures 3-48 to 3-50. The Euler-Godunov results presented here do not include afterburning. The Euler-Godunov solver predicted much lower peak reflected overpressures than the Euler-FCT solver for the same mesh (see Section 3.11.2). The analysis runtimes were longer with the Euler-Godunov solver. However, the Euler-Godunov solver can accommodate multiple materials in a single element (e.g., air and detonation product gases) and TNT can be modeled with the JWL EOS in both the 1D and 3D analysis. Afterburning can be modeled only if the JWL EOS is retained for the entire analysis. Thus, even though the FCT solver is more efficient, its inability to model afterburning may curb its utility.

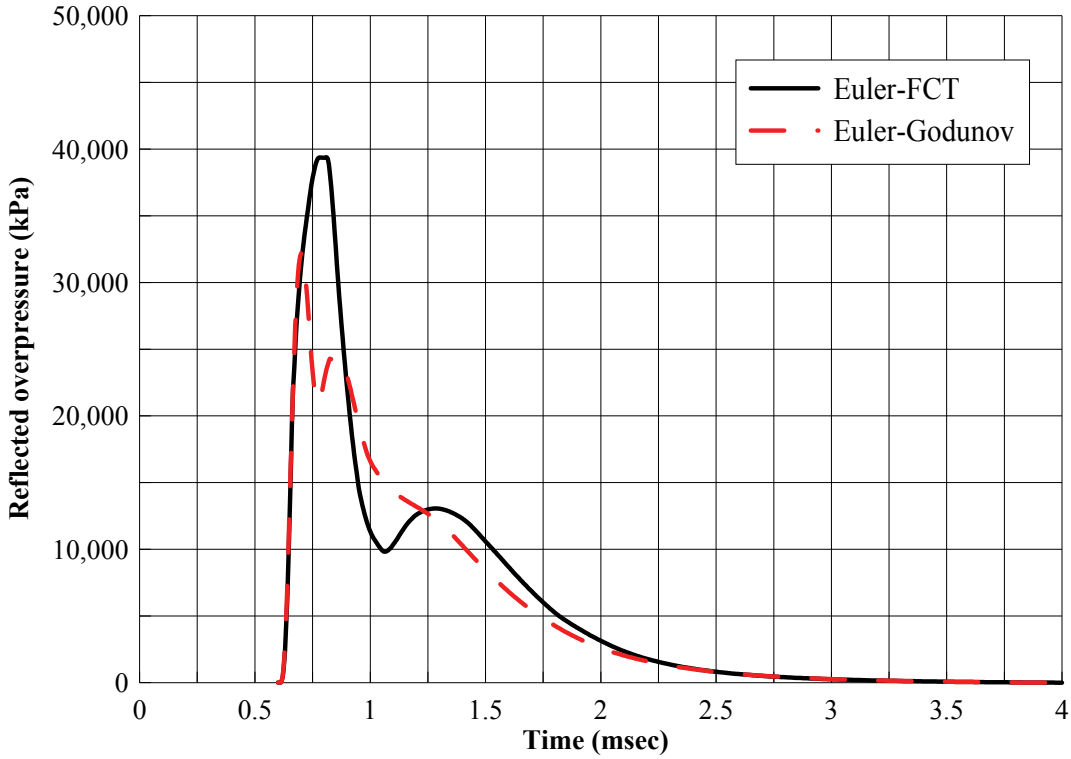

Figure 3-48: Overpressure histories at Point A obtained using the two Euler solvers

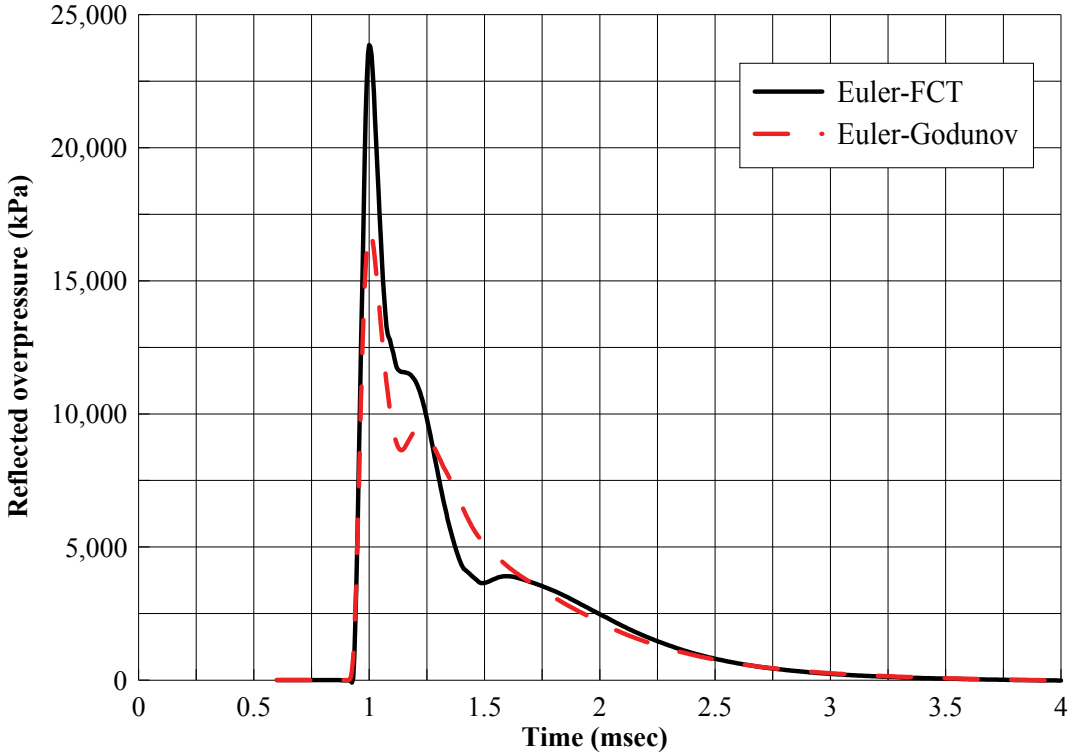

Figure 3-49: Overpressure histories at Point B obtained using the two Euler solvers

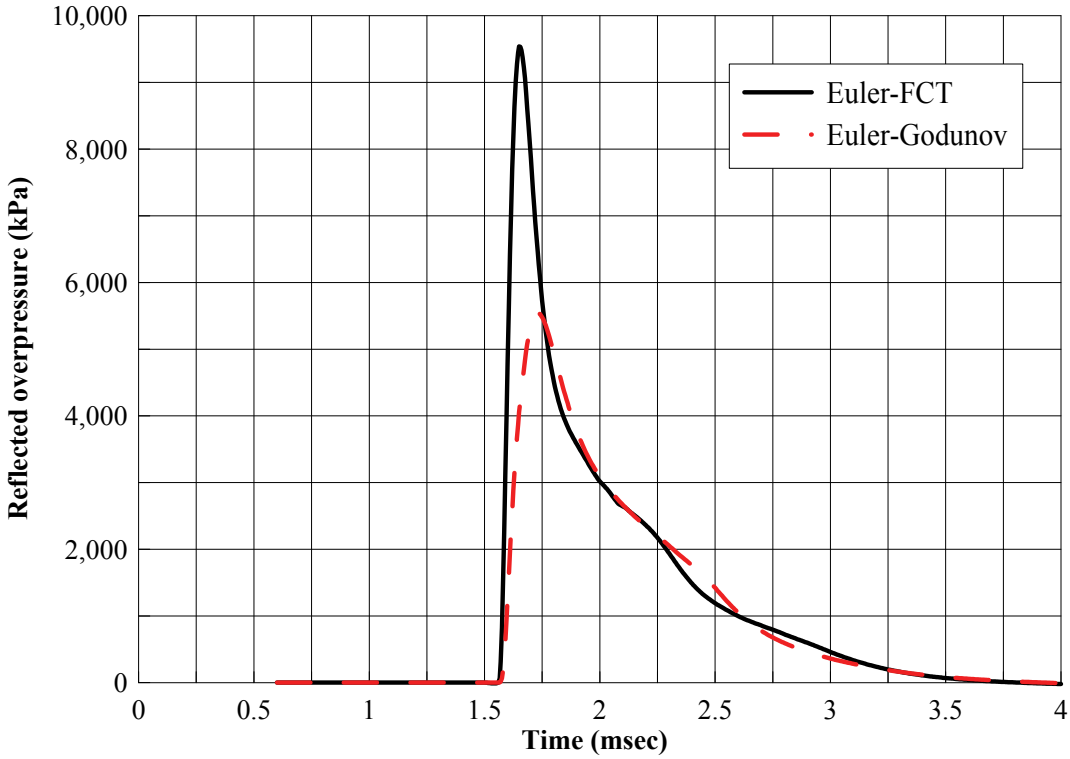

Figure 3-50: Overpressure histories at Point C obtained using the two Euler solvers

3.12 Comparison of Analysis Results Obtained Using LS-DYNA, Air3D, AUTODYN and UFC-3-340

The detonation problem described in section 3.7 was modeled with three codes: LS-DYNA, Air3D and AUTODYN. Results were presented in sections 3.8, 3.9 and 3.10 in the form of reflected overpressure histories at the three monitoring points on the face of the column. The most robust solution for each FE code is presented in Figures 3-51 to 3-53. The LS-DYNA results are for the analysis that used the '*INITIAL_VOLUME_FRACTION_GEOMETRY' option. The Euler-FCT solver was used for the AUTDOYN analyses and therefore afterburning was not considered.

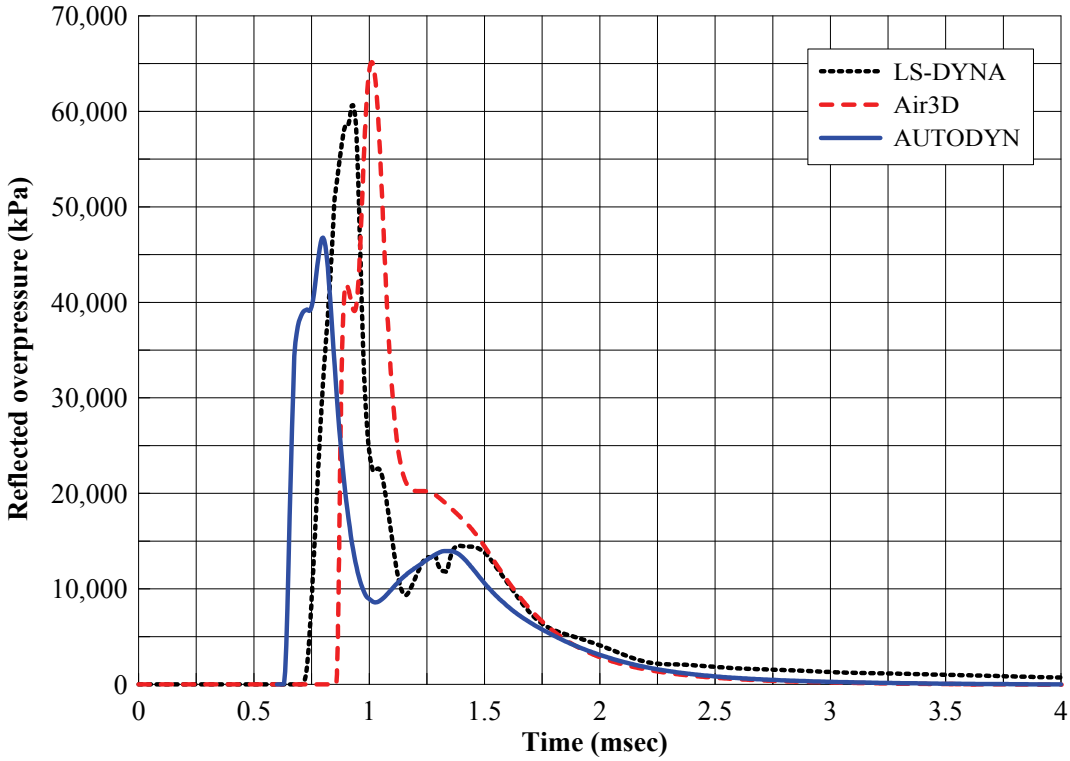

Figure 3-51: Reflected overpressure histories at point A obtained by numerical analyses

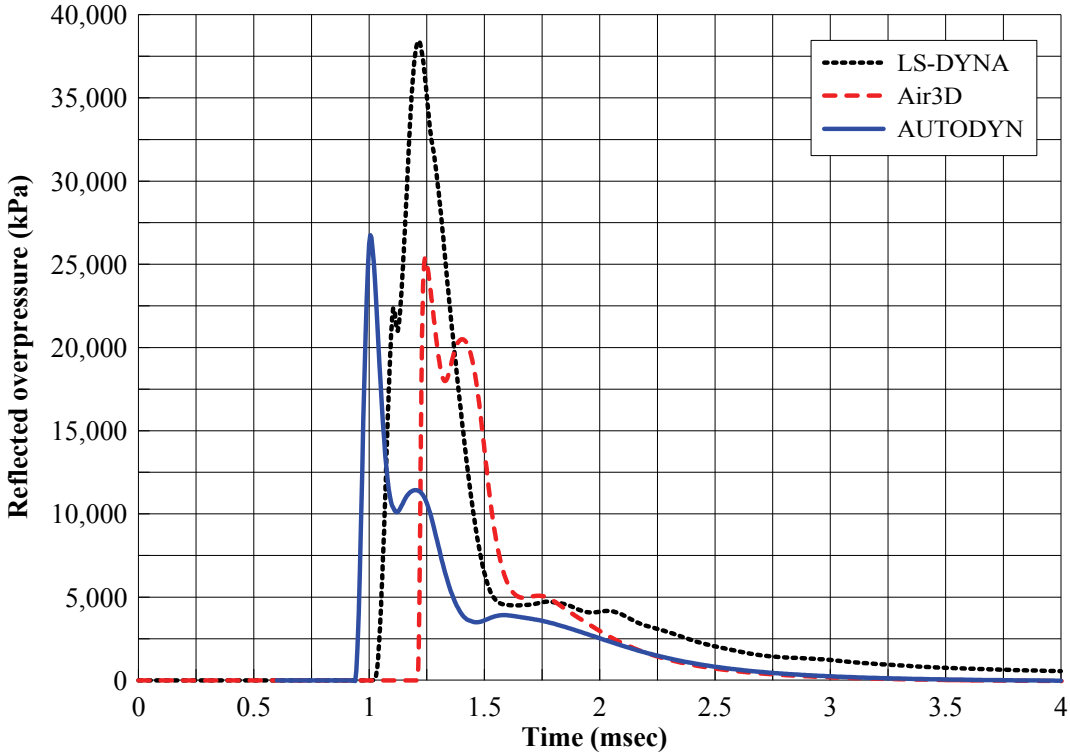

Figure 3-52: Reflected overpressure histories at point B obtained by numerical analyses

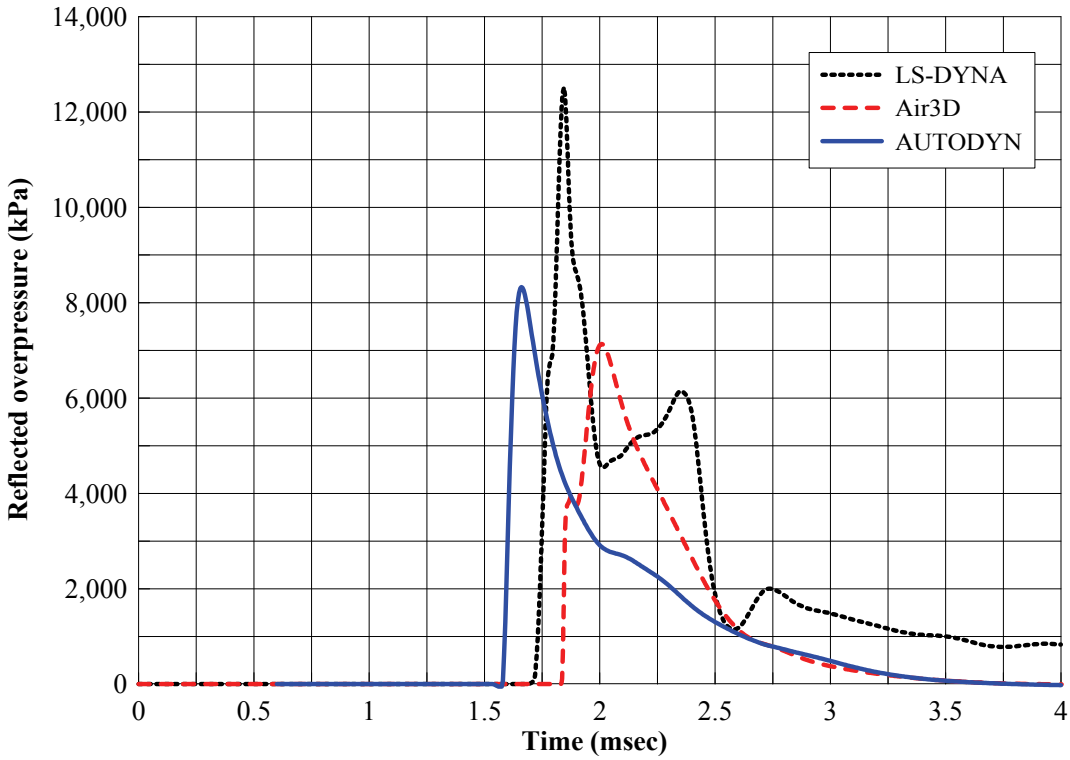

Figure 3-53: Reflected overpressure histories at point C obtained by numerical analyses

There is significant variation in the peak reflected overpressures, the overpressure histories and the arrival times at the three monitoring points. Although Air3D produced greater peak reflected overpressure at point A, the peak reflected overpressures at points B and C were lower than those obtained from LS-DYNA and AUTODYN. The peak reflected overpressures at points B and C from Air3D and AUTODYN are similar, whereas those obtained from LS-DYNA are significantly higher. A similar trend is seen with reflected impulses. The data presented in Tables 3-18 to 3-20 enables a comparison of the FE results with those of UFC-3-340; clearing was not addressed in the UFC calculations. The UFC tends to predict greater values of peak reflected overpressure and reflected impulse than the FE/CFD codes.

Table 3-18: Blast-wave parameters at point A from numerical analyses and UFC-3-340

	Air3D	LS-DYNA	AUTODYN	UFC-3-340
Peak incident overpressure (MPa)	6.57	7.81	9.19	9.0
Peak reflected overpressure (MPa)	65.2	60.8	46.8	79.2
Time of arrival (msec)	0.86	0.80	0.70	0.65
Incident impulse (MPa-msec)	1.11	1.22	1.56	1.70
Reflected impulse (MPa-msec)	23.4	25.1	20.5	32.0

Table 3-19: Blast-wave parameters at point B from numerical analyses and UFC-3-340

	Air3D	LS-DYNA	AUTODYN	UFC-3-340
Peak incident overpressure (MPa)	5.20	5.66	6.24	6.0
Peak reflected overpressure (MPa)	25.4	38.4	26.8	36.0
Time of arrival (msec)	1.21	1.10	0.95	1.0
Incident impulse (MPa-msec)	1.12	1.31	1.62	1.50
Reflected impulse (MPa-msec)	9.24	15.6	8.43	14.0

Table 3-20: Blast-wave parameters at point C from numerical analyses and UFC-3-340

	Air3D	LS-DYNA	AUTODYN	UFC-3-340
Peak incident overpressure (MPa)	3.53	3.51	3.52	3.0
Peak reflected overpressure (MPa)	7.13	12.5	8.33	11.1
Time of arrival (msec)	1.83	1.77	1.61	1.90
Incident impulse (MPa-msec)	1.37	1.26	1.92	1.70
Reflected impulse (MPa-msec)	3.41	6.33	3.73	5.40

One of the reasons for the differences in the pressures and impulses is likely the solution methodologies used in the three codes. Air3D has been known to predict the overpressures incorrectly in the near-field (e.g., Anderson, et al., 2002). The balloon analog on which Air3D is based gives good results in the mid and far-field but is not intended to model the physics of the complex near-field flows as described by its developers.

The LS-DYNA results are very mesh dependent. The peak reflected overpressures and the overpressure histories at the monitoring points changed slightly with variations in the JWL EOS parameters and timesteps between advection cycles (NADV). The coupling algorithm of LS-DYNA was unable to properly simulate the fluid-structure interaction between the blast-wave and the column. Unlike the results of the AUTODYN and Air3D analysis, an irregular overpressure distribution was observed at the 3rd monitoring point in the LS-DYNA analysis.

Table 3-21 summarizes analysis results at a point of normal reflection on the column. Data from CONWEP (Hyde, 1988) are also provided. Normal reflection will occur at the centre of the front face of the column. CONWEP provides similar values of peak reflected overpressures and reflected impulses to those obtained from UFC-3-340, which is an expected result because CONWEP uses the same empirical relationships (Kingery and Bulmash, 1984) used to derive the charts in UFC-3-340.

Table 3-21: Comparison of blast-wave parameters at a point of normal reflection (centre of the face of the column)

	CONWEP	Air3D	LS-DYNA	AUTODYN	UFC-3-340
Peak incident overpressure (MPa)	8.80	6.65	7.81	9.20	9.0
Peak reflected overpressure (MPa)	81.5	69.7	74.6	48.2	82.0
Time of arrival (msec)	0.70	0.85	0.90	0.79	0.70
Incident impulse (MPa-msec)	1.50	1.12	1.22	1.48	1.60
Reflected impulse (MPa-msec)	31.0	24.6	35.8	21.4	31.0

An issue that warrants discussion here is the application of the ideal gas EOS that assumes a constant ratio of specific heat, γ , given that the temperatures in the region are very high. In the numerical models, it was assumed that the temperatures generated by the explosion were sufficiently low so that the ideal gas law would be appropriate to represent the behavior of ambient air. This assumption was violated because the computed temperatures were in the range of 4000 ^{o}K to 18,000 ^{o}K. Molecules of Oxygen and Nitrogen in the air start to dissociate when the temperatures reach 2500 ^{o}K and 4000 ^{o}K, respectively, and the air becomes reactive (Anderson and Anderson, 2002). At higher temperatures, γ is not constant. As the temperature and pressure increases, the value of γ decreases from the value of 1.4 at 293 ^{o}K to 1 at very high temperatures. Decreasing the value of γ has the effect of increasing the reflected overpressure for a given incident overpressure (Courant and Friedrichs, 1948). Not considering the variation of γ in the numerical analyses likely results in an under-prediction of the reflected overpressures at the three monitoring locations. However, the percentage reduction could not be estimated from the available data and further study of this topic is warranted.

3.13 Clearing Effects

One observation that can be made from analysis of the data in Tables 3-18 to 3-20 is that the computer codes, with the exception of LS-DYNA, produced much lower reflected impulses than those calculated from UFC-3-340. One likely reason is that the UFC-3-340 charts assume a reflecting surface of infinite size whereas the reflecting surface in the numerical analyses was of finite width; clearing could have reduced the reflected impulse in the numerical analyses.

Texts by Norris et al. (1959), Baker (1973) and Smith and Hetherington (1994), among others, discuss clearing. Clearing occurs when a shock front encounters an obstacle of finite size and diffracts around it. At the instant of diffraction, adjacent regions of high pressure (reflected overpressures at the point of reflection) and low pressure (side-on overpressures of the incident shock wave) are created; see Figure 3-54. A rarefaction wave, which propagates from the low pressure region at the side of the obstacle to the high pressure region on its front face, reduces (clears) the reflected overpressure to the stagnation pressure.

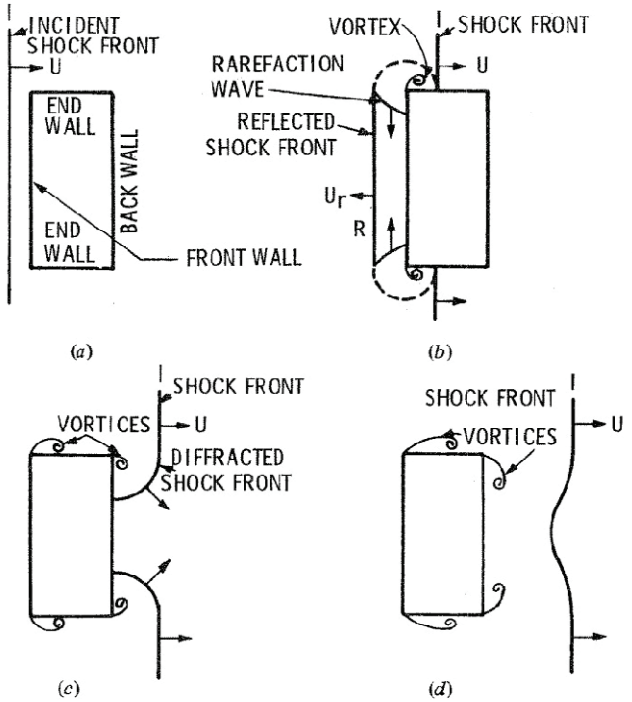

Figure 3-54: Shock front interaction with a structure of finite dimensions (Norris, et al., 1959)

Ballantyne et al. (2010) have shown that clearing can significantly reduce the reflected impulse on the front face of a structure of finite width. To verify the effect of clearing on the reduction of the reflected impulse in the present study, an analysis was performed using AUTODYN with the coarse grid described in Table 3-15. A 3D air domain was modeled in AUTODYN with dimensions $3\text{m}\times4\text{m}\times7\text{m}$ and a reflecting boundary condition was applied at the upper *yz*-plane so that it represented a reflecting surface of a size that could be considered infinite: sufficiently large for clearing to have no effect on the reflected impulse values at the monitoring location. The analysis procedure was identical to that followed in sections 3.11.1 and 3.11.2. A total of six gauges were added at the same heights as those of the points A, B and C, separated by a distance of 97 mm, across the half-width of the front face of the column: A1, A2, B1, B2, C1, and C2. The values of the reflected overpressure and impulse with and without clearing at the 9 monitoring gauges are presented in Table 3-22 for the detonation of 1000 kg of TNT at a standoff distance of 3 m from point A (see Figure 3-8). The data that includes clearing is reproduced from the analysis results of section 3.11.3 with the addition of data from the additional monitoring points.

Table 3-22: Effect of clearing on peak reflected overpressure and reflected impulse

Monitoring location	Peak reflected overpressure (MPa)		Reflected impulse (MPa-msec)		Percent reduction due to clearing	
	Clearing included	Clearing ignored	Clearing included	Clearing ignored	Reflected overpressure	Reflected impulse
Point A	39.4	47.1	20	25.5	16	22
Point A1	39.1	47.1	20	25.5	17	22
Point A2	37.8	47	18.8	25.4	20	26
Point B	23.9	25	8.48	12.2	4	30
Point B1	23.3	25	8.45	12.2	7	31
Point B2	19.1	25	7.75	12.2	24	36
Point C	9.54	10.4	3.79	5.51	8	31
Point C1	9.6	10.4	3.82	5.51	8	31
Point C2	9.26	10.3	3.62	5.51	10	34

From analysis of the data in the table, it is clear that both the reflected impulse and the peak reflected overpressure are affected by clearing at the monitoring points. Significant reductions in the reflected impulse are seen at all 9 monitoring locations, with the greatest percent reductions at a given height occurring at the monitoring locations closest to the flange outstand (i.e., A2, B2, and C2). The reductions in overpressures on the front face of the column range from small to moderate. Although the reductions in reflected impulse were anticipated, the reductions in peak reflected overpressure were not because the rise time from ambient to peak reflected overpressure has traditionally been assumed to be zero (see Figure 1-4, taken from UFC-3-340). The reflected overpressure histories presented previously in this chapter show a finite rise time to the peak values. A plausible explanation for the reductions in overpressures is that the rarefaction wave, which propagates at the speed of sound in the higher pressure region, reduces the overpressure before the peak value is reached. The speed of sound at point A was calculated using equation 3-15 (Anderson and Anderson, 2002), where c is the speed of sound in air, $\mathbb{R}$ is the universal gas constant, T is temperature and M is the molecular weight of air.

$$c = \sqrt{\frac{\gamma \, \mathbb{R} \, T}{M}} \tag{3-15}$$

From Figure 3-44, the temperature at point A at the instant when the blast wave reflects from the column was approximately 11,000 ^{o}K. Substituting the values of γ (= 1.4), $\mathbb{R}$ (= 8.314 J/^{o}K-mol), M (29) and T (= 11000 ^{o}K), the speed of sound at point A is approximately 2100 m/s (Mach 6)[17]. The time required by the rarefaction wave to travel across the half-width of the front face of the column is equal to 203/2100 = 0.1 msec, if the sound speed remains constant, which is a reasonable assumption for the purpose of this analysis.

The overpressure histories at points A2, A1 and A, with and without clearing, are presented in Figures 3-55, 3-56 and 3-57, respectively. The overpressure histories are shown only for the time interval between

[17] Multiples of sound speed are generally denoted as Mach. Mach 2 means the speed is equal to twice the speed of sound.

the arrival of the shock wave and a time shortly after the peak overpressure has been reached. The purpose here is to enable greater resolution of the overpressure profile near its peak. In each of these figures, the two pressure profiles deviate at some time after the arrival time, but before the peak overpressure is reached. The deviation occurs at different instants in time for the 3 points: $t = 0.65$ for A2, $t = 0.67$ for A1, and $t = 0.68$ for A. This deviation is attributed to the propagation of the rarefaction wave across the half-width of the column. The propagation of the rarefaction wave from the side of the column to the centre of the front face starts at the arrival time of the shock front ($t = 0.6$ msec). The rarefaction wave reaches point A2, which is closest to the edge of the front face, at $t = 0.65$. In Figure 3-55, the overpressure history starts to deviate from that of the column of infinite width (clearing is ignored) because of the arrival of the rarefaction wave, resulting in a smaller value of peak reflected overpressure. The arrival of the rarefaction wave at points A1 and A can also be identified by the instant at which the overpressure histories start to deviate. The greatest reduction in peak overpressure is at point A2 because the rarefaction wave reaches at A2 first, followed by A1 and finally A, where the effect of clearing on the peak reflected overpressure is the least.

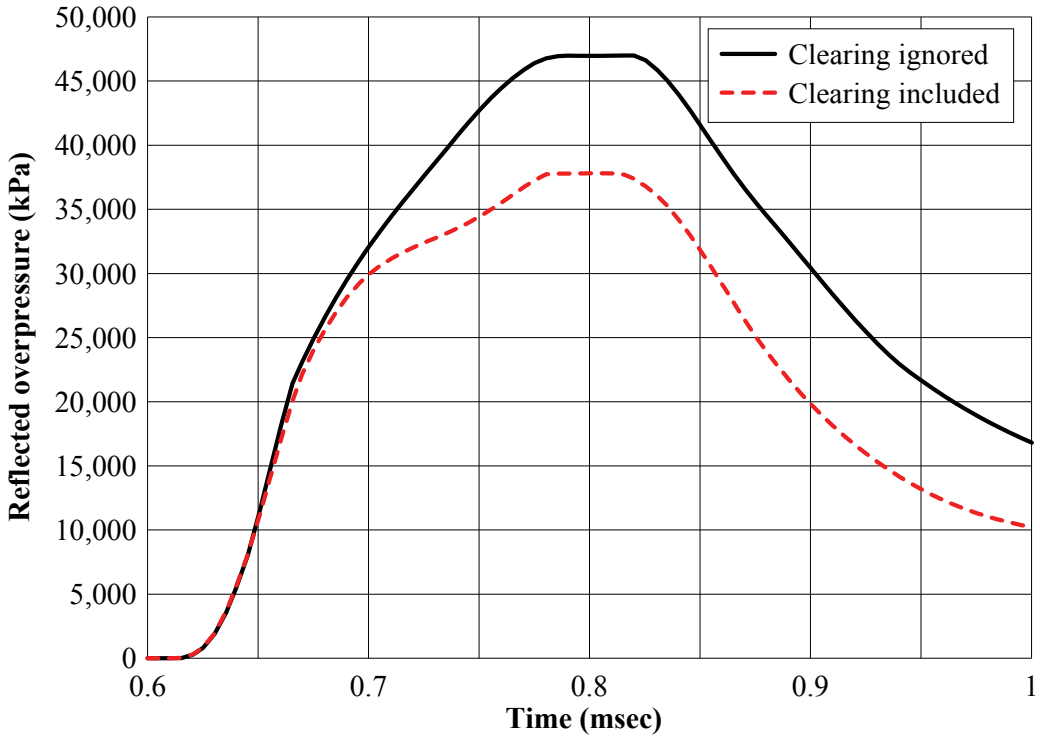

Figure 3-55: Reflected overpressure histories at point A2 with and without clearing

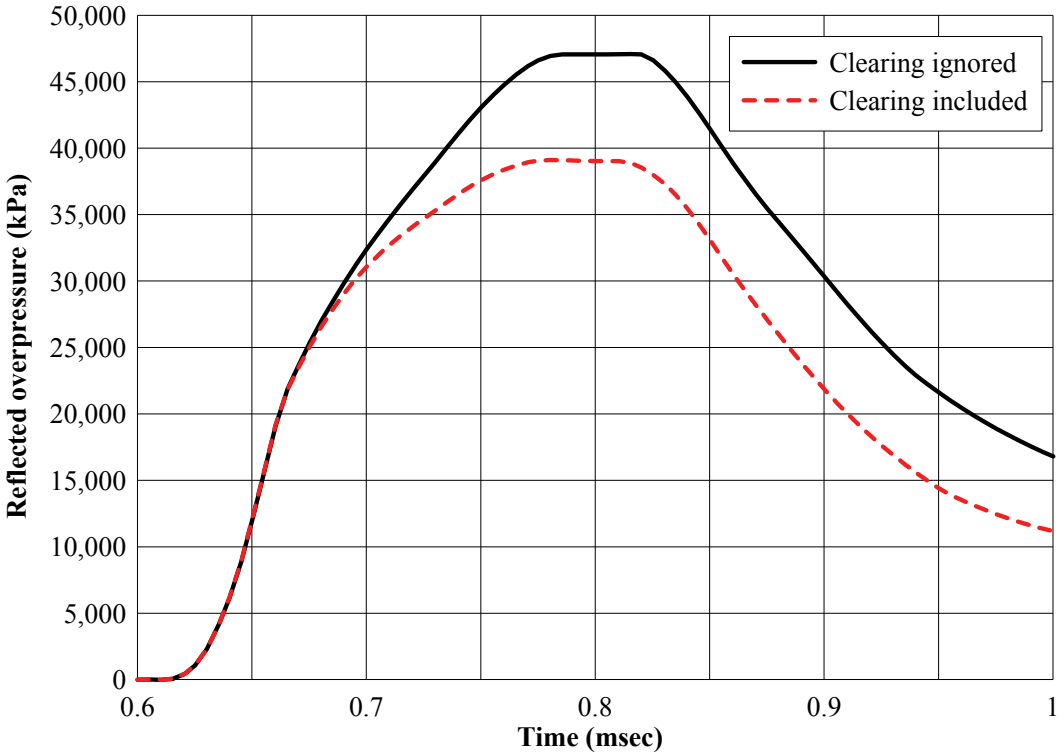

Figure 3-56: Reflected overpressure histories at point A1 with and without clearing

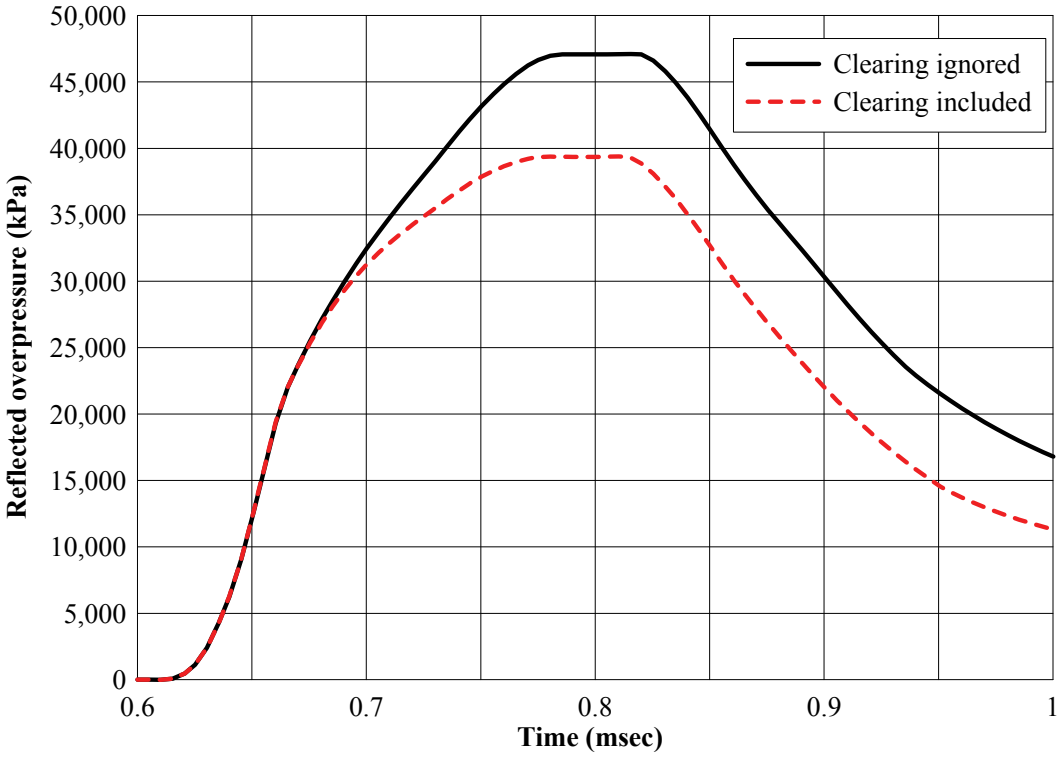

Figure 3-57: Reflected overpressure histories at point A with and without clearing

A widely used analytical expression for calculating the clearing time, t_c, is presented in equation 3-16 (from UFC-3-340, (DoD, 2008)) where, S is the shortest distance from the point to a free edge, and U_s is the shock front velocity. Clearing time is defined in the UFC as the time required for the rarefaction wave to reduce the reflected overpressure to the stagnation pressure[18].

$$t_c = \frac{3S}{U_s} \tag{3-16}$$

The clearing time is used in blast-resistant design to reduce the reflected impulse to account for the finite size of structural components but not to reduce the peak reflected overpressure. Clearing has a significant effect on both the peak reflected overpressures and reflected impulses on near-field targets with finite dimensions. It is unclear whether the analytical procedure described in the UFC-3-340 is appropriate for blast-resistant design in the near-field and the procedure must be used with caution for such problems. Further study of rarefaction-wave propagation, clearing and its effect on the response of structural components for near-field detonations is warranted and is underway (Venkateshan, 2011).

[18] Stagnation pressure = Ambient pressure + $C_D \times$ dynamic pressure, where C_D is the drag coefficient.

SECTION 4

INFLUENCE OF CHARGE SHAPE, ORIENTATION AND POINT OF DETONATION

4.1 Introduction

This chapter presents the results of numerical analyses performed using AUTODYN (Century Dynamics, 2009b) to study the effect of charge shape, orientation and point of detonation on overpressure distributions. A cylindrical shaped charge is used for this purpose and results are benchmarked using the industry-standard spherical shape. The effect of varying the aspect ratio of a cylindrical charge on the overpressure distributions in the radial and axial directions is discussed in section 4.2. A scaled distance beyond which the effect of charge shape can be ignored is sought next, where the analysis is based on both the peak overpressure and impulse at different scaled distances, and contour plots of overpressure. The effect of point of detonation within the cylindrical charge is studied in section 4.3. The effect of charge shape on the response of a steel column is examined in section 4.4. Results are reported using reaction histories, maximum displacements and fringe plots of plastic strain. The purpose of this study is to learn whether attention should be paid to charge shape and orientation when analyzing the response of structural components subjected to air-blast effects.

4.2 Influence of Charge Shape on Overpressure Histories

4.2.1 Sample problem

To investigate the effect of charge shape on distributions of overpressure, a free-air burst of 10 kg of TNT-equivalent explosive was analyzed. A baseline analysis was performed with a spherical charge. The incident overpressures and impulses were monitored at every charge diameter in the range of 5 (Z = 0.53 m/kg$^{0.33}$) to 40 (Z = 4.22 m/kg$^{0.33}$) from the point of detonation. A set of analyses was then performed with cylindrical charges of the same mass but with varying ratios of length, L, to diameter, D (L/D = 1 to 5). Similar to the analysis of the spherical charge, the incident overpressures and impulses

were monitored at distances up to 40 charge diameters[19] but in both the radial and axial, directions. A central detonation was assumed for these analyses.

4.2.2 AUTODYN analyses

Only 1D and 2D analyses were performed as the problem described in 4.2.1 allows the use of radial (spherical charges) and axial symmetry (cylindrical charges). All analyses were performed in two stages: 1) initial expansion of the explosive until the blast wave reached 3 charge diameters, and 2) subsequent propagation of the blast-wave through to the analysis termination time. This approach was adopted to allow the use of finer meshes in the initial stages of the blast-wave expansion.

4.2.2.1 10 kg spherical charge

For the spherical charge analysis, the first stage consisted of a 1D wedge analysis using radial symmetry. The explosive was modeled with the JWL EOS and the air with an ideal gas EOS ($\gamma = 1.4$). The radius of the 10 kg TNT spherical charge is 0.227 m. An element size of 0.5 mm was used for both the explosive and the air. The procedure for performing a 1D wedge analysis in AUTODYN, described in section 3.11.1, was then followed and the analysis was run until the blast wave reached a distance of 3 charge diameters (0.681 m).

The output of the 1D analysis was then mapped into an axially-symmetric 2D air domain with dimensions of $10\text{m} \times 10\text{m}$. As the charge was centrally detonated, $x = 0$ is a plane of symmetry. Therefore, only 1/2 of the axially symmetric charge and air domain was modeled. The 2D domain consisted of air modeled as an ideal gas and initialized at atmospheric pressure. The air was modeled with 800×800 elements, resulting in an element size of 12.5 mm. The single material Euler-FCT solver was used for the air. The pressure contours at the beginning of the 2D analysis are presented in Figure 4-1. The monitoring gauges are also shown. A 1D wedge analysis with radial symmetry and smaller elements would have resulted in

[19] Charge diameter is defined here as the diameter of the spherical charge.

more accurate results. However, because radial symmetry cannot be used for analysis of the cylindrical charges, and to use similar grid sizes, 2D analysis was performed for the spherical charge. The termination time for the analysis was set such that it was sufficient to capture the overpressure history at the last monitoring gauge. According to the UFC-3-340 chart of Figure 3-9, the time of arrival of the blast wave at a scaled distance of 4 m/kg$^{0.33}$ is 13 msec and the positive phase duration is 7 msec. Based on this information, the analysis was terminated at a t = 25 msec.

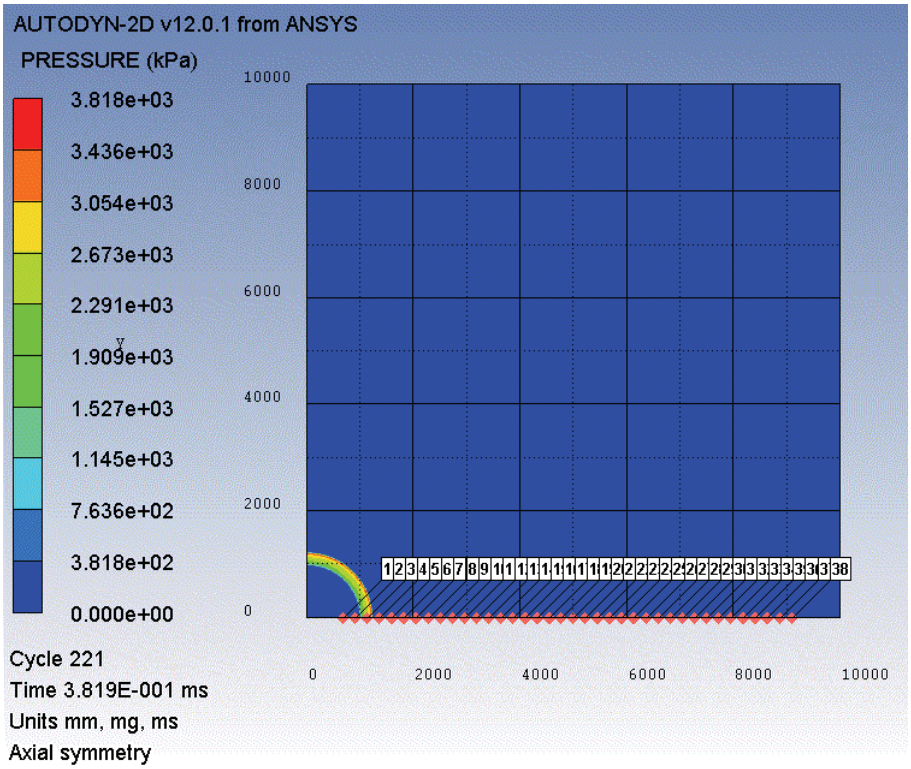

Figure 4-1: Pressure contours (kPa) at the beginning of the 2D analysis with the spherical charge

4.2.2.2 10 kg cylindrical charges

Two dimensional analyses were performed in both stages for the cylindrical charge. A similar modeling procedure to that described in section 4.2.2.1 was used. The axially symmetric models for the cylindrical charges with aspect ratios 1 and 3 used in the first stage of the analysis are presented in Figures 4-2a and 4-2b, respectively. The detonation point, which is also the origin of the model, is the centre of the cylindrical charge and is identified by a red dot in the figure. For the cylindrical charges, the x- and y-axes

are the axial and radial directions, respectively. Only 1/2 of the axially symmetric charge and the air domain was modeled, similar to the model of the spherical charge. The element sizes near the origin were altered to suit the dimensions of the cylindrical charge. The dimensions of the cylindrical charges in the models differed from the target values by very small percentages due to modeling constraints.

The first stage analyses were run until the blast-wave had expanded to a distance of 3 charge diameters. The output was then remapped to a larger 2D domain, similar to the spherical charge domain of Figure 4-1. The size of the air domain, element sizes and the termination time were the same as those used for the analysis of the spherical charge. Monitoring gauges were located in both radial and axial directions as shown in Figure 4-3. Table 4-1 lists the notation used for the 5 geometries of cylindrical charge. The dimensions of the charges are also listed.

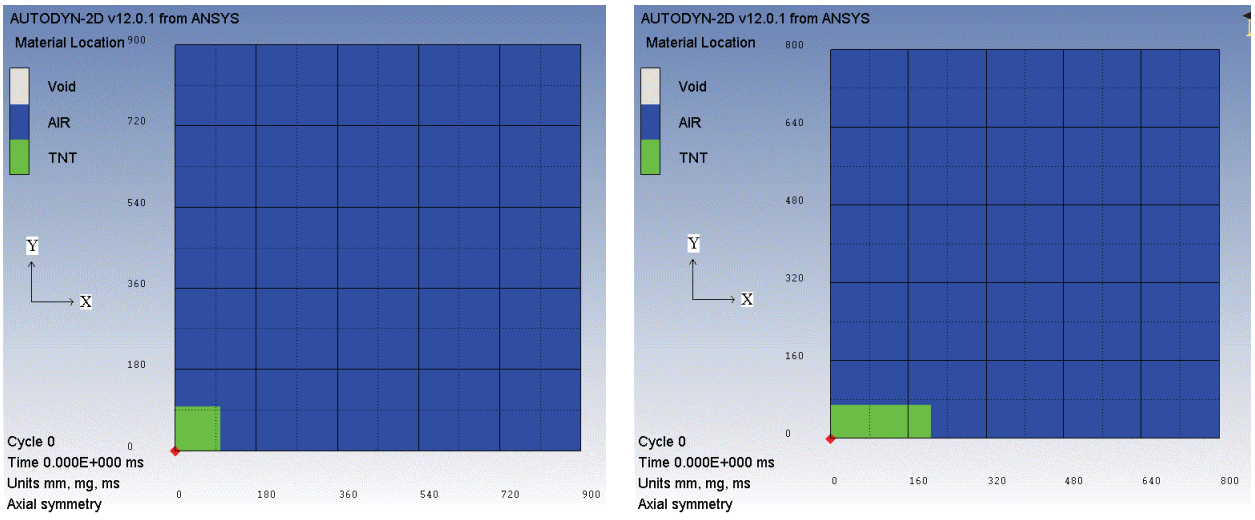

a) Cylindrical charge with $L/D = 1$ b) Cylindrical charge with $L/D = 3$

Figure 4-2: AUTODYN 2D models for the first stage of the analyses

Table 4-1: Notation for the cylindrical charges

Aspect ratio of cylindrical charge	Notation	Dimensions	
		L (mm)	*D* (mm)
1	*Cyl_I*	198.4	198.4
2	*Cyl_II*	315.0	157.5
3	*Cyl_III*	412.8	137.6
4	*Cyl_IV*	500.1	125.0
5	*Cyl_V*	580.3	116.1

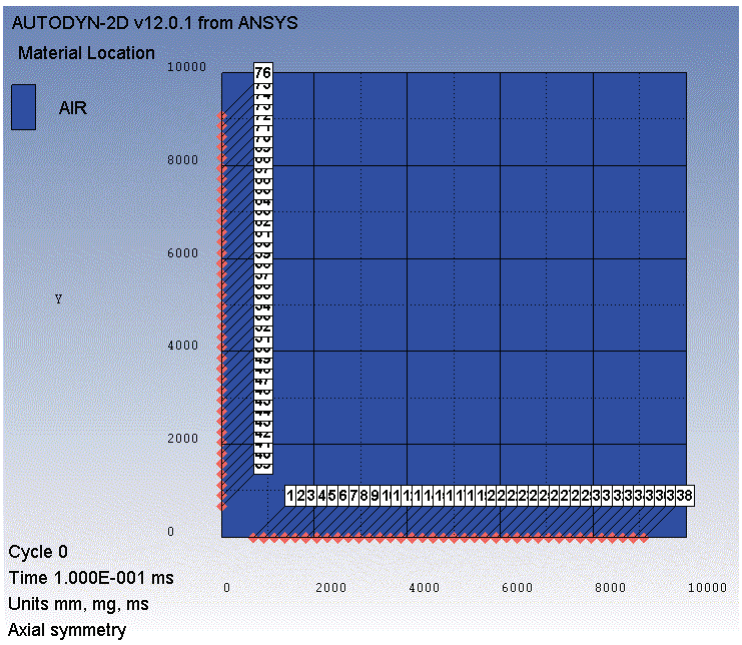

Figure 4-3: Monitoring gauges in the radial and axial directions of the cylindrical charges (second stage of analysis)

4.2.3 Results and discussion

The incident overpressure histories produced by the cylindrical and spherical charges at distances of 10, 20, 30 and 40 charge diameters in the axial direction are presented in Figures 4-4 to 4-7. Additional plots

are presented in Appendix A, including one for a distance equal to 5 charge diameters. The important observations that can be made from these figures include:

1. Charge shape has a significant effect on peak overpressure. At a distance of 10 charge diameters, all of the cylindrical charges produced a greater peak incident overpressure than that generated by the spherical charge. The difference decreased with increasing aspect ratio (with the exception of *Cyl_I*, which produced slightly lower peak overpressure than *Cyl_II*) and scaled distance. The peak overpressures generated by *Cyl_I* and *Cyl_II* are greater than those generated from the spherical charge even at a distance of 20 charge diameters ($Z = 2.10$ m/kg$^{0.33}$).
2. The overpressure history decays more rapidly (or impulse decreases) as the aspect ratio is increased, which implies that less energy is directed in the axial direction for higher aspect ratios. This observation is consistent with the results of experimental and numerical studies cited in section 2.7. This effect is more apparent at 10 charge diameters than at 20 or 30 charge diameters due to the difference in arrival times of the primary blast waves.
3. For the cylindrical charges, the arrival time of the shock front at a distance of 10+ charge diameters increases with increasing aspect ratio. For distances of 5- charge diameters, the opposite is the case as seen in Figure A-1. In the axial direction, the length of the charge and thus the distance traversed by the shock front in the explosive increases with aspect ratio. For a given distance, the greater the aspect ratio, the smaller the distance traversed by the shock front in air. The shock front travels faster in the explosive than in air. Once in air, the velocity of the shock front is a function of the incident overpressure (Courant and Friedrichs, 1948), which is greater for lower aspect ratios at distances of 10+ charge diameters.
4. The overpressure histories generated by the cylindrical charges include secondary and tertiary shocks. At a distance of 10 charge diameters, these secondary shocks are only clearly visible for *Cyl_I* and *Cyl_II*. As the scaled distance increases (1.05 m/kg$^{0.33}$ to 4.20 m/kg$^{0.33}$), these shocks become significant and beyond a distance of 30 charge diameters, the peak overpressures and

impulses associated with these secondary shocks exceed those associated with the primary shocks. At a distance of 40 charge diameters a clear trend is seen in the strength[20] of these shocks. The secondary shocks become more significant than the primary shocks. This effect increases with increasing aspect ratios. No significant secondary shocks are seen in the overpressure histories generated by the spherical charge. Although the secondary shocks are more pronounced at greater scaled distances, it is important to note that the amplitude of the peak overpressure is reduced by a factor of between 40 and 50 with an increase in the scaled distance of a factor of 4.

Brode (1959) provided a thorough treatment on the origin and propagation of secondary and tertiary shocks generated by a spherical charge. According to Brode, when the primary shock wave crosses the spherical explosive-air boundary (contact surface), a rarefaction wave is generated in the explosive followed by a secondary shock (compression) wave. Both the rarefaction and compression waves travel back towards the origin (point of detonation). The compression wave arises from the need to match the negative pressure gradient across the rarefaction wave to the positive pressure gradient across the primary shock wave. The secondary shock is initially weak but grows in strength as it moves towards the origin where it implodes. The secondary shock is then reflected and propagates outwards until it reaches the expanding contact surface. A second set of rarefaction and compression waves are generated and the process proceeds as above until all the energy of the detonation product gases (N_2, CO and CO_2) is exhausted.

This explanation is applied now to the cylindrical charges. Multiple shocks are seen in the overpressure histories generated by the cylindrical charges in Figures 4-5 and 4-6. These shocks are the result of multiple reflections and constructive interferences occurring with the explosive-air boundary (contact surface) and the inward-moving shock waves. Unlike the spherical charges, where the inward-moving

[20] Shock strength is defined here using peak incident overpressure and impulse.

shocks are uniform along a radius and travel at the same velocity, the inward-moving shock waves in the cylindrical charges have different strengths, sizes and arrival times. These differences increase with aspect ratio. This observation may explain why the secondary shock waves are more significant for cylindrical charges than spherical charges. The cylindrical charge *Cyl_I* warrants a separate treatment because the arrival times of the inward-moving shocks in the radial and axial directions are similar, although their shapes and sizes will differ because the contact surfaces in the radial and axial directions are different. Some constructive interference in *Cyl_I* is expected but the interference is greater in *Cyl_II* as seen in the overpressure histories.

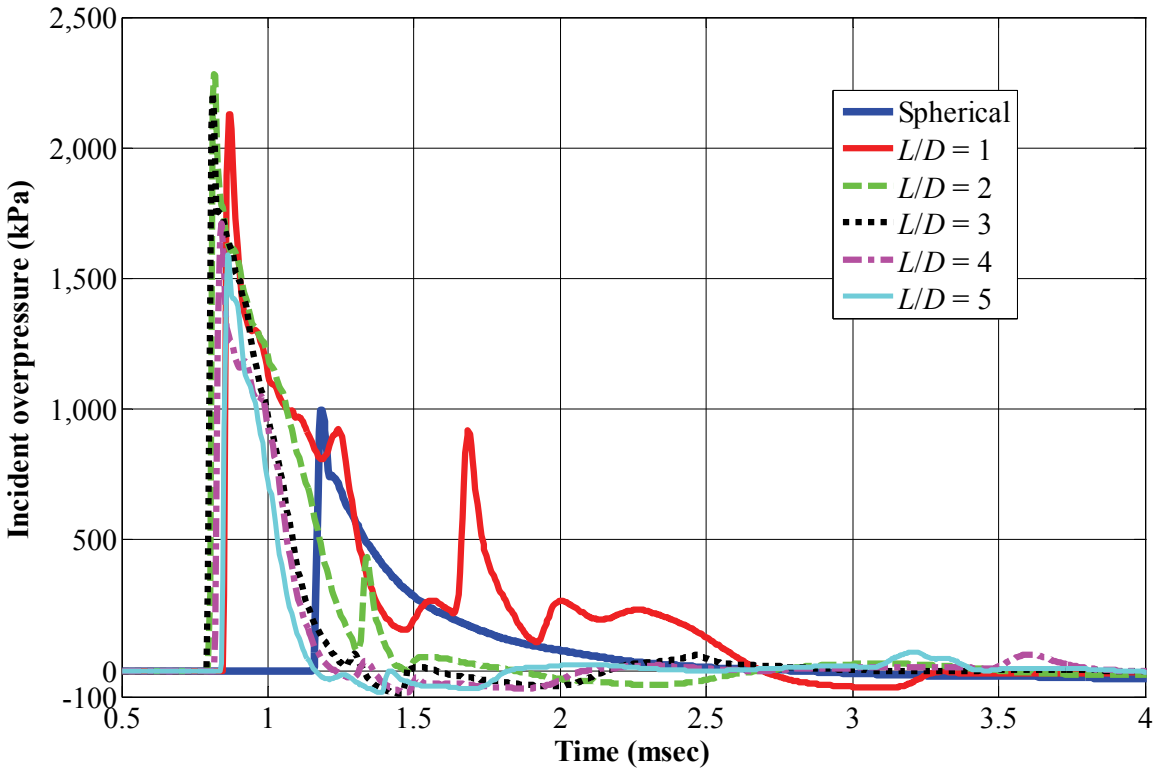

Figure 4-4: Overpressure histories at an axial distance of 10 charge diameters (Z = 1.05 m/kg$^{0.33}$)

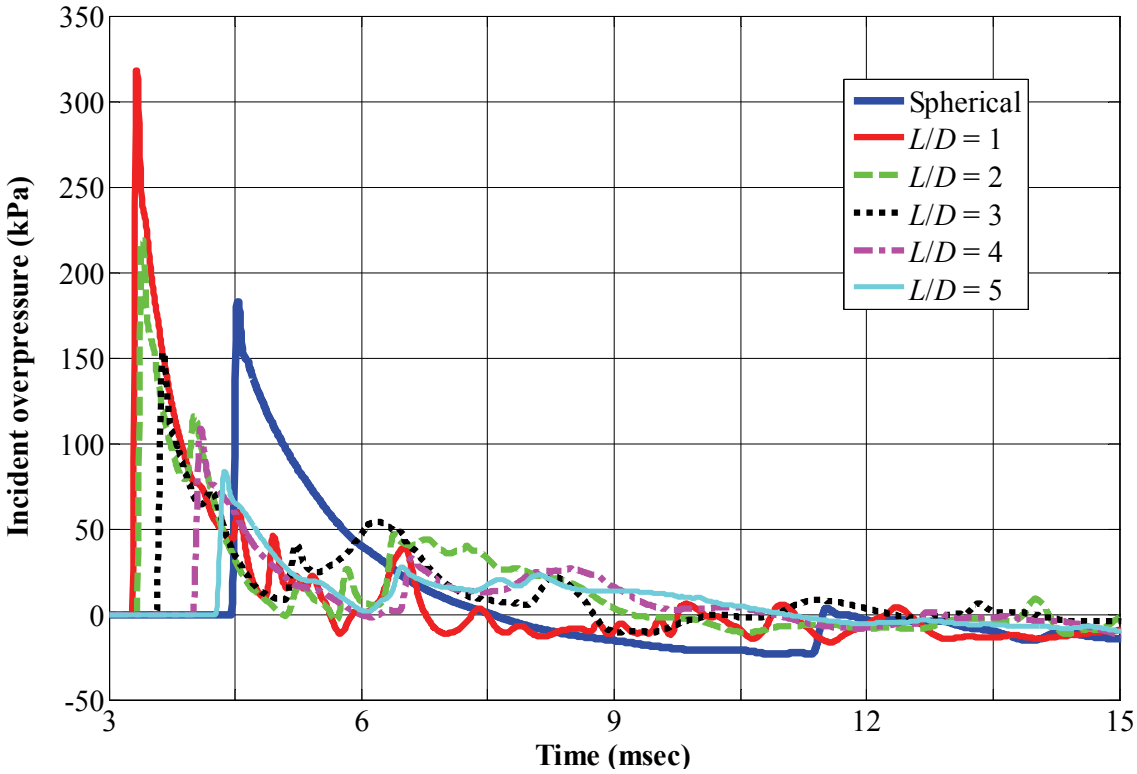

Figure 4-5: Overpressure histories at an axial distance of 20 charge diameters (Z = 2.10 m/kg$^{0.33}$)

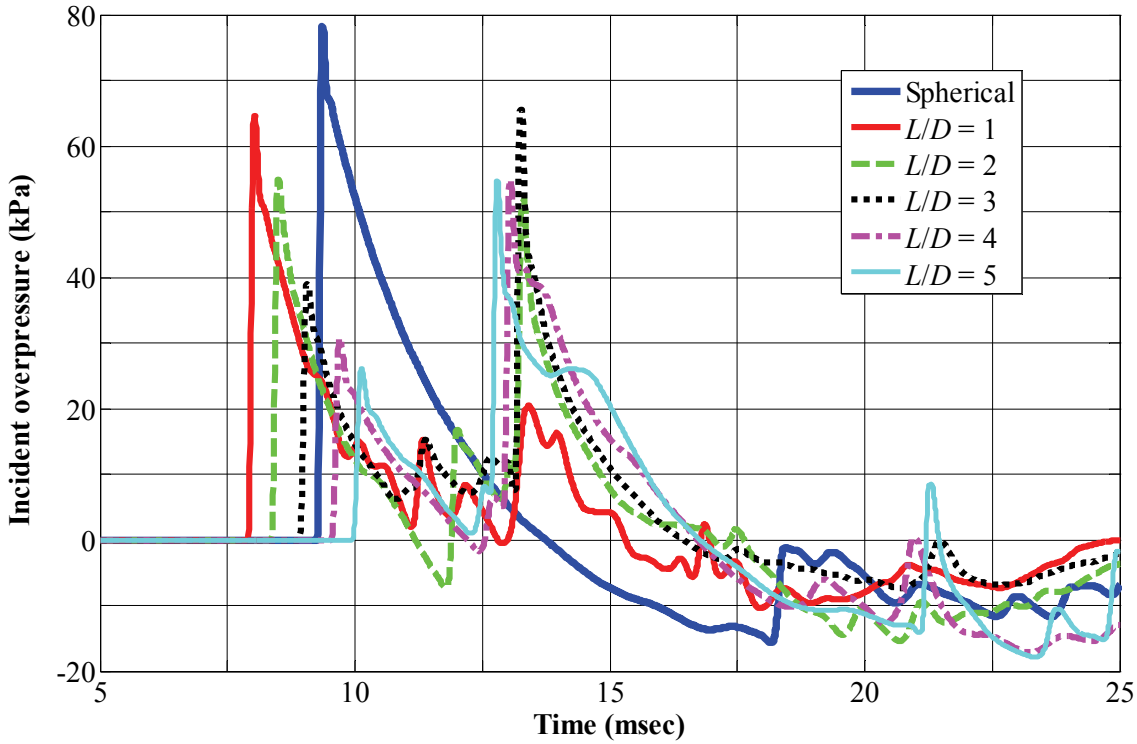

Figure 4-6: Overpressure histories at an axial distance of 30 charge diameters (Z = 3.15 m/kg$^{0.33}$)

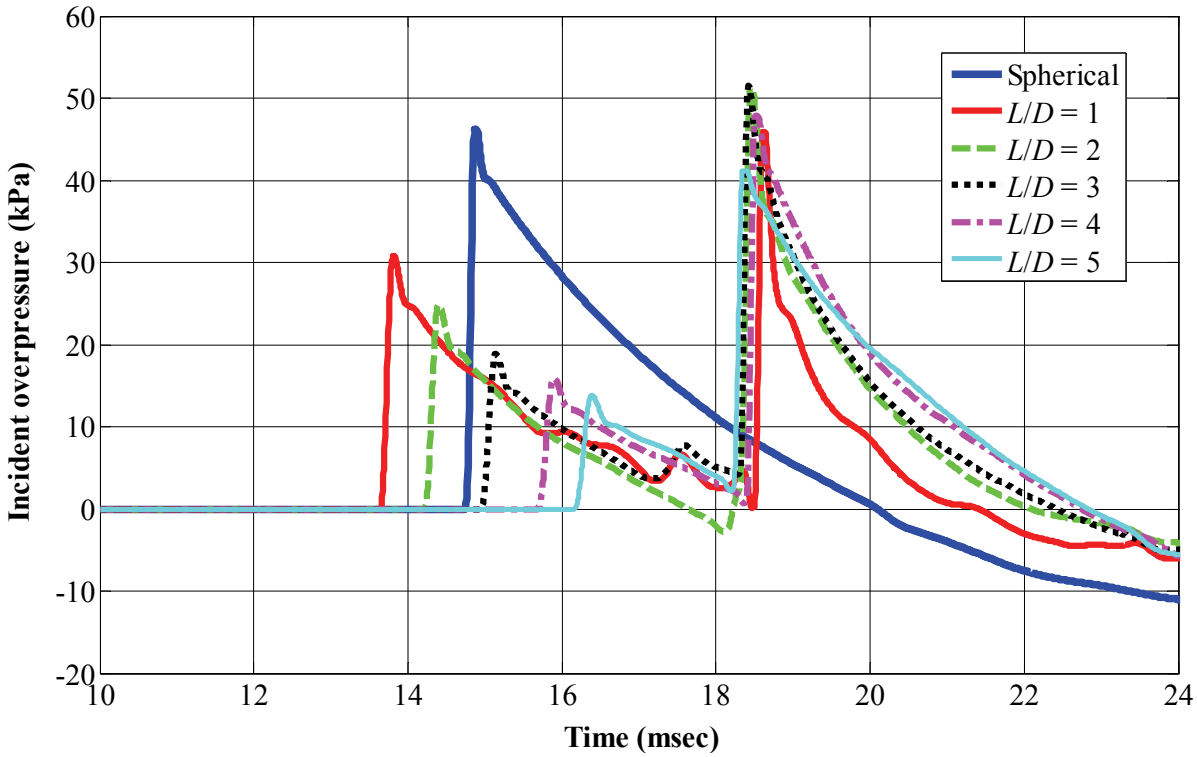

Figure 4-7: Overpressure histories at an axial distance of 40 charge diameters (Z = 4.20 m/kg$^{0.33}$)

The overpressure histories from the spherical and cylindrical charges at radial distances of 10, 20, 30 and 40 charge diameters are presented in Figures 4-8 to 4-11, respectively. The important observations that can be made from analysis of these figures are:

1. Charge shape has an effect on the peak overpressure histories in the radial direction. The peak overpressure increases with aspect ratio although the effect is less pronounced than in the axial direction.
2. Few secondary and tertiary shocks are seen in the radial direction overpressure histories for the cylindrical charges. Secondary shocks are clearly seen in the overpressure histories at a distance of 40 charge diameters but are small compared with the primary shocks and are insignificant from a design perspective. One reason for the absence of secondary shocks may be the curved shape of the contact surface in the radial direction, which makes the surface somewhat similar to a spherical charge.

3. In the radial direction, the shock fronts from the cylindrical charges arrive sooner than that from the spherical charge, although the differences in the arrival time are small, which is due in part to the overpressures. (Appendix A provides additional overpressure histories, including a history at a radial distance of 5 charge diameters)

Figures 4-12 through 4-15 present incident overpressure and impulse data as a function of distance that is measured in multiples of (spherical) charge diameter. Figure 4-16 and text below describe the calculation of peak incident overpressure and incident impulse for detonations that generate secondary and tertiary shocks. For the cylindrical charges, the impulse increases (decreases) with aspect ratio in the radial (axial) direction.

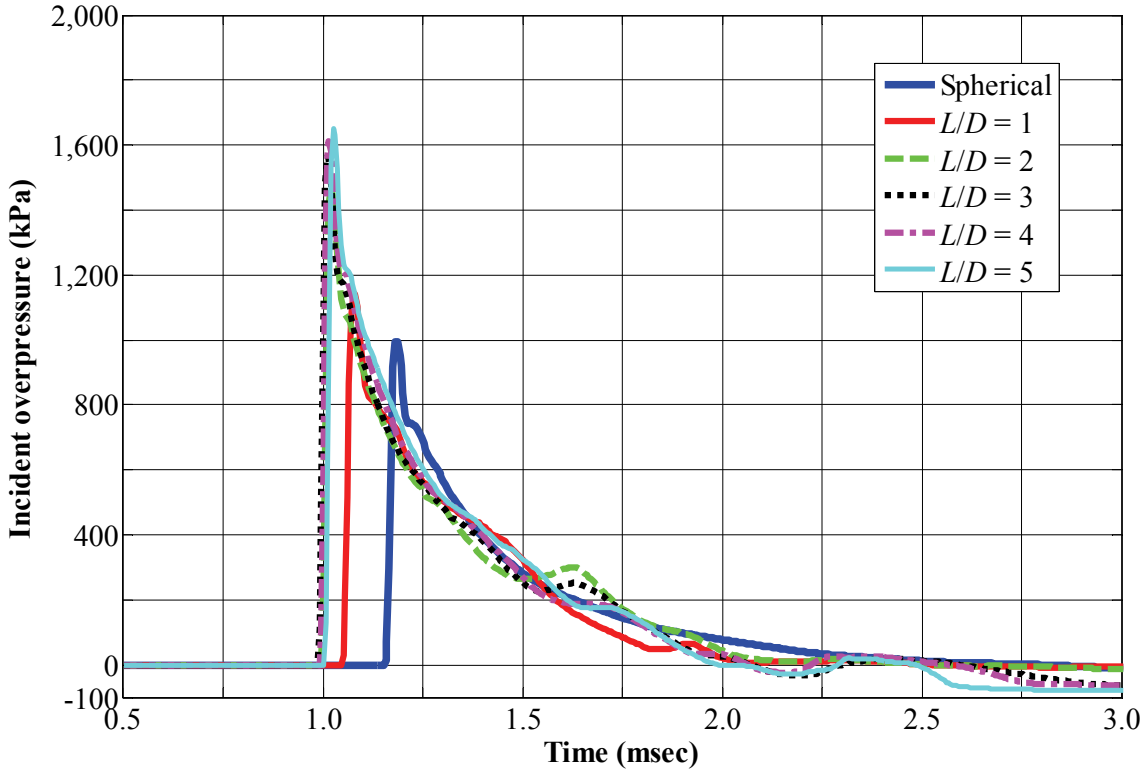

Figure 4-8: Overpressure histories at a radial distance of 10 charge diameters (Z = 1.05 m/kg$^{0.33}$)

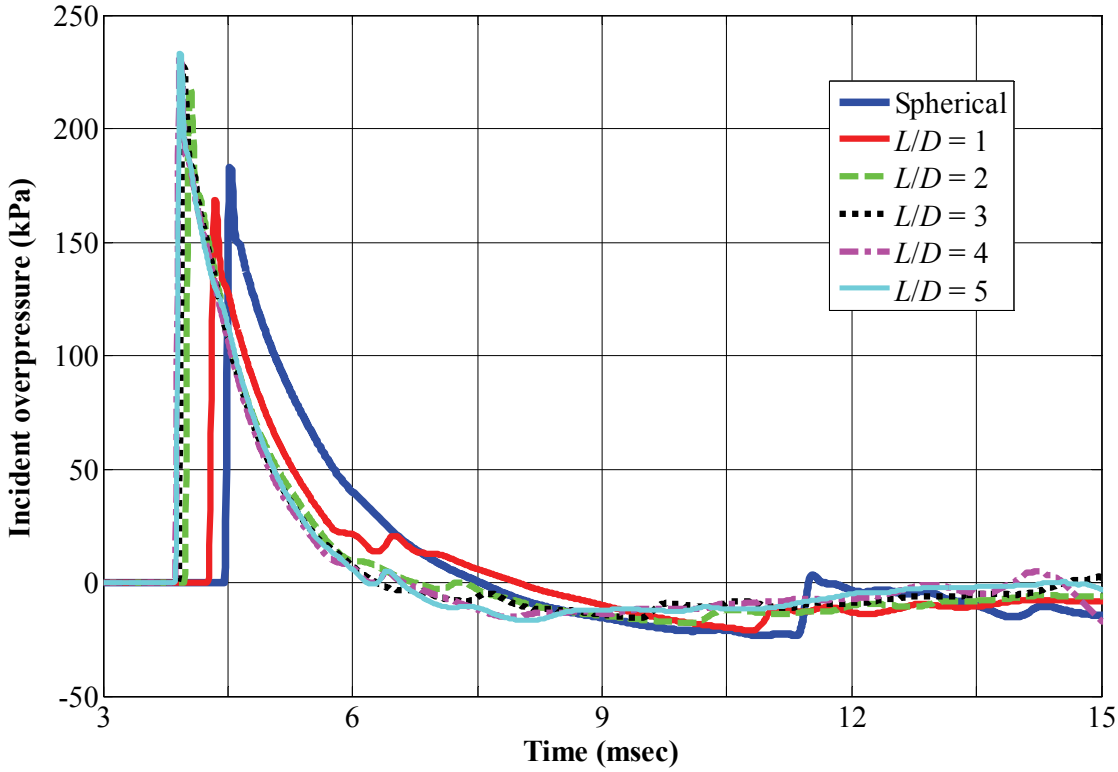

Figure 4-9: Overpressure histories at a radial distance of 20 charge diameters (Z = 2.10 m/kg$^{0.33}$)

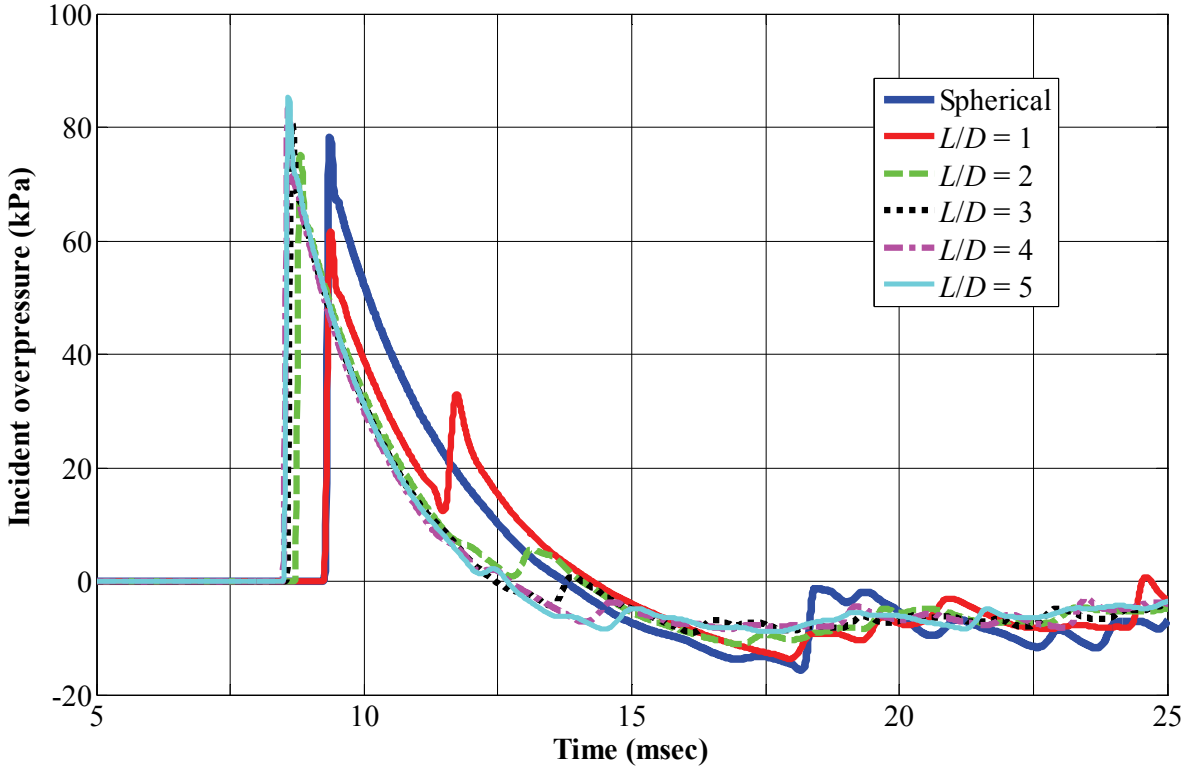

Figure 4-10: Overpressure histories at a radial distance of 30 charge diameters (Z = 3.15 m/kg$^{0.33}$)

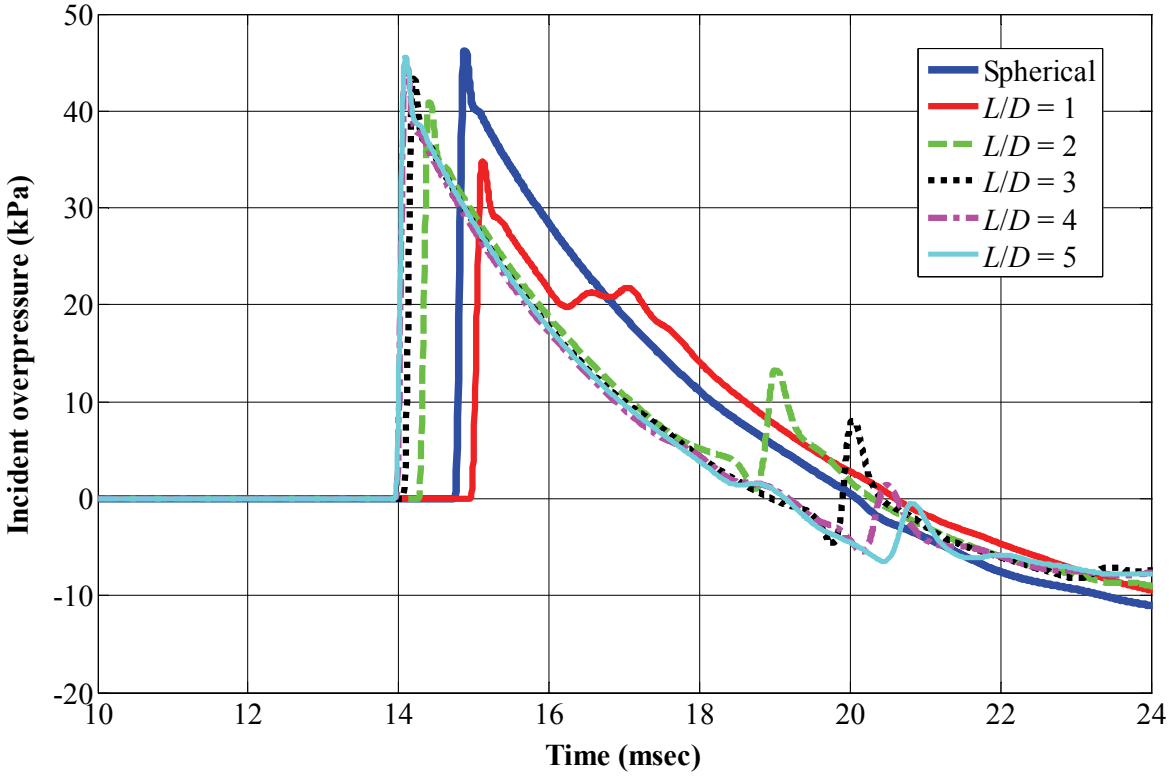

Figure 4-11: Overpressure histories at a radial distance of 40 charge diameters (Z = 4.20 m/kg$^{0.33}$)

The calculation of peak incident overpressures and incident impulses presented in Figures 4-12 to 4-15 warrants discussion. In the radial direction, the calculation of peak overpressure and impulse was straightforward because the positive phase is easily defined and secondary shocks are insignificant. However, in the axial direction, the calculation is not straightforward due to the presence of secondary and tertiary shocks. Beyond a certain scaled distance in the axial direction, the strengths of some secondary shocks exceed those of the corresponding primary shocks. In some cases, the secondary shock fronts arrive before the end of the positive phase associated with the primary shock. Consider Figure 4-5 and *Cyl_III*, where the duration of the positive phase is increased due to the arrival of the secondary and tertiary shocks. New definitions of peak incident overpressure, positive phase duration and incident impulse were developed to report data where significant secondary and tertiary shocks were observed. The positive phase of the primary wave was defined as the time difference between the arrival time and time t, where t is the smaller of the time when a) the overpressure from the primary wave drops to a very low value (= 5 kPa) for the first time, or b) the overpressure starts increasing due to the arrival of the

secondary shock front. The peak overpressure reported here is the maximum value of the primary or secondary shock fronts. The calculation is illustrated in Figure 4-16 in which the red markers on each overpressure time series denote the end of positive phase of the primary wave and the blue markers indicate the peak overpressures.

The values of impulse presented in Figures 4-13 and 4-15 do not include the impulse associated with the secondary and tertiary shocks. Calculations that include the impulse associated with the secondary and tertiary shocks are presented in Figures A-9 and A-10. From Figures 4-12 and 4-14, it can be seen that the peak overpressures from the cylindrical charges are no greater than 110% of that of the spherical charge at 25 charge diameters (Z = 2.64 m/kg$^{0.33}$) in the radial and axial directions. The impulse from the spherical charges equal or exceed those of the cylindrical charges at a distance equal to 20 charge diameters (Z = 2.10 m/kg$^{0.33}$) in both the axial and radial directions.

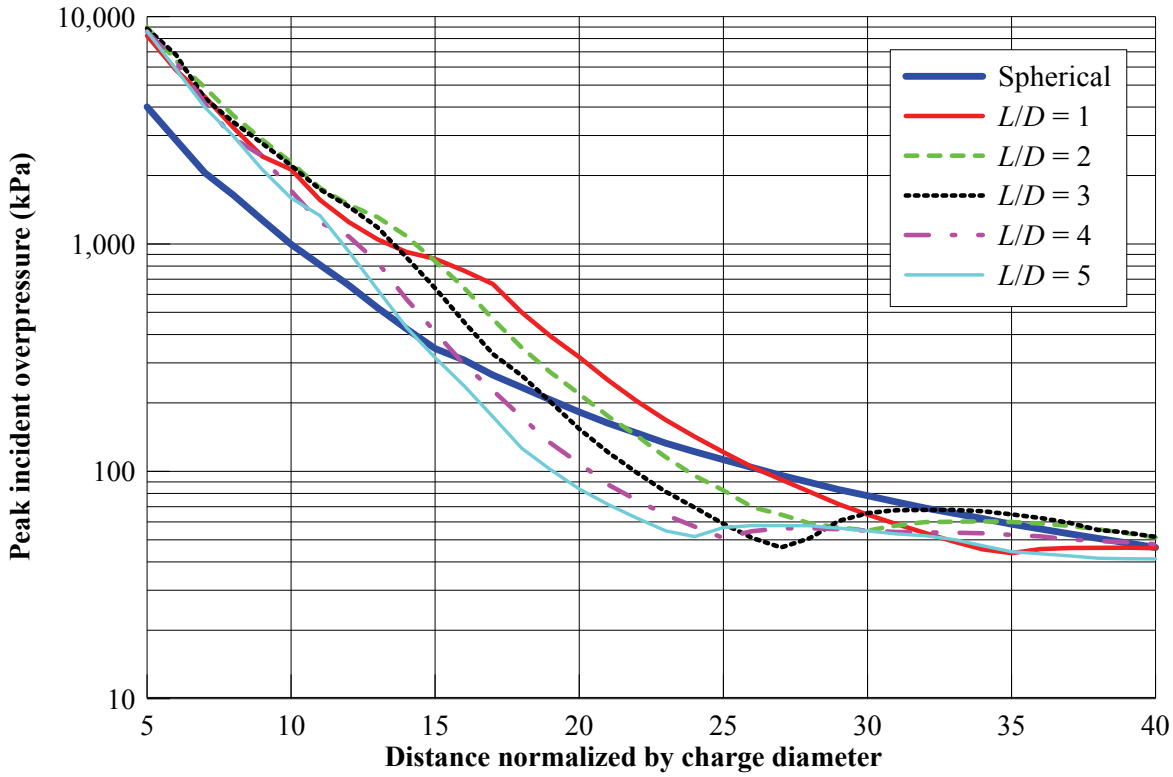

Figure 4-12: Peak incident overpressure in the axial direction as a function of normalized distance

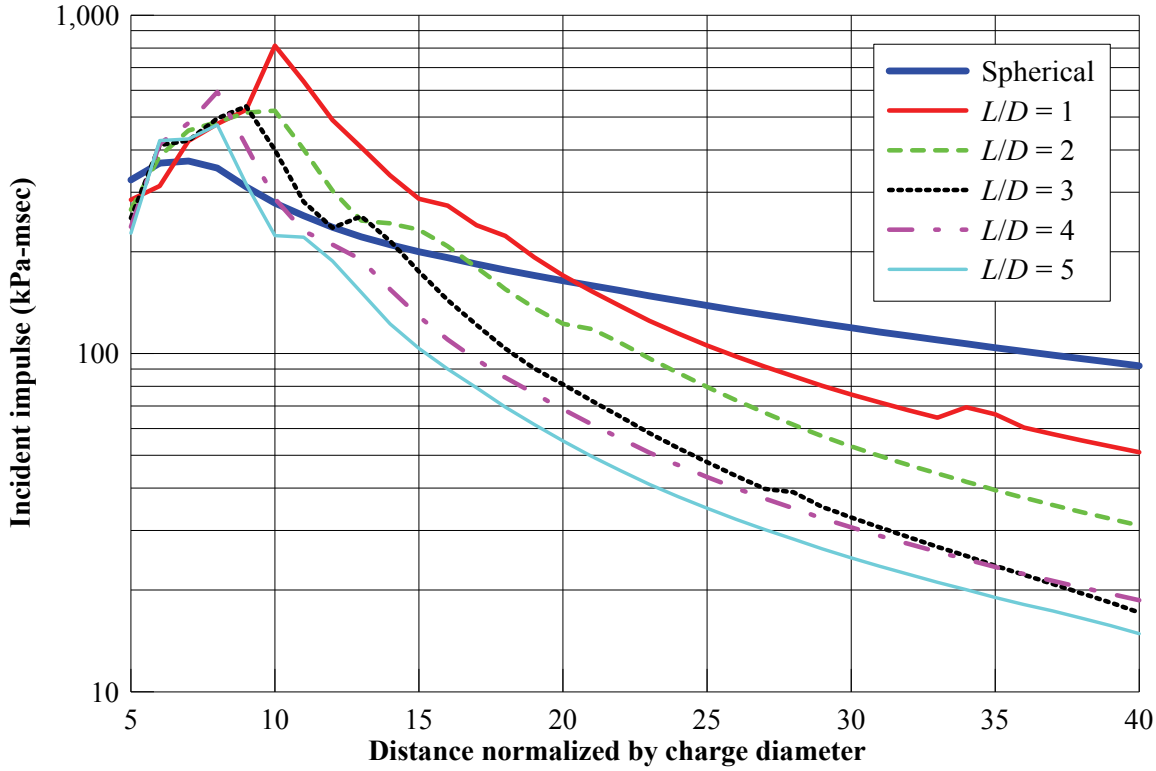

Figure 4-13: Incident impulse in the axial direction as a function of normalized distance

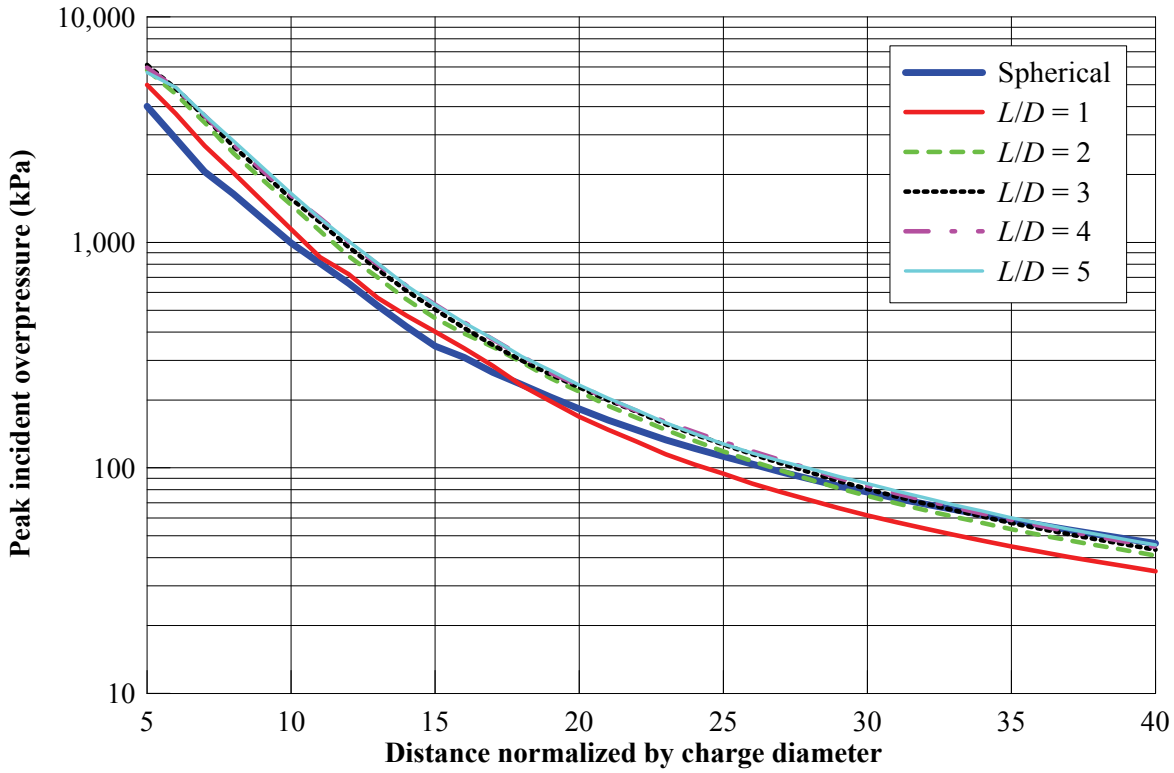

Figure 4-14: Peak incident overpressure in the radial direction as a function of normalized distance

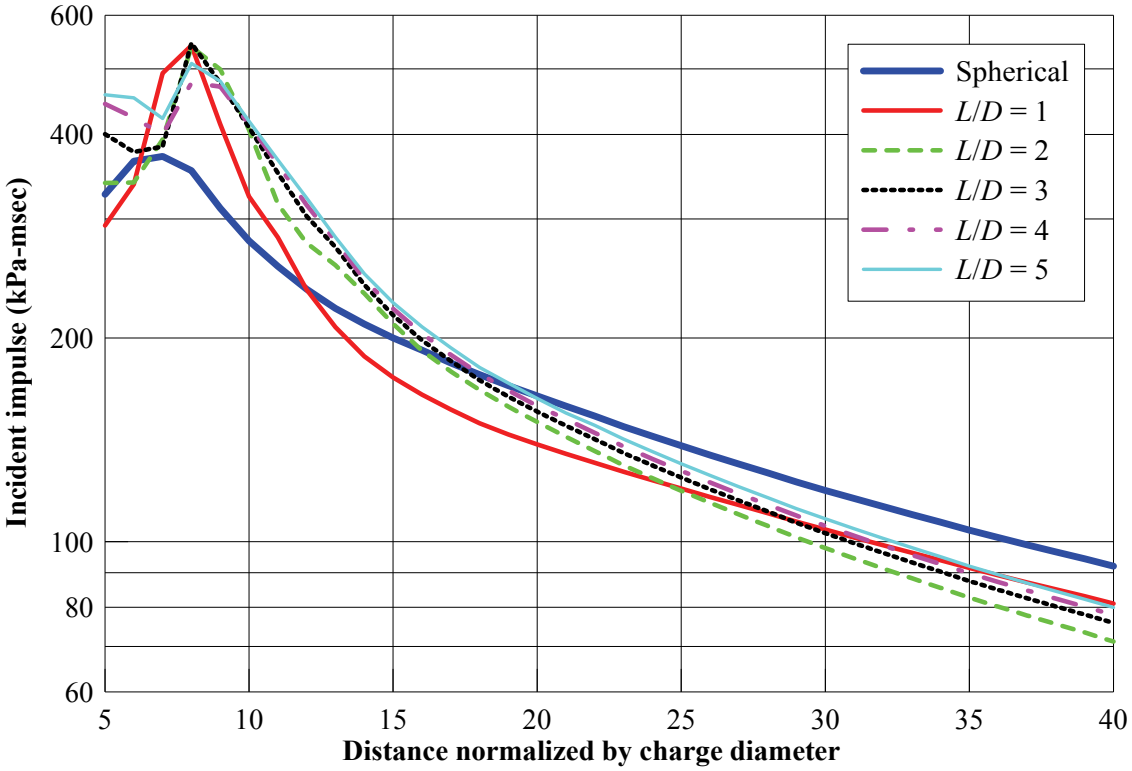

Figure 4-15: Incident impulse in the radial direction as a function of normalized distance

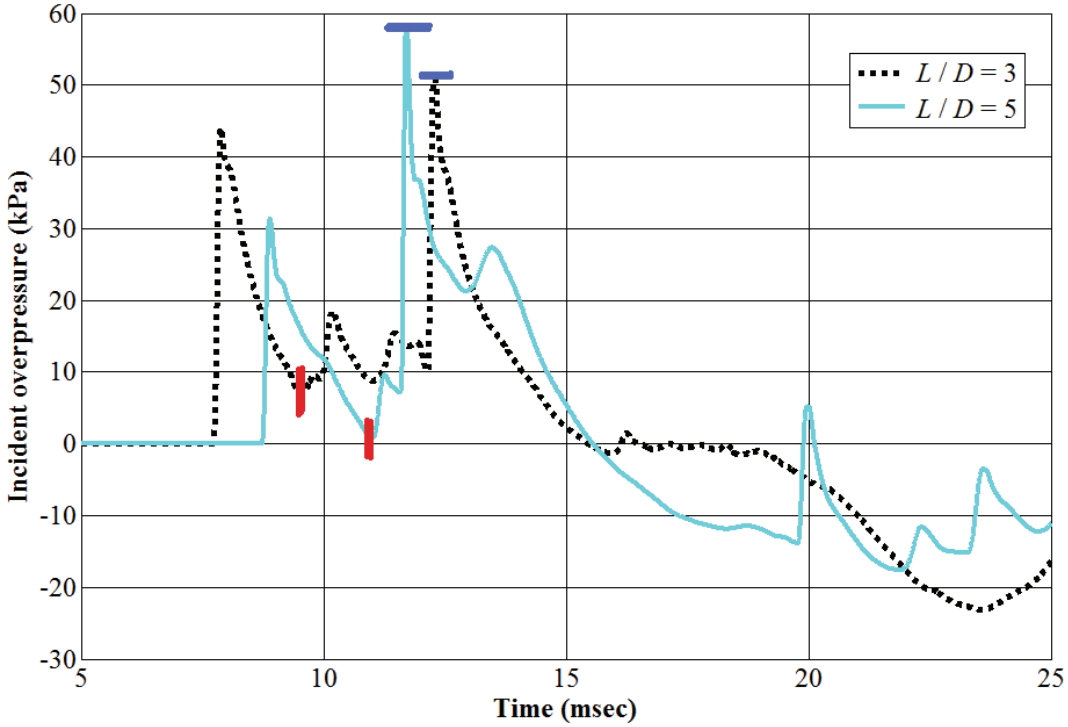

Figure 4-16: Calculation of peak incident overpressure and positive phase incident impulse

Although this information is instructive, it is not sufficient to identify the scaled distance beyond which the effect of charge shape can be ignored. Additional information is needed, such as the peak overpressures and impulses in directions other than the radial and axial directions. Pressure contours provide qualitative information on the peak overpressures and overall shape of the blast wave. Figures 4-17 to 4-19 enable a comparison of the (total) pressure contours for the spherical charge and the cylindrical charges *Cyl_I*, *Cyl_III* and *Cyl_V,* respectively. The pressure contours are presented on the vertical plane that bisects the charge. The pressure contours for the spherical and cylindrical charges are separated in the figure by the plane of symmetry ($x = 0$); the longitudinal axis of the charge is horizontal. The range in each panel is (+, -) the approximate number of charge diameters[21] identified in the corresponding subtitle. The evolution of the blast waves from the cylindrical charges is traced until they reach the edge of the air domain ($Z = 4$ m/kg$^{0.33}$). One thing that features prominently in these contour plots is the bridge wave, described in section 2.7. At the beginning of the analysis, spherical waves emanate from the cylindrical charges in the radial and axial directions. Initially, the pressures in the axial direction are higher than those in the radial direction: see panels a and b in Figure 4-17. As these waves propagate, they overlap in the region between the axial and radial directions giving rise to a bridge wave. For *Cyl_I*, the evolution of the bridge wave can be seen in panels c and d of Figure 4-17. With further expansion, the bridge wave grows in size and the overall shape of the blast wave approaches a circle in panels e and f.

In panel c of Figure 4-17, the pressures at the shock front from *Cyl_I* are within 110% of those of the spherical shock front. However the blast wave from *Cyl_I* has traveled a greater distance than the spherical blast wave in the axial direction. The differences are smaller in panel d than panel c. Based on peak overpressures, impulses and the pressure contour plots, the effect of charge shape can be neglected beyond a distance of 26 charge diameters for *Cyl_I*, that is, beyond a scaled distance of 2.78 m/kg$^{0.33}$.

---

[21] The diameter of a 10 kg spherical charge of TNT is approximately 227 mm. The (x, y) range in panel a is $(\pm 1400, \pm 1400)$ mm or $(\pm 6.5, \pm 6.5)$ charge diameters.

The contour plots also explain the significant secondary shocks seen in the overpressure histories of the cylindrical charges at large scaled distances in the axial (*x*-) direction. The amplitude of these secondary shocks exceeded those of the primary shocks. From the pressure-contour plots presented in panels e and f of Figures 4-17, 4-18 and 4-19 it can be observed that the secondary shocks are the bridge waves seen traveling behind the primary wave in the axial direction. These secondary shocks are designated as the reflected end waves in Figure 2-7 and become distinct only at large scaled distances.

In the pressure contours for *Cyl_III* and *Cyl_V*, presented in Figures 4-18 and 4-19, respectively, the effect of increasing aspect ratio on the overall shape of the blast wave and pressures can be seen clearly. The blast wave is concentrated more in the radial (*y*-) direction than the axial (*x*-) direction. Similar to *Cyl_I*, the bridge wave is seen in the pressure contours for *Cyl_III* and *Cyl_V* but it is less pronounced. A distinct feature in the pressure-contour plots for *Cyl_III* and *Cyl_V* is the secondary wave behind the primary wave in the axial direction seen in panel f of Figures 4-18 and 4-19. The pressures at the secondary shock front are greater than those at the primary shock front. In panel d of these figures, the shock front pressures from *Cyl_III* and *Cyl_V* are less than 110% of that of the spherical charge. Based on this observation and the comparison of peak overpressures and impulses presented previously, the effect of charge shape can be neglected a distance greater than 25 charge diameters for *Cyl_III* and *Cyl_V*, that is, at a scaled distance of 2.64 $m/kg^{0.33}$. The same conclusion can be drawn for *Cyl_II* and *Cyl_IV*. Note that these conclusions ignore the increase in impulse associated with the secondary and tertiary shocks.

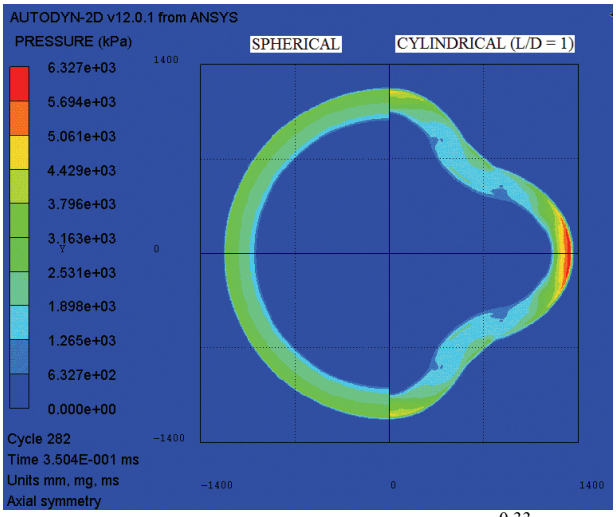

a) 6 charge diameters (Z = 0.63 m/kg$^{0.33}$)

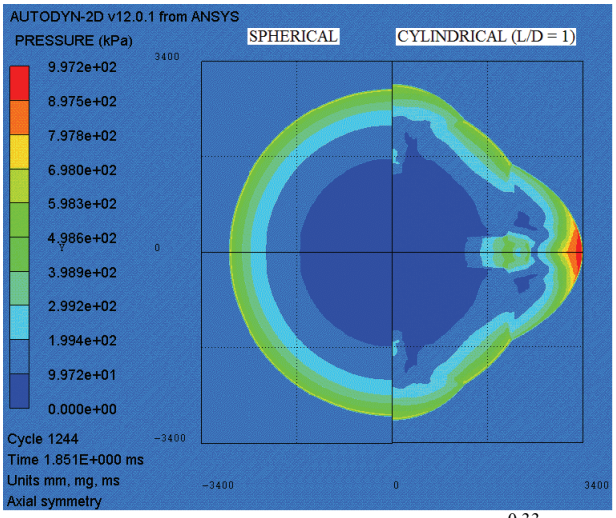

b) 15 charge diameters (Z = 1.58 m/kg$^{0.33}$)

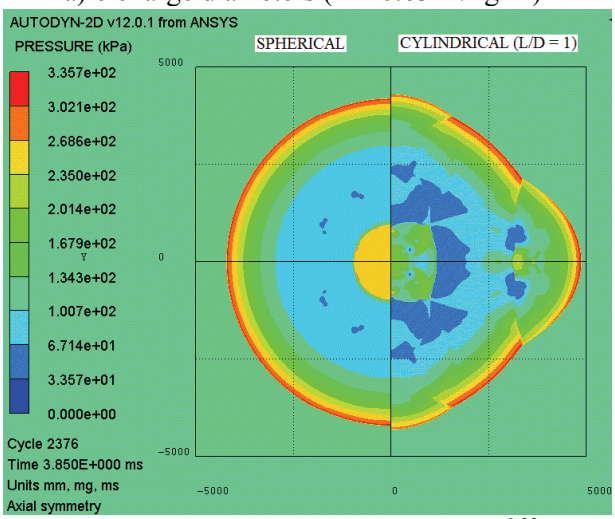

c) 22 charge diameters (Z = 2.32 m/kg$^{0.33}$)

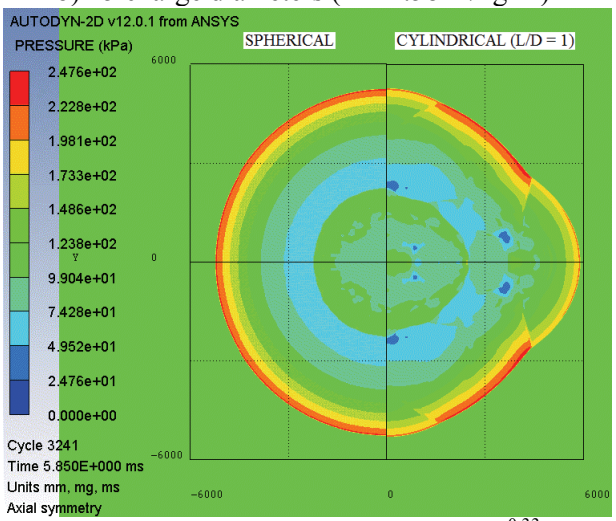

d) 26 charge diameters (Z = 2.78 m/kg$^{0.33}$)

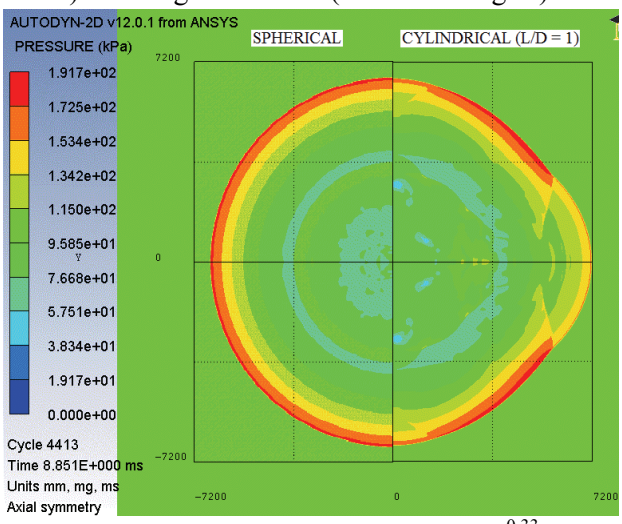

e) 32 charge diameters (Z = 3.34 m/kg$^{0.33}$)

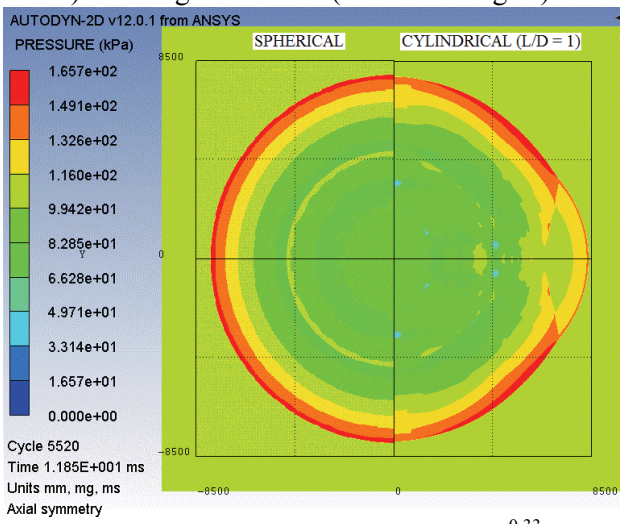

f) 37 charge diameters (Z = 3.94 m/kg$^{0.33}$)

Figure 4-17: Pressure contours (kPa) for the spherical and *Cyl_I* charges

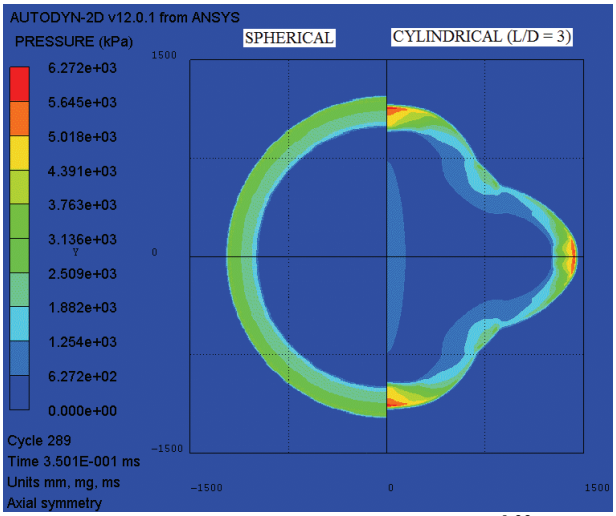

a) 6 charge diameters ($Z = 0.63$ m/kg$^{0.33}$)

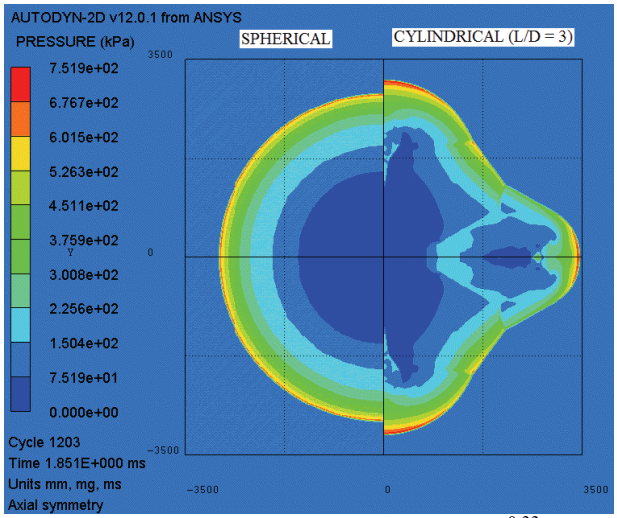

b) 15 charge diameters ($Z = 1.58$ m/kg$^{0.33}$)

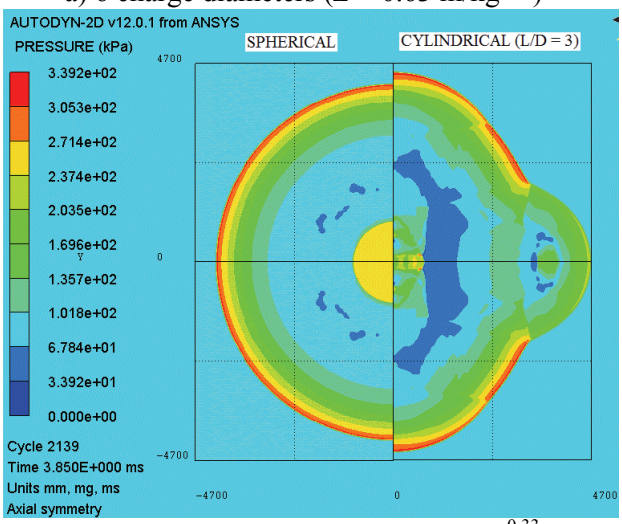

c) 20 charge diameters ($Z = 2.14$ m/kg$^{0.33}$)

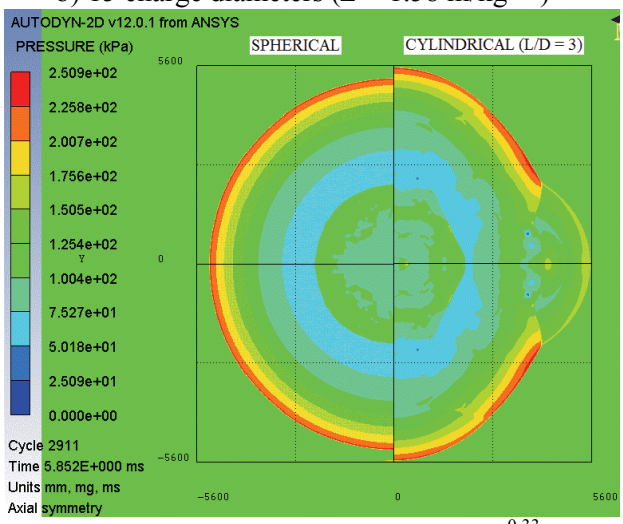

d) 25 charge diameters ($Z = 2.64$ m/kg$^{0.33}$)

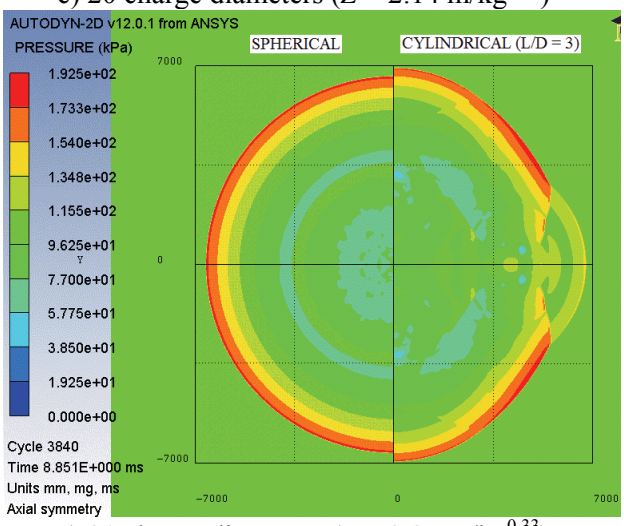

e) 31 charge diameters ($Z = 3.25$ m/kg$^{0.33}$)

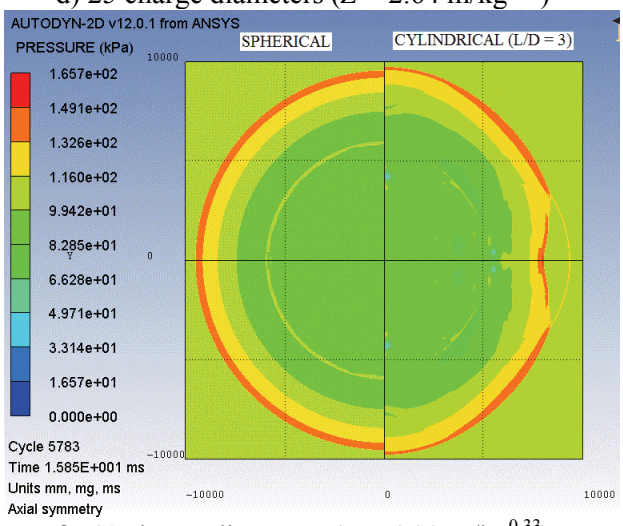

f) 41 charge diameters ($Z = 4.32$ m/kg$^{0.33}$)

Figure 4-18: Pressure contours (kPa) for the spherical and *Cyl_III* charges

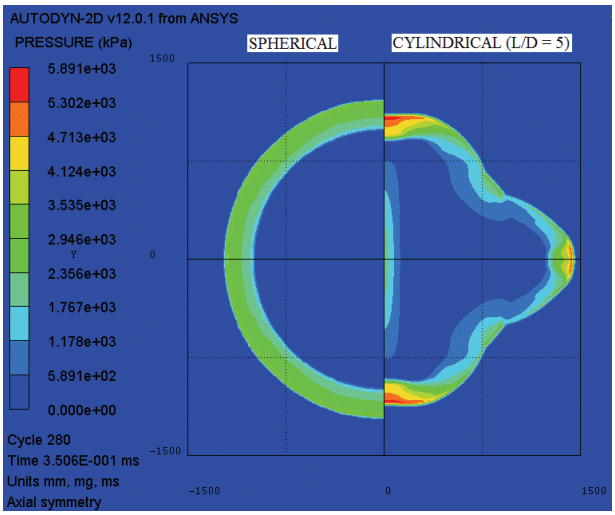

a) 6 charge diameters ($Z = 0.63$ m/kg$^{0.33}$)

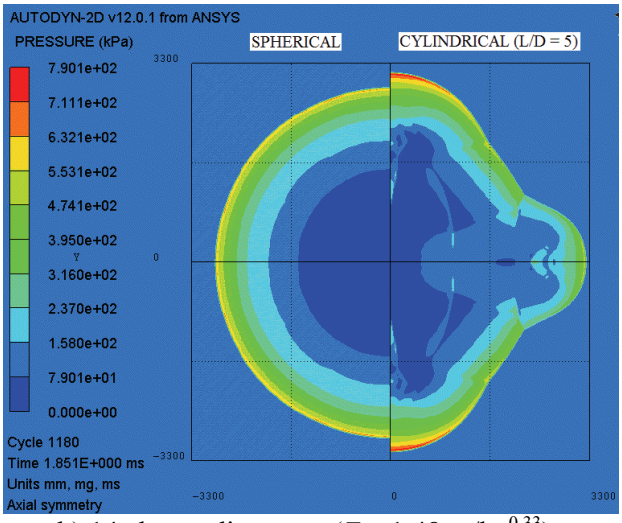

b) 14 charge diameters ($Z = 1.48$ m/kg$^{0.33}$)

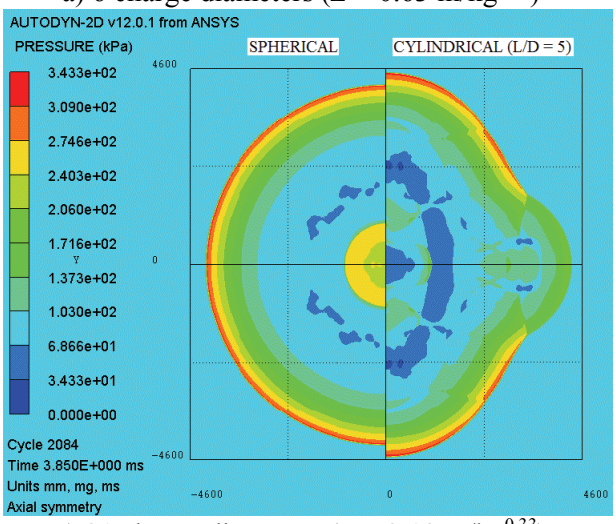

c) 21 charge diameters ($Z = 2.18$ m/kg$^{0.33}$)

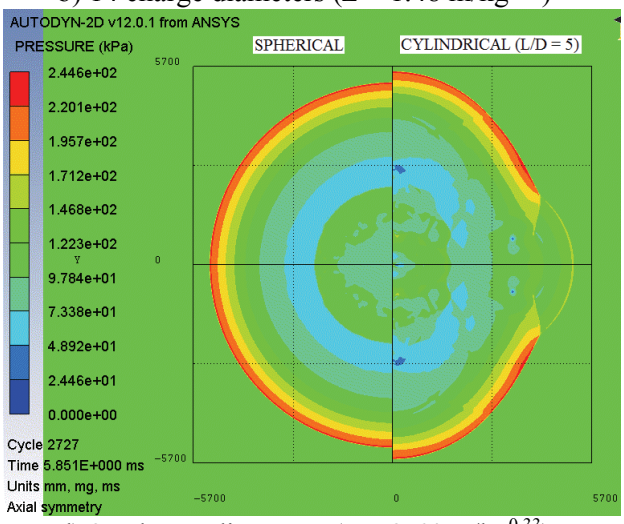

d) 25 charge diameters ($Z = 2.64$ m/kg$^{0.33}$)

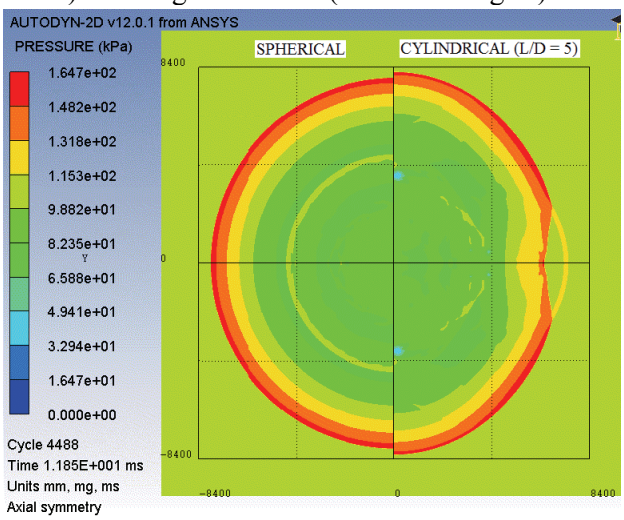

e) 37 charge diameters ($Z = 3.90$ m/kg$^{0.33}$)

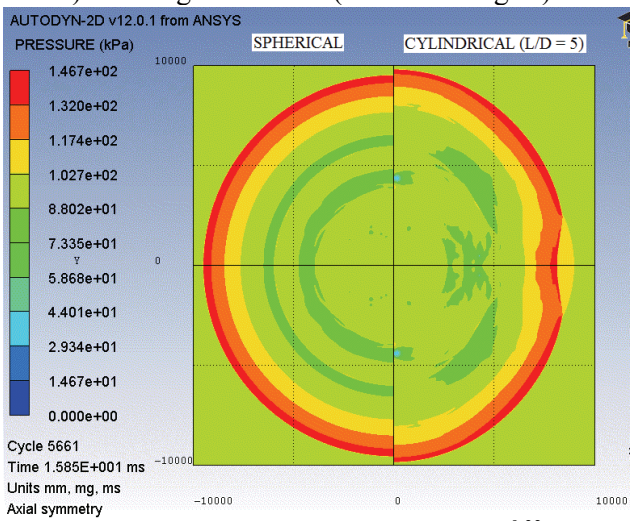

f) 43 charge diameters ($Z = 4.53$ m/kg$^{0.33}$)

Figure 4-19: Pressure contours (kPa) for the spherical and *Cyl_V* charges

Figures 4-20 and 4-21 characterize the magnitude of the secondary impulse as a function of normalized distance (distance divided by charge diameter) in the axial and radial directions, respectively. The secondary impulse is presented as a percentage of the primary impulse. The secondary impulse is calculated as the difference between the total impulse and primary impulse (as defined previously). The calculation of the total impulse includes the positive phase impulses from the secondary, tertiary and later shocks. In the radial direction, the secondary impulse is less than 10% of the primary impulse at distances greater than 9 charge diameters (Z = 0.95 m/kg$^{0.33}$). In the axial direction, the secondary impulse is significant at all normalized distances. At a distance of 40 charge diameters, the secondary impulse is about 70% of the primary impulse for *Cyl_I* and 500+% for *Cyl_V*.

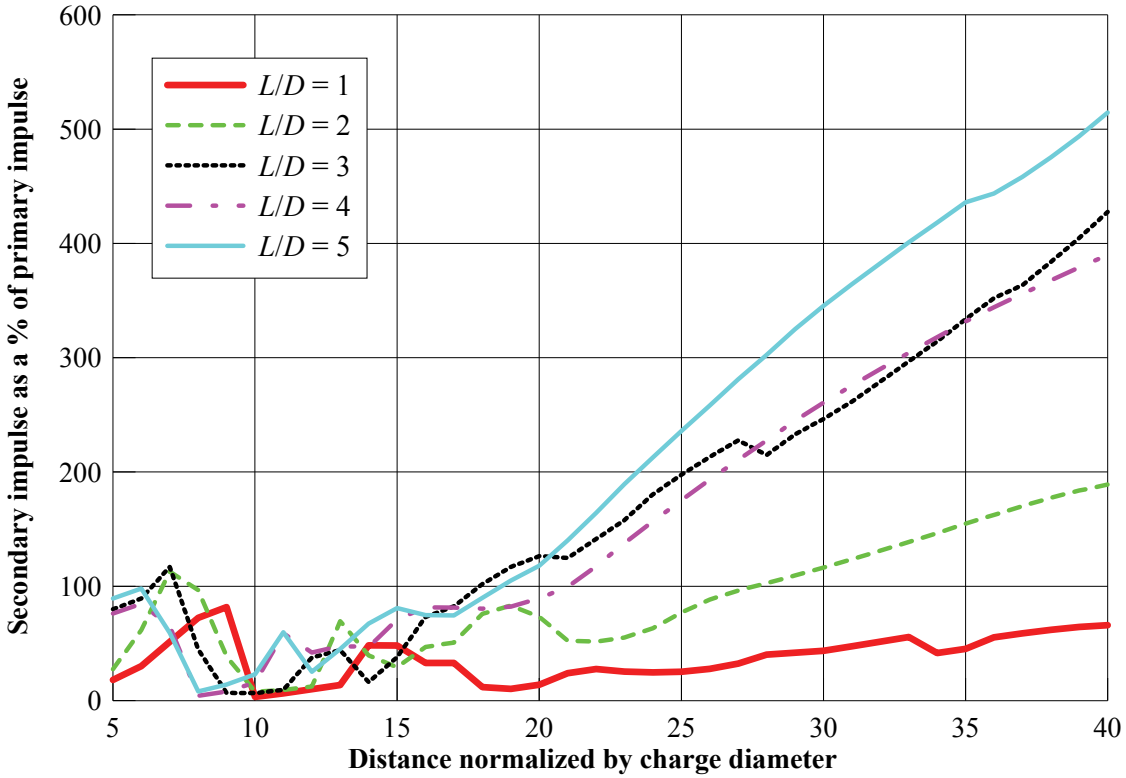

Figure 4-20: Secondary impulse in the axial direction as a function of normalized distance

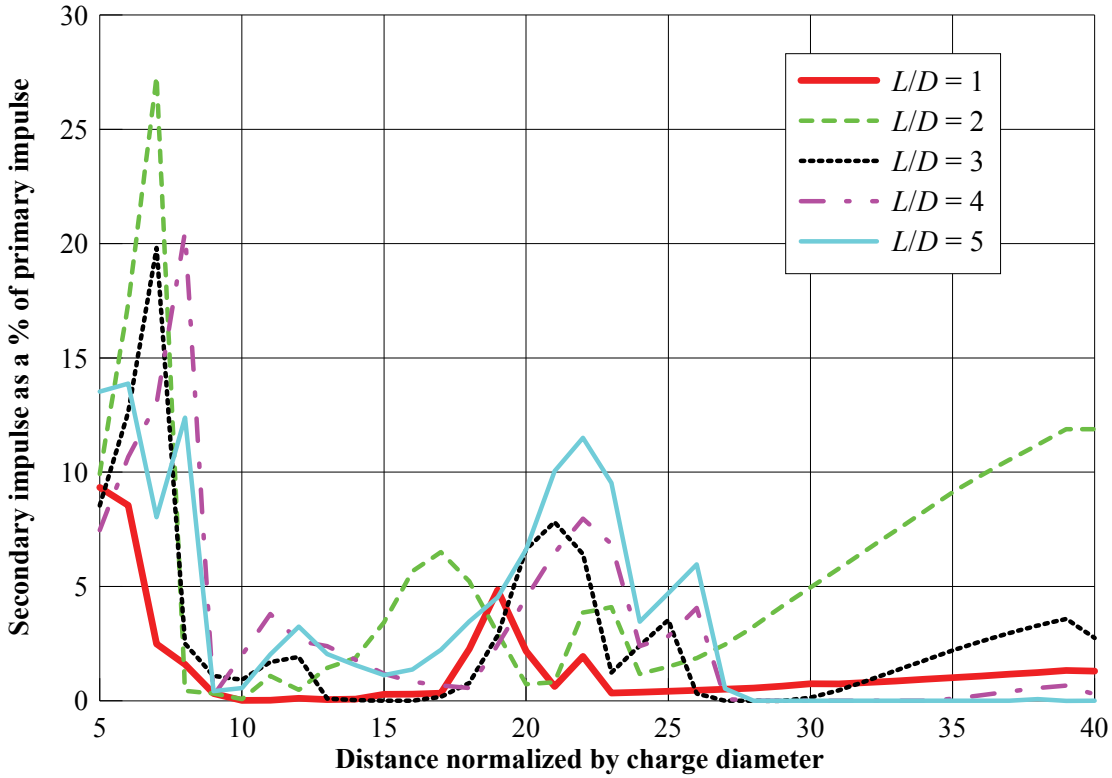

Figure 4-21: Secondary impulse in the radial direction as a function of normalized distance

4.2.4 Effect of charge mass

Conclusions on the effect of charge shape on overpressure distributions were drawn in 4.2.3 on the basis of analysis of 10 kg detonations. To judge whether the conclusions drawn to date are a function of charge mass, a set of companion analyses were performed with a 1000 kg charge. The analyses of section 4.2.2.1 and 4.2.2.2 were repeated for the spherical charge and the *Cyl_I*, *Cyl_III* and *Cyl_V* charges but with a mass of 1000 kg. The dimensions of the charge, range of the air domain and the termination time were revised accordingly. The overpressure histories at distances of 10 and 30 charge diameters in the axial and radial directions are presented in Figures 4-22 through 4-25. The same trends in peak overpressure, decay rate, and secondary shocks seen previously for the 10 kg charges are seen in the overpressure histories for the 1000 kg charges.

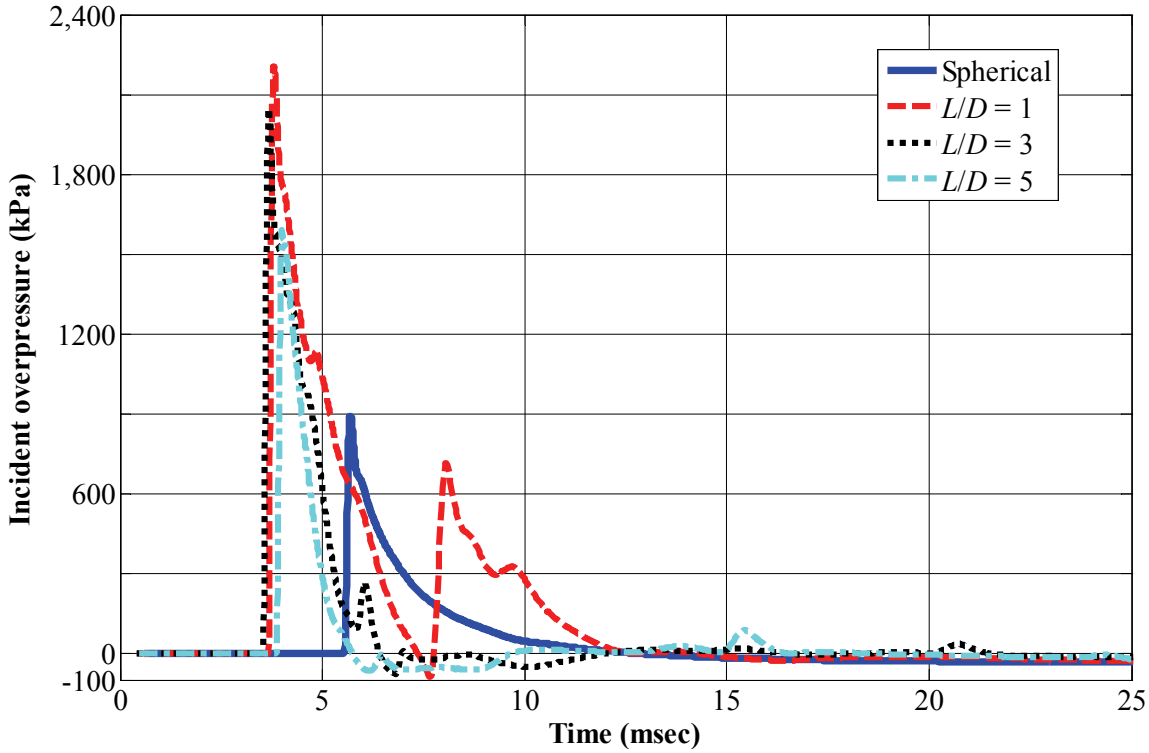

Figure 4-22: Overpressure histories at an axial distance of 10 charge diameters (Z = 1.05 m/kg$^{0.33}$)

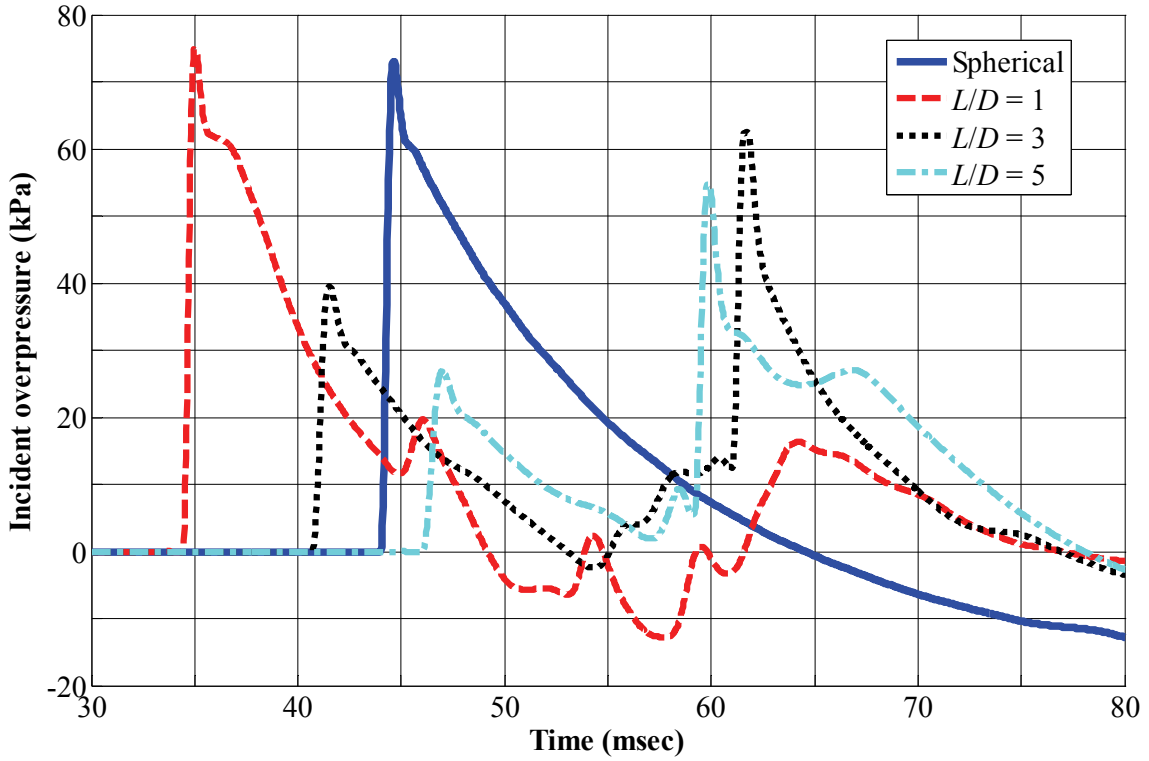

Figure 4-23: Overpressure histories at an axial distance of 30 charge diameters (Z = 3.15 m/kg$^{0.33}$)

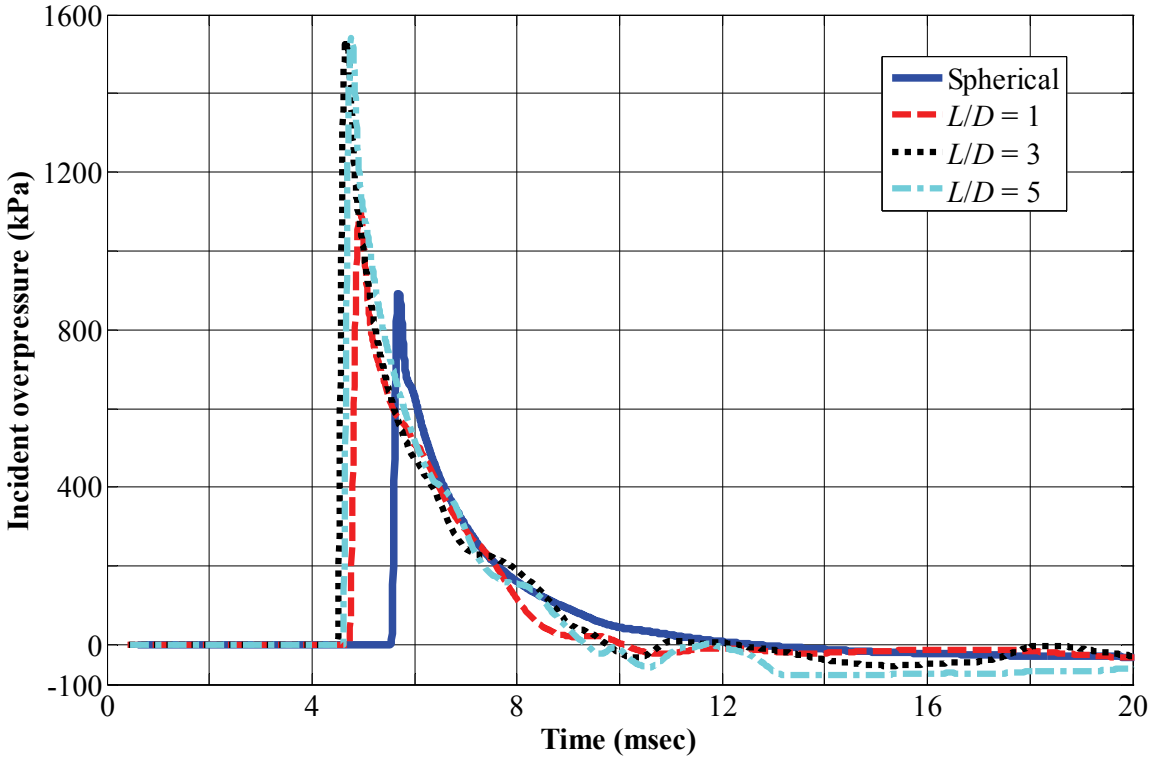

Figure 4-24: Overpressure histories at a radial distance of 10 charge diameters (Z = 1.05 m/kg$^{0.33}$)

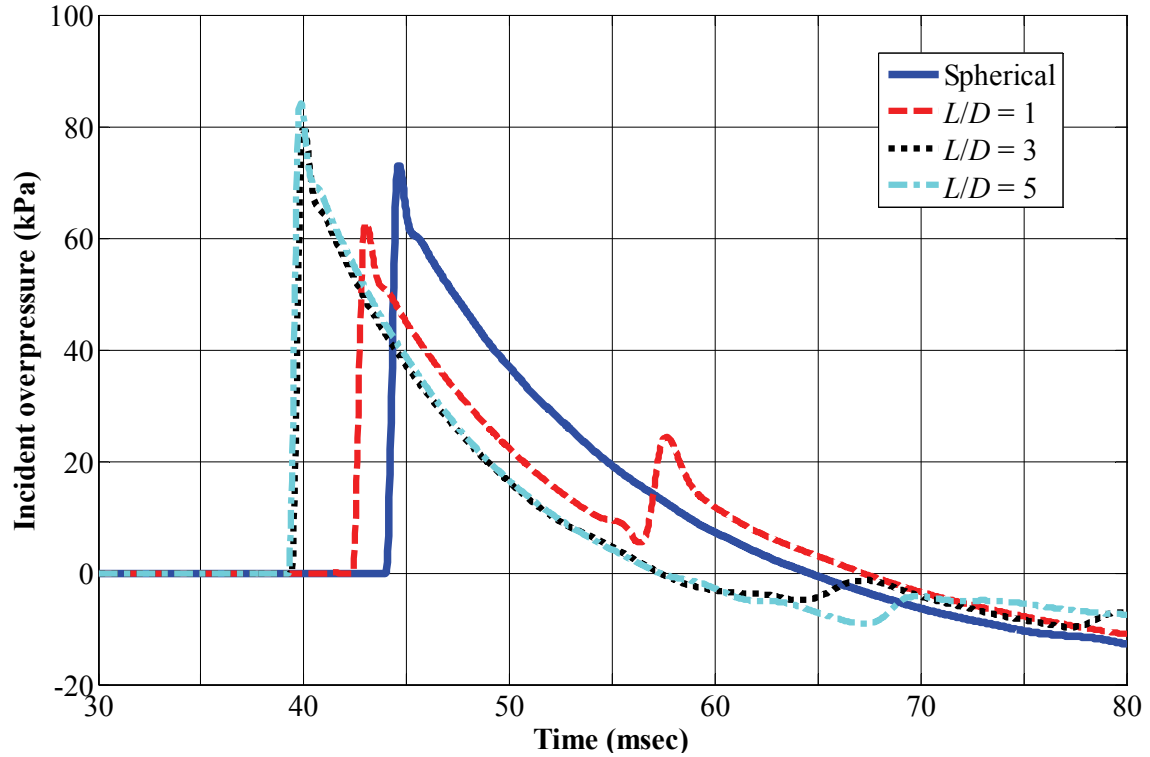

Figure 4-25: Overpressure histories at a radial distance of 30 charge diameters (Z = 3.15 m/kg$^{0.33}$)

Figures 4-26 and 4-27 enable a comparison of the overpressure histories from the 10 kg and 1000 kg cylindrical charges, *Cyl_I* and *Cyl_V*, at a scaled distance of 2.1 m/kg$^{0.33}$ in the axial and radial directions, respectively. The overpressure histories are similar in the radial directions, although there are small differences in the peak overpressures and arrival times for the two masses. In the axial direction, there are moderate differences in the peak overpressures for the two charges at the same scaled distance. The secondary shock in the overpressure history of the 1000 kg *Cyl_I* charge in the axial direction is significant compared with that in the overpressure history of the 10 kg *Cyl_I* charge. The different grid sizes likely contributed to these differences.

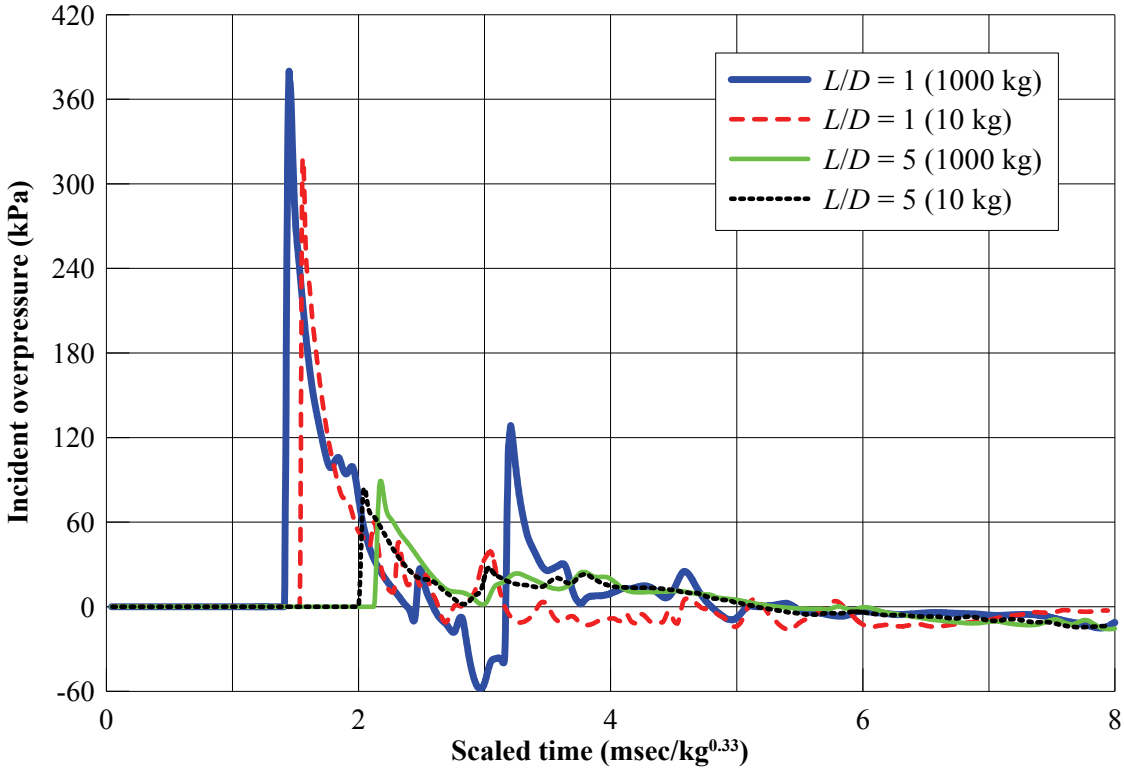

Figure 4-26: Incident overpressure at a scaled distance of 2.1 m/kg$^{0.33}$ in the axial direction

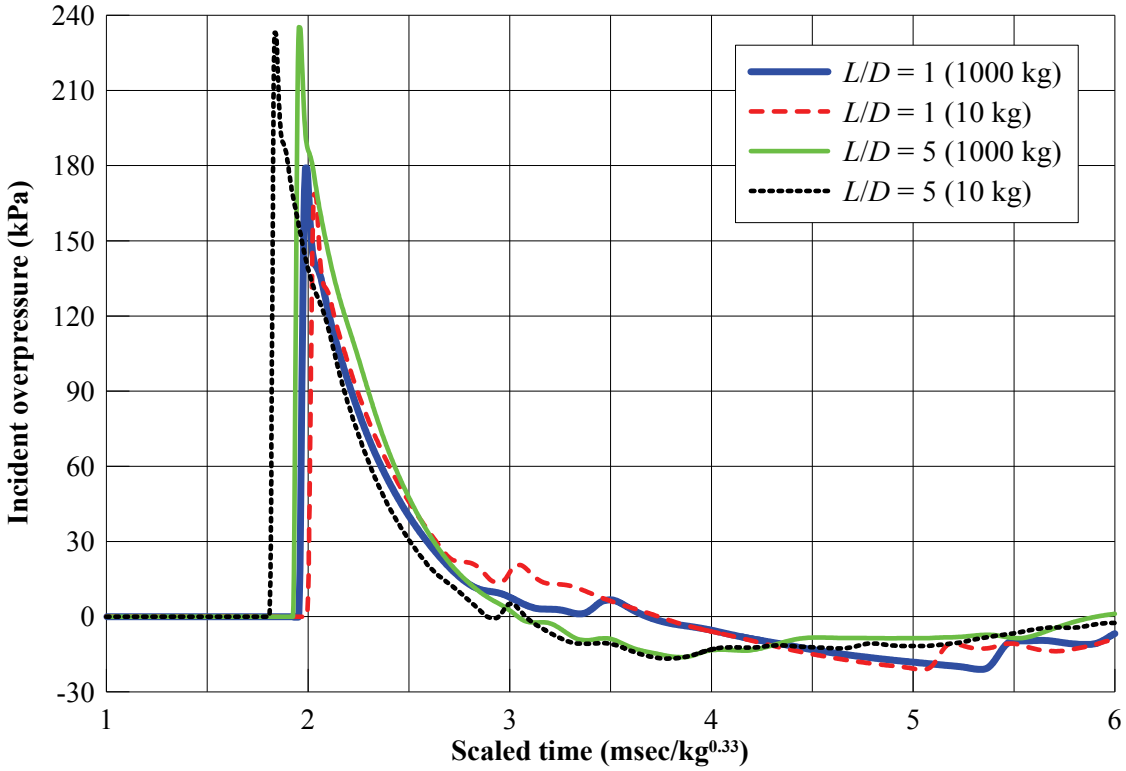

Figure 4-27: Incident overpressure at a scaled distance of 2.1 m/kg$^{0.33}$ in the radial direction

The peak incident overpressures and impulses in the axial and radial directions are presented in Figures 4-28 through 4-31. The peak overpressures from the cylindrical charges drop to those from the spherical charge at 30 charge diameters in the axial direction, whereas the corresponding distance in the radial direction is 35 charge diameters. However, the overpressures at these distances have dropped to values less than 1 atmosphere, which are not significant for blast resistant design. The overpressures from the cylindrical charges values are no greater than 115% of those from the spherical charge at 30 charge diameters. The impulses from the spherical charge exceed those from the cylindrical charges beyond a distance of 27 charge diameters. These trends shown by the 1000 kg charges are similar to those shown earlier by the 10 kg charges, except for a slight increase in the normalized distance beyond which the effect of charge shape can be ignored. For the 1000 kg charge, the charge shape can be ignored beyond a distance of 30 charge diameters, that is, a scaled distance of 3.16 m/kg$^{0.33}$; an 18% increase in scaled distance for a 100-fold increase in charge mass.

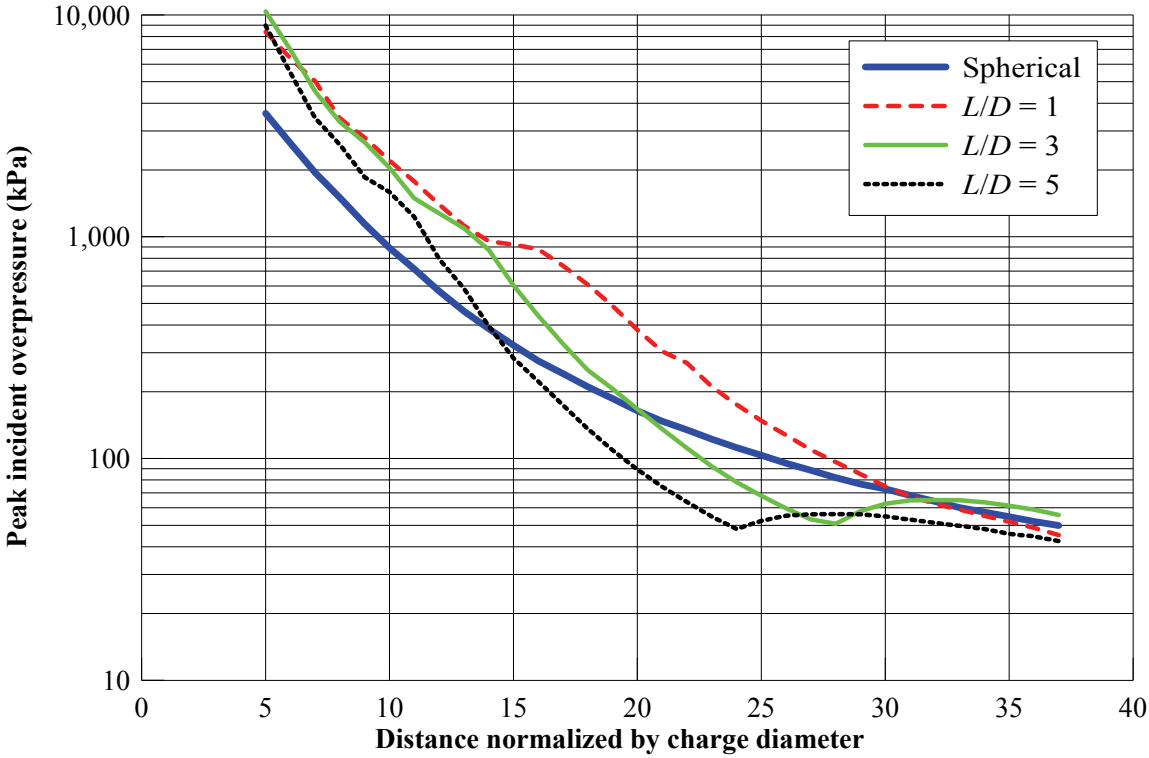

Figure 4-28: Peak incident overpressure in the axial direction as a function of normalized distance

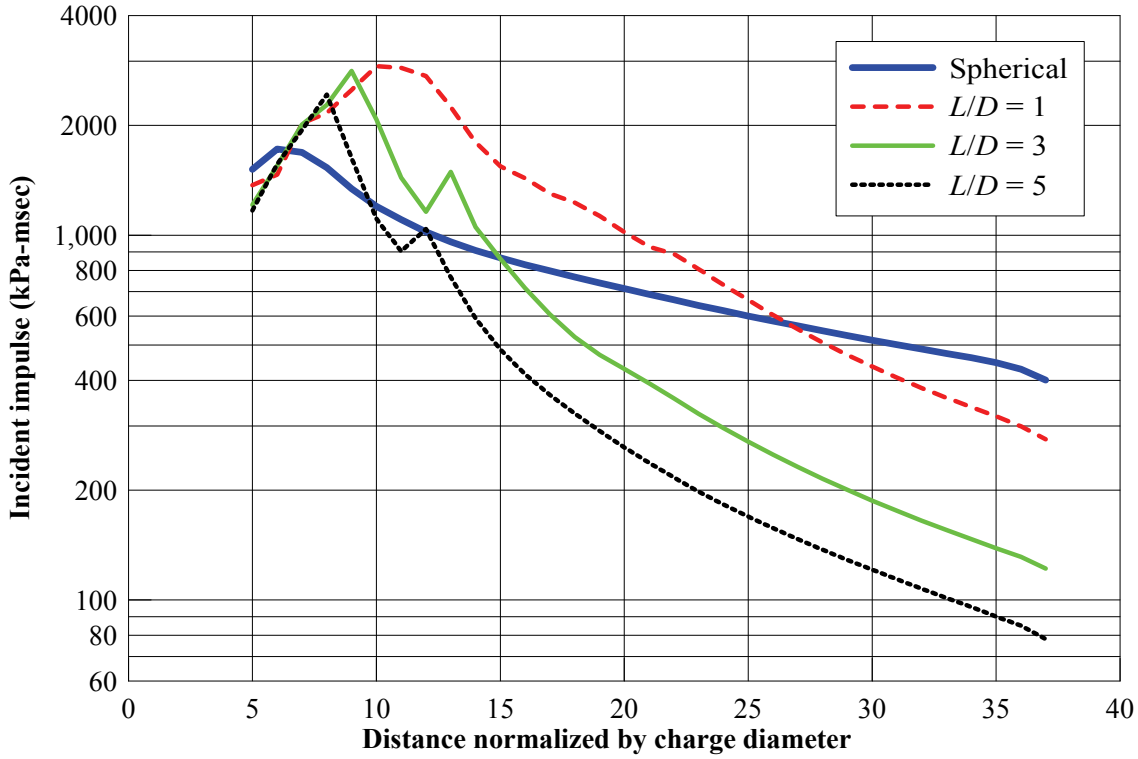

Figure 4-29: Incident impulse in the axial direction as a function of normalized distance

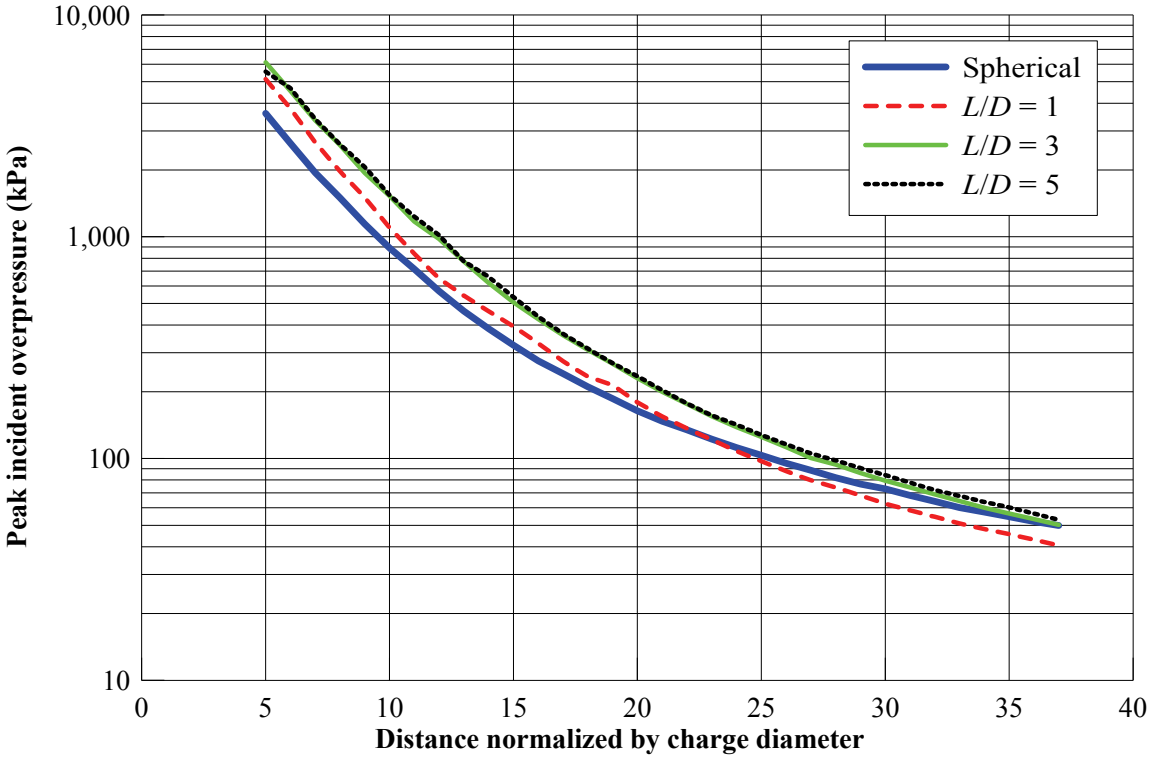

Figure 4-30: Peak incident overpressure in the radial direction as a function of normalized distance

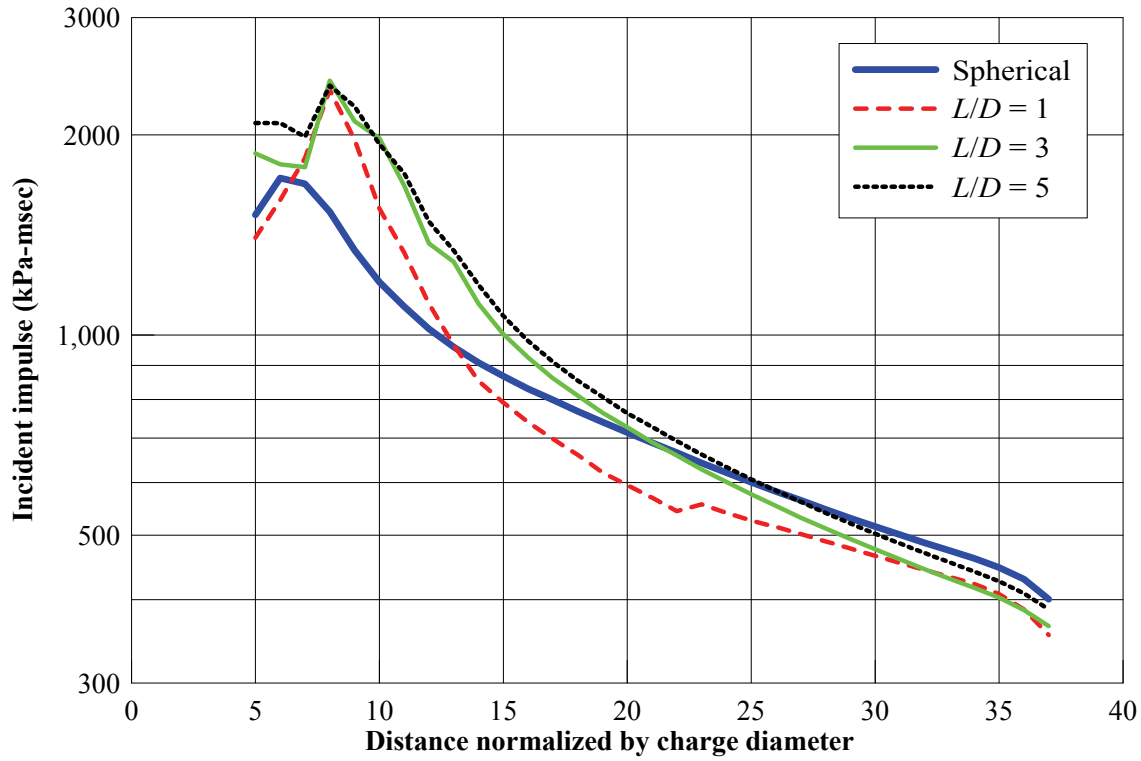

Figure 4-31: Incident impulse in the axial direction as a function of normalized distance

4.3 Influence of Detonation Point on Overpressure Histories

4.3.1 Modeling and analysis

In the sample problem described in section 4.2.1, a central detonation was assumed for the spherical and cylindrical charge. However, cylindrical charges are more easily detonated at an end. Zimmerman et al. (1999) and Tham (2009) studied the effect of point of detonation on the incident impulse along alternate ray-paths to the charge axis. Zimmerman et al. used end-detonated cylindrical charges with varying aspect ratios to demonstrate this effect. Tham used three different initiating strategies for detonating the cylindrical charges: 1) detonated at one end, 2) detonated at both ends simultaneously and 3) detonated at both ends with a time delay, to examine the effect on impulse in the near field. Their studies showed that for the end-detonated charges, the impulse and peak overpressures were significantly different at the two ends of the charge in the near-field.

In the present study, three charges with aspect ratios 1, 3 and 5 were used to demonstrate the effect of point of detonation within the charge. An axially symmetric 2D model was generated similar to those presented in Figure 4-2. The cylindrical charges *Cyl_I*, *Cyl_III* and *Cyl_V* modeled for the AUTODYN analyses of section 4.2.2.2 were used. However, the point of detonation was moved to the left-hand end of the charge axis. The centrally detonated charges had a symmetric plane at $x = 0$ and hence only 1/2 of these axially symmetric charges were modeled. No such symmetry could be used for the end-detonated charges. The axially symmetric 2D model for the end-detonated cylindrical charge, *Cyl_V*, is presented in Figure 4-32. The analyses for all the charges were performed in two stages, similar to the analyses in section described in 4.2.2.2. A termination time of 25 msec, used for the analyses with centrally detonated charges, was adopted. The results of the analysis are presented in the following section in terms of contour plots that compare the two charges with different detonation points for three aspect ratios: 1, 3 and 5. For convenience, ‘CD’ and ‘ED’ subscripts are added to denote centrally detonated and end-detonated charges, respectively.

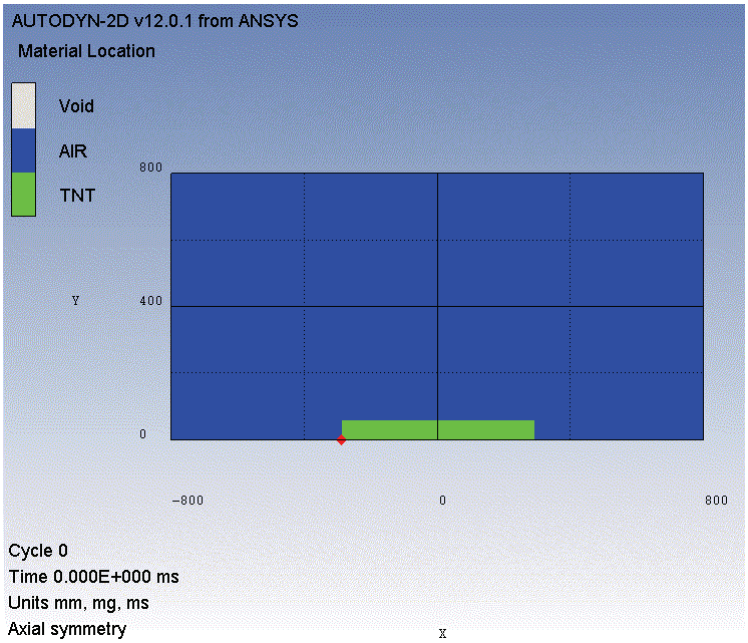

Figure 4-32: 2D axially symmetric model of the end-detonated cylindrical charge, *Cyl_V*

4.3.2 Results and discussion

Contour plots for *Cyl_I*$_{CD}$ and *Cyl_I*$_{ED}$ are presented in the upper and lower halves, respectively, in each panel of Figure 4-33. Data are presented as a function of distance normalized by the diameter of the spherical charge. The range in each panel is (+, -) the approximate number of charge diameters[22] identified in the corresponding subtitle. The shapes of the plots are complex for both points of detonation and change with an increase in scaled distance.

Panels a and b of Figure 4-33 are plots for the initial stages of the detonation. For reference, the length and diameter of *Cyl_I* are 198 mm. The charge is shown in panel a of the figure. The shock front overpressures in the axial direction (-*x*, +*x*) of the end-detonated charge are significantly different but are similar in the radial direction. The pressure contours are expected to differ in the axial direction because a) the points of detonation are different, and (b) the shock front propagates through different distances in the explosive and air domains for the two charges. For values of the scaled range less than approximately

[22] Charge diameter is the diameter of the spherical charge and is equal to 227 mm for the 10 kg TNT charge.

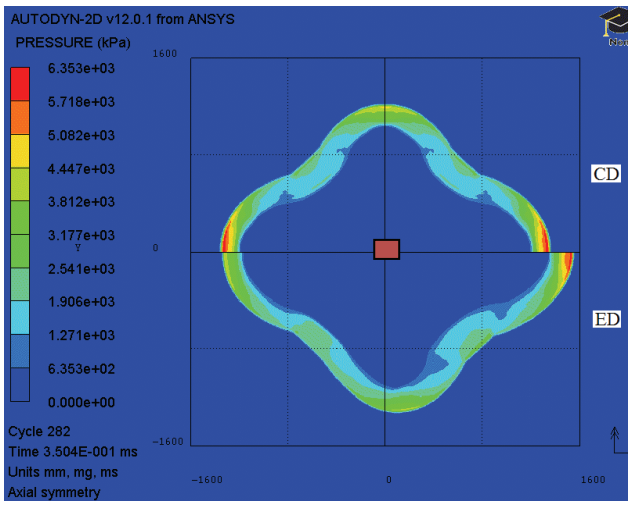

a) 6 charge diameters ($Z = 0.64$ m/kg$^{0.33}$)

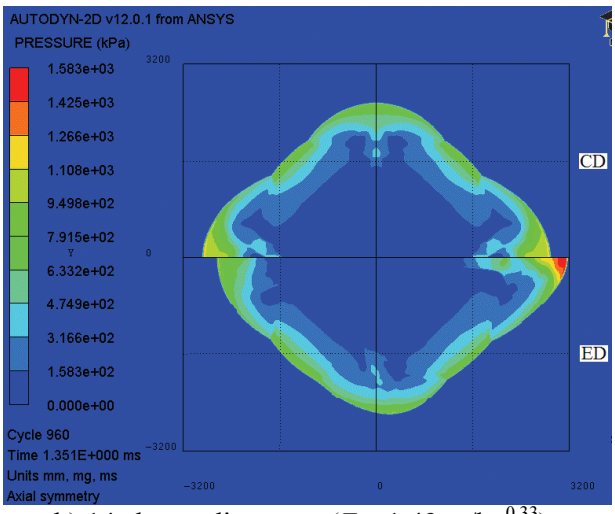

b) 14 charge diameters ($Z = 1.49$ m/kg$^{0.33}$)

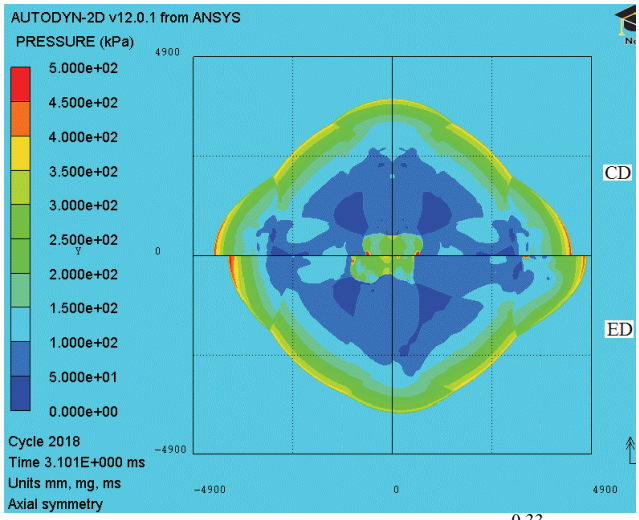

c) 21 charge diameters ($Z = 2.23$ m/kg$^{0.33}$)

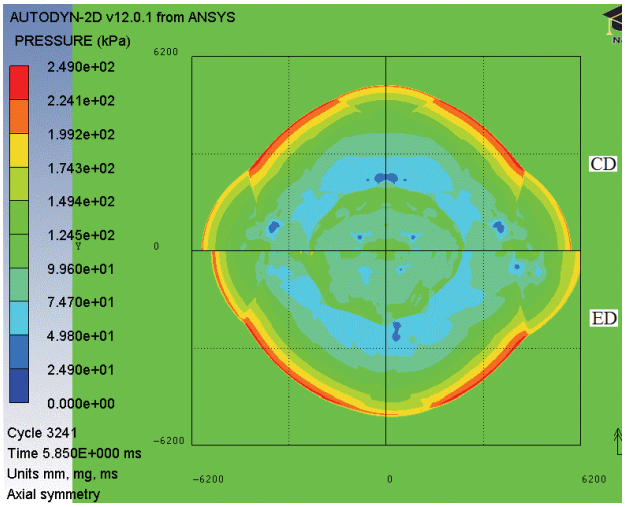

d) 27 charge diameters ($Z = 2.87$ m/kg$^{0.33}$)

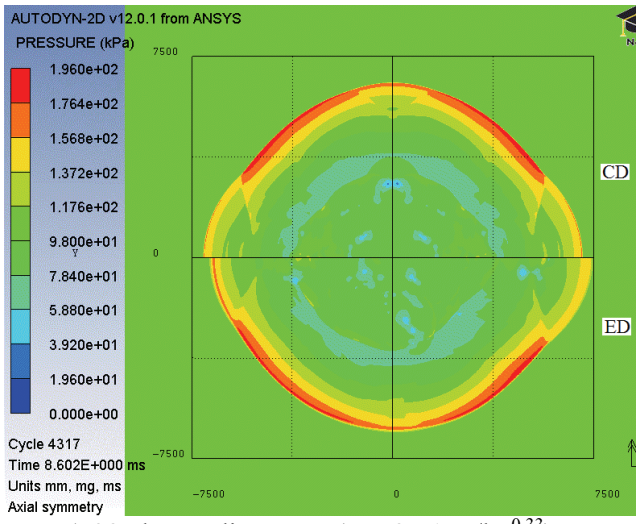

e) 33 charge diameters ($Z = 3.51$ m/kg$^{0.33}$)

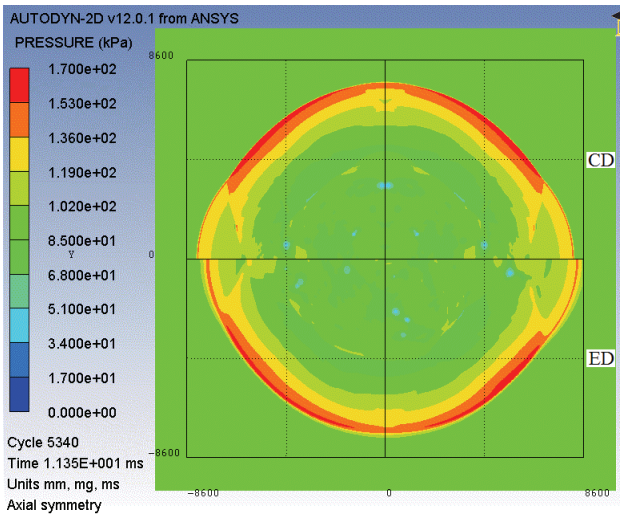

f) 38 charge diameters ($Z = 4.04$ m/kg$^{0.33}$)

Figure 4-33: Pressure contours for the *Cyl_I*$_{CD}$ and *Cyl_I*$_{ED}$ charges

2.0 m/kg$^{0.33}$, the peak axial overpressures are higher in the direction of propagation of the detonation (+x) for the end-detonated charge.

For the centrally detonated charge, the peak overpressures in the axial (radial) direction are greater than those in the radial (axial) direction for values of scaled range less (greater) than approximately 2.5 m/kg$^{0.33}$. In panel d of the figure, where the range is $(\pm 6200, \pm 6200)$ mm, or ± 27 charge diameters, the shapes of the two shock fronts and the magnitude of the peak pressures are virtually identical for the centrally detonated and end-detonated charges. However, the peak overpressure (total pressure minus ambient [101 kPa]) in panel d is less than 3% of the peak overpressure in panel a.

Contour plots for *Cyl_III* and *Cyl_V* are presented in Figures 4-34 and 4-35, respectively. The increase in aspect ratio of the centrally detonated charge produces an increase in the peak pressure in the radial direction for a given scaled distance and changes the shape of the pressure field. At scaled distances of greater than 3.0 m/kg$^{0.33}$, the increase in aspect ratio changes the shape of the pressure field from circular ($L / D = 1$; see Figure 4-33e) to oval with a major axis in the radial direction ($L / D = 5$; see Figure 4-35e). For large values of aspect ratio (e.g., $L / D = 5$) and small values of scaled distance (say $Z \leq 2.0$ m/kg$^{0.33}$), the overpressures in the radial direction are significantly greater than those in the axial direction, regardless of where the charge was detonated.

The overpressure histories at 30 and 40 charge diameters for the cylindrical and spherical charges in the +x (direction of detonation) and -x directions are presented in Figures 4-36 through 4-39, respectively. Similar to the centrally detonated charges, the effects of the secondary shocks become significant at these scaled distances. At 30 charge diameters, both the primary and secondary shocks are clearly seen. At 40 charge diameters, the secondary shocks have caught and reinforced the primary shocks.

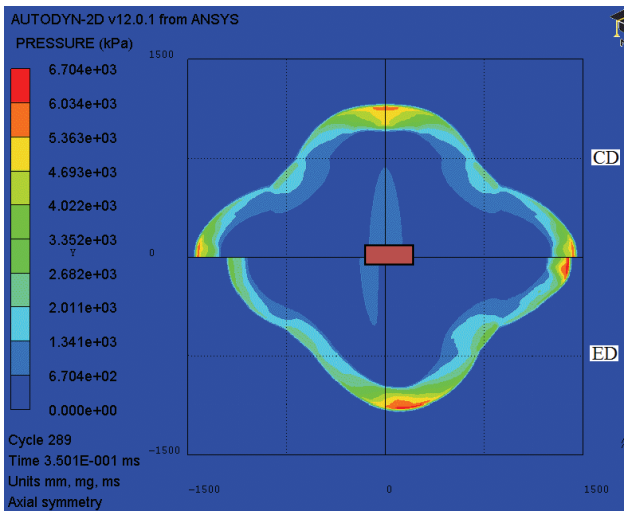

a) 6 charge diameters ($Z = 0.64$ m/kg$^{0.33}$)

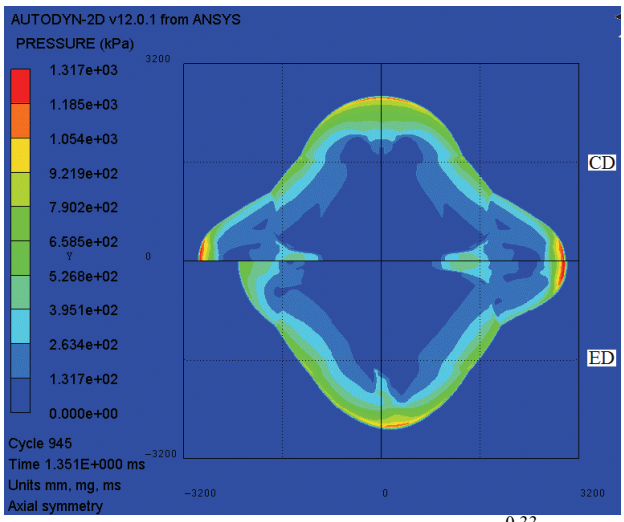

b) 14 charge diameters ($Z = 1.49$ m/kg$^{0.33}$)

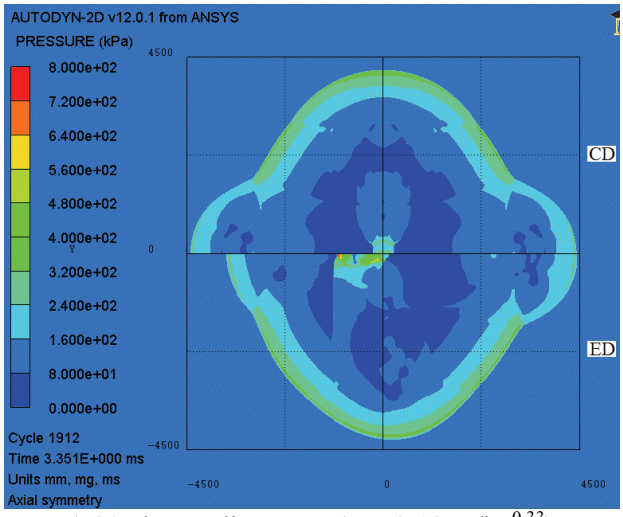

c) 20 charge diameters ($Z = 2.13$ m/kg$^{0.33}$)

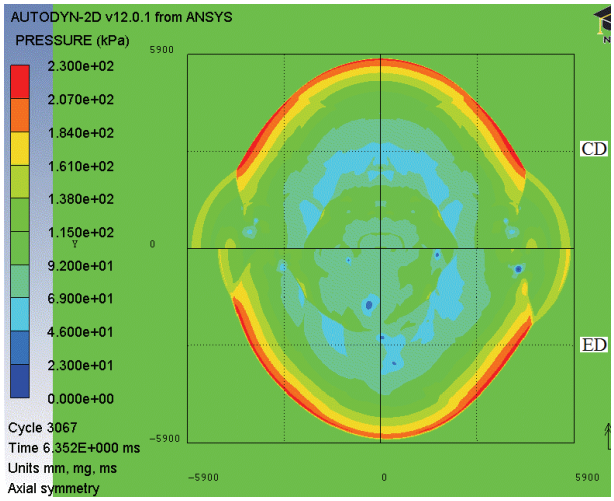

d) 26 charge diameters ($Z = 2.76$ m/kg$^{0.33}$)

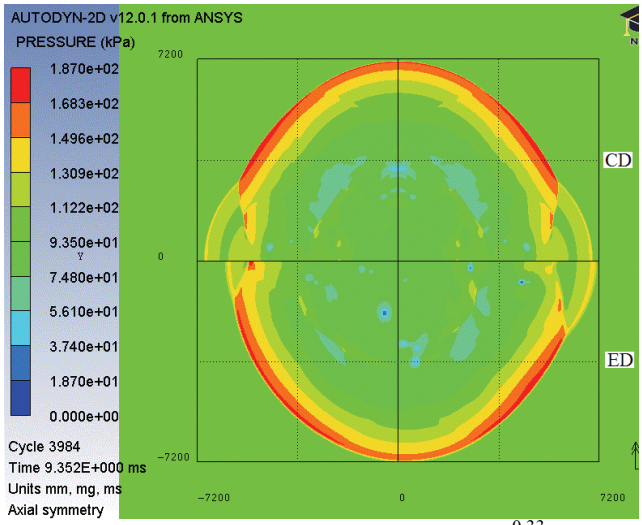

e) 32 charge diameters ($Z = 3.40$ m/kg$^{0.33}$)

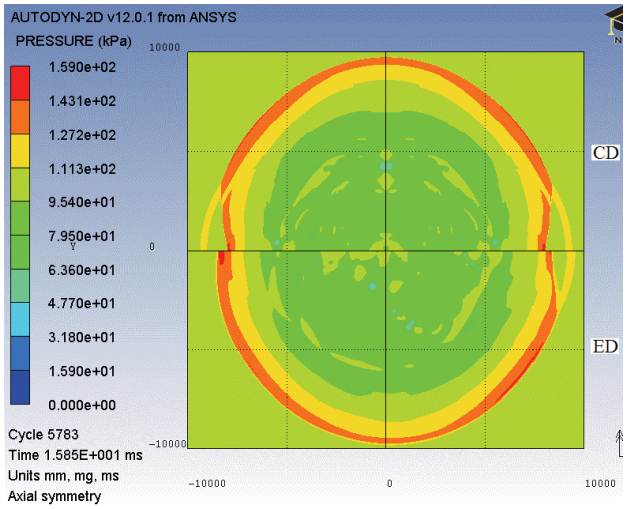

f) 41 charge diameters ($Z = 4.36$ m/kg$^{0.33}$)

Figure 4-34: Pressure contours for the *Cyl_III*$_{CD}$ and *Cyl_III*$_{ED}$ charges

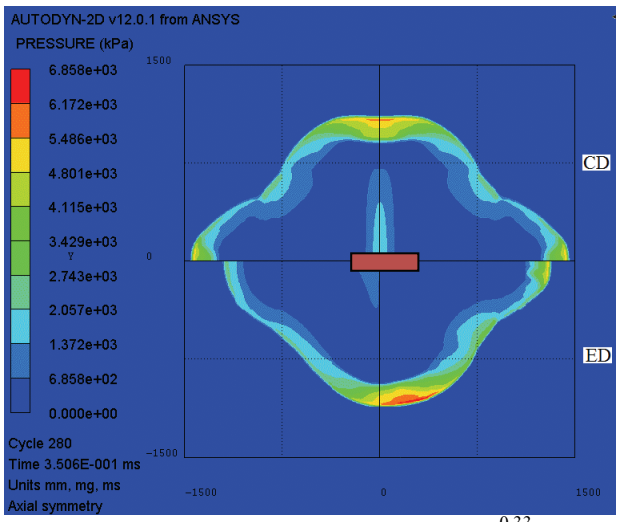

a) 6 charge diameters ($Z = 0.64$ m/kg$^{0.33}$)

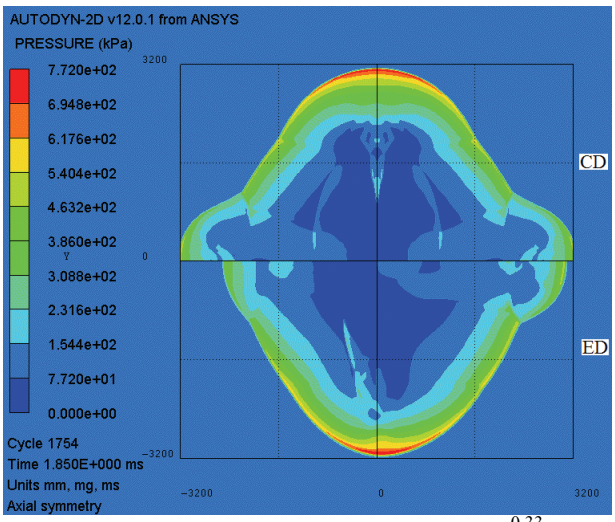

b) 14 charge diameters ($Z = 1.49$ m/kg$^{0.33}$)

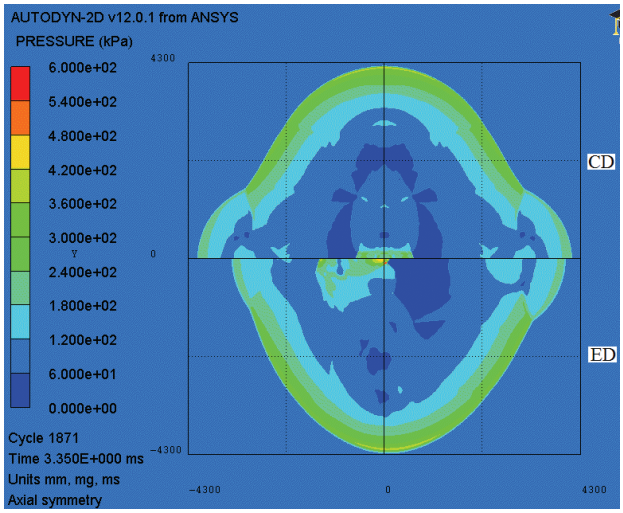

c) 20 charge diameters ($Z = 2.13$ m/kg$^{0.33}$)

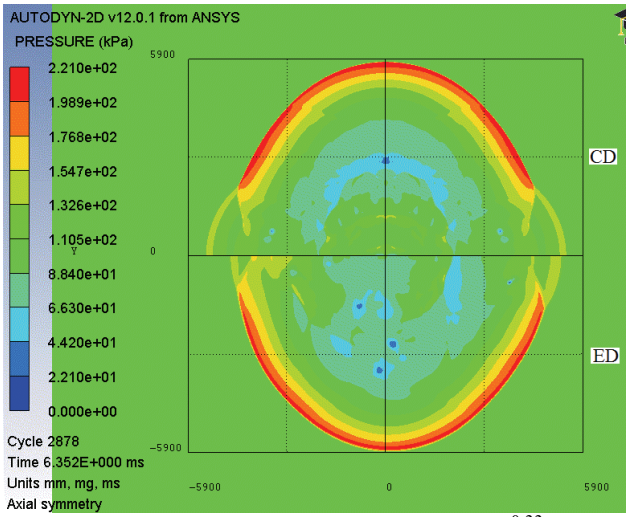

d) 26 charge diameters ($Z = 2.76$ m/kg$^{0.33}$)

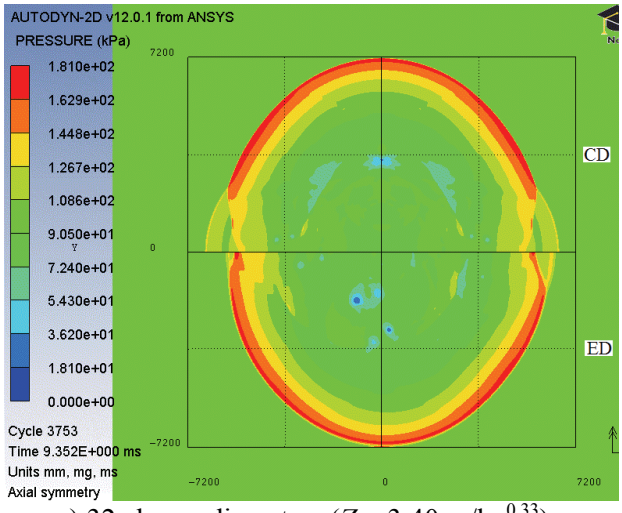

e) 32 charge diameters ($Z = 3.40$ m/kg$^{0.33}$)

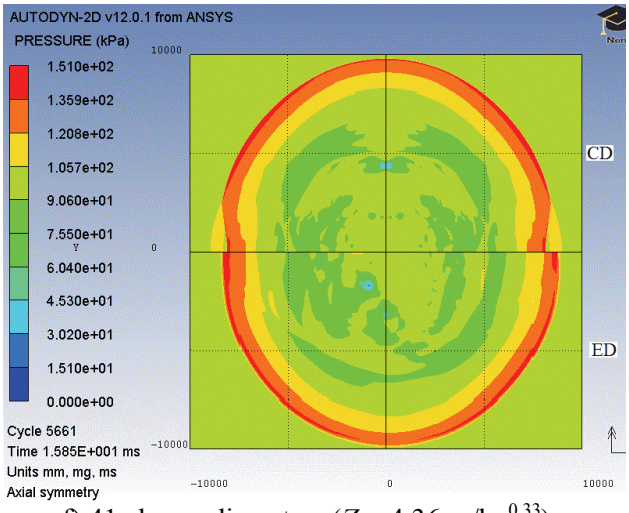

f) 41 charge diameters ($Z = 4.36$ m/kg$^{0.33}$)

Figure 4-35: Pressure contours for the *Cyl_V*$_{CD}$ and *Cyl_V*$_{ED}$ charges

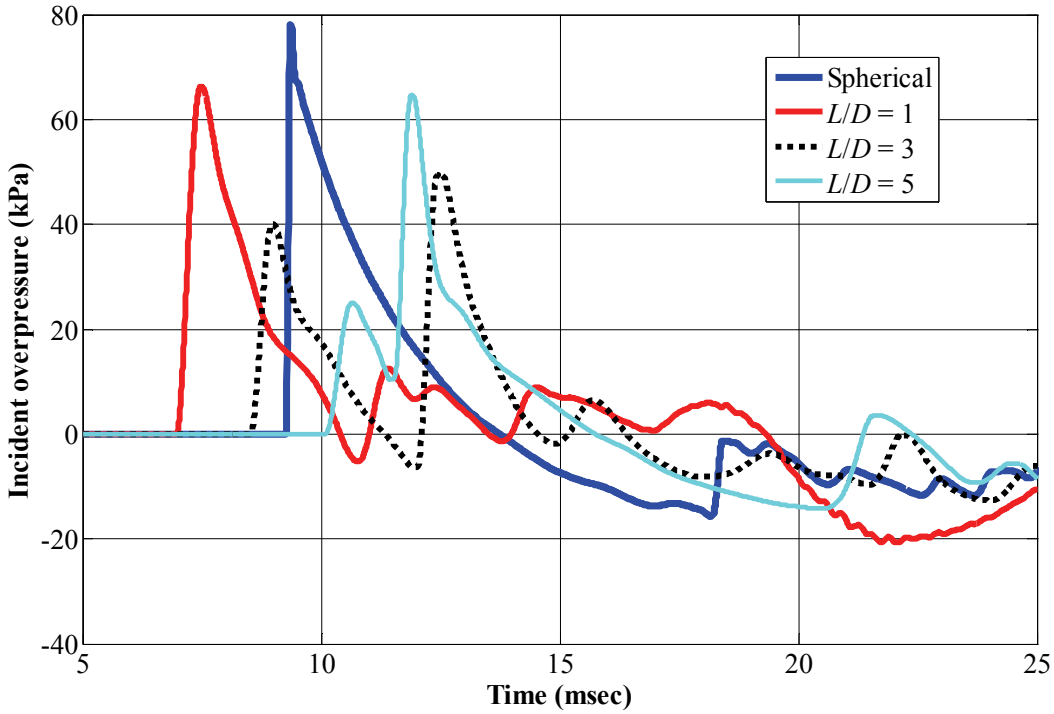

Figure 4-36: Overpressure history in the +*x* direction at a normalized distance of 30 charge diameters

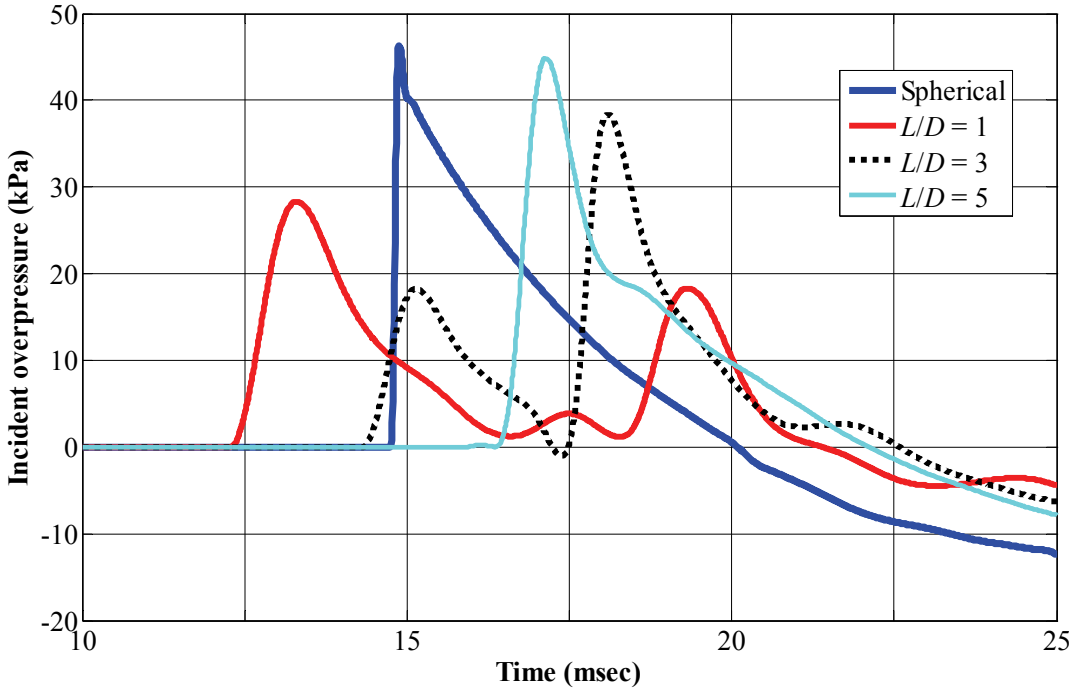

Figure 4-37: Overpressure history in the +*x* direction at a normalized distance of 40 charge diameters

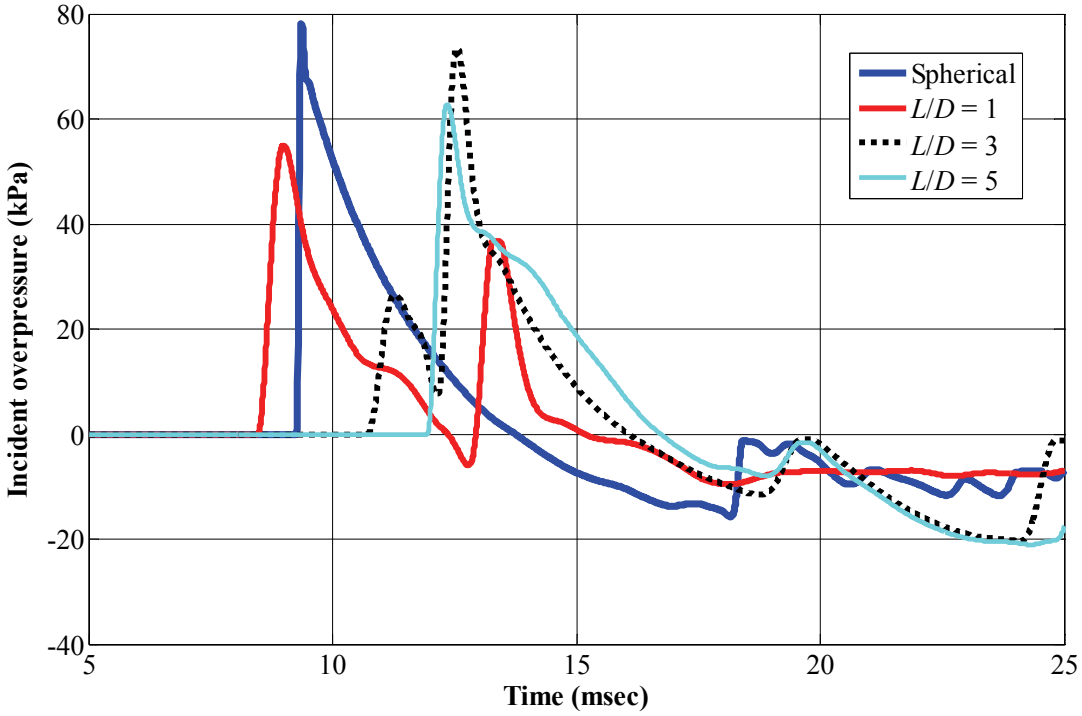

Figure 4-38: Overpressure history in the -*x* direction at a normalized distance of 30 charge diameters

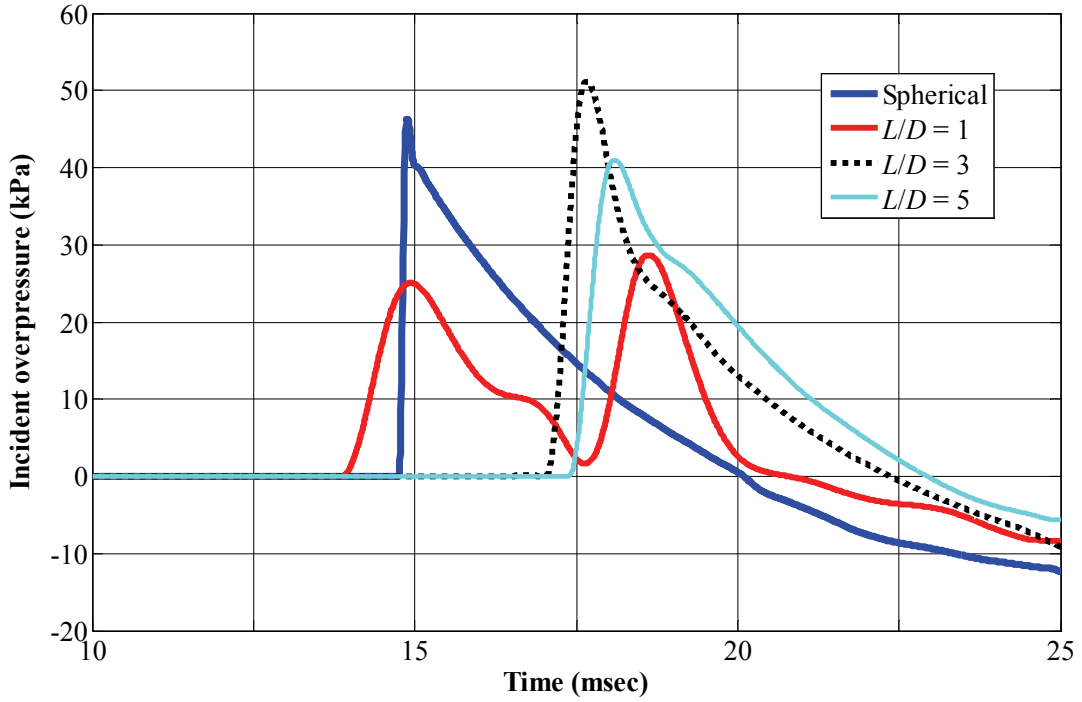

Figure 4-39: Overpressure history in the -*x* direction at a normalized distance of 40 charge diameters

The definition of positive phase presented in section 4.2.3 cannot be used for calculating the positive phase impulse for the end-detonated charges because it is not possible to separate the primary and secondary shocks at some normalized distances. Instead, the total impulse is presented in the axial (+x,-x) and radial directions in Figures 4-40 through 4-42, respectively. From these figures, it can be seen that the total impulses from the cylindrical charges drop to values equal to or less than 110% of that of the spherical charge within 29 ($Z \leq 3.05$ m/kg$^{0.33}$), 22 ($Z \leq 2.39$ m/kg$^{0.33}$) and 18 ($Z \leq 1.89$ m/kg$^{0.33}$) charge diameters in the +x, -x and radial directions, respectively.

In summary, the shape of the pressure field and the magnitudes of the peak overpressures and impulses are influenced by the point of detonation within the explosive for scaled distances, $Z \leq 3$ m/kg$^{0.33}$. For larger values of the scaled distance, the point of detonation becomes less important.

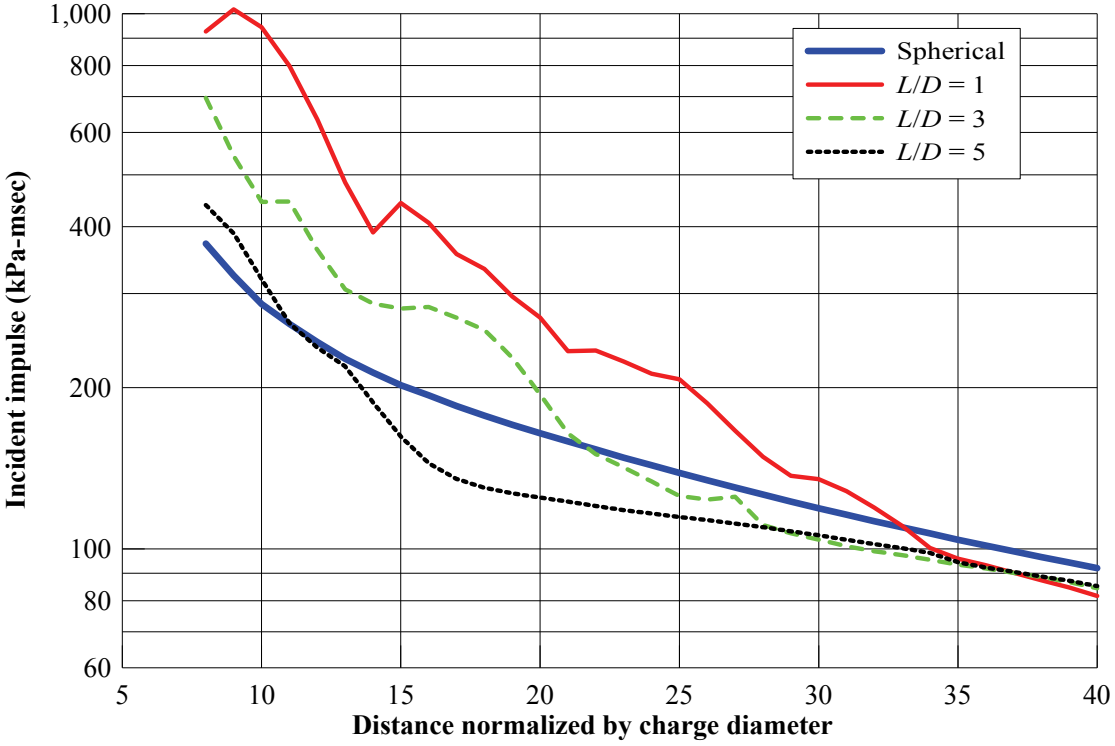

Figure 4-40: Incident impulse as a function of normalized distance in the +x direction

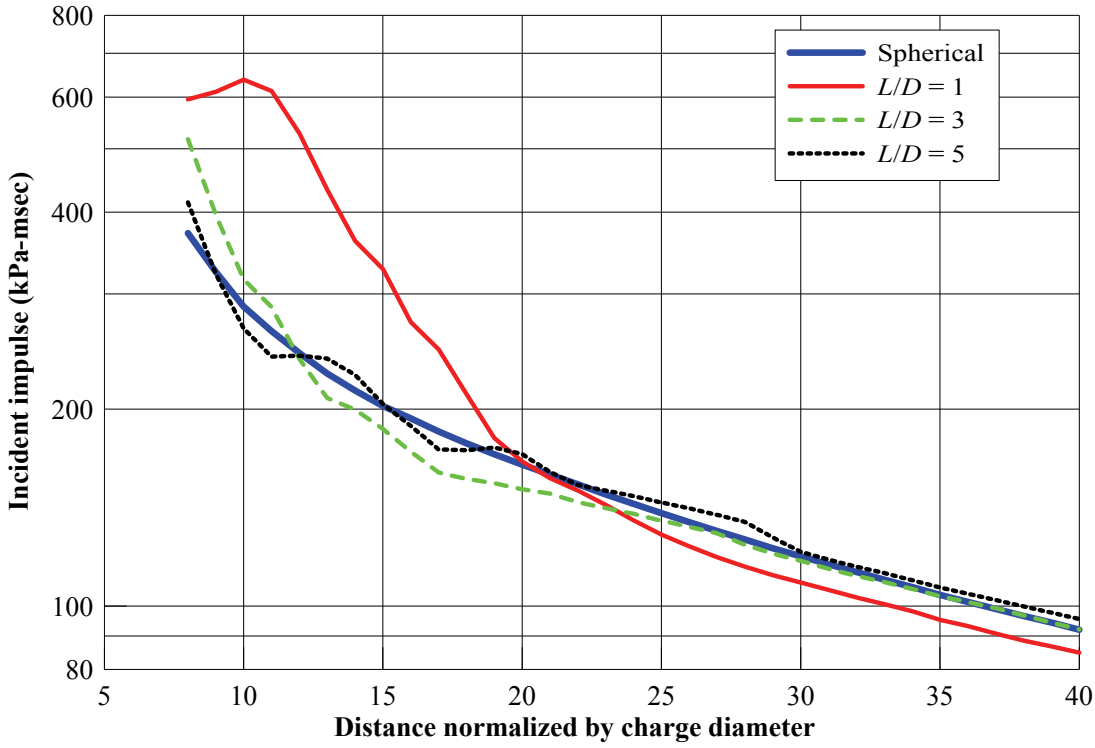

Figure 4-41: Incident impulse as a function of normalized distance in the *-x* direction

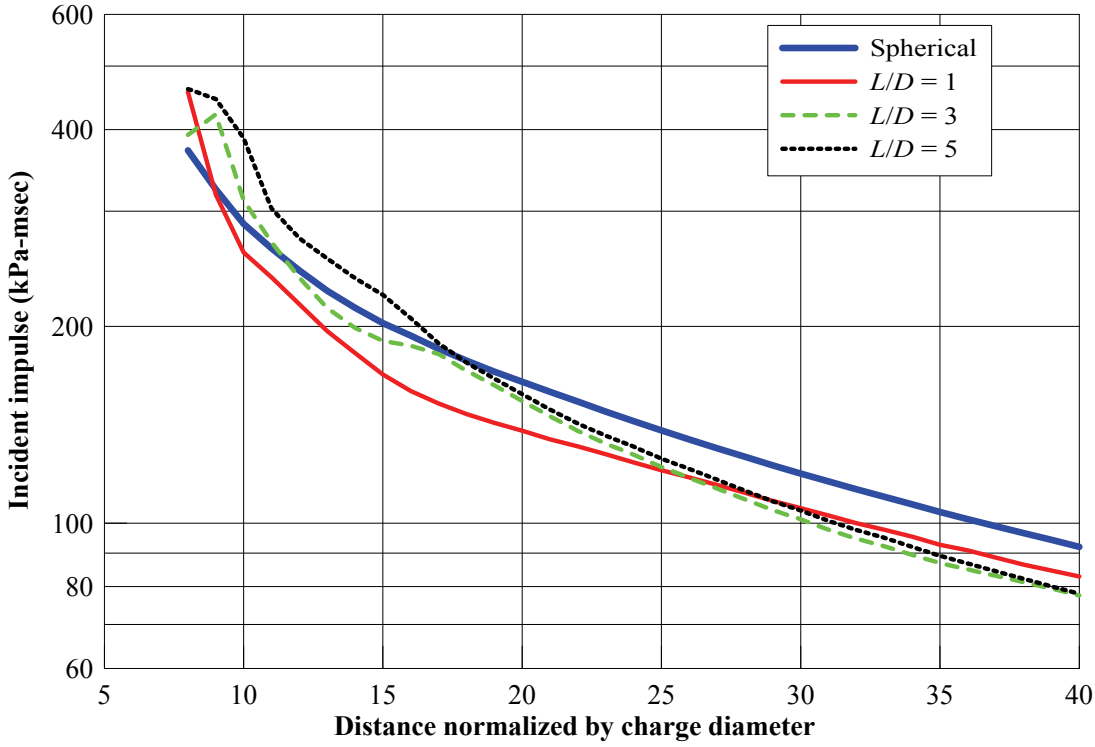

Figure 4-42: Incident impulse as a function of normalized distance in the radial direction

4.4 Influence of Charge Shape on Structural Response

4.4.1 Sample problem and numerical models

The analyses reported in section 4.2 showed that the charge shape significantly influences the peak incident overpressures and impulses, especially in the near field. Significant secondary and tertiary shocks were observed in overpressure histories from the cylindrical charges in the axial direction. For small values of scaled distance ($Z \leq 1$ m/kg$^{0.33}$), the impulse added due to the secondary shocks was as great as that due to the primary shock for some charge aspect ratios.

The influence of charge shape need not be considered in design unless variations in charge shape (for a given mass) affect substantially the response of structural components. To study the effect of charge shape on structural response, numerical simulations on a sample structural steel column were performed using AUTODYN. Although not conclusive, these analyses can inform decisions on modeling, analysis and design of structural components to resist air-blast loadings.

A baseline analysis was performed first using a spherical charge. The blast loading was generated by a detonation of 1000 kg of TNT in front of an A992 Grade 50 (350 MPa) W14$\times$257 steel column at a standoff distance of 3 m to the column flange ($Z \leq 0.3$ m/kg$^{0.33}$). The numerical analysis was performed in two steps: 1) 1D analysis that involved detonation of the explosive and the consequent wave propagation until the blast wave reached the column; and 2) 3D analysis after the results of the 1D analysis were remapped into a 3D numerical model that consisted of the air and the W14$\times$257 steel column. The response of the column is reported using reaction histories and fringe plots of deformation and effective plastic strain.

The 1D analysis of the sample problem was described in section 3.11.1. The results of this analysis were remapped into a 3D numerical model. The 3D model in AUTODYN consisted of an air domain with dimensions of 4m$\times$3m$\times$6m . The air was modeled with 750,000 elements with an element size of 40 mm and an aspect ratio 1. The steel column was modeled with 30,000 elements such that there were two

elements through the thickness of the flanges and across width of the web. The meshes for the air and the column, and the location of the explosive are presented in Figure 4-43. The coordinate system is shown in panel a of the figure. The column was 5 m long and was loaded about its strong axis. A fixed boundary condition was applied at both ends of the column by restraining the translational and rotational velocities of all boundary nodes. All boundaries of the air domain except the $x = 0$ plane were set to transmit to prevent reflection of the blast wave back into the domain. The $x = 0$ plane was a plane of symmetry and no boundary conditions were imposed on this plane. AUTODYN sets all the boundaries of an Euler domain to reflect by default. Air is modeled as an ideal gas with a constant specific heat ratio, γ, equal to 1.4, and was initialized at an atmospheric pressure of 101.3 kPa (1 atm).

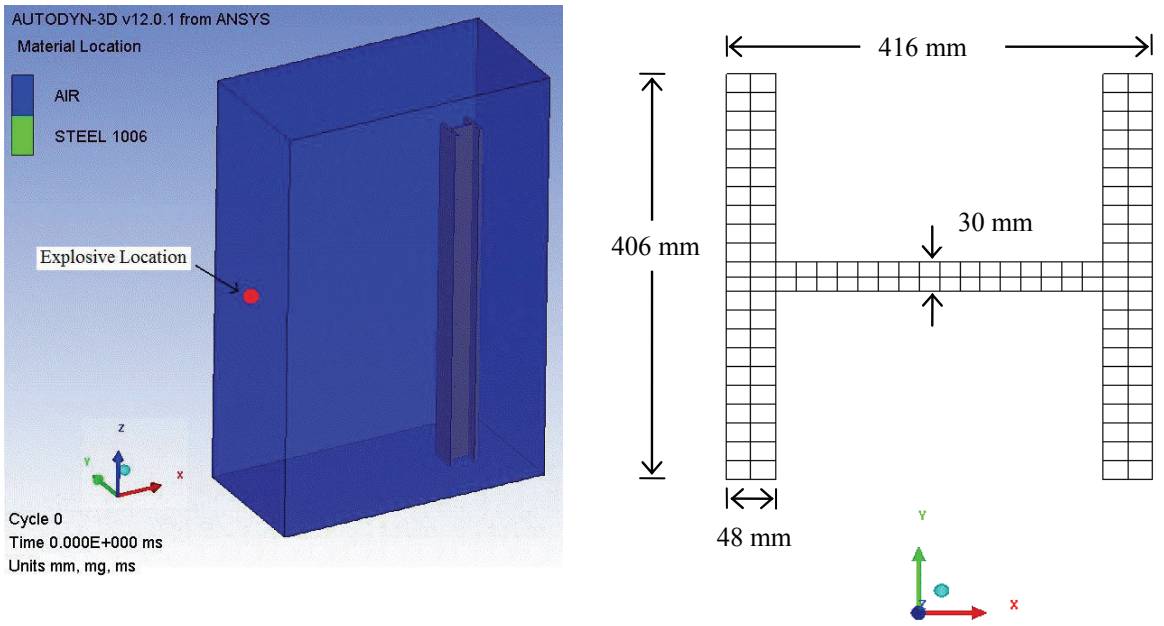

a) Air and column meshes b) Finite element mesh of the W14×257 column

Figure 4-43: AUTODYN numerical models of the sample problem

The yield stress of steel increases with strain rate. One of the most widely used constitutive material models for metals is the Johnson-Cook (1983) model. The Johnson-Cook (J-C) model is reproduced in equation 4-1a. The values of the constants and parameters of the material model for various metals are provided by Johnson and Cook (1983) and Meyers (1994).

$$\sigma = (A + B\,\varepsilon^{n})\,(1 + C\,\ln\frac{\dot{\varepsilon}}{\dot{\varepsilon}_o})\,(1 - [T^*]^m) \tag{4-1a}$$

$$T^* = \frac{T - T_r}{T_m - T_r} \tag{4-1b}$$

where

A = Minimum yield stress

n = Hardening coefficient

m = Thermal softening exponent

$\dot{\varepsilon}_o$ = Reference strain rate

T^* = Normalized temperature

T_m, T_r = Melting temperature and reference temperature, respectively

B, C = Material constants that are determined by experiments

The values of the parameters for the J-C model are not available for ASTM A992 (Grade 50) structural steel that is used for rolled steel shapes in the United States. Instead, the values of the parameters for AISI 1006 carbon steel that are listed in Table 4-2 (Meyers, 1994) were used. Figure 4-44 presents the quasi-static stress-strain relationship for A992 Grade 50 steel and the quasi-static stress-strain relationship used for numerical studies.

The two stress-strain curves are similar to an axial strain of 0.1. The stress-strain relationship for the ASTM A992 Grade 50 steel is a lower bound on strength because nominal and not expected values are presented. A reasonable increase in yield strength from the nominal to expected value is 10% (AISC, 2006). Based on this information, it is reasonable to assume that the values of the parameters of the J-C model used for AISI 1006 steel can be applied to ASTM 992 steel without a significant loss in accuracy.

Table 4-2: Values of parameters in the J-C model for AISI 1006 steel (Johnson and Cook, 1983)

Parameter	Value
A (MPa)	350
n	0.36
m	1
$\dot{\varepsilon}_o$ (/sec)	1
T_m (^{o}K)	1811
T_r (^{o}K)	300
B (MPa)	275
C	0.022

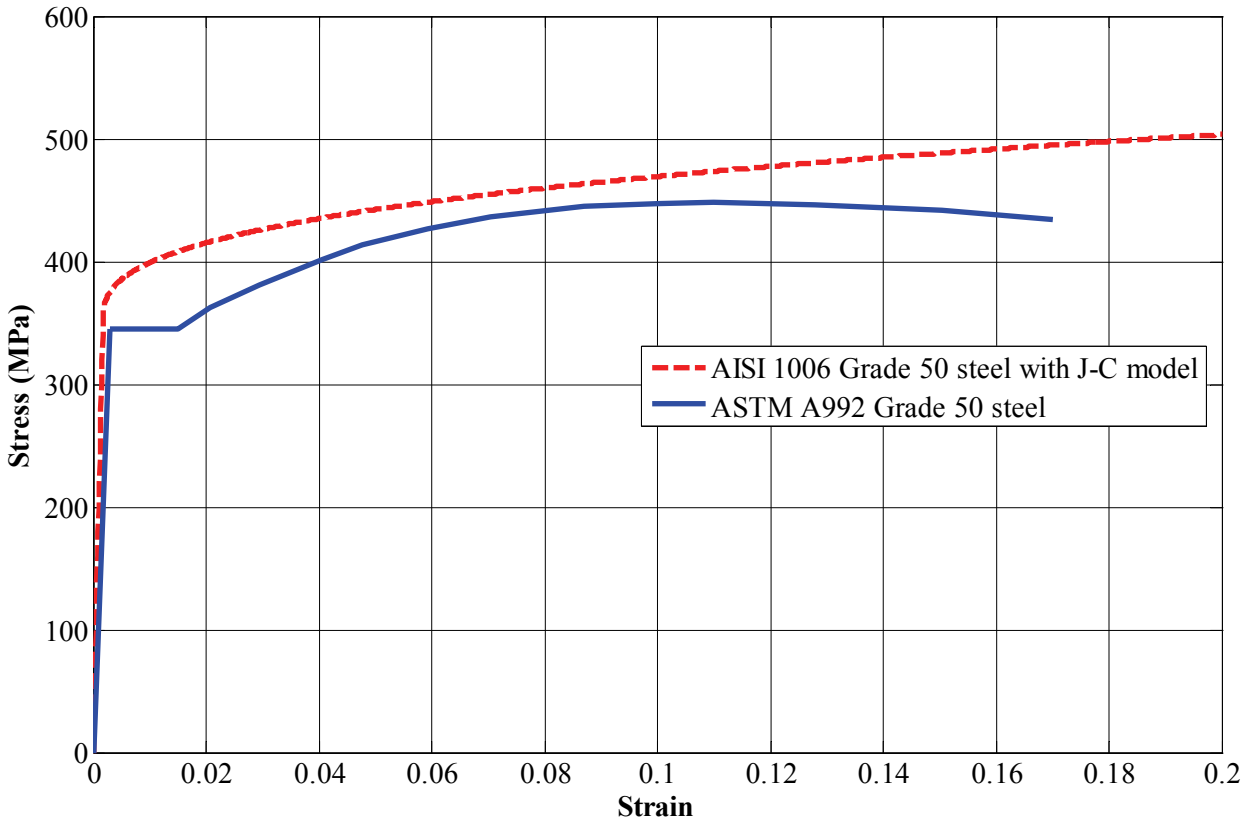

Figure 4-44: Stress-strain relationships for AISI 1006 and ASTM A992 steels

The reaction histories at only one boundary were monitored because the loading on the column was symmetric. Gauges were placed at the mid-height, the quarter height and near the top boundary to monitor the reflected overpressures and temperatures a few millimeters from the surface of the column as shown in Figure 4-45a. Five gauges were placed through the depth of the column at its mid-height, at the locations shown in Figure 4-45b, to monitor the change in temperature of the steel column.

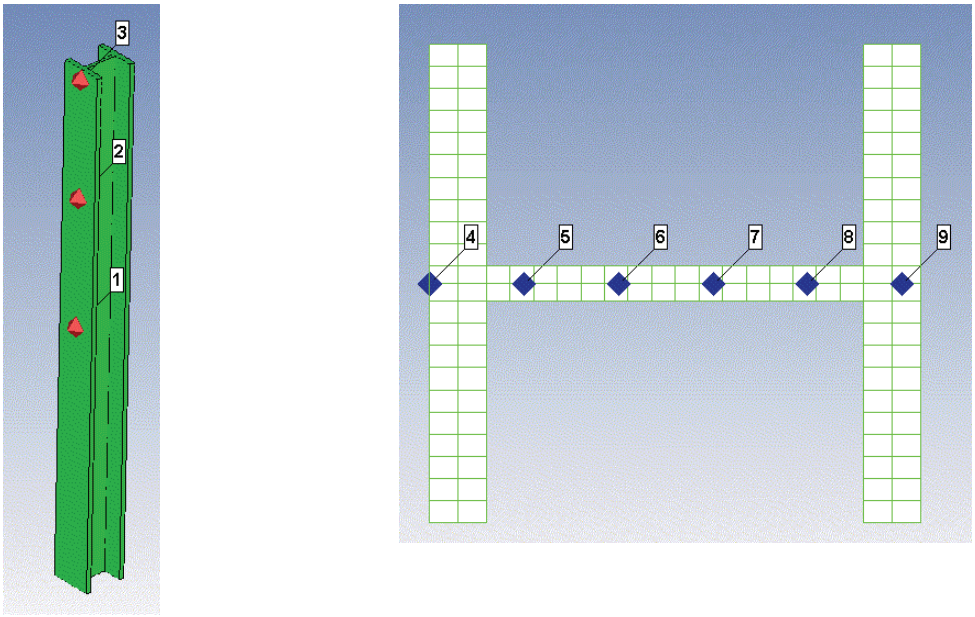

a) Gauges near the surface of the column b) Gauges through the depth of the column at mid-height

Figure 4-45: Locations of the monitoring gauges

4.4.2 Results and discussion of the baseline analysis using a spherical charge

The overpressure and temperature histories at the surface of the column at the mid-height, quarter height and near the top boundary are presented in Figures 4-46, 4-47, and 4-48, respectively. It is clear from these figures that the temperature is very high on the surface of the column at the three locations. However, the increase in temperature at gauge no. 4, which is just below the surface of the column at its mid-height (see Figure 4-45b) is negligible (= 0.2%). There is no discernible increase in temperature at the other gauges through the depth of the cross-section: 5, 6, 7, 8 and 9. These results are attributed to the very short duration of the thermal loading on the column. Accordingly, the effect of temperature rise on

the yield stress of the steel in this column, and thus the response of the column, can be assumed to be zero.

Figure 4-49 presents the (total) pressure contour plots in a plane at the mid-height of the column as the shock front propagates across and around the column. In panel a of the figure, the shock front has yet to reach the column. Although the pressures at the shock front (10 MPa) are much lower than those near the origin of the explosive (approximately 40MPa), the pressures near the origin are orders of magnitude smaller than those at the instant of detonation (of the order of 18 GPa; see section 3.11.4). In panel b, the shock front is being reflected from the front flange of the column. The shock front propagates along the depth of the section in panels c and d; the reflected overpressures are much greater than the incident (side-on) overpressures. The peak reflected overpressure is greater at the center of the column flange than at the edge of the outstand.

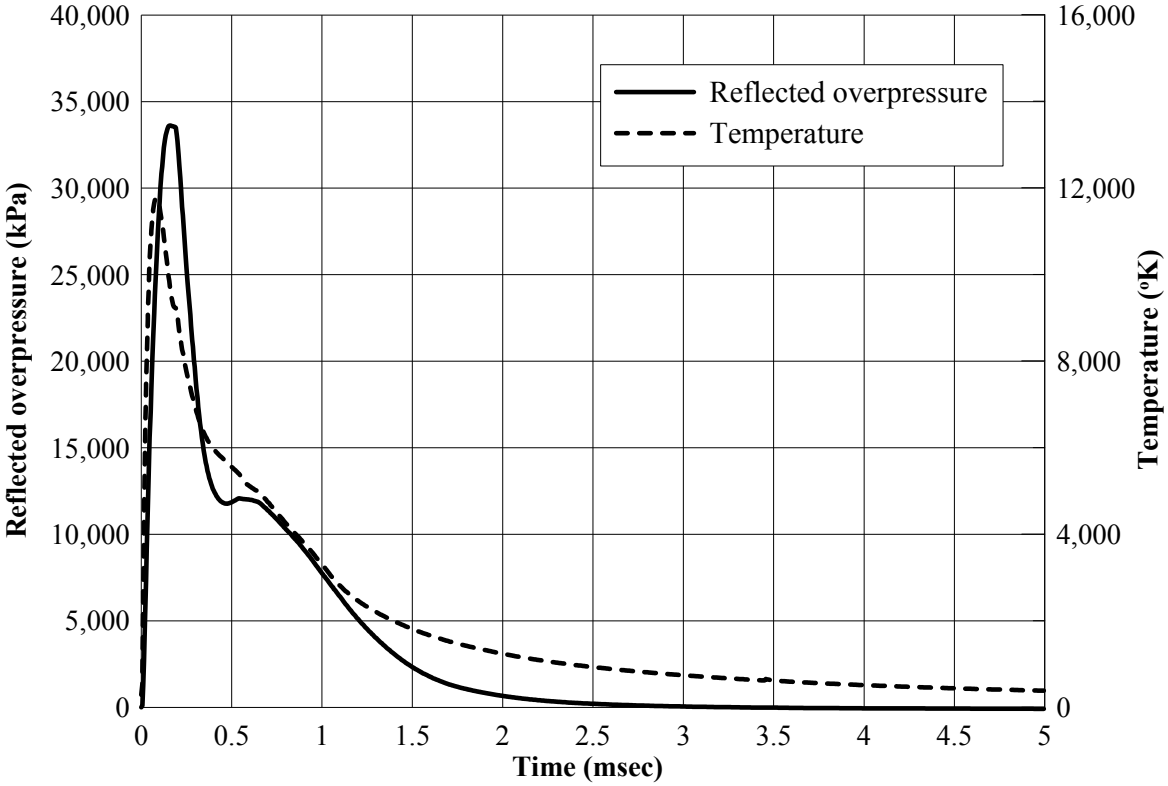

Figure 4-46: Reflected overpressure and temperature histories at the mid-height of the column on its front face

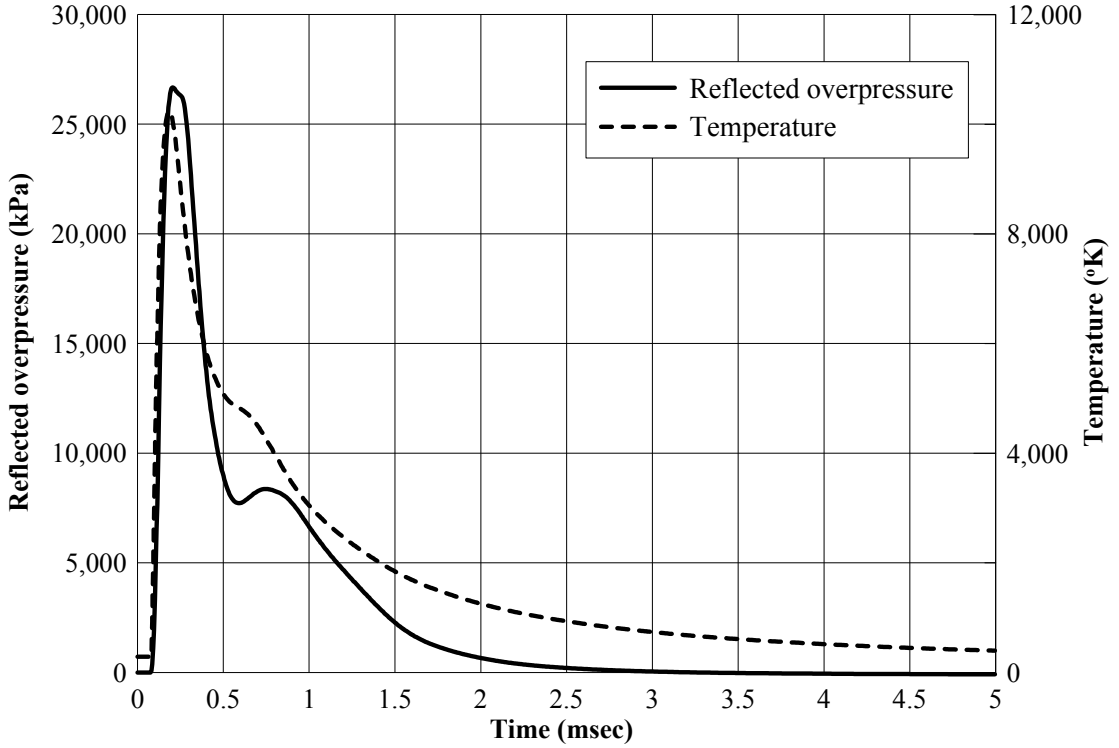

Figure 4-47: Reflected overpressure and temperature histories at the quarter height of the column on its front face

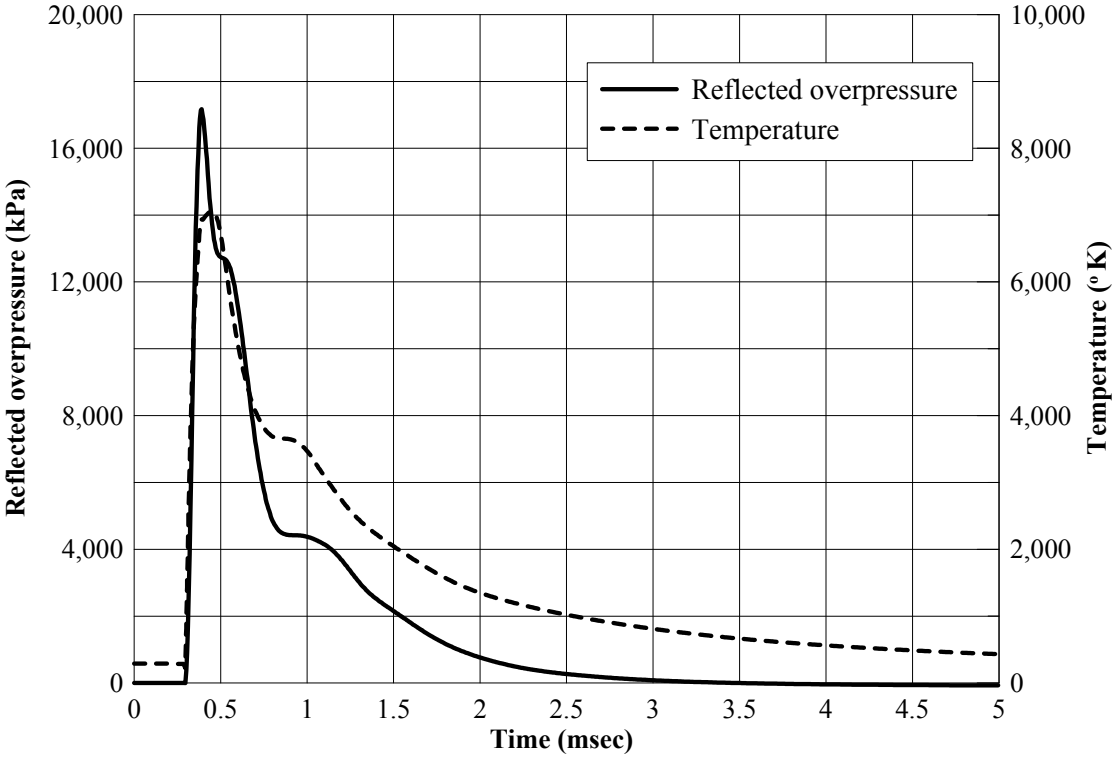

Figure 4-48: Reflected overpressure and temperature histories near the top boundary of the column on its front face

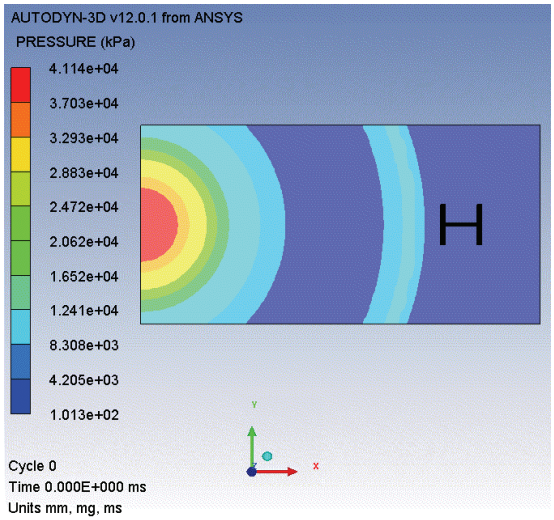

a) $t = 0$ msec

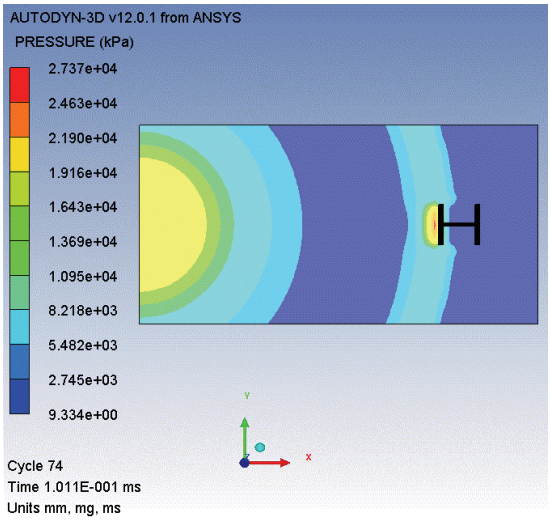

b) $t = 0.1$ msec

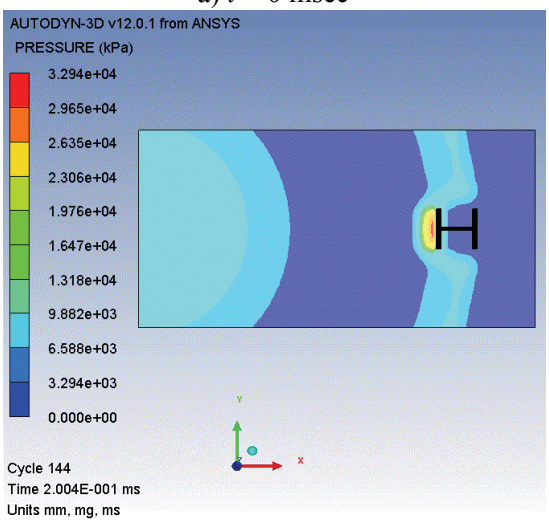

c) $t = 0.2$ msec

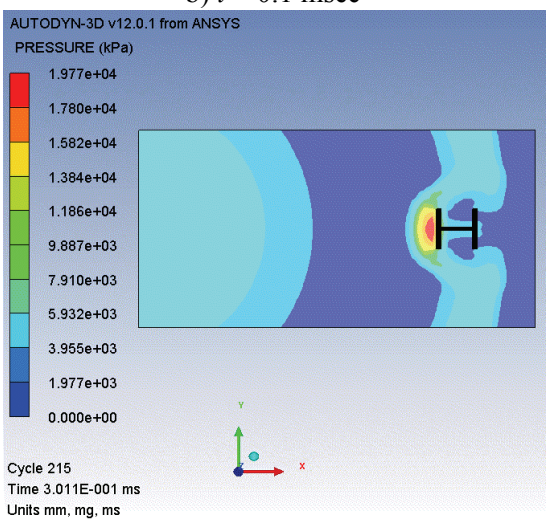

d) $t = 0.3$ msec

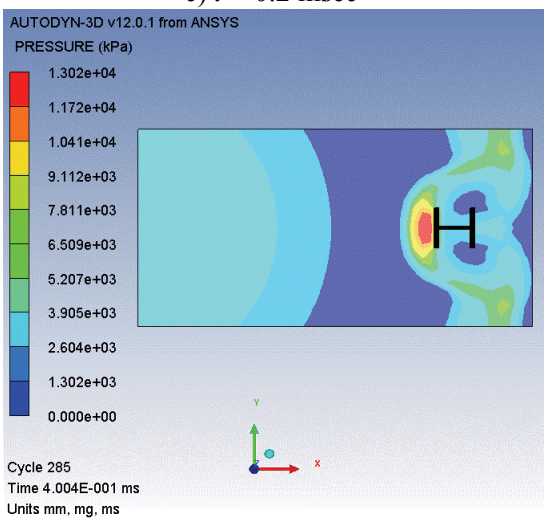

e) $t = 0.4$ msec

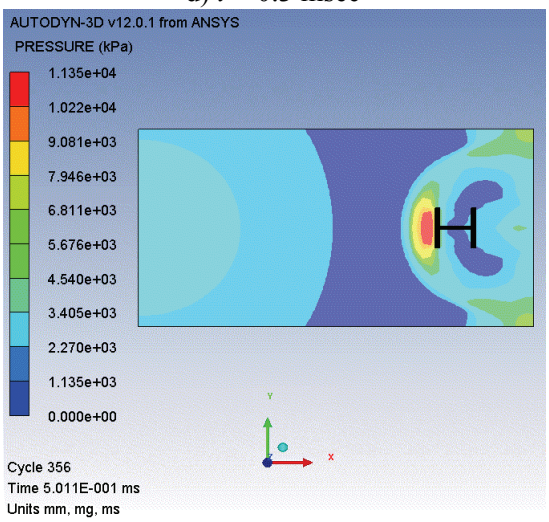

f) $t = 0.5$ msec

Figure 4-49: Fringe plots of pressure on a horizontal plane at the mid-height of the column

The shear force history at the boundary and the displacement history at the mid-height of the column are presented in Figure 4-50. The maximum displacement at mid-height in the web is 33.9 mm and occurs at a time of 4.6 msec (after the loading phase; see Figures 4-46, 4-47 and 4-48). The maximum reaction (shear force) is 3.04 MN and is recorded at t = 4.9 msec. The peak displacement and peak shear force reaction occur at similar times. It is evident from the figure that there is permanent deformation in the column (= 13 mm at mid-height). The fringe plot of effective plastic strain in the column at the time of peak displacement (which is approximately equal to the time of peak shear force) at the column mid-height is presented in Figure 4-51. The peak effective plastic strain (an indicator of damage) is 0.021 (12 times the yield strain) and is concentrated in the web of column, near the two boundaries. The shear yielding of the web of the column limits the maximum shear force in the column. (For reference, the nominal shear yielding strength of a 350 MPa W14×257 column [depth = 416 mm, web thickness = 30 mm] is 2.62 MN, in the absence of strain hardening and strain-rate enhancement of material strength.)

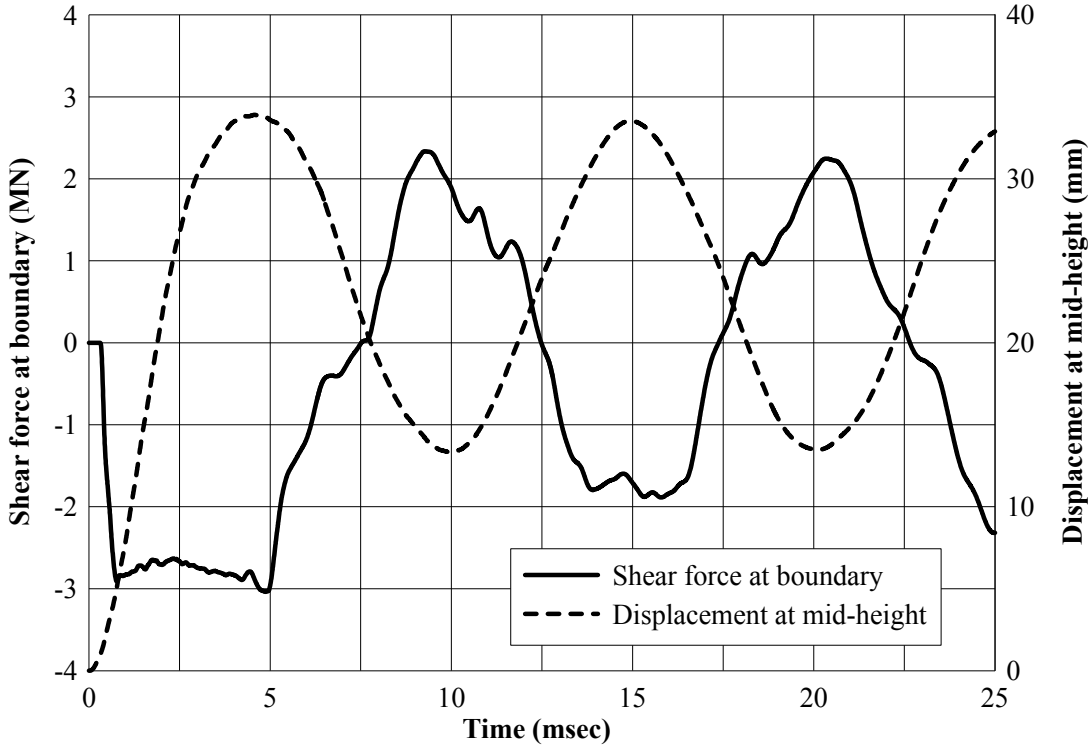

Figure 4-50: Shear force history at the top boundary and displacement history at the mid-height of the column for the spherical charge

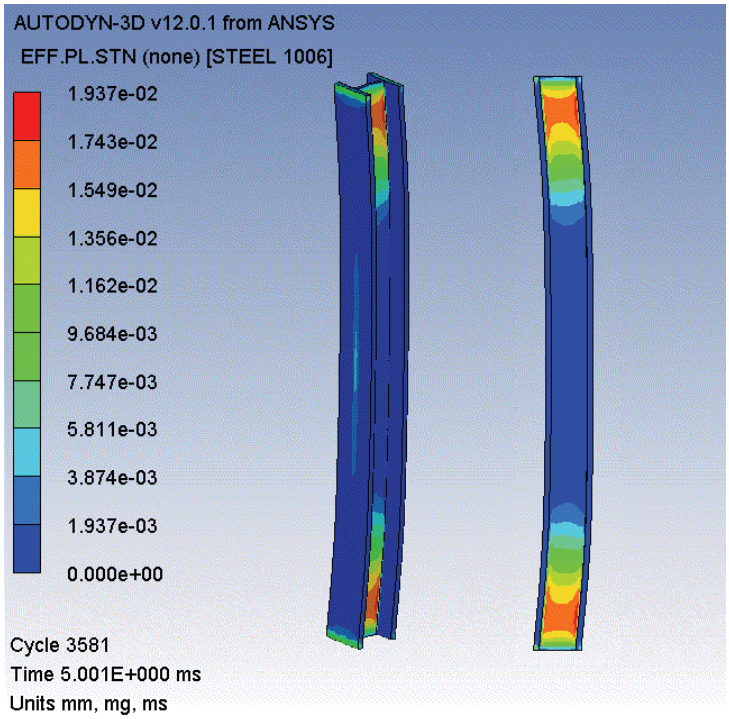

Figure 4-51: Fringe plot of effective plastic strain at peak displacement

To quantify the effects of strain-rate on the response of the column, a companion analysis was performed in which the strain-rate effects were ignored. Temperature effects were also ignored for the reasons given previously. The values of the parameters of Johnson-Cook model were revised accordingly to consider only the effect of strain hardening. The peak displacement increased from 33.9 mm to 34.4 mm, the peak reaction (shear force) increased from 3.04 MN to 3.12 MN, and the peak effective plastic strain increased from 0.021 to 0.023. The response of this column is not affected significantly by strain-rate effects. Nonetheless, strain-rate effects on yield stress were included in all subsequent analyses described below.

4.4.3 Analysis using cylindrical charges

To study the effect of charge shape on the response of the column, the analyses of section 4.4.2 were repeated with cylindrical charges *Cyl_I* and *Cyl_V*. The analyses were performed in two stages: 1) a 2D axially symmetric analysis until the detonation products expanded to 3m, and 2) a 3D analysis with the output of the 2D analysis mapped into a 3D domain that contained the air (initialized at atmospheric pressure) and the column.

Four analyses were performed; two for each charge with the charges oriented horizontally and vertically. The 3D numerical models with the two charge orientations are presented in Figure 4-52. In panel a of the figure, the longitudinal axis of the charge is parallel to the longitudinal axis of the column, whereas in panel b, the longitudinal axis of the charge is perpendicular to the longitudinal axis of the column. The two orientations of the charge are denoted as *A* (vertical) and *B* (horizontal). Analyses were performed for two aspect ratios: 1 and 5. The subscripts *A* and *B* are added to the charge names to identify their orientation.

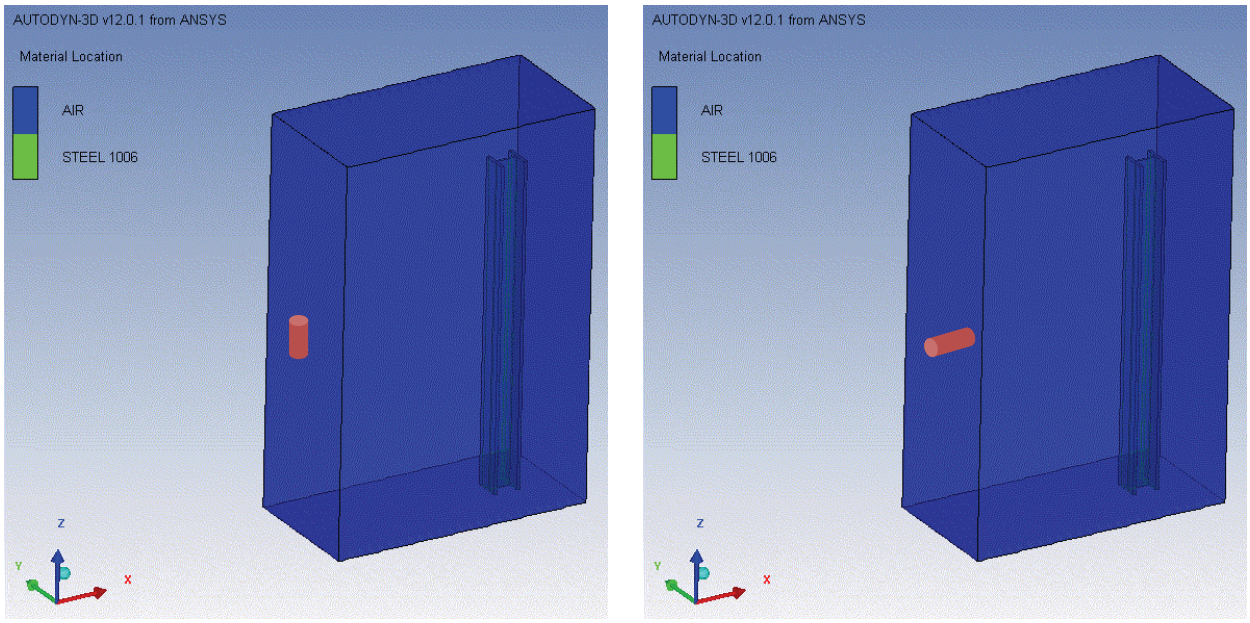

a) Orientation *A* with the charge axis vertical b) Orientation *B* with the charge axis horizontal

Figure 4-52: Two orientations of the cylindrical charges

4.4.4 Results and discussions of analysis using cylindrical charges

Figure 4-53 presents the reflected overpressure histories at points A, B and C (monitoring gauges 1, 2 and 3, respectively in Figure 4-45a) for the vertically oriented charges and the spherical charge. Figure 4-54 presents the reflected overpressure histories at points A, B and C for the horizontally oriented charges and the spherical charge. The reflected overpressure histories vary significantly along the height of the column for each charge (spherical, vertical cylinder×2 , horizontal cylinder×2) in terms of peak values, reflected impulses and arrival times. Table 4-3 presents the peak reflected overpressure and reflected

impulse at points A, B and C. The assumption of uniform loading, which underpins single-degree-of-freedom analysis, is clearly inappropriate for near-field detonations.

The shear force and column mid-height displacement histories for the detonations of the vertically oriented (*A*) charges are presented in Figures 4-55and 4-56, respectively. The responses for the spherical charge are included in each figure to enable a direct comparison with the results of the detonations of the cylindrical charges. The fringe plots of effective plastic strain at the time of peak mid-height displacement (which is approximately the time of peak shear force reaction) are presented in Figure 4-57; two views of the column are shown in the figure.

There is little difference between the peak shear forces resulting from the detonation of the vertically oriented charges and the spherical charge, which is due in significant part to the shear yielding of the column (evident in the fringe plots of Figure 4-57), that limits the magnitude of the shear force.

The displacement histories presented in Figure 4-56 have similar shapes but different amplitudes. Although residual (permanent) displacement of the column is evident for all three charges, the maximum residual displacements is measured for the Cyl_V_A charge, which produced the maximum values of peak shear force and equivalent plastic strain in the web. The maximum transient and residual displacements increase with aspect ratio. This observation is consistent with the results presented in section 4.2.3, which show that the impulse in the radial direction increases with aspect ratio. The fringe plots of effective plastic strain show that the extent of shear yielding in the web of the column also increases with aspect ratio.

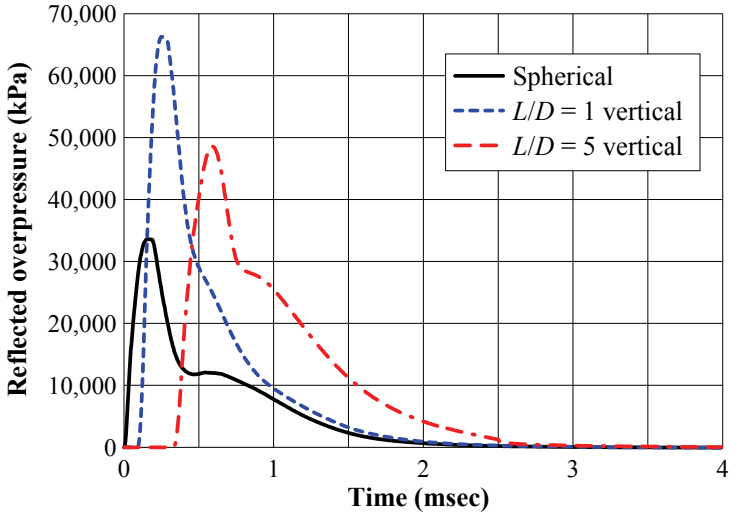

a) point A

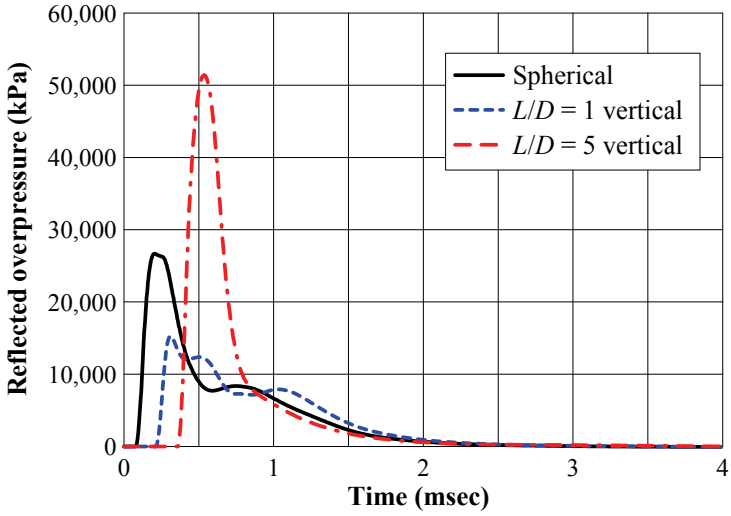

b) point B

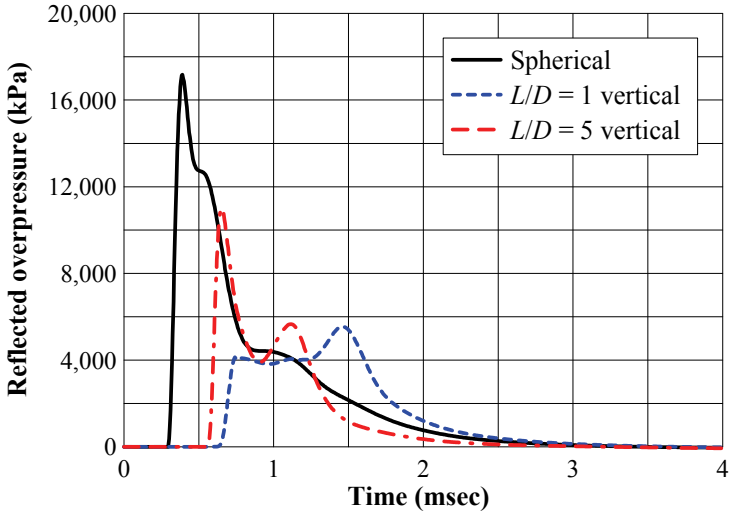

c) point C

Figure 4-53: Reflected overpressure histories for the spherical and vertical (*A*) cylindrical charges

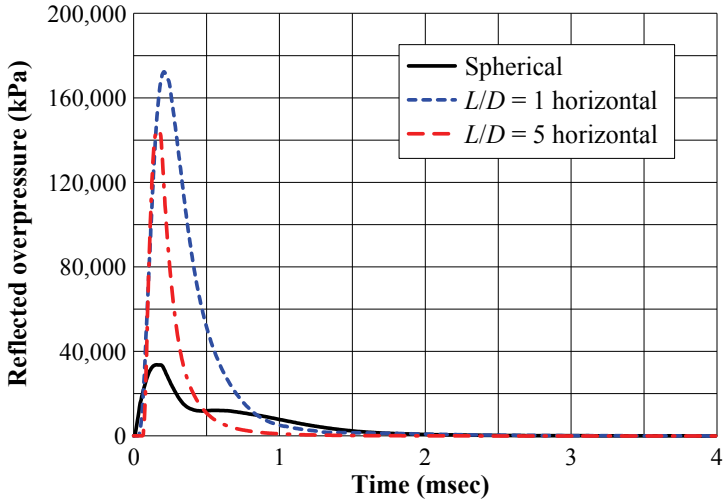

a) point A

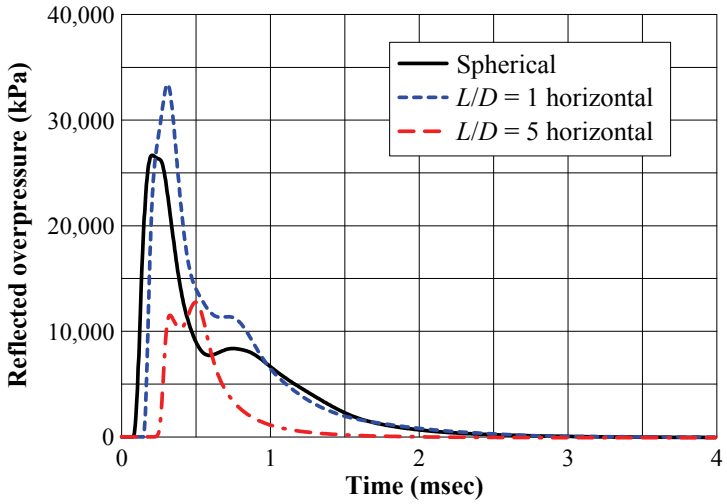

b) point B

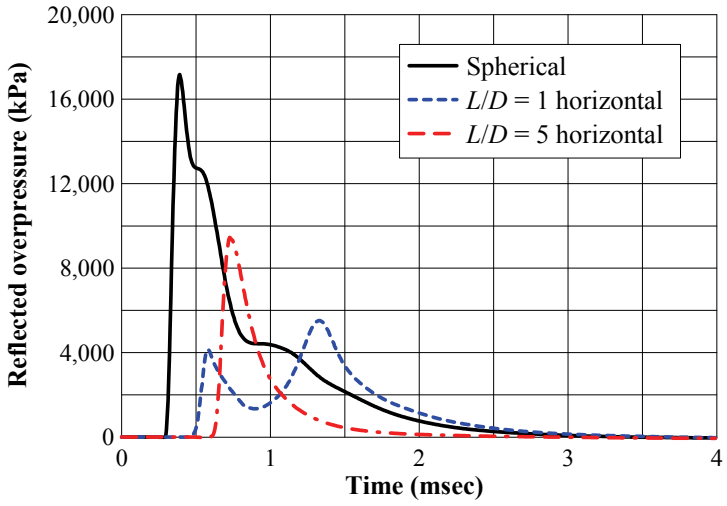

c) point C

Figure 4-54: Reflected overpressure histories for the spherical and horizontal (*B*) cylindrical charges

Table 4-3: Peak reflected overpressure and reflected impulse on the W14 × 257 column

Charge	Peak reflected overpressure (MPa)			Reflected impulse (MPa-msec)		
	Point A	Point B	Point C	Point A	Point B	Point C
Spherical	33.6	26.7	17.2	18.6	14.4	8.72
L/D = 1 vertical	66.3	15.3	5.54	31.1	11.7	5.12
L/D = 5 vertical	48.6	51.4	11.0	34.7	16.8	4.79
L/D = 1 horizontal	172.3	33.4	5.52	61.0	16.0	4.28
L/D = 5 horizontal	144.6	12.8	9.46	28.8	5.15	2.90

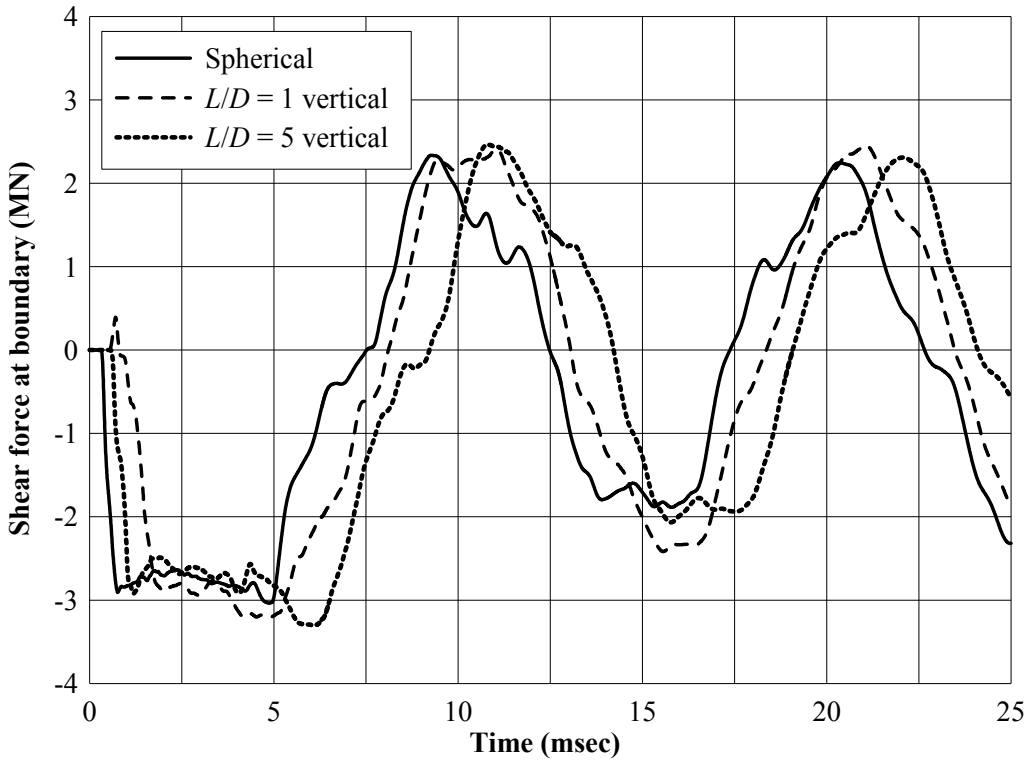

Figure 4-55: Shear force histories for the spherical and vertical (*A*) cylindrical charges

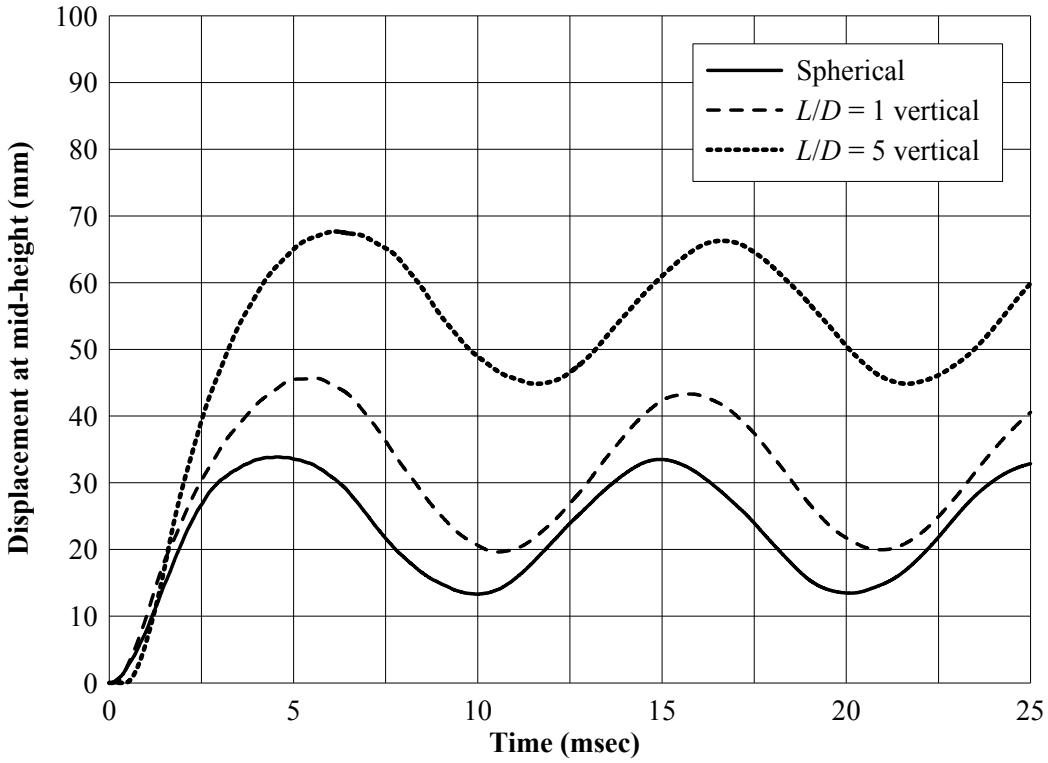

Figure 4-56: Displacement histories for the spherical and vertical (*A*) cylindrical charges

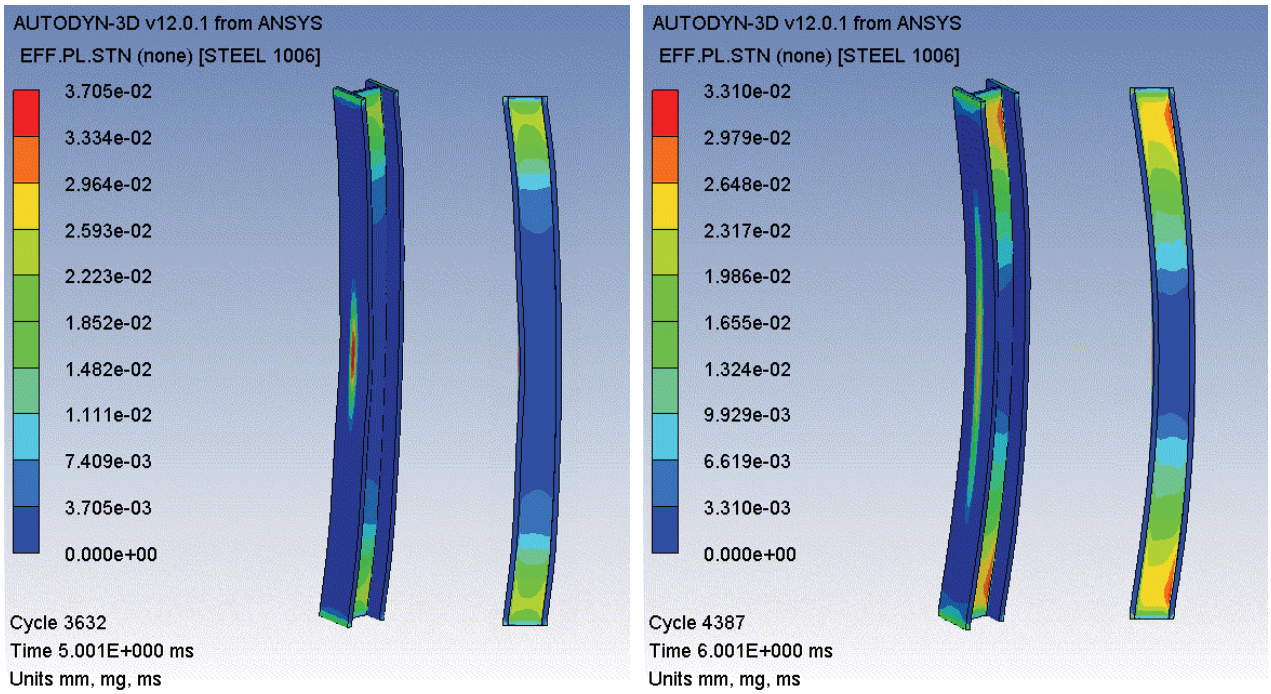

a) *L*/*D* = 1 vertical b) *L*/*D* = 5 vertical

Figure 4-57: Fringe plots of effective plastic strain at peak displacement for the vertical (*A*) cylindrical charges

The shear force and column mid-height displacement histories for the detonations of the horizontally oriented (*B*) charges are presented in Figures 4-58 and 4-59, respectively. The responses for the spherical charge are included in each figure for the reason given previously. The fringe plots of effective plastic strain at the time of peak mid-height displacement (which is approximately the time of peak shear force reaction) are presented in Figure 4-60.

For the horizontally oriented charges, the peak shear force for Cyl_I_B is approximately 25% higher than that for the Cyl_V_B and spherical charges. The plastic strains in the web near the boundaries are much greater for Cyl_I_B than Cyl_V_B, which enables the steel to strain harden and increases the shear resistance of the column. The peak shear force for Cyl_I_B occurs some time after that of the other two charges. This is consistent with the arrival times of shock waves from cylindrical charges in the axial direction in the near-field as shown in section 4.2.3: see Figure A-1.

The displacement histories for the horizontally oriented charges show that the peak displacement decreases with increasing aspect ratio. The peak displacements for the Cyl_V_B and spherical charges are almost identical but the peak displacement for Cyl_I_B is almost four times that for Cyl_V_B. The response of this column is sensitive to the change in aspect ratio of the cylindrical charge in orientation *B* (axis horizontal).

In panel a of Figure 4-60, the effective plastic strain is maximized ($\simeq 100\varepsilon_y$) at the mid-height of the column due to local bending of the flanges. The peak reflected overpressures (impulses) for the *Cyl_I* cylindrical charge at point A for the horizontally oriented charges are 2.6 (2.0) times the values for the vertically oriented charge, which is the reason that more damage is observed at the mid-height of the column in Figure 4-60a than in Figure 4-57a.

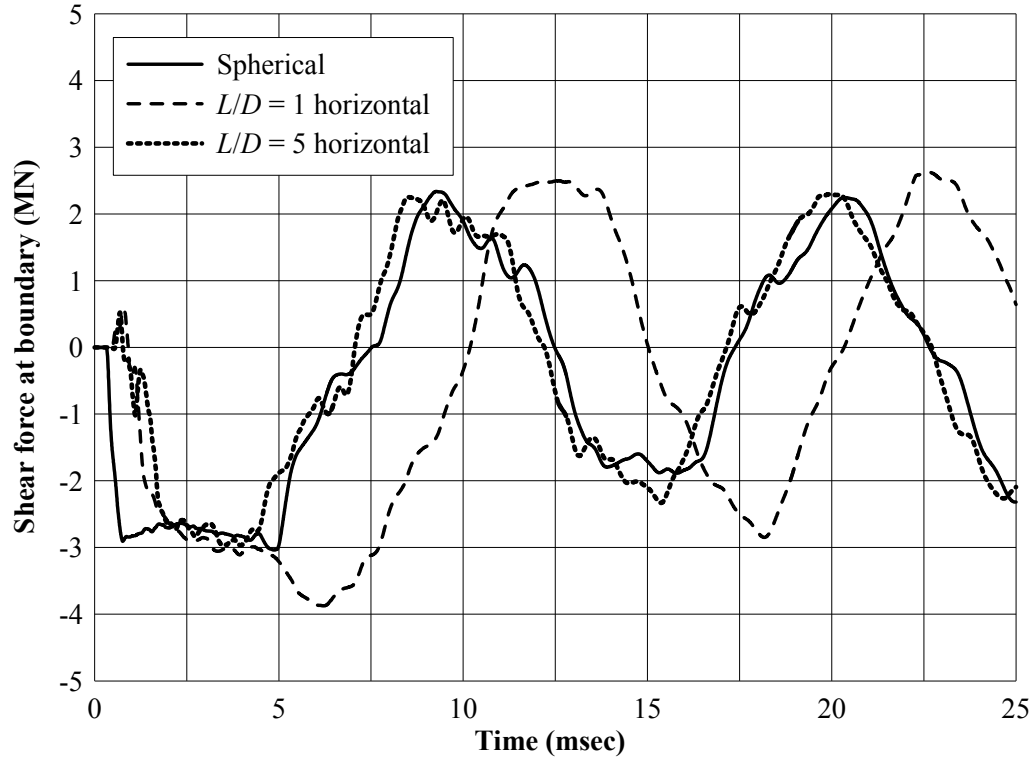

Figure 4-58: Shear force reaction histories for the spherical and horizontal (*B*) cylindrical charges

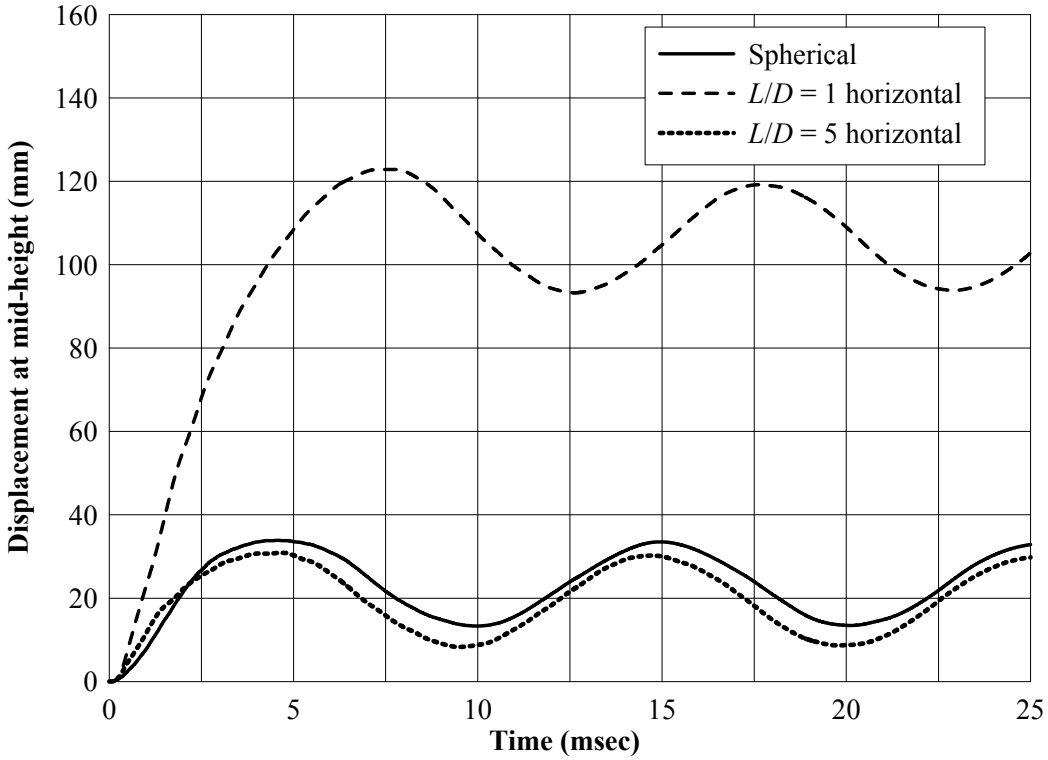

Figure 4-59: Displacement histories for the spherical and horizontal (*B*) cylindrical charges

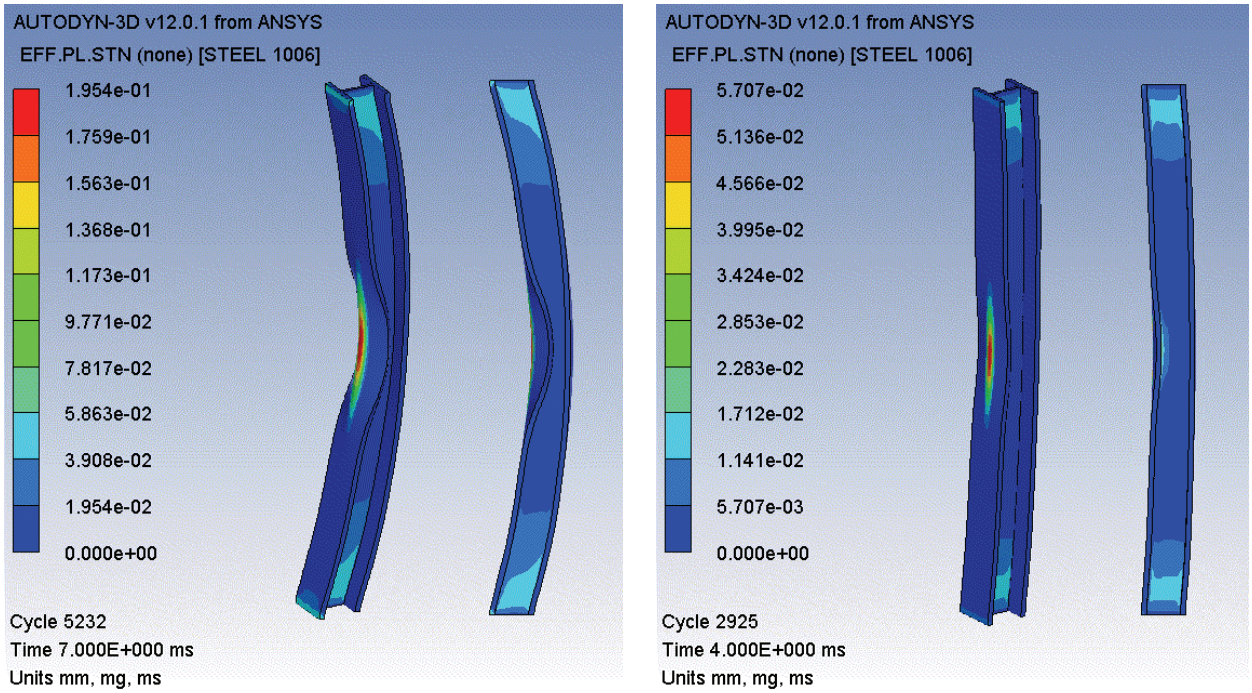

a) L/D = 1 horizontal b) L/D = 5 horizontal

Figure 4-60: Fringe plots of effective plastic strain at peak displacement for the horizontal (*B*) cylindrical charges

Table 4-4 enables a comparison of the key response parameters for the spherical and cylindrical charges. The response of the column subjected to a near-field blast loading is significantly affected by charge shape. The vertically oriented cylindrical charges produce greater peak displacements, peak shear forces and peak effective plastic strains than the spherical charge. Of the charges considered, the greatest damage is caused by the horizontal *Cyl_I* charge. The response of this column is much more sensitive to a change in the aspect ratio of the horizontally oriented charges than the vertically orientated charges.

Table 4-4: Comparison of key response parameters for the spherical and cylindrical charges

Charge	Peak *x*-displacement at mid-height (mm)	Peak shear force reaction at boundary (MN)	Peak effective plastic strain	
			Column web (near the boundaries)	Column flange (at the column mid-height)
Spherical	33.9	3.04	0.002	0.004
L/D = 1 vertical	45.7	3.21	0.031	0.038
L/D = 5 vertical	67.7	3.31	0.036	0.023
L/D = 1 horizontal	122.9	3.87	0.078	0.195
L/D = 5 horizontal	30.9	2.97	0.018	0.058

SECTION 5
SUMMARY, CONCLUSIONS AND RECOMMENDATIONS

5.1 Summary

Blast loads on structures and components thereof are determined using either empirical design curves provided in technical manuals such as the UFC-3-340 or by modeling the detonation using computational fluid dynamics (CFD). Numerical modeling using CFD codes requires an understanding of the physical and chemical phenomena involved in a detonation. A literature review on the complex processes involved in the detonation of high explosives, including shock wave propagation and chemistry, is presented in Chapter 2. The review includes a discussion on modeling of detonations in the computer codes LS-DYNA, AUTODYN and Air3D.

A comprehensive survey of the different strategies available in these computer codes to model detonations is presented in Chapter 3. The detonation of a spherical charge of TNT and the fluid-structure interaction with a rigid column in the near-field was modeled and analyzed using these codes. The results are compared with those computed using the empirical design curves in UFC-3-340. The effects of blast-wave clearing and afterburning are also investigated.

Chapter 4 presents the results of a numerical study on the influence of charge shape, charge orientation and point of detonation on overpressure distributions. The overpressure histories in the axial and radial direction, resulting from the detonation of 10 kg cylindrical charges and a 10 kg spherical charge are compared. The influence of point of detonation is investigated by comparing contour plots of pressure for the end detonated and centrally detonated charges. The effect of charge shape and orientation on the response of a column in the near-field subjected to a detonation of 1000 kg of TNT is studied. Results are reported in the form of displacement and reaction histories and contour plots of effective plastic strain.

5.2 Conclusions and Recommendations for Modeling and Analysis

The scope of the numerical studies reported in Chapters 3 and 4 of this report is broad, ranging from modeling detonations and detonations effects to computing the response of a structural component for a near-field detonation of a large explosive. The key conclusions of the studies and recommendations for modeling and analysis of near-field detonations are:

1. The peak reflected overpressures, overpressure histories and impulses in the near-field obtained using three widely used codes for blast analysis (LS-DYNA, AUTODYN, and Air3D) are significantly different than those computed using the industry-standard UFC-3-340. The three codes estimate different values of the reflected overpressure, impulse and shock-front arrival time on the face of a rigid column subjected to near-field detonation of a spherical TNT charge of large size.
2. If LS-DYNA is used to model the effects of detonations of high-explosives in the near field, element sizes should be small for the explosive (< 10 mm) and the air (< 25 mm). LS-DYNA results are especially dependent on element size, and vary with time-step and the input parameters of the coupling algorithm. Sensitivity analyses must be performed. The 'Constrained_Lagrange_in_Solid' option in the coupling algorithm should be used with caution if the meshes for the fluid and structure have different geometries (e.g., radial and cuboid).
3. If AUTODYN is used to model the effects of detonations of high-explosives in the near-field, remapping capabilities should be used whenever possible. The Euler-FCT solver should be used for air unless afterburning is to be modeled, in which case the multi-material Euler-Godunov solver has to be used.
4. If Air-3D is used to model the effects of detonations of high-explosives in the near field, the results do not vary much with grid refinement. The cell size recommended in the User's Manual can be used.

5. For a large explosive (say 1000 kg), the temperatures in the vicinity of the explosive after detonation are much higher than those at which the dissociation of oxygen and nitrogen molecules in air can occur. The assumption of a constant value for the ratio of specific heats, γ, for air is incorrect in this region. The assumption of $\gamma = 1.4$ for air is also violated in regions where very high incident overpressures are reflected, which is indirectly addressed in UFC-3-340 where values of the reflection coefficient can exceed 8. Hard-coded Equations of State that allow γ to vary should be implemented in LS-DYNA and AUTODYN.
6. Afterburning can significantly increase the reflected impulse in the near field for under-oxidized explosives such as TNT. AUTODYN is capable of modeling the release of afterburning energy but guidance on the amount of energy, time of release, and rate of release is lacking. For the sample problem studied in this report, the effects of afterburning were modest.
7. In the near-field region (as measured by small scaled distance), clearing reduces both the peak reflected overpressure and the reflected impulse. The rise time to peak reflected overpressure is not instantaneous. The UFC-3-340 design procedures do not account for the reduction of peak reflected overpressure on near-field targets of finite dimensions and may overestimate values of peak reflected overpressure and reflected impulse.
8. Charge shape influences substantially the overpressure distributions in the near- and mid-field regions. The incident overpressures and impulses generated by a cylindrical charge are significantly greater than those generated by a spherical charge. Ignoring charge shape in the analysis and design of structural components and framing systems subjected to near-field detonations may result in low estimates of response and inappropriate conclusions regarding the level of performance.
9. For cylindrical charges and a given scaled distance, a) the incident impulse increases (decreases) in the radial (axial) directions with increasing aspect ratio; b) the peak overpressures are greater in the axial direction than the radial direction; c) significant secondary shocks are present in the

overpressure histories at large scaled distances (Z > 3.15 m/kg$^{0.33}$) in the axial direction; d) multiple shocks, which are less significant than the primary shocks, are seen at all scaled ranges (Z = 0.53 to 4.2 m/kg$^{0.33}$) and increase substantially the total impulse. If the impulses due to secondary and tertiary shocks exceed 20% of the primary shock, nonlinear response-history analysis should be performed to estimate the response of structural components and framing systems. If the impulse due to secondary and tertiary shocks is ignored, the effect of cylindrical charge shape on the incident overpressures, impulses, and the overall shape of the blast wave, becomes negligible beyond a scaled distance of 2.64 m/kg$^{0.33}$; that is a spherical charge can be used for analysis.

10. The effects of charge shape described in 8) and 9) are substantially independent of the mass of the explosive. A study of limited scope indicated that the value of scaled distance beyond which the effect of charge shape effect can be ignored increased by less than 20% for a 100-fold increase in the charge mass.
11. The effect of point of detonation (center, end) in a cylindrical charge on the overpressure distributions and the overall shape of the blast wave is important for small scaled distances but can be ignored for scaled distances greater than 3 m/kg$^{0.33}$.
12. Charge shape (spherical or cylindrical) and orientation (axis vertical, axis horizontal) affect the response of a column subjected to a near-field detonation. Horizontally detonated charges (axial direction of the charge perpendicular to the front face of the structure) produces localized damage in the column, whereas the damage due to the vertically detonated charges is widespread. Furthermore, the response of the column is more sensitive to the change in aspect ratio of the horizontally detonated charges than that in the vertically detonated charges.
13. For the sample problem, which may be representative of many blast-resistant analyses/designs of building structures in North America in terms of threat (weapon size and standoff), the increase in temperature of the component under consideration was negligible, and inclusion of thermal effects in the constitutive model is unnecessary. For the sample problem that involved a heavy

W14×257 rolled column of Grade A992 steel, the effect of strain-rate on yield stress was minimal and the inclusion of strain-rate effects in the Johnson-Cook model did not significantly alter the local or global response of the column. The use of a Dynamic Increase Factor (DIF), which is provided in UFC-3-340 and other design guidelines for blast-resistant design of structures subjected to should be reconsidered.

5.3 Recommendations for Future Research

Although the numerical studies described in this report addressed a wide range of topics, much additional study is needed before definitive conclusions can be drawn for design practice. Topics for further study include:

1. Afterburning increases the reflected impulse for certain types of explosives. Although afterburning was studied using AUTODYN, the amount of energy released and its release duration were assumed on the basis of available information, which is incomplete. Additional test data are needed. Improved strategies for incorporating afterburning should be developed and implemented in LS-DYNA and AUTODYN.
2. The assumption of constant γ is violated at very high temperatures. Data relating γ to high temperature and pressure (e.g., Gilmore, 1955), should be used to calibrate an Equation of State for implementation in LS-DYNA and AUTODYN.
3. Clearing was shown to affect both the peak reflected overpressure and reflected impulse in the near field. More work is needed to understand a) the propagation of rarefaction waves across the front face of a target of finite width, and b) the influence of rarefaction waves on the peak reflected overpressure and reflected impulse.
4. Technical manuals such as UFC-3-340 focus primarily on detonations of spherical and hemispherical explosives. Charge shape, charge orientation and point of detonation have a significant influence on overpressure histories in the near-field. Empirical design charts that

address these variables should be developed. Experimental data should be collected to validate all design charts.

5. Near-field detonations of explosives do not generate uniform load effects on structural components and single-degree-freedom assumptions cannot be made. Simplified, yet robust procedures should be developed for structural components to resist the effects of near-field detonations.
6. Split Hopkinson Pressure Bar tests should be performed to determine the parameters of the Johnson-Cook model in compression and tension for steels used in rolled shapes.
7. A simplified model of a W-shape column was assumed for the numerical studies reported in this report; the ground at the base of the column was considered to be a transmitting surface; and explosives were detonated at the mid-height of the column. Further studies are needed to consider alternate column shapes and boundary conditions, and surface or near-surface detonations.

SECTION 6

REFERENCES

Adamik, V., Vagenknecht, J., Vavra, P. and Trzcinski, W. (2004). "Effect of TNT charge orientation on generated air blast waves - Numerical simulation using LS-DYNA". *Proceedings of the 7th Seminar on New Trends in Research of Energy Materials*, University of Pardubice, Faculty of Chemical Technology, Pardubice, Czech Republic.

Akhavan, J. (2004). *The Chemistry of Explosives*, 2nd edition., Springer, New York.

Alia, A. and Souli, M. (2006). "High explosive simulation using multi-material formulations". *Applied Thermal Engineering,* 26(10), 1032-1042.

American Concrete Institute (ACI). (2008). Building Code Requirements for Structural Concrete. Detroit, MI.

American Institute of Steel Construction (AISC). (2005). Steel Construction Manual, 13th Edition. Chicago, IL.

American Institute of Steel Construction (AISC). (2006). Seismic Design Manual. Chicago, IL.

American Society of Civil Engineers (ASCE). (forthcoming). Blast Protection of Buildings, Standard in preparation. Reston, VA.

Anderson, J. D. and Anderson, J. (2002). *Modern Compressible Flow: With Historical Perspective*, 3rd edition., McGraw-Hill Science/Engineering/Math.

Anderson, J. G., Katselis, G. and Caputo, C. (2002). "Analysis of a Generic Warhead Part I: Experimental and Computational Assessment of Free Field Overpressure". *Technical Report No. DSTO-TR-1313*, Defence Science and Technology Organisation, Systems Sciences Lab, Salisbury, Australia.

ANSYS Academic Research. (2009). ANSYS Modeling and Meshing Guide (Version 12.0). ANSYS INC., Canonsburg, PA.

Baker, W. (1973). *Explosions in Air*, University of Texas Press, Austin.

Ballantyne, G. J., Whittaker, A. S., Dargush, G. F. and Aref, A. J. (2010). "Air-blast effects on structural shapes of finite width". *Journal of Structural Engineering,* 136(2), 152-159.

Biggs, J. (1964). *Introduction to Structural Dynamics*, McGraw Hill, New York.

Birnbaum, N. K., Francis, N. J. and Gerber, B. I. (1999). "Coupled techniques for the simulation of fluid-structure and impact problems". *Computer Assisted Mechanics and Engineering Sciences,* 6(3-4), 295-311.

Borve, S., Bjerke, A., Omang, M. and Truslen, J. (2008). "A comparative study of ANSYS AUTODYN and RSPH simulations of blast waves". *Proceedings of the 3rd ERCOFTAC SPHERIC Workshop on SPH applications*, Lausanne, Switzerland.

Brode, H. L. (1956). "The blast wave in air resulting from a high temperature, high pressure sphere of air". *Research Memorandum No. RM-1825-AEC*, Rand Corporation, Santa Monica, CA.

Brode, H. L. (1959). "Blast wave from a spherical charge". *Physics of Fluids,* 2(2), 217-229.

Burton, D. (1992). "Connectivity structures and differencing techniques for staggered-grid free-Lagrange hydrodynamics". *Report No. UCRL–JC–110555*, Lawrence Livermore National Laboratory, Livermore, CA.

Burton, D. (1994). "Consistent finite-volume discretization of hydrodynamic conservation laws for unstructured grids". *Report No. UCRL–JC–118788*, Lawrence Livermore National Laboratory, Livermore, CA.

CD Adapco Group. (2001). Methodology STAR-CD (Version 3.15). Computational Dynamics Limited Corporation, UK.

Century Dynamics. (2005). AUTODYN Remapping Tutorial (Version 4.3), Horsham, UK.

Century Dynamics. (2009a). AUTODYN Theory Manual (Version 4.3), Horsham, UK.

Century Dynamics. (2009b). AUTODYN User Manual (Version 12), Horsham, UK.

Chafi, M. S., Karami, G. and Ziejewski, M. (2009). "Numerical analysis of blast-induced wave propagation using FSI and ALE multi-material formulations". *International Journal of Impact Engineering,* 36(10-11), 1269-1275.

Cooper, P. and Kurowski, S. (1996). *Introduction to Technology of Explosives*, Wiley-VCH.

Courant, R. and Friedrichs, K. O. (1948). *Supersonic Flow and Shock Waves*, Interscience Publishers, New York.

Cowperthwaite, M. and Zwisler, W. H. (1972). "The JCZ equations of state for detonation products and their incorporation into the TIGER code". *Proceedings of the 6th Symposium (International) on Detonation*, Coronado, CA.

Davis, W. (1982). "High explosives: the interaction of chemistry and explosives". *Los Alamos Science,* 2(1), 48-75.

Dobratz, B. and Crawford, P. (1985). "LLNL explosives handbook". *Report No. UCRL-52997*, Lawrence Livermore National Laboratory, Livermore, CA.

DoD. (2008). "Design of structures to resist the effects of accidental explosions". *Report No. UFC-3-340-02*, Washington D.C.

Donahue, L. K. (2009). "Afterburning of TNT detonation products in air". *M.A.Sc. Thesis*, Dalhousie University, Halifax, Nova Scotia.

Dusenberry, D. (2010). *Handbook for Blast Resistant Design of Buildings*, John Wiley and Sons, Inc., Hoboken, NJ.

Fairlie, G. E. (1998). "The numerical simulation of high explosives using AUTODYN-2D & 3D". *Proceedings of the Explo '98, Institute of Explosive Engineers 4th Biannual Symposium*, UK.

Fickett, W. (1962). "Detonation properties of condensed explosives calculated with an equation of state based on intermolecular potentials". *Report No. LA-2712*, Los Alamos Scientific Laboratory, Los Alamos, NM.

FLUENT Inc. (2003). FLUENT 6.0 User's Guide. FLUENT Inc., Canonsburg, PA.

Fried, L. E., Howard, W. M. and Souers, P. C. (1998). Cheetah 2.0 User's Manual, Lawrence Livermore National Laboratory, Livermore, CA.

Gilmore, F. (1955). "Equilibrium composition and thermodynamic properties of air to 24,000 ^{o}K". *Research Memorandum No. RM-1543*, Rand Corporation, Santa Monica, CA.

Glasstone, S. and Dolan, P. (1977). *The Effects of Nuclear Weapons*, 3rd edition., US Department of Defense, Washington, D.C.

Hamashima, H., Itoh, S., Kato, Y. and Murata, K. (2003). "Determination of JWL paramters from underwater explosion test for ideal and non-ideal explosives". *Sci Technol Energ Mater* 64(6), 248-253.

Hyde, D. (1988). "User's guide for microcomputer programs CONWEP and FUNPRO – Applications of TM 5-855-1". U.S. Army Engineer Waterways Experimental Station, Vicksburg, MS.

Ismail, M. M. and Murray, S. G. (1993). "Study of the blast waves from the explosion of nonspherical charges". *Propellants, Explosives, Pyrotechnics,* 18(3), 132-138.

Johnson, G. and Cook, W. (1983). "A constitutive model and data for metals subjected to large strains, high strain rates and high temperatures". *Proceedings of the Seventh International Symposium on Ballistics*, The Hague, Netherlands.

Kim, J.-H. and Shin, H.-C. (2008). "Application of the ALE technique for underwater explosion analysis of a submarine liquefied oxygen tank". *Ocean Engineering,* 35(8-9), 812-822.

Kingery, C. N. and Bulmash, G. (1984). "Airblast parameters from TNT spherical air burst and hemispherical surface burst". *Technical Report No. ARBL-TR-02555*, US Army BRL, Aberdeen Proving Ground, MD.

Kury, J. W., Hornig, H. C., Lee, E. L., Mcdonnel, J. L., Ornellas, D. L., Finger, M., Strange, F. M. and Wilkins, M. L. (1965). "Metal acceleration by chemical explosives". *Proceedings of the Fourth Symposium on Detonation*, Office of Naval Research, Arlington, TX.

LSTC. (2006). LS-DYNA Theory Manual. Livermore Software Technology Corporation, Livermore, CA.

LSTC. (2007). LS-DYNA Keyword User's Manual (Version 971). Livermore Software Technology Corporation, Livermore, CA.

Luccioni, B., Ambrosini, D. and Danesi, R. (2006). "Blast load assessment using hydrocodes". *Engineering Structures,* 28(12), 1736-1744.

Mader, C. L. (1963). "Detonation properties of condensed explosives computed using the Becker-Kistiakowsky-Wilson Equation of State". *Report No. LA-2900*, Los Alamos Scientific Laboratory, Los Alamos, NM.

Mader, C. L. (1967). "FORTRAN BKW: A code for computing the detonation properties of explosives". *Report No. LA-3704*, Los Alamos Scientific Laboratory, Los Alamos, NM.

Mader, C. L. (2007). *Numerical Modeling of Explosives and Propellants*, 3rd edition., CRC Press.

Mandell, D., Burton, D. and Lund, C. (1998). "High explosive programmed burn in the Flag code". *Report No. LA-13406*, Los Alamos National Laboratory, Los Alamos, NM.

Martec Limited. (2008). Chinook Input Manual (Version SM-07-01). Martec Limited, Halifax, Canada.

Meyers, M. (1994). *Dynamic Behavior of Materials*, Wiley-Interscience, New York.

MSC Software Corporation. (1999). MSC/PATRAN User Manual, Version 4.7, Santa Ana, CA.

Norris, C. H., Hansen, R., Holley, M., Biggs, J., Namyet, S. and Nirrami, J. (1959). *Structural Design for Dynamic Loads*, McGraw Hill, New York.

Reisler, R. C. (1972). "Explosive yield criteria". *Minutes of the Fourteenth Explosive Seminar*, Department of Explosives Safety Board, New Orleans, LA.

Rider, W. J. and Kothe, D. B. (1998). "Reconstructing volume tracking". *Journal of Computational Physics,* 141(2), 112-152.

Ripley, R. C., Donahue, L., Dunbar, T. E., Murray, S. B., Anderson, C. J., Zhang, F. and Ritzel, D. V. (2009). "Ground reflection interaction with height-of-burst metalized explosions", in *Shock waves, 26th International Symposium on Shock Waves* (pp. 281-286) Springer, Berlin.

Ritzel, D. V. and Mathews, K. (1997). "An adjustable explosion-source model for CFD blast calculations". *Proceedings of the 21st International Symposium on Shock Waves*, Great Keppel Island, Australia.

Rose, T. (2006). Air3d User's Guide (Version 9), Engineering Systems Department, Cranfield University, UK.

Slavik, T. (2009). "A coupling of empirical explosive blast loads to ALE air domains in LS-DYNA". *Proceedings of the 7th European LS-DYNA Conference*, Salzburg, Austria.

Smith, P. and Hetherington, J. (1994). *Blast and Ballistic Loading of Structures*, Butterworth-Heinemann, Boston.

Sundararajan, R. and Jain, S. R. (1982). "A simple method of estimating the detonation velocity from chemical composition of organic explosives". *Combustion and Flame,* 45, 47-52.

Tham, C. Y. (2009). "Numerical simulation on the interaction of blast waves with a series of aluminum cylinders at near-field". *International Journal of Impact Engineering,* 36(1), 122-131.

Toro, E. F. (1997). *Riemann solvers and numerical methods for fluid dynamics : a practical introduction*, Springer, New York.

Venkateshan, S. (2011). "Modeling clearing for near-field detonations". *M.S. thesis in preparation*, University at Buffalo (SUNY), Buffalo.

Wada, Y. and Liou, M.-S. (1997). "An accurate and robust flux splitting scheme for shock and contact discontinuities". *SIAM J. Sci. Comput.,* 18(3), 633-657.

Webster, K. G. (2007). "Investigation of close proximity underwater explosion effects on a ship-like structure using the multi-material Arbitrary Lagrangian Eulerian finite element method". *M.S. Thesis*, Virginia Polytechnic Institute and State University, Blacksburg, VA.

Woodruff, J. P. (1973). "KOVEC User's Manual". *Report No. UCRL-51079*, Lawrence Livermore National Laboratory, Livermore, CA.

Wu, C., Fattori, G., Whittaker, A. S. and Oehlers, D. J. (2010). "Investigation of air-blast effects from spherical and cylindrical-shaped charges". *International Journal of Protective Structures* (accepted for publication, June 2010).

Youngs, D. L. (1982). "Time-dependent multi-material flow with large fluid distortion", in *Numerical Methods for Fluid Dynamics* (pp. 273-285). K. W. Morton & M. J. Baines (editors.), Academic Press.

Zimmerman, H. D., Nguyen, C. T. and Hookham, P. A. (1999). "Investigation of spherical vs cylindrical charge shape effects on peak free-air overpressure and impulse". *Proceedings of the 9th International Symposium on Interaction of the Effects of Munitions with Structures*, Berlin.

Zukas, J. and Walters, W. (1998). *Explosive Effects and Applications*, Springer, New York.

Zukas, J. A. (2004). *Introduction to Hydrocodes*, Elsevier, Boston.

Appendix A

Supplemental Overpressure Histories

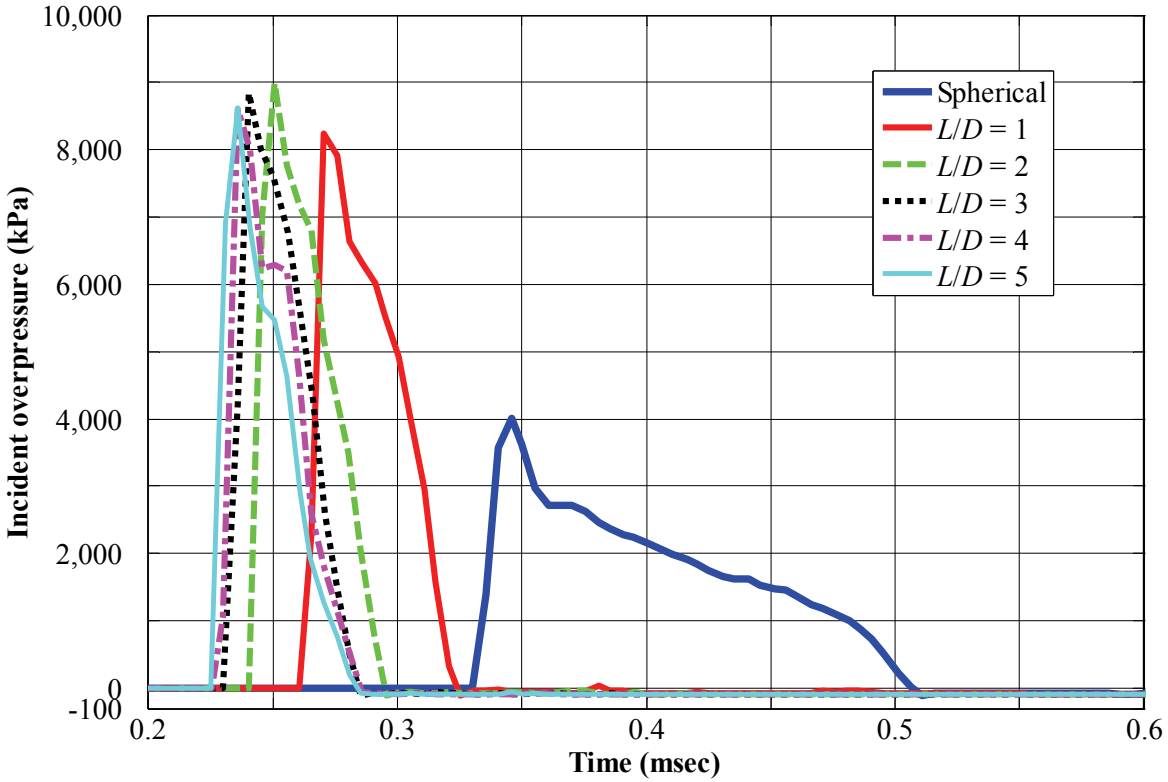

Figure A-1: Overpressure histories at an axial distance of 5 charge diameters (Z = 0.53 m/kg$^{0.33}$)

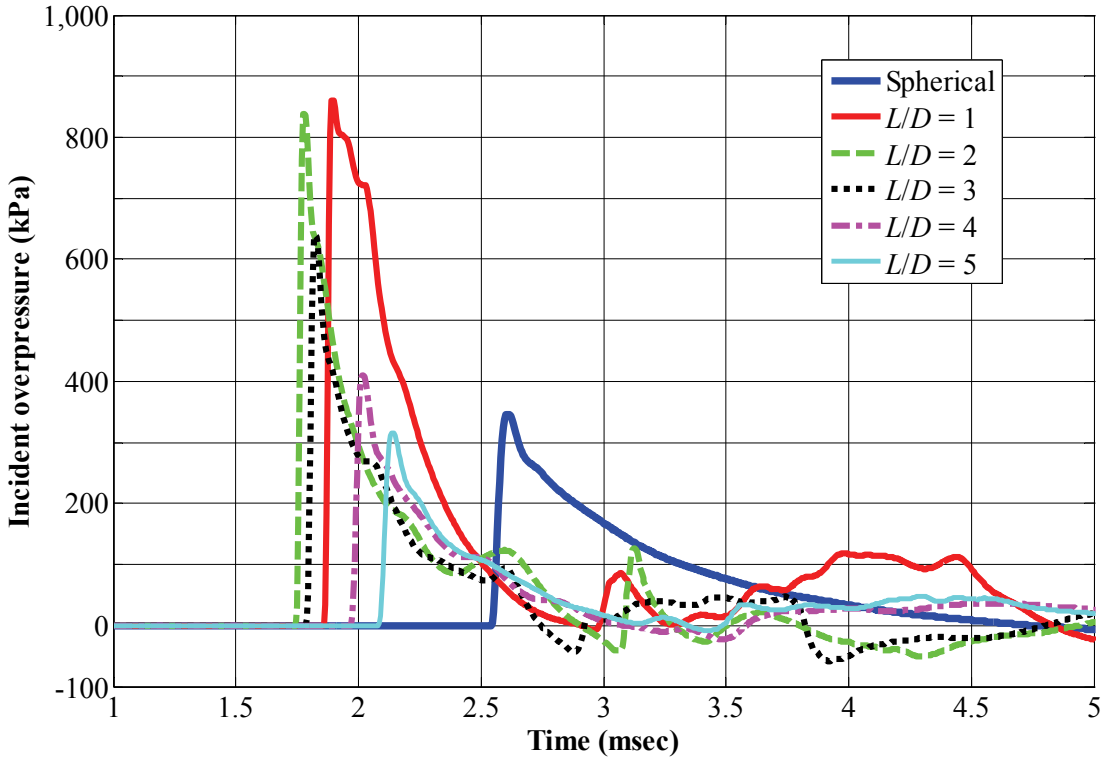

Figure A-2: Overpressure histories at an axial distance of 15 charge diameters (Z = 1.58 m/kg$^{0.33}$)

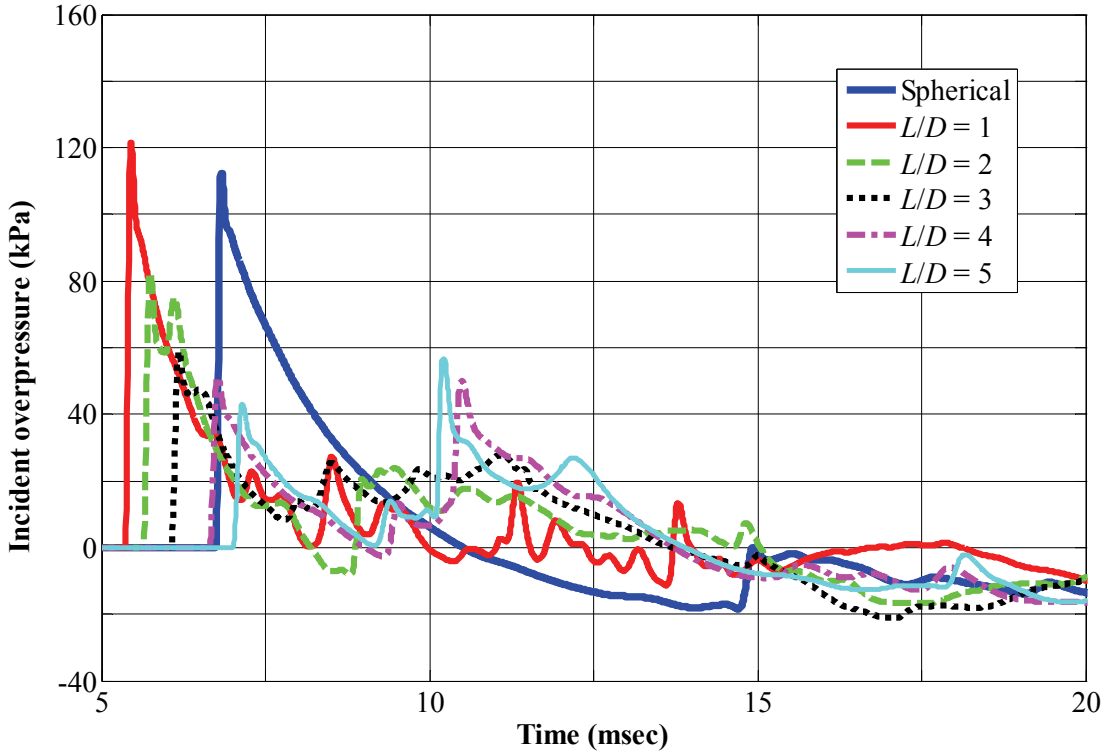

Figure A-3: Overpressure histories at an axial distance of 25 charge diameters (Z = 2.64 m/kg$^{0.33}$)

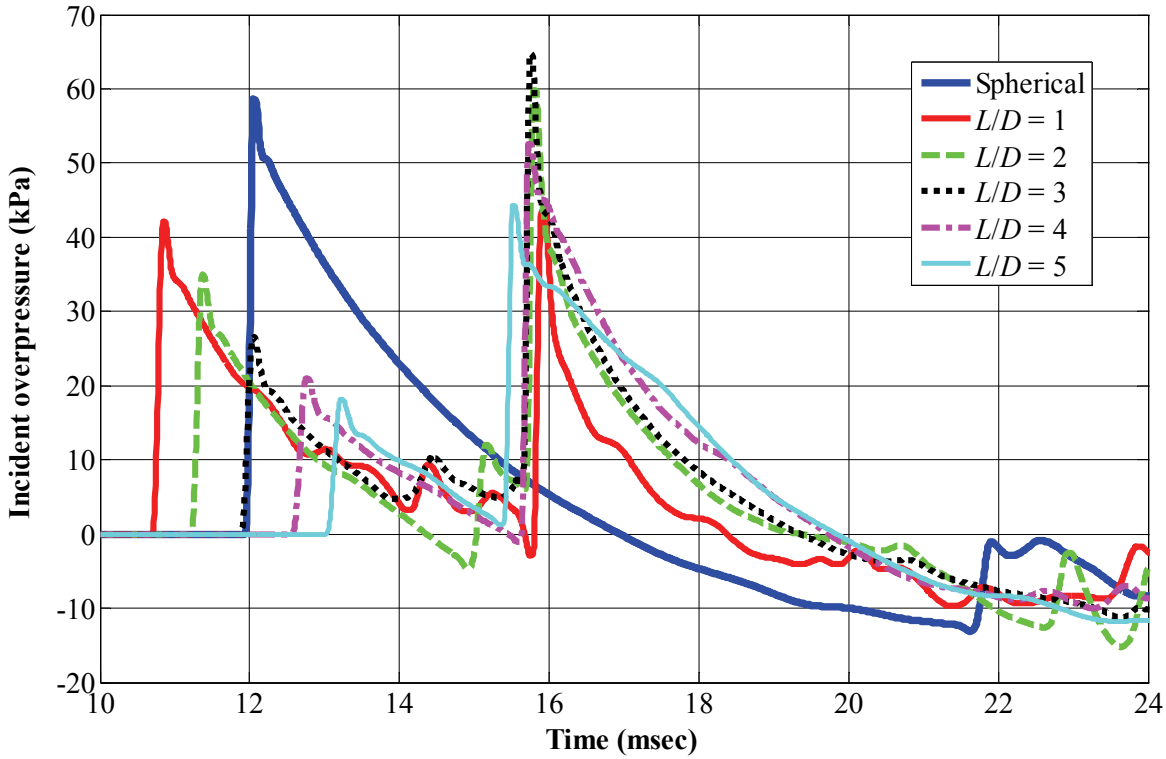

Figure A-4: Overpressure histories at an axial distance of 35 charge diameters (Z = 3.69 m/kg$^{0.33}$)

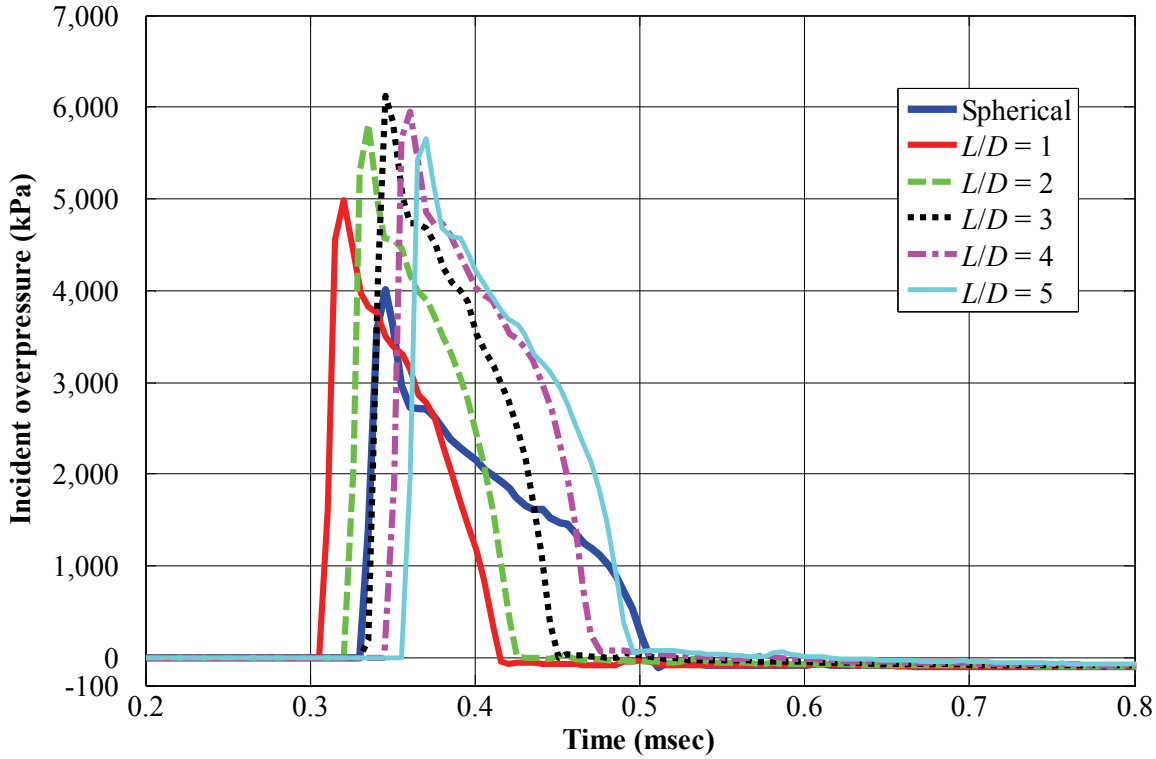

Figure A-5: Overpressure histories at a radial distance of 5 charge diameters (Z = 0.53 m/kg$^{0.33}$)

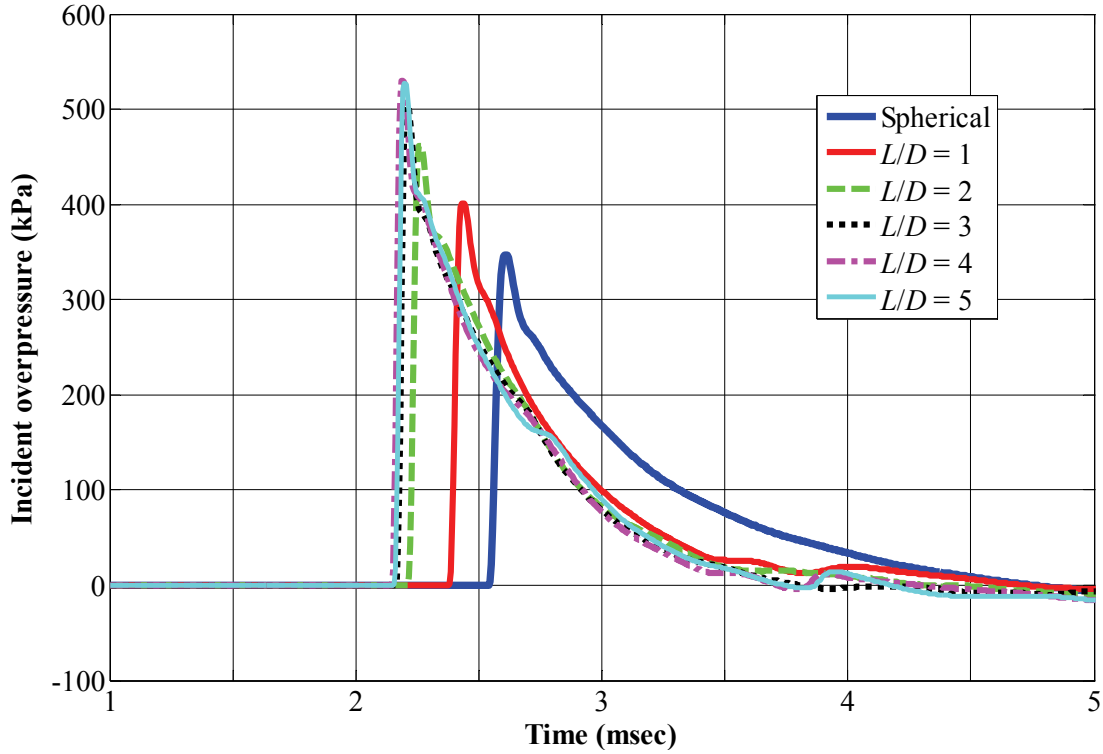

Figure A-6: Overpressure histories at a radial distance of 15 charge diameters (Z = 1.58 m/kg$^{0.33}$)

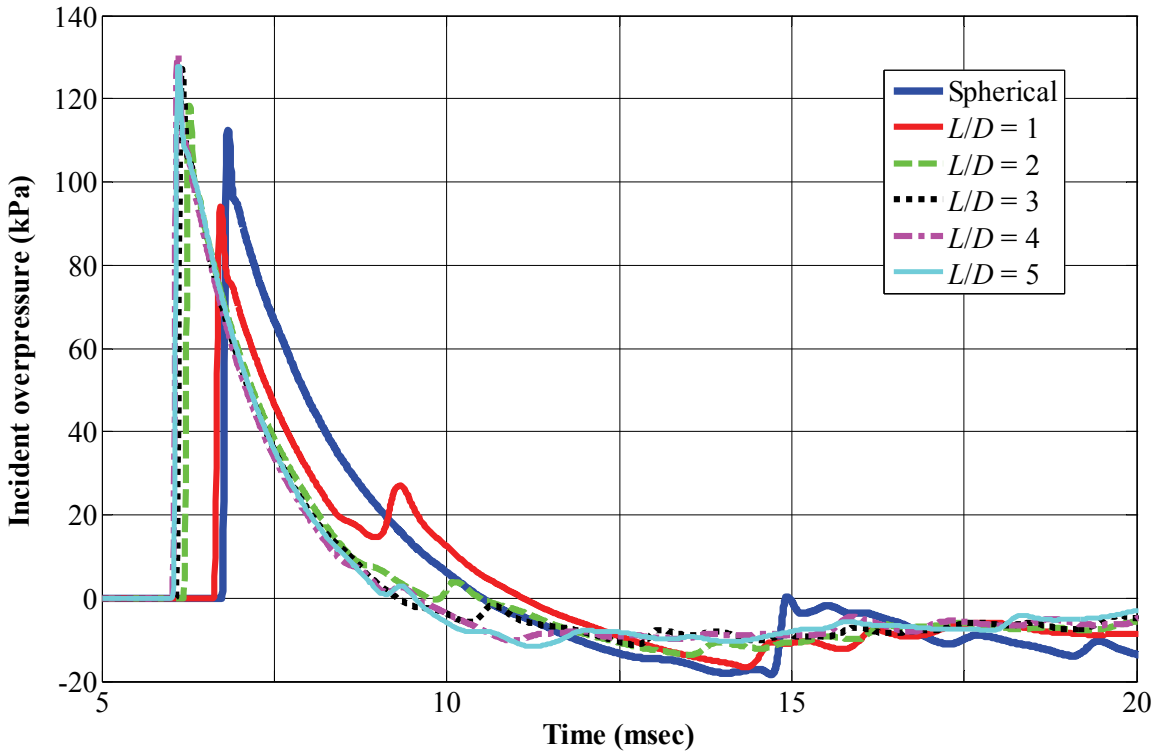

Figure A-7: Overpressure histories at a radial distance of 25 charge diameters (Z = 2.64 m/kg$^{0.33}$)

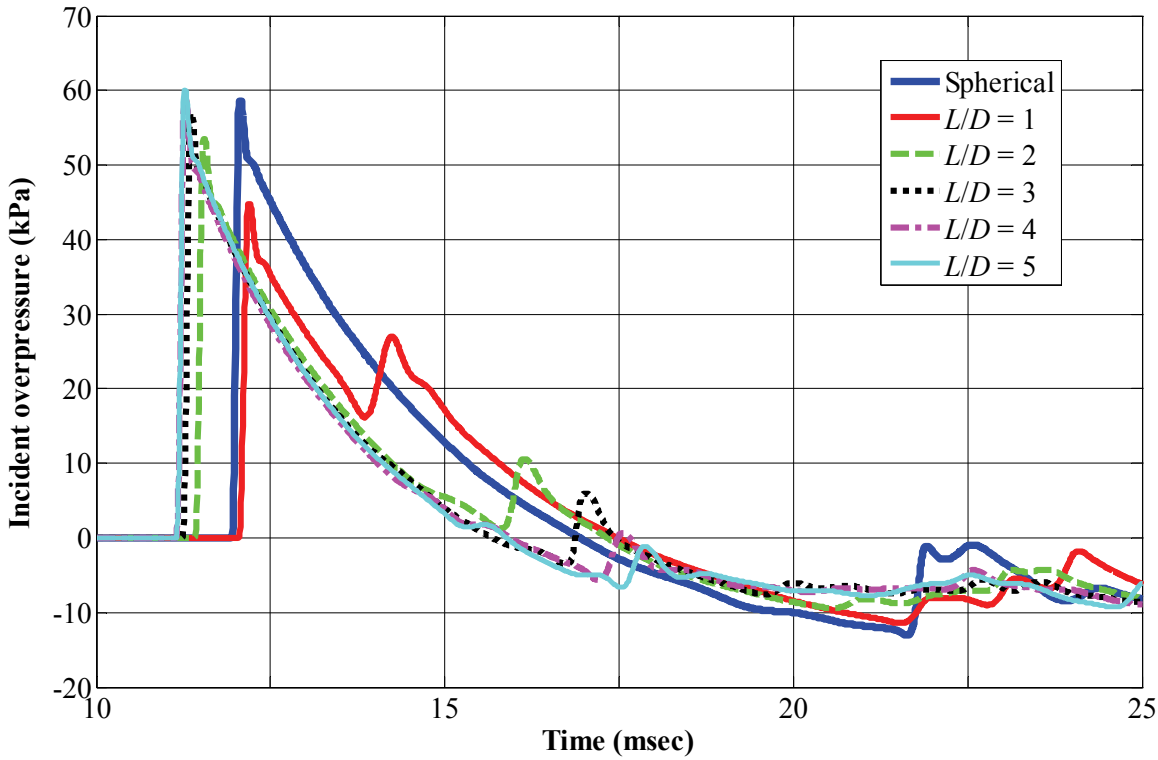

Figure A-8: Overpressure histories at a radial distance of 35 charge diameters (Z = 3.69 m/kg$^{0.33}$)

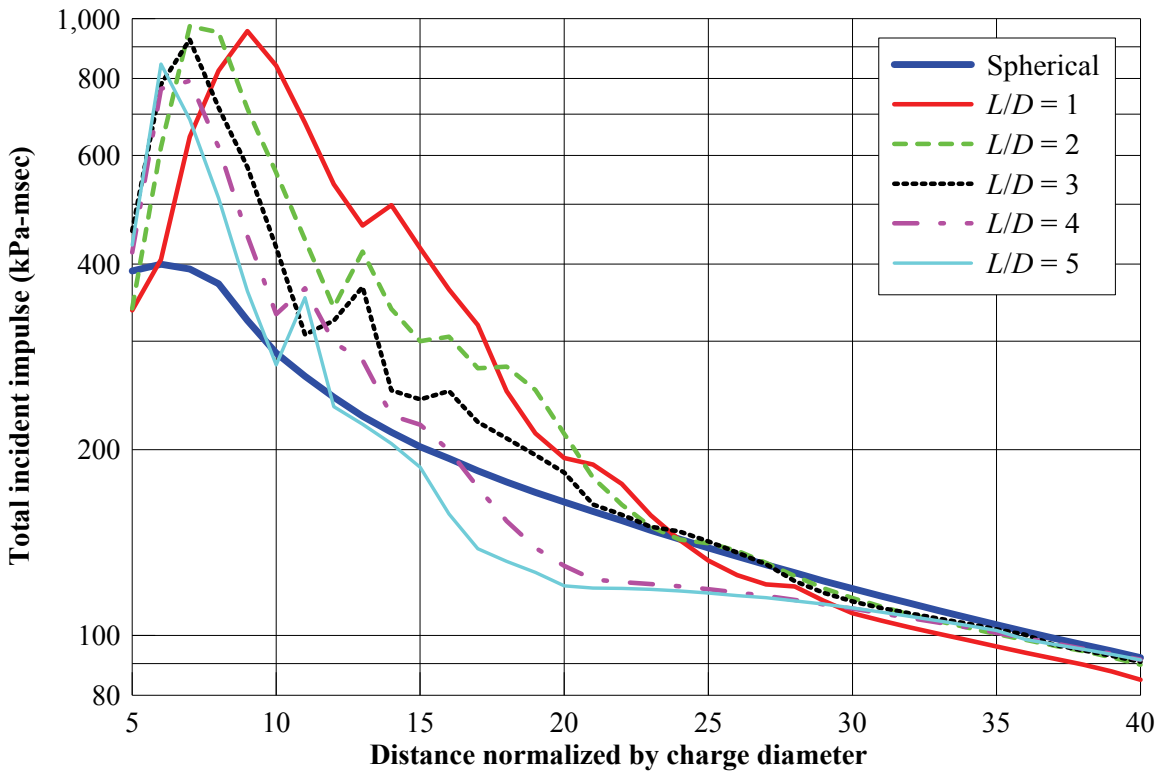

Figure A-9: Total incident impulse vs. normalized distance in the axial direction

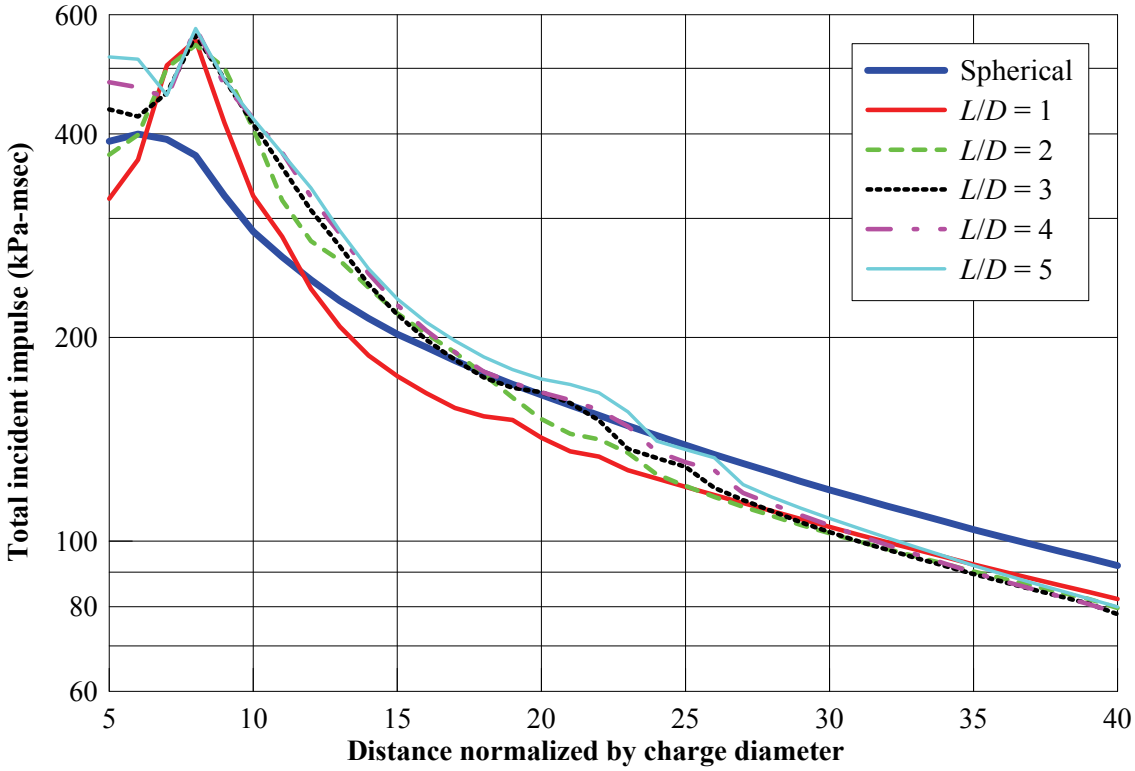

Figure A-10: Total incident impulse vs. normalized distance in the radial direction

MCEER Technical Reports

MCEER publishes technical reports on a variety of subjects written by authors funded through MCEER. These reports are available from both MCEER Publications and the National Technical Information Service (NTIS). Requests for reports should be directed to MCEER Publications, MCEER, University at Buffalo, State University of New York, 133A Ketter Hall, Buffalo, New York 14260. Reports can also be requested through NTIS, P.O. Box 1425, Springfield, Virginia 22151. NTIS accession numbers are shown in parenthesis, if available.

NCEER-87-0001 "First-Year Program in Research, Education and Technology Transfer," 3/5/87, (PB88-134275, A04, MF-A01).

NCEER-87-0002 "Experimental Evaluation of Instantaneous Optimal Algorithms for Structural Control," by R.C. Lin, T.T. Soong and A.M. Reinhorn, 4/20/87, (PB88-134341, A04, MF-A01).

NCEER-87-0003 "Experimentation Using the Earthquake Simulation Facilities at University at Buffalo," by A.M. Reinhorn and R.L. Ketter, to be published.

NCEER-87-0004 "The System Characteristics and Performance of a Shaking Table," by J.S. Hwang, K.C. Chang and G.C. Lee, 6/1/87, (PB88-134259, A03, MF-A01). This report is available only through NTIS (see address given above).

NCEER-87-0005 "A Finite Element Formulation for Nonlinear Viscoplastic Material Using a Q Model," by O. Gyebi and G. Dasgupta, 11/2/87, (PB88-213764, A08, MF-A01).

NCEER-87-0006 "Symbolic Manipulation Program (SMP) - Algebraic Codes for Two and Three Dimensional Finite Element Formulations," by X. Lee and G. Dasgupta, 11/9/87, (PB88-218522, A05, MF-A01).

NCEER-87-0007 "Instantaneous Optimal Control Laws for Tall Buildings Under Seismic Excitations," by J.N. Yang, A. Akbarpour and P. Ghaemmaghami, 6/10/87, (PB88-134333, A06, MF-A01). This report is only available through NTIS (see address given above).

NCEER-87-0008 "IDARC: Inelastic Damage Analysis of Reinforced Concrete Frame - Shear-Wall Structures," by Y.J. Park, A.M. Reinhorn and S.K. Kunnath, 7/20/87, (PB88-134325, A09, MF-A01). This report is only available through NTIS (see address given above).

NCEER-87-0009 "Liquefaction Potential for New York State: A Preliminary Report on Sites in Manhattan and Buffalo," by M. Budhu, V. Vijayakumar, R.F. Giese and L. Baumgras, 8/31/87, (PB88-163704, A03, MF-A01). This report is available only through NTIS (see address given above).

NCEER-87-0010 "Vertical and Torsional Vibration of Foundations in Inhomogeneous Media," by A.S. Veletsos and K.W. Dotson, 6/1/87, (PB88-134291, A03, MF-A01). This report is only available through NTIS (see address given above).

NCEER-87-0011 "Seismic Probabilistic Risk Assessment and Seismic Margins Studies for Nuclear Power Plants," by Howard H.M. Hwang, 6/15/87, (PB88-134267, A03, MF-A01). This report is only available through NTIS (see address given above).

NCEER-87-0012 "Parametric Studies of Frequency Response of Secondary Systems Under Ground-Acceleration Excitations," by Y. Yong and Y.K. Lin, 6/10/87, (PB88-134309, A03, MF-A01). This report is only available through NTIS (see address given above).

NCEER-87-0013 "Frequency Response of Secondary Systems Under Seismic Excitation," by J.A. HoLung, J. Cai and Y.K. Lin, 7/31/87, (PB88-134317, A05, MF-A01). This report is only available through NTIS (see address given above).

NCEER-87-0014 "Modelling Earthquake Ground Motions in Seismically Active Regions Using Parametric Time Series Methods," by G.W. Ellis and A.S. Cakmak, 8/25/87, (PB88-134283, A08, MF-A01). This report is only available through NTIS (see address given above).

NCEER-87-0015 "Detection and Assessment of Seismic Structural Damage," by E. DiPasquale and A.S. Cakmak, 8/25/87, (PB88-163712, A05, MF-A01). This report is only available through NTIS (see address given above).

NCEER-87-0016 "Pipeline Experiment at Parkfield, California," by J. Isenberg and E. Richardson, 9/15/87, (PB88-163720, A03, MF-A01). This report is available only through NTIS (see address given above).

NCEER-87-0017 "Digital Simulation of Seismic Ground Motion," by M. Shinozuka, G. Deodatis and T. Harada, 8/31/87, (PB88-155197, A04, MF-A01). This report is available only through NTIS (see address given above).

NCEER-87-0018 "Practical Considerations for Structural Control: System Uncertainty, System Time Delay and Truncation of Small Control Forces," J.N. Yang and A. Akbarpour, 8/10/87, (PB88-163738, A08, MF-A01). This report is only available through NTIS (see address given above).

NCEER-87-0019 "Modal Analysis of Nonclassically Damped Structural Systems Using Canonical Transformation," by J.N. Yang, S. Sarkani and F.X. Long, 9/27/87, (PB88-187851, A04, MF-A01).

NCEER-87-0020 "A Nonstationary Solution in Random Vibration Theory," by J.R. Red-Horse and P.D. Spanos, 11/3/87, (PB88-163746, A03, MF-A01).

NCEER-87-0021 "Horizontal Impedances for Radially Inhomogeneous Viscoelastic Soil Layers," by A.S. Veletsos and K.W. Dotson, 10/15/87, (PB88-150859, A04, MF-A01).

NCEER-87-0022 "Seismic Damage Assessment of Reinforced Concrete Members," by Y.S. Chung, C. Meyer and M. Shinozuka, 10/9/87, (PB88-150867, A05, MF-A01). This report is available only through NTIS (see address given above).

NCEER-87-0023 "Active Structural Control in Civil Engineering," by T.T. Soong, 11/11/87, (PB88-187778, A03, MF-A01).

NCEER-87-0024 "Vertical and Torsional Impedances for Radially Inhomogeneous Viscoelastic Soil Layers," by K.W. Dotson and A.S. Veletsos, 12/87, (PB88-187786, A03, MF-A01).

NCEER-87-0025 "Proceedings from the Symposium on Seismic Hazards, Ground Motions, Soil-Liquefaction and Engineering Practice in Eastern North America," October 20-22, 1987, edited by K.H. Jacob, 12/87, (PB88-188115, A23, MF-A01). This report is available only through NTIS (see address given above).

NCEER-87-0026 "Report on the Whittier-Narrows, California, Earthquake of October 1, 1987," by J. Pantelic and A. Reinhorn, 11/87, (PB88-187752, A03, MF-A01). This report is available only through NTIS (see address given above).

NCEER-87-0027 "Design of a Modular Program for Transient Nonlinear Analysis of Large 3-D Building Structures," by S. Srivastav and J.F. Abel, 12/30/87, (PB88-187950, A05, MF-A01). This report is only available through NTIS (see address given above).

NCEER-87-0028 "Second-Year Program in Research, Education and Technology Transfer," 3/8/88, (PB88-219480, A04, MF-A01).

NCEER-88-0001 "Workshop on Seismic Computer Analysis and Design of Buildings With Interactive Graphics," by W. McGuire, J.F. Abel and C.H. Conley, 1/18/88, (PB88-187760, A03, MF-A01). This report is only available through NTIS (see address given above).

NCEER-88-0002 "Optimal Control of Nonlinear Flexible Structures," by J.N. Yang, F.X. Long and D. Wong, 1/22/88, (PB88-213772, A06, MF-A01).

NCEER-88-0003 "Substructuring Techniques in the Time Domain for Primary-Secondary Structural Systems," by G.D. Manolis and G. Juhn, 2/10/88, (PB88-213780, A04, MF-A01).

NCEER-88-0004 "Iterative Seismic Analysis of Primary-Secondary Systems," by A. Singhal, L.D. Lutes and P.D. Spanos, 2/23/88, (PB88-213798, A04, MF-A01).

NCEER-88-0005 "Stochastic Finite Element Expansion for Random Media," by P.D. Spanos and R. Ghanem, 3/14/88, (PB88-213806, A03, MF-A01).

NCEER-88-0006 "Combining Structural Optimization and Structural Control," by F.Y. Cheng and C.P. Pantelides, 1/10/88, (PB88-213814, A05, MF-A01).

NCEER-88-0007 "Seismic Performance Assessment of Code-Designed Structures," by H.H-M. Hwang, J-W. Jaw and H-J. Shau, 3/20/88, (PB88-219423, A04, MF-A01). This report is only available through NTIS (see address given above).

NCEER-88-0008 "Reliability Analysis of Code-Designed Structures Under Natural Hazards," by H.H-M. Hwang, H. Ushiba and M. Shinozuka, 2/29/88, (PB88-229471, A07, MF-A01). This report is only available through NTIS (see address given above).

NCEER-88-0009 "Seismic Fragility Analysis of Shear Wall Structures," by J-W Jaw and H.H-M. Hwang, 4/30/88, (PB89-102867, A04, MF-A01).

NCEER-88-0010 "Base Isolation of a Multi-Story Building Under a Harmonic Ground Motion - A Comparison of Performances of Various Systems," by F-G Fan, G. Ahmadi and I.G. Tadjbakhsh, 5/18/88, (PB89-122238, A06, MF-A01). This report is only available through NTIS (see address given above).

NCEER-88-0011 "Seismic Floor Response Spectra for a Combined System by Green's Functions," by F.M. Lavelle, L.A. Bergman and P.D. Spanos, 5/1/88, (PB89-102875, A03, MF-A01).

NCEER-88-0012 "A New Solution Technique for Randomly Excited Hysteretic Structures," by G.Q. Cai and Y.K. Lin, 5/16/88, (PB89-102883, A03, MF-A01).

NCEER-88-0013 "A Study of Radiation Damping and Soil-Structure Interaction Effects in the Centrifuge," by K. Weissman, supervised by J.H. Prevost, 5/24/88, (PB89-144703, A06, MF-A01).

NCEER-88-0014 "Parameter Identification and Implementation of a Kinematic Plasticity Model for Frictional Soils," by J.H. Prevost and D.V. Griffiths, to be published.

NCEER-88-0015 "Two- and Three- Dimensional Dynamic Finite Element Analyses of the Long Valley Dam," by D.V. Griffiths and J.H. Prevost, 6/17/88, (PB89-144711, A04, MF-A01).

NCEER-88-0016 "Damage Assessment of Reinforced Concrete Structures in Eastern United States," by A.M. Reinhorn, M.J. Seidel, S.K. Kunnath and Y.J. Park, 6/15/88, (PB89-122220, A04, MF-A01). This report is only available through NTIS (see address given above).

NCEER-88-0017 "Dynamic Compliance of Vertically Loaded Strip Foundations in Multilayered Viscoelastic Soils," by S. Ahmad and A.S.M. Israil, 6/17/88, (PB89-102891, A04, MF-A01).

NCEER-88-0018 "An Experimental Study of Seismic Structural Response With Added Viscoelastic Dampers," by R.C. Lin, Z. Liang, T.T. Soong and R.H. Zhang, 6/30/88, (PB89-122212, A05, MF-A01). This report is available only through NTIS (see address given above).

NCEER-88-0019 "Experimental Investigation of Primary - Secondary System Interaction," by G.D. Manolis, G. Juhn and A.M. Reinhorn, 5/27/88, (PB89-122204, A04, MF-A01).

NCEER-88-0020 "A Response Spectrum Approach For Analysis of Nonclassically Damped Structures," by J.N. Yang, S. Sarkani and F.X. Long, 4/22/88, (PB89-102909, A04, MF-A01).

NCEER-88-0021 "Seismic Interaction of Structures and Soils: Stochastic Approach," by A.S. Veletsos and A.M. Prasad, 7/21/88, (PB89-122196, A04, MF-A01). This report is only available through NTIS (see address given above).

NCEER-88-0022 "Identification of the Serviceability Limit State and Detection of Seismic Structural Damage," by E. DiPasquale and A.S. Cakmak, 6/15/88, (PB89-122188, A05, MF-A01). This report is available only through NTIS (see address given above).

NCEER-88-0023 "Multi-Hazard Risk Analysis: Case of a Simple Offshore Structure," by B.K. Bhartia and E.H. Vanmarcke, 7/21/88, (PB89-145213, A05, MF-A01).

NCEER-88-0024 "Automated Seismic Design of Reinforced Concrete Buildings," by Y.S. Chung, C. Meyer and M. Shinozuka, 7/5/88, (PB89-122170, A06, MF-A01). This report is available only through NTIS (see address given above).

NCEER-88-0025 "Experimental Study of Active Control of MDOF Structures Under Seismic Excitations," by L.L. Chung, R.C. Lin, T.T. Soong and A.M. Reinhorn, 7/10/88, (PB89-122600, A04, MF-A01).

NCEER-88-0026 "Earthquake Simulation Tests of a Low-Rise Metal Structure," by J.S. Hwang, K.C. Chang, G.C. Lee and R.L. Ketter, 8/1/88, (PB89-102917, A04, MF-A01).

NCEER-88-0027 "Systems Study of Urban Response and Reconstruction Due to Catastrophic Earthquakes," by F. Kozin and H.K. Zhou, 9/22/88, (PB90-162348, A04, MF-A01).

NCEER-88-0028 "Seismic Fragility Analysis of Plane Frame Structures," by H.H-M. Hwang and Y.K. Low, 7/31/88, (PB89-131445, A06, MF-A01).

NCEER-88-0029 "Response Analysis of Stochastic Structures," by A. Kardara, C. Bucher and M. Shinozuka, 9/22/88, (PB89-174429, A04, MF-A01).

NCEER-88-0030 "Nonnormal Accelerations Due to Yielding in a Primary Structure," by D.C.K. Chen and L.D. Lutes, 9/19/88, (PB89-131437, A04, MF-A01).

NCEER-88-0031 "Design Approaches for Soil-Structure Interaction," by A.S. Veletsos, A.M. Prasad and Y. Tang, 12/30/88, (PB89-174437, A03, MF-A01). This report is available only through NTIS (see address given above).

NCEER-88-0032 "A Re-evaluation of Design Spectra for Seismic Damage Control," by C.J. Turkstra and A.G. Tallin, 11/7/88, (PB89-145221, A05, MF-A01).

NCEER-88-0033 "The Behavior and Design of Noncontact Lap Splices Subjected to Repeated Inelastic Tensile Loading," by V.E. Sagan, P. Gergely and R.N. White, 12/8/88, (PB89-163737, A08, MF-A01).

NCEER-88-0034 "Seismic Response of Pile Foundations," by S.M. Mamoon, P.K. Banerjee and S. Ahmad, 11/1/88, (PB89-145239, A04, MF-A01).

NCEER-88-0035 "Modeling of R/C Building Structures With Flexible Floor Diaphragms (IDARC2)," by A.M. Reinhorn, S.K. Kunnath and N. Panahshahi, 9/7/88, (PB89-207153, A07, MF-A01).

NCEER-88-0036 "Solution of the Dam-Reservoir Interaction Problem Using a Combination of FEM, BEM with Particular Integrals, Modal Analysis, and Substructuring," by C-S. Tsai, G.C. Lee and R.L. Ketter, 12/31/88, (PB89-207146, A04, MF-A01).

NCEER-88-0037 "Optimal Placement of Actuators for Structural Control," by F.Y. Cheng and C.P. Pantelides, 8/15/88, (PB89-162846, A05, MF-A01).

NCEER-88-0038 "Teflon Bearings in Aseismic Base Isolation: Experimental Studies and Mathematical Modeling," by A. Mokha, M.C. Constantinou and A.M. Reinhorn, 12/5/88, (PB89-218457, A10, MF-A01). This report is available only through NTIS (see address given above).

NCEER-88-0039 "Seismic Behavior of Flat Slab High-Rise Buildings in the New York City Area," by P. Weidlinger and M. Ettouney, 10/15/88, (PB90-145681, A04, MF-A01).

NCEER-88-0040 "Evaluation of the Earthquake Resistance of Existing Buildings in New York City," by P. Weidlinger and M. Ettouney, 10/15/88, to be published.

NCEER-88-0041 "Small-Scale Modeling Techniques for Reinforced Concrete Structures Subjected to Seismic Loads," by W. Kim, A. El-Attar and R.N. White, 11/22/88, (PB89-189625, A05, MF-A01).

NCEER-88-0042 "Modeling Strong Ground Motion from Multiple Event Earthquakes," by G.W. Ellis and A.S. Cakmak, 10/15/88, (PB89-174445, A03, MF-A01).

NCEER-88-0043 "Nonstationary Models of Seismic Ground Acceleration," by M. Grigoriu, S.E. Ruiz and E. Rosenblueth, 7/15/88, (PB89-189617, A04, MF-A01).

NCEER-88-0044 "SARCF User's Guide: Seismic Analysis of Reinforced Concrete Frames," by Y.S. Chung, C. Meyer and M. Shinozuka, 11/9/88, (PB89-174452, A08, MF-A01).

NCEER-88-0045 "First Expert Panel Meeting on Disaster Research and Planning," edited by J. Pantelic and J. Stoyle, 9/15/88, (PB89-174460, A05, MF-A01).

NCEER-88-0046 "Preliminary Studies of the Effect of Degrading Infill Walls on the Nonlinear Seismic Response of Steel Frames," by C.Z. Chrysostomou, P. Gergely and J.F. Abel, 12/19/88, (PB89-208383, A05, MF-A01).

NCEER-88-0047 "Reinforced Concrete Frame Component Testing Facility - Design, Construction, Instrumentation and Operation," by S.P. Pessiki, C. Conley, T. Bond, P. Gergely and R.N. White, 12/16/88, (PB89-174478, A04, MF-A01).

NCEER-89-0001 "Effects of Protective Cushion and Soil Compliancy on the Response of Equipment Within a Seismically Excited Building," by J.A. HoLung, 2/16/89, (PB89-207179, A04, MF-A01).

NCEER-89-0002 "Statistical Evaluation of Response Modification Factors for Reinforced Concrete Structures," by H.H-M. Hwang and J-W. Jaw, 2/17/89, (PB89-207187, A05, MF-A01).

NCEER-89-0003 "Hysteretic Columns Under Random Excitation," by G-Q. Cai and Y.K. Lin, 1/9/89, (PB89-196513, A03, MF-A01).

NCEER-89-0004 "Experimental Study of `Elephant Foot Bulge' Instability of Thin-Walled Metal Tanks," by Z-H. Jia and R.L. Ketter, 2/22/89, (PB89-207195, A03, MF-A01).

NCEER-89-0005 "Experiment on Performance of Buried Pipelines Across San Andreas Fault," by J. Isenberg, E. Richardson and T.D. O'Rourke, 3/10/89, (PB89-218440, A04, MF-A01). This report is available only through NTIS (see address given above).

NCEER-89-0006 "A Knowledge-Based Approach to Structural Design of Earthquake-Resistant Buildings," by M. Subramani, P. Gergely, C.H. Conley, J.F. Abel and A.H. Zaghw, 1/15/89, (PB89-218465, A06, MF-A01).

NCEER-89-0007 "Liquefaction Hazards and Their Effects on Buried Pipelines," by T.D. O'Rourke and P.A. Lane, 2/1/89, (PB89-218481, A09, MF-A01).

NCEER-89-0008 "Fundamentals of System Identification in Structural Dynamics," by H. Imai, C-B. Yun, O. Maruyama and M. Shinozuka, 1/26/89, (PB89-207211, A04, MF-A01).

NCEER-89-0009 "Effects of the 1985 Michoacan Earthquake on Water Systems and Other Buried Lifelines in Mexico," by A.G. Ayala and M.J. O'Rourke, 3/8/89, (PB89-207229, A06, MF-A01).

NCEER-89-R010 "NCEER Bibliography of Earthquake Education Materials," by K.E.K. Ross, Second Revision, 9/1/89, (PB90-125352, A05, MF-A01). This report is replaced by NCEER-92-0018.

NCEER-89-0011 "Inelastic Three-Dimensional Response Analysis of Reinforced Concrete Building Structures (IDARC-3D), Part I - Modeling," by S.K. Kunnath and A.M. Reinhorn, 4/17/89, (PB90-114612, A07, MF-A01). This report is available only through NTIS (see address given above).

NCEER-89-0012 "Recommended Modifications to ATC-14," by C.D. Poland and J.O. Malley, 4/12/89, (PB90-108648, A15, MF-A01).

NCEER-89-0013 "Repair and Strengthening of Beam-to-Column Connections Subjected to Earthquake Loading," by M. Corazao and A.J. Durrani, 2/28/89, (PB90-109885, A06, MF-A01).

NCEER-89-0014 "Program EXKAL2 for Identification of Structural Dynamic Systems," by O. Maruyama, C-B. Yun, M. Hoshiya and M. Shinozuka, 5/19/89, (PB90-109877, A09, MF-A01).

NCEER-89-0015 "Response of Frames With Bolted Semi-Rigid Connections, Part I - Experimental Study and Analytical Predictions," by P.J. DiCorso, A.M. Reinhorn, J.R. Dickerson, J.B. Radziminski and W.L. Harper, 6/1/89, to be published.

NCEER-89-0016 "ARMA Monte Carlo Simulation in Probabilistic Structural Analysis," by P.D. Spanos and M.P. Mignolet, 7/10/89, (PB90-109893, A03, MF-A01).

NCEER-89-P017 "Preliminary Proceedings from the Conference on Disaster Preparedness - The Place of Earthquake Education in Our Schools," Edited by K.E.K. Ross, 6/23/89, (PB90-108606, A03, MF-A01).

NCEER-89-0017 "Proceedings from the Conference on Disaster Preparedness - The Place of Earthquake Education in Our Schools," Edited by K.E.K. Ross, 12/31/89, (PB90-207895, A012, MF-A02). This report is available only through NTIS (see address given above).

NCEER-89-0018 "Multidimensional Models of Hysteretic Material Behavior for Vibration Analysis of Shape Memory Energy Absorbing Devices, by E.J. Graesser and F.A. Cozzarelli, 6/7/89, (PB90-164146, A04, MF-A01).

NCEER-89-0019 "Nonlinear Dynamic Analysis of Three-Dimensional Base Isolated Structures (3D-BASIS)," by S. Nagarajaiah, A.M. Reinhorn and M.C. Constantinou, 8/3/89, (PB90-161936, A06, MF-A01). This report has been replaced by NCEER-93-0011.

NCEER-89-0020 "Structural Control Considering Time-Rate of Control Forces and Control Rate Constraints," by F.Y. Cheng and C.P. Pantelides, 8/3/89, (PB90-120445, A04, MF-A01).

NCEER-89-0021 "Subsurface Conditions of Memphis and Shelby County," by K.W. Ng, T-S. Chang and H-H.M. Hwang, 7/26/89, (PB90-120437, A03, MF-A01).

NCEER-89-0022 "Seismic Wave Propagation Effects on Straight Jointed Buried Pipelines," by K. Elhmadi and M.J. O'Rourke, 8/24/89, (PB90-162322, A10, MF-A02).

NCEER-89-0023 "Workshop on Serviceability Analysis of Water Delivery Systems," edited by M. Grigoriu, 3/6/89, (PB90-127424, A03, MF-A01).

NCEER-89-0024 "Shaking Table Study of a 1/5 Scale Steel Frame Composed of Tapered Members," by K.C. Chang, J.S. Hwang and G.C. Lee, 9/18/89, (PB90-160169, A04, MF-A01).

NCEER-89-0025 "DYNA1D: A Computer Program for Nonlinear Seismic Site Response Analysis - Technical Documentation," by Jean H. Prevost, 9/14/89, (PB90-161944, A07, MF-A01). This report is available only through NTIS (see address given above).

NCEER-89-0026 "1:4 Scale Model Studies of Active Tendon Systems and Active Mass Dampers for Aseismic Protection," by A.M. Reinhorn, T.T. Soong, R.C. Lin, Y.P. Yang, Y. Fukao, H. Abe and M. Nakai, 9/15/89, (PB90-173246, A10, MF-A02). This report is available only through NTIS (see address given above).

NCEER-89-0027 "Scattering of Waves by Inclusions in a Nonhomogeneous Elastic Half Space Solved by Boundary Element Methods," by P.K. Hadley, A. Askar and A.S. Cakmak, 6/15/89, (PB90-145699, A07, MF-A01).

NCEER-89-0028 "Statistical Evaluation of Deflection Amplification Factors for Reinforced Concrete Structures," by H.H.M. Hwang, J-W. Jaw and A.L. Ch'ng, 8/31/89, (PB90-164633, A05, MF-A01).

NCEER-89-0029 "Bedrock Accelerations in Memphis Area Due to Large New Madrid Earthquakes," by H.H.M. Hwang, C.H.S. Chen and G. Yu, 11/7/89, (PB90-162330, A04, MF-A01).

NCEER-89-0030 "Seismic Behavior and Response Sensitivity of Secondary Structural Systems," by Y.Q. Chen and T.T. Soong, 10/23/89, (PB90-164658, A08, MF-A01).

NCEER-89-0031 "Random Vibration and Reliability Analysis of Primary-Secondary Structural Systems," by Y. Ibrahim, M. Grigoriu and T.T. Soong, 11/10/89, (PB90-161951, A04, MF-A01).

NCEER-89-0032 "Proceedings from the Second U.S. - Japan Workshop on Liquefaction, Large Ground Deformation and Their Effects on Lifelines, September 26-29, 1989," Edited by T.D. O'Rourke and M. Hamada, 12/1/89, (PB90-209388, A22, MF-A03).

NCEER-89-0033 "Deterministic Model for Seismic Damage Evaluation of Reinforced Concrete Structures," by J.M. Bracci, A.M. Reinhorn, J.B. Mander and S.K. Kunnath, 9/27/89, (PB91-108803, A06, MF-A01).

NCEER-89-0034 "On the Relation Between Local and Global Damage Indices," by E. DiPasquale and A.S. Cakmak, 8/15/89, (PB90-173865, A05, MF-A01).

NCEER-89-0035 "Cyclic Undrained Behavior of Nonplastic and Low Plasticity Silts," by A.J. Walker and H.E. Stewart, 7/26/89, (PB90-183518, A10, MF-A01).

NCEER-89-0036 "Liquefaction Potential of Surficial Deposits in the City of Buffalo, New York," by M. Budhu, R. Giese and L. Baumgrass, 1/17/89, (PB90-208455, A04, MF-A01).

NCEER-89-0037 "A Deterministic Assessment of Effects of Ground Motion Incoherence," by A.S. Veletsos and Y. Tang, 7/15/89, (PB90-164294, A03, MF-A01).

NCEER-89-0038 "Workshop on Ground Motion Parameters for Seismic Hazard Mapping," July 17-18, 1989, edited by R.V. Whitman, 12/1/89, (PB90-173923, A04, MF-A01).

NCEER-89-0039 "Seismic Effects on Elevated Transit Lines of the New York City Transit Authority," by C.J. Costantino, C.A. Miller and E. Heymsfield, 12/26/89, (PB90-207887, A06, MF-A01).

NCEER-89-0040 "Centrifugal Modeling of Dynamic Soil-Structure Interaction," by K. Weissman, Supervised by J.H. Prevost, 5/10/89, (PB90-207879, A07, MF-A01).

NCEER-89-0041 "Linearized Identification of Buildings With Cores for Seismic Vulnerability Assessment," by I-K. Ho and A.E. Aktan, 11/1/89, (PB90-251943, A07, MF-A01).

NCEER-90-0001 "Geotechnical and Lifeline Aspects of the October 17, 1989 Loma Prieta Earthquake in San Francisco," by T.D. O'Rourke, H.E. Stewart, F.T. Blackburn and T.S. Dickerman, 1/90, (PB90-208596, A05, MF-A01).

NCEER-90-0002 "Nonnormal Secondary Response Due to Yielding in a Primary Structure," by D.C.K. Chen and L.D. Lutes, 2/28/90, (PB90-251976, A07, MF-A01).

NCEER-90-0003 "Earthquake Education Materials for Grades K-12," by K.E.K. Ross, 4/16/90, (PB91-251984, A05, MF-A05). This report has been replaced by NCEER-92-0018.

NCEER-90-0004 "Catalog of Strong Motion Stations in Eastern North America," by R.W. Busby, 4/3/90, (PB90-251984, A05, MF-A01).

NCEER-90-0005 "NCEER Strong-Motion Data Base: A User Manual for the GeoBase Release (Version 1.0 for the Sun3)," by P. Friberg and K. Jacob, 3/31/90 (PB90-258062, A04, MF-A01).

NCEER-90-0006 "Seismic Hazard Along a Crude Oil Pipeline in the Event of an 1811-1812 Type New Madrid Earthquake," by H.H.M. Hwang and C-H.S. Chen, 4/16/90, (PB90-258054, A04, MF-A01).

NCEER-90-0007 "Site-Specific Response Spectra for Memphis Sheahan Pumping Station," by H.H.M. Hwang and C.S. Lee, 5/15/90, (PB91-108811, A05, MF-A01).

NCEER-90-0008 "Pilot Study on Seismic Vulnerability of Crude Oil Transmission Systems," by T. Ariman, R. Dobry, M. Grigoriu, F. Kozin, M. O'Rourke, T. O'Rourke and M. Shinozuka, 5/25/90, (PB91-108837, A06, MF-A01).

NCEER-90-0009 "A Program to Generate Site Dependent Time Histories: EQGEN," by G.W. Ellis, M. Srinivasan and A.S. Cakmak, 1/30/90, (PB91-108829, A04, MF-A01).

NCEER-90-0010 "Active Isolation for Seismic Protection of Operating Rooms," by M.E. Talbott, Supervised by M. Shinozuka, 6/8/9, (PB91-110205, A05, MF-A01).

NCEER-90-0011 "Program LINEARID for Identification of Linear Structural Dynamic Systems," by C-B. Yun and M. Shinozuka, 6/25/90, (PB91-110312, A08, MF-A01).

NCEER-90-0012 "Two-Dimensional Two-Phase Elasto-Plastic Seismic Response of Earth Dams," by A.N. Yiagos, Supervised by J.H. Prevost, 6/20/90, (PB91-110197, A13, MF-A02).

NCEER-90-0013 "Secondary Systems in Base-Isolated Structures: Experimental Investigation, Stochastic Response and Stochastic Sensitivity," by G.D. Manolis, G. Juhn, M.C. Constantinou and A.M. Reinhorn, 7/1/90, (PB91-110320, A08, MF-A01).

NCEER-90-0014 "Seismic Behavior of Lightly-Reinforced Concrete Column and Beam-Column Joint Details," by S.P. Pessiki, C.H. Conley, P. Gergely and R.N. White, 8/22/90, (PB91-108795, A11, MF-A02).

NCEER-90-0015 "Two Hybrid Control Systems for Building Structures Under Strong Earthquakes," by J.N. Yang and A. Danielians, 6/29/90, (PB91-125393, A04, MF-A01).

NCEER-90-0016 "Instantaneous Optimal Control with Acceleration and Velocity Feedback," by J.N. Yang and Z. Li, 6/29/90, (PB91-125401, A03, MF-A01).

NCEER-90-0017 "Reconnaissance Report on the Northern Iran Earthquake of June 21, 1990," by M. Mehrain, 10/4/90, (PB91-125377, A03, MF-A01).

NCEER-90-0018 "Evaluation of Liquefaction Potential in Memphis and Shelby County," by T.S. Chang, P.S. Tang, C.S. Lee and H. Hwang, 8/10/90, (PB91-125427, A09, MF-A01).

NCEER-90-0019 "Experimental and Analytical Study of a Combined Sliding Disc Bearing and Helical Steel Spring Isolation System," by M.C. Constantinou, A.S. Mokha and A.M. Reinhorn, 10/4/90, (PB91-125385, A06, MF-A01). This report is available only through NTIS (see address given above).

NCEER-90-0020 "Experimental Study and Analytical Prediction of Earthquake Response of a Sliding Isolation System with a Spherical Surface," by A.S. Mokha, M.C. Constantinou and A.M. Reinhorn, 10/11/90, (PB91-125419, A05, MF-A01).

NCEER-90-0021 "Dynamic Interaction Factors for Floating Pile Groups," by G. Gazetas, K. Fan, A. Kaynia and E. Kausel, 9/10/90, (PB91-170381, A05, MF-A01).

NCEER-90-0022 "Evaluation of Seismic Damage Indices for Reinforced Concrete Structures," by S. Rodriguez-Gomez and A.S. Cakmak, 9/30/90, PB91-171322, A06, MF-A01).

NCEER-90-0023 "Study of Site Response at a Selected Memphis Site," by H. Desai, S. Ahmad, E.S. Gazetas and M.R. Oh, 10/11/90, (PB91-196857, A03, MF-A01).

NCEER-90-0024 "A User's Guide to Strongmo: Version 1.0 of NCEER's Strong-Motion Data Access Tool for PCs and Terminals," by P.A. Friberg and C.A.T. Susch, 11/15/90, (PB91-171272, A03, MF-A01).

NCEER-90-0025 "A Three-Dimensional Analytical Study of Spatial Variability of Seismic Ground Motions," by L-L. Hong and A.H.-S. Ang, 10/30/90, (PB91-170399, A09, MF-A01).

NCEER-90-0026 "MUMOID User's Guide - A Program for the Identification of Modal Parameters," by S. Rodriguez-Gomez and E. DiPasquale, 9/30/90, (PB91-171298, A04, MF-A01).

NCEER-90-0027 "SARCF-II User's Guide - Seismic Analysis of Reinforced Concrete Frames," by S. Rodriguez-Gomez, Y.S. Chung and C. Meyer, 9/30/90, (PB91-171280, A05, MF-A01).

NCEER-90-0028 "Viscous Dampers: Testing, Modeling and Application in Vibration and Seismic Isolation," by N. Makris and M.C. Constantinou, 12/20/90 (PB91-190561, A06, MF-A01).

NCEER-90-0029 "Soil Effects on Earthquake Ground Motions in the Memphis Area," by H. Hwang, C.S. Lee, K.W. Ng and T.S. Chang, 8/2/90, (PB91-190751, A05, MF-A01).

NCEER-91-0001 "Proceedings from the Third Japan-U.S. Workshop on Earthquake Resistant Design of Lifeline Facilities and Countermeasures for Soil Liquefaction, December 17-19, 1990," edited by T.D. O'Rourke and M. Hamada, 2/1/91, (PB91-179259, A99, MF-A04).

NCEER-91-0002 "Physical Space Solutions of Non-Proportionally Damped Systems," by M. Tong, Z. Liang and G.C. Lee, 1/15/91, (PB91-179242, A04, MF-A01).

NCEER-91-0003 "Seismic Response of Single Piles and Pile Groups," by K. Fan and G. Gazetas, 1/10/91, (PB92-174994, A04, MF-A01).

NCEER-91-0004 "Damping of Structures: Part 1 - Theory of Complex Damping," by Z. Liang and G. Lee, 10/10/91, (PB92-197235, A12, MF-A03).

NCEER-91-0005 "3D-BASIS - Nonlinear Dynamic Analysis of Three Dimensional Base Isolated Structures: Part II," by S. Nagarajaiah, A.M. Reinhorn and M.C. Constantinou, 2/28/91, (PB91-190553, A07, MF-A01). This report has been replaced by NCEER-93-0011.

NCEER-91-0006 "A Multidimensional Hysteretic Model for Plasticity Deforming Metals in Energy Absorbing Devices," by E.J. Graesser and F.A. Cozzarelli, 4/9/91, (PB92-108364, A04, MF-A01).

NCEER-91-0007 "A Framework for Customizable Knowledge-Based Expert Systems with an Application to a KBES for Evaluating the Seismic Resistance of Existing Buildings," by E.G. Ibarra-Anaya and S.J. Fenves, 4/9/91, (PB91-210930, A08, MF-A01).

NCEER-91-0008 "Nonlinear Analysis of Steel Frames with Semi-Rigid Connections Using the Capacity Spectrum Method," by G.G. Deierlein, S-H. Hsieh, Y-J. Shen and J.F. Abel, 7/2/91, (PB92-113828, A05, MF-A01).

NCEER-91-0009 "Earthquake Education Materials for Grades K-12," by K.E.K. Ross, 4/30/91, (PB91-212142, A06, MF-A01). This report has been replaced by NCEER-92-0018.

NCEER-91-0010 "Phase Wave Velocities and Displacement Phase Differences in a Harmonically Oscillating Pile," by N. Makris and G. Gazetas, 7/8/91, (PB92-108356, A04, MF-A01).

NCEER-91-0011 "Dynamic Characteristics of a Full-Size Five-Story Steel Structure and a 2/5 Scale Model," by K.C. Chang, G.C. Yao, G.C. Lee, D.S. Hao and Y.C. Yeh," 7/2/91, (PB93-116648, A06, MF-A02).

NCEER-91-0012 "Seismic Response of a 2/5 Scale Steel Structure with Added Viscoelastic Dampers," by K.C. Chang, T.T. Soong, S-T. Oh and M.L. Lai, 5/17/91, (PB92-110816, A05, MF-A01).

NCEER-91-0013 "Earthquake Response of Retaining Walls; Full-Scale Testing and Computational Modeling," by S. Alampalli and A-W.M. Elgamal, 6/20/91, to be published.

NCEER-91-0014 "3D-BASIS-M: Nonlinear Dynamic Analysis of Multiple Building Base Isolated Structures," by P.C. Tsopelas, S. Nagarajaiah, M.C. Constantinou and A.M. Reinhorn, 5/28/91, (PB92-113885, A09, MF-A02).

NCEER-91-0015 "Evaluation of SEAOC Design Requirements for Sliding Isolated Structures," by D. Theodossiou and M.C. Constantinou, 6/10/91, (PB92-114602, A11, MF-A03).

NCEER-91-0016 "Closed-Loop Modal Testing of a 27-Story Reinforced Concrete Flat Plate-Core Building," by H.R. Somaprasad, T. Toksoy, H. Yoshiyuki and A.E. Aktan, 7/15/91, (PB92-129980, A07, MF-A02).

NCEER-91-0017 "Shake Table Test of a 1/6 Scale Two-Story Lightly Reinforced Concrete Building," by A.G. El-Attar, R.N. White and P. Gergely, 2/28/91, (PB92-222447, A06, MF-A02).

NCEER-91-0018 "Shake Table Test of a 1/8 Scale Three-Story Lightly Reinforced Concrete Building," by A.G. El-Attar, R.N. White and P. Gergely, 2/28/91, (PB93-116630, A08, MF-A02).

NCEER-91-0019 "Transfer Functions for Rigid Rectangular Foundations," by A.S. Veletsos, A.M. Prasad and W.H. Wu, 7/31/91, to be published.

NCEER-91-0020 "Hybrid Control of Seismic-Excited Nonlinear and Inelastic Structural Systems," by J.N. Yang, Z. Li and A. Danielians, 8/1/91, (PB92-143171, A06, MF-A02).

NCEER-91-0021 "The NCEER-91 Earthquake Catalog: Improved Intensity-Based Magnitudes and Recurrence Relations for U.S. Earthquakes East of New Madrid," by L. Seeber and J.G. Armbruster, 8/28/91, (PB92-176742, A06, MF-A02).

NCEER-91-0022 "Proceedings from the Implementation of Earthquake Planning and Education in Schools: The Need for Change - The Roles of the Changemakers," by K.E.K. Ross and F. Winslow, 7/23/91, (PB92-129998, A12, MF-A03).

NCEER-91-0023 "A Study of Reliability-Based Criteria for Seismic Design of Reinforced Concrete Frame Buildings," by H.H.M. Hwang and H-M. Hsu, 8/10/91, (PB92-140235, A09, MF-A02).

NCEER-91-0024 "Experimental Verification of a Number of Structural System Identification Algorithms," by R.G. Ghanem, H. Gavin and M. Shinozuka, 9/18/91, (PB92-176577, A18, MF-A04).

NCEER-91-0025 "Probabilistic Evaluation of Liquefaction Potential," by H.H.M. Hwang and C.S. Lee," 11/25/91, (PB92-143429, A05, MF-A01).

NCEER-91-0026 "Instantaneous Optimal Control for Linear, Nonlinear and Hysteretic Structures - Stable Controllers," by J.N. Yang and Z. Li, 11/15/91, (PB92-163807, A04, MF-A01).

NCEER-91-0027 "Experimental and Theoretical Study of a Sliding Isolation System for Bridges," by M.C. Constantinou, A. Kartoum, A.M. Reinhorn and P. Bradford, 11/15/91, (PB92-176973, A10, MF-A03).

NCEER-92-0001 "Case Studies of Liquefaction and Lifeline Performance During Past Earthquakes, Volume 1: Japanese Case Studies," Edited by M. Hamada and T. O'Rourke, 2/17/92, (PB92-197243, A18, MF-A04).

NCEER-92-0002 "Case Studies of Liquefaction and Lifeline Performance During Past Earthquakes, Volume 2: United States Case Studies," Edited by T. O'Rourke and M. Hamada, 2/17/92, (PB92-197250, A20, MF-A04).

NCEER-92-0003 "Issues in Earthquake Education," Edited by K. Ross, 2/3/92, (PB92-222389, A07, MF-A02).

NCEER-92-0004 "Proceedings from the First U.S. - Japan Workshop on Earthquake Protective Systems for Bridges," Edited by I.G. Buckle, 2/4/92, (PB94-142239, A99, MF-A06).

NCEER-92-0005 "Seismic Ground Motion from a Haskell-Type Source in a Multiple-Layered Half-Space," A.P. Theoharis, G. Deodatis and M. Shinozuka, 1/2/92, to be published.

NCEER-92-0006 "Proceedings from the Site Effects Workshop," Edited by R. Whitman, 2/29/92, (PB92-197201, A04, MF-A01).

NCEER-92-0007 "Engineering Evaluation of Permanent Ground Deformations Due to Seismically-Induced Liquefaction," by M.H. Baziar, R. Dobry and A-W.M. Elgamal, 3/24/92, (PB92-222421, A13, MF-A03).

NCEER-92-0008 "A Procedure for the Seismic Evaluation of Buildings in the Central and Eastern United States," by C.D. Poland and J.O. Malley, 4/2/92, (PB92-222439, A20, MF-A04).

NCEER-92-0009 "Experimental and Analytical Study of a Hybrid Isolation System Using Friction Controllable Sliding Bearings," by M.Q. Feng, S. Fujii and M. Shinozuka, 5/15/92, (PB93-150282, A06, MF-A02).

NCEER-92-0010 "Seismic Resistance of Slab-Column Connections in Existing Non-Ductile Flat-Plate Buildings," by A.J. Durrani and Y. Du, 5/18/92, (PB93-116812, A06, MF-A02).

NCEER-92-0011 "The Hysteretic and Dynamic Behavior of Brick Masonry Walls Upgraded by Ferrocement Coatings Under Cyclic Loading and Strong Simulated Ground Motion," by H. Lee and S.P. Prawel, 5/11/92, to be published.

NCEER-92-0012 "Study of Wire Rope Systems for Seismic Protection of Equipment in Buildings," by G.F. Demetriades, M.C. Constantinou and A.M. Reinhorn, 5/20/92, (PB93-116655, A08, MF-A02).

NCEER-92-0013 "Shape Memory Structural Dampers: Material Properties, Design and Seismic Testing," by P.R. Witting and F.A. Cozzarelli, 5/26/92, (PB93-116663, A05, MF-A01).

NCEER-92-0014 "Longitudinal Permanent Ground Deformation Effects on Buried Continuous Pipelines," by M.J. O'Rourke, and C. Nordberg, 6/15/92, (PB93-116671, A08, MF-A02).

NCEER-92-0015 "A Simulation Method for Stationary Gaussian Random Functions Based on the Sampling Theorem," by M. Grigoriu and S. Balopoulou, 6/11/92, (PB93-127496, A05, MF-A01).

NCEER-92-0016 "Gravity-Load-Designed Reinforced Concrete Buildings: Seismic Evaluation of Existing Construction and Detailing Strategies for Improved Seismic Resistance," by G.W. Hoffmann, S.K. Kunnath, A.M. Reinhorn and J.B. Mander, 7/15/92, (PB94-142007, A08, MF-A02).

NCEER-92-0017 "Observations on Water System and Pipeline Performance in the Limón Area of Costa Rica Due to the April 22, 1991 Earthquake," by M. O'Rourke and D. Ballantyne, 6/30/92, (PB93-126811, A06, MF-A02).

NCEER-92-0018 "Fourth Edition of Earthquake Education Materials for Grades K-12," Edited by K.E.K. Ross, 8/10/92, (PB93-114023, A07, MF-A02).

NCEER-92-0019 "Proceedings from the Fourth Japan-U.S. Workshop on Earthquake Resistant Design of Lifeline Facilities and Countermeasures for Soil Liquefaction," Edited by M. Hamada and T.D. O'Rourke, 8/12/92, (PB93-163939, A99, MF-E11).

NCEER-92-0020 "Active Bracing System: A Full Scale Implementation of Active Control," by A.M. Reinhorn, T.T. Soong, R.C. Lin, M.A. Riley, Y.P. Wang, S. Aizawa and M. Higashino, 8/14/92, (PB93-127512, A06, MF-A02).

NCEER-92-0021 "Empirical Analysis of Horizontal Ground Displacement Generated by Liquefaction-Induced Lateral Spreads," by S.F. Bartlett and T.L. Youd, 8/17/92, (PB93-188241, A06, MF-A02).

NCEER-92-0022 "IDARC Version 3.0: Inelastic Damage Analysis of Reinforced Concrete Structures," by S.K. Kunnath, A.M. Reinhorn and R.F. Lobo, 8/31/92, (PB93-227502, A07, MF-A02).

NCEER-92-0023 "A Semi-Empirical Analysis of Strong-Motion Peaks in Terms of Seismic Source, Propagation Path and Local Site Conditions, by M. Kamiyama, M.J. O'Rourke and R. Flores-Berrones, 9/9/92, (PB93-150266, A08, MF-A02).

NCEER-92-0024 "Seismic Behavior of Reinforced Concrete Frame Structures with Nonductile Details, Part I: Summary of Experimental Findings of Full Scale Beam-Column Joint Tests," by A. Beres, R.N. White and P. Gergely, 9/30/92, (PB93-227783, A05, MF-A01).

NCEER-92-0025 "Experimental Results of Repaired and Retrofitted Beam-Column Joint Tests in Lightly Reinforced Concrete Frame Buildings," by A. Beres, S. El-Borgi, R.N. White and P. Gergely, 10/29/92, (PB93-227791, A05, MF-A01).

NCEER-92-0026 "A Generalization of Optimal Control Theory: Linear and Nonlinear Structures," by J.N. Yang, Z. Li and S. Vongchavalitkul, 11/2/92, (PB93-188621, A05, MF-A01).

NCEER-92-0027 "Seismic Resistance of Reinforced Concrete Frame Structures Designed Only for Gravity Loads: Part I - Design and Properties of a One-Third Scale Model Structure," by J.M. Bracci, A.M. Reinhorn and J.B. Mander, 12/1/92, (PB94-104502, A08, MF-A02).

NCEER-92-0028 "Seismic Resistance of Reinforced Concrete Frame Structures Designed Only for Gravity Loads: Part II - Experimental Performance of Subassemblages," by L.E. Aycardi, J.B. Mander and A.M. Reinhorn, 12/1/92, (PB94-104510, A08, MF-A02).

NCEER-92-0029 "Seismic Resistance of Reinforced Concrete Frame Structures Designed Only for Gravity Loads: Part III - Experimental Performance and Analytical Study of a Structural Model," by J.M. Bracci, A.M. Reinhorn and J.B. Mander, 12/1/92, (PB93-227528, A09, MF-A01).

NCEER-92-0030 "Evaluation of Seismic Retrofit of Reinforced Concrete Frame Structures: Part I - Experimental Performance of Retrofitted Subassemblages," by D. Choudhuri, J.B. Mander and A.M. Reinhorn, 12/8/92, (PB93-198307, A07, MF-A02).

NCEER-92-0031 "Evaluation of Seismic Retrofit of Reinforced Concrete Frame Structures: Part II - Experimental Performance and Analytical Study of a Retrofitted Structural Model," by J.M. Bracci, A.M. Reinhorn and J.B. Mander, 12/8/92, (PB93-198315, A09, MF-A03).

NCEER-92-0032 "Experimental and Analytical Investigation of Seismic Response of Structures with Supplemental Fluid Viscous Dampers," by M.C. Constantinou and M.D. Symans, 12/21/92, (PB93-191435, A10, MF-A03). This report is available only through NTIS (see address given above).

NCEER-92-0033 "Reconnaissance Report on the Cairo, Egypt Earthquake of October 12, 1992," by M. Khater, 12/23/92, (PB93-188621, A03, MF-A01).

NCEER-92-0034 "Low-Level Dynamic Characteristics of Four Tall Flat-Plate Buildings in New York City," by H. Gavin, S. Yuan, J. Grossman, E. Pekelis and K. Jacob, 12/28/92, (PB93-188217, A07, MF-A02).

NCEER-93-0001 "An Experimental Study on the Seismic Performance of Brick-Infilled Steel Frames With and Without Retrofit," by J.B. Mander, B. Nair, K. Wojtkowski and J. Ma, 1/29/93, (PB93-227510, A07, MF-A02).

NCEER-93-0002 "Social Accounting for Disaster Preparedness and Recovery Planning," by S. Cole, E. Pantoja and V. Razak, 2/22/93, (PB94-142114, A12, MF-A03).

NCEER-93-0003 "Assessment of 1991 NEHRP Provisions for Nonstructural Components and Recommended Revisions," by T.T. Soong, G. Chen, Z. Wu, R-H. Zhang and M. Grigoriu, 3/1/93, (PB93-188639, A06, MF-A02).

NCEER-93-0004 "Evaluation of Static and Response Spectrum Analysis Procedures of SEAOC/UBC for Seismic Isolated Structures," by C.W. Winters and M.C. Constantinou, 3/23/93, (PB93-198299, A10, MF-A03).

NCEER-93-0005 "Earthquakes in the Northeast - Are We Ignoring the Hazard? A Workshop on Earthquake Science and Safety for Educators," edited by K.E.K. Ross, 4/2/93, (PB94-103066, A09, MF-A02).

NCEER-93-0006 "Inelastic Response of Reinforced Concrete Structures with Viscoelastic Braces," by R.F. Lobo, J.M. Bracci, K.L. Shen, A.M. Reinhorn and T.T. Soong, 4/5/93, (PB93-227486, A05, MF-A02).

NCEER-93-0007 "Seismic Testing of Installation Methods for Computers and Data Processing Equipment," by K. Kosar, T.T. Soong, K.L. Shen, J.A. HoLung and Y.K. Lin, 4/12/93, (PB93-198299, A07, MF-A02).

NCEER-93-0008 "Retrofit of Reinforced Concrete Frames Using Added Dampers," by A. Reinhorn, M. Constantinou and C. Li, to be published.

NCEER-93-0009 "Seismic Behavior and Design Guidelines for Steel Frame Structures with Added Viscoelastic Dampers," by K.C. Chang, M.L. Lai, T.T. Soong, D.S. Hao and Y.C. Yeh, 5/1/93, (PB94-141959, A07, MF-A02).

NCEER-93-0010 "Seismic Performance of Shear-Critical Reinforced Concrete Bridge Piers," by J.B. Mander, S.M. Waheed, M.T.A. Chaudhary and S.S. Chen, 5/12/93, (PB93-227494, A08, MF-A02).

NCEER-93-0011 "3D-BASIS-TABS: Computer Program for Nonlinear Dynamic Analysis of Three Dimensional Base Isolated Structures," by S. Nagarajaiah, C. Li, A.M. Reinhorn and M.C. Constantinou, 8/2/93, (PB94-141819, A09, MF-A02).

NCEER-93-0012 "Effects of Hydrocarbon Spills from an Oil Pipeline Break on Ground Water," by O.J. Helweg and H.H.M. Hwang, 8/3/93, (PB94-141942, A06, MF-A02).

NCEER-93-0013 "Simplified Procedures for Seismic Design of Nonstructural Components and Assessment of Current Code Provisions," by M.P. Singh, L.E. Suarez, E.E. Matheu and G.O. Maldonado, 8/4/93, (PB94-141827, A09, MF-A02).

NCEER-93-0014 "An Energy Approach to Seismic Analysis and Design of Secondary Systems," by G. Chen and T.T. Soong, 8/6/93, (PB94-142767, A11, MF-A03).

NCEER-93-0015 "Proceedings from School Sites: Becoming Prepared for Earthquakes - Commemorating the Third Anniversary of the Loma Prieta Earthquake," Edited by F.E. Winslow and K.E.K. Ross, 8/16/93, (PB94-154275, A16, MF-A02).

NCEER-93-0016 "Reconnaissance Report of Damage to Historic Monuments in Cairo, Egypt Following the October 12, 1992 Dahshur Earthquake," by D. Sykora, D. Look, G. Croci, E. Karaesmen and E. Karaesmen, 8/19/93, (PB94-142221, A08, MF-A02).

NCEER-93-0017 "The Island of Guam Earthquake of August 8, 1993," by S.W. Swan and S.K. Harris, 9/30/93, (PB94-141843, A04, MF-A01).

NCEER-93-0018 "Engineering Aspects of the October 12, 1992 Egyptian Earthquake," by A.W. Elgamal, M. Amer, K. Adalier and A. Abul-Fadl, 10/7/93, (PB94-141983, A05, MF-A01).

NCEER-93-0019 "Development of an Earthquake Motion Simulator and its Application in Dynamic Centrifuge Testing," by I. Krstelj, Supervised by J.H. Prevost, 10/23/93, (PB94-181773, A-10, MF-A03).

NCEER-93-0020 "NCEER-Taisei Corporation Research Program on Sliding Seismic Isolation Systems for Bridges: Experimental and Analytical Study of a Friction Pendulum System (FPS)," by M.C. Constantinou, P. Tsopelas, Y-S. Kim and S. Okamoto, 11/1/93, (PB94-142775, A08, MF-A02).

NCEER-93-0021 "Finite Element Modeling of Elastomeric Seismic Isolation Bearings," by L.J. Billings, Supervised by R. Shepherd, 11/8/93, to be published.

NCEER-93-0022 "Seismic Vulnerability of Equipment in Critical Facilities: Life-Safety and Operational Consequences," by K. Porter, G.S. Johnson, M.M. Zadeh, C. Scawthorn and S. Eder, 11/24/93, (PB94-181765, A16, MF-A03).

NCEER-93-0023 "Hokkaido Nansei-oki, Japan Earthquake of July 12, 1993, by P.I. Yanev and C.R. Scawthorn, 12/23/93, (PB94-181500, A07, MF-A01).

NCEER-94-0001 "An Evaluation of Seismic Serviceability of Water Supply Networks with Application to the San Francisco Auxiliary Water Supply System," by I. Markov, Supervised by M. Grigoriu and T. O'Rourke, 1/21/94, (PB94-204013, A07, MF-A02).

NCEER-94-0002 "NCEER-Taisei Corporation Research Program on Sliding Seismic Isolation Systems for Bridges: Experimental and Analytical Study of Systems Consisting of Sliding Bearings, Rubber Restoring Force Devices and Fluid Dampers," Volumes I and II, by P. Tsopelas, S. Okamoto, M.C. Constantinou, D. Ozaki and S. Fujii, 2/4/94, (PB94-181740, A09, MF-A02 and PB94-181757, A12, MF-A03).

NCEER-94-0003 "A Markov Model for Local and Global Damage Indices in Seismic Analysis," by S. Rahman and M. Grigoriu, 2/18/94, (PB94-206000, A12, MF-A03).

NCEER-94-0004 "Proceedings from the NCEER Workshop on Seismic Response of Masonry Infills," edited by D.P. Abrams, 3/1/94, (PB94-180783, A07, MF-A02).

NCEER-94-0005 "The Northridge, California Earthquake of January 17, 1994: General Reconnaissance Report," edited by J.D. Goltz, 3/11/94, (PB94-193943, A10, MF-A03).

NCEER-94-0006 "Seismic Energy Based Fatigue Damage Analysis of Bridge Columns: Part I - Evaluation of Seismic Capacity," by G.A. Chang and J.B. Mander, 3/14/94, (PB94-219185, A11, MF-A03).

NCEER-94-0007 "Seismic Isolation of Multi-Story Frame Structures Using Spherical Sliding Isolation Systems," by T.M. Al-Hussaini, V.A. Zayas and M.C. Constantinou, 3/17/94, (PB94-193745, A09, MF-A02).

NCEER-94-0008 "The Northridge, California Earthquake of January 17, 1994: Performance of Highway Bridges," edited by I.G. Buckle, 3/24/94, (PB94-193851, A06, MF-A02).

NCEER-94-0009 "Proceedings of the Third U.S.-Japan Workshop on Earthquake Protective Systems for Bridges," edited by I.G. Buckle and I. Friedland, 3/31/94, (PB94-195815, A99, MF-A06).

NCEER-94-0010 "3D-BASIS-ME: Computer Program for Nonlinear Dynamic Analysis of Seismically Isolated Single and Multiple Structures and Liquid Storage Tanks," by P.C. Tsopelas, M.C. Constantinou and A.M. Reinhorn, 4/12/94, (PB94-204922, A09, MF-A02).

NCEER-94-0011 "The Northridge, California Earthquake of January 17, 1994: Performance of Gas Transmission Pipelines," by T.D. O'Rourke and M.C. Palmer, 5/16/94, (PB94-204989, A05, MF-A01).

NCEER-94-0012 "Feasibility Study of Replacement Procedures and Earthquake Performance Related to Gas Transmission Pipelines," by T.D. O'Rourke and M.C. Palmer, 5/25/94, (PB94-206638, A09, MF-A02).

NCEER-94-0013 "Seismic Energy Based Fatigue Damage Analysis of Bridge Columns: Part II - Evaluation of Seismic Demand," by G.A. Chang and J.B. Mander, 6/1/94, (PB95-18106, A08, MF-A02).

NCEER-94-0014 "NCEER-Taisei Corporation Research Program on Sliding Seismic Isolation Systems for Bridges: Experimental and Analytical Study of a System Consisting of Sliding Bearings and Fluid Restoring Force/Damping Devices," by P. Tsopelas and M.C. Constantinou, 6/13/94, (PB94-219144, A10, MF-A03).

NCEER-94-0015 "Generation of Hazard-Consistent Fragility Curves for Seismic Loss Estimation Studies," by H. Hwang and J-R. Huo, 6/14/94, (PB95-181996, A09, MF-A02).

NCEER-94-0016 "Seismic Study of Building Frames with Added Energy-Absorbing Devices," by W.S. Pong, C.S. Tsai and G.C. Lee, 6/20/94, (PB94-219136, A10, A03).

NCEER-94-0017 "Sliding Mode Control for Seismic-Excited Linear and Nonlinear Civil Engineering Structures," by J. Yang, J. Wu, A. Agrawal and Z. Li, 6/21/94, (PB95-138483, A06, MF-A02).

NCEER-94-0018 "3D-BASIS-TABS Version 2.0: Computer Program for Nonlinear Dynamic Analysis of Three Dimensional Base Isolated Structures," by A.M. Reinhorn, S. Nagarajaiah, M.C. Constantinou, P. Tsopelas and R. Li, 6/22/94, (PB95-182176, A08, MF-A02).

NCEER-94-0019 "Proceedings of the International Workshop on Civil Infrastructure Systems: Application of Intelligent Systems and Advanced Materials on Bridge Systems," Edited by G.C. Lee and K.C. Chang, 7/18/94, (PB95-252474, A20, MF-A04).

NCEER-94-0020 "Study of Seismic Isolation Systems for Computer Floors," by V. Lambrou and M.C. Constantinou, 7/19/94, (PB95-138533, A10, MF-A03).

NCEER-94-0021 "Proceedings of the U.S.-Italian Workshop on Guidelines for Seismic Evaluation and Rehabilitation of Unreinforced Masonry Buildings," Edited by D.P. Abrams and G.M. Calvi, 7/20/94, (PB95-138749, A13, MF-A03).

NCEER-94-0022 "NCEER-Taisei Corporation Research Program on Sliding Seismic Isolation Systems for Bridges: Experimental and Analytical Study of a System Consisting of Lubricated PTFE Sliding Bearings and Mild Steel Dampers," by P. Tsopelas and M.C. Constantinou, 7/22/94, (PB95-182184, A08, MF-A02).

NCEER-94-0023 “Development of Reliability-Based Design Criteria for Buildings Under Seismic Load,” by Y.K. Wen, H. Hwang and M. Shinozuka, 8/1/94, (PB95-211934, A08, MF-A02).

NCEER-94-0024 “Experimental Verification of Acceleration Feedback Control Strategies for an Active Tendon System,” by S.J. Dyke, B.F. Spencer, Jr., P. Quast, M.K. Sain, D.C. Kaspari, Jr. and T.T. Soong, 8/29/94, (PB95-212320, A05, MF-A01).

NCEER-94-0025 “Seismic Retrofitting Manual for Highway Bridges,” Edited by I.G. Buckle and I.F. Friedland, published by the Federal Highway Administration (PB95-212676, A15, MF-A03).

NCEER-94-0026 “Proceedings from the Fifth U.S.-Japan Workshop on Earthquake Resistant Design of Lifeline Facilities and Countermeasures Against Soil Liquefaction,” Edited by T.D. O’Rourke and M. Hamada, 11/7/94, (PB95-220802, A99, MF-E08).

NCEER-95-0001 "Experimental and Analytical Investigation of Seismic Retrofit of Structures with Supplemental Damping: Part 1 - Fluid Viscous Damping Devices," by A.M. Reinhorn, C. Li and M.C. Constantinou, 1/3/95, (PB95-266599, A09, MF-A02).

NCEER-95-0002 "Experimental and Analytical Study of Low-Cycle Fatigue Behavior of Semi-Rigid Top-And-Seat Angle Connections," by G. Pekcan, J.B. Mander and S.S. Chen, 1/5/95, (PB95-220042, A07, MF-A02).

NCEER-95-0003 "NCEER-ATC Joint Study on Fragility of Buildings," by T. Anagnos, C. Rojahn and A.S. Kiremidjian, 1/20/95, (PB95-220026, A06, MF-A02).

NCEER-95-0004 "Nonlinear Control Algorithms for Peak Response Reduction," by Z. Wu, T.T. Soong, V. Gattulli and R.C. Lin, 2/16/95, (PB95-220349, A05, MF-A01).

NCEER-95-0005 "Pipeline Replacement Feasibility Study: A Methodology for Minimizing Seismic and Corrosion Risks to Underground Natural Gas Pipelines," by R.T. Eguchi, H.A. Seligson and D.G. Honegger, 3/2/95, (PB95-252326, A06, MF-A02).

NCEER-95-0006 "Evaluation of Seismic Performance of an 11-Story Frame Building During the 1994 Northridge Earthquake," by F. Naeim, R. DiSulio, K. Benuska, A. Reinhorn and C. Li, to be published.

NCEER-95-0007 "Prioritization of Bridges for Seismic Retrofitting," by N. Basöz and A.S. Kiremidjian, 4/24/95, (PB95-252300, A08, MF-A02).

NCEER-95-0008 "Method for Developing Motion Damage Relationships for Reinforced Concrete Frames," by A. Singhal and A.S. Kiremidjian, 5/11/95, (PB95-266607, A06, MF-A02).

NCEER-95-0009 "Experimental and Analytical Investigation of Seismic Retrofit of Structures with Supplemental Damping: Part II - Friction Devices," by C. Li and A.M. Reinhorn, 7/6/95, (PB96-128087, A11, MF-A03).

NCEER-95-0010 "Experimental Performance and Analytical Study of a Non-Ductile Reinforced Concrete Frame Structure Retrofitted with Elastomeric Spring Dampers," by G. Pekcan, J.B. Mander and S.S. Chen, 7/14/95, (PB96-137161, A08, MF-A02).

NCEER-95-0011 "Development and Experimental Study of Semi-Active Fluid Damping Devices for Seismic Protection of Structures," by M.D. Symans and M.C. Constantinou, 8/3/95, (PB96-136940, A23, MF-A04).

NCEER-95-0012 "Real-Time Structural Parameter Modification (RSPM): Development of Innervated Structures," by Z. Liang, M. Tong and G.C. Lee, 4/11/95, (PB96-137153, A06, MF-A01).

NCEER-95-0013 "Experimental and Analytical Investigation of Seismic Retrofit of Structures with Supplemental Damping: Part III - Viscous Damping Walls," by A.M. Reinhorn and C. Li, 10/1/95, (PB96-176409, A11, MF-A03).

NCEER-95-0014 "Seismic Fragility Analysis of Equipment and Structures in a Memphis Electric Substation," by J-R. Huo and H.H.M. Hwang, 8/10/95, (PB96-128087, A09, MF-A02).

NCEER-95-0015 "The Hanshin-Awaji Earthquake of January 17, 1995: Performance of Lifelines," Edited by M. Shinozuka, 11/3/95, (PB96-176383, A15, MF-A03).

NCEER-95-0016 "Highway Culvert Performance During Earthquakes," by T.L. Youd and C.J. Beckman, available as NCEER-96-0015.

NCEER-95-0017 "The Hanshin-Awaji Earthquake of January 17, 1995: Performance of Highway Bridges," Edited by I.G. Buckle, 12/1/95, to be published.

NCEER-95-0018 "Modeling of Masonry Infill Panels for Structural Analysis," by A.M. Reinhorn, A. Madan, R.E. Valles, Y. Reichmann and J.B. Mander, 12/8/95, (PB97-110886, MF-A01, A06).

NCEER-95-0019 "Optimal Polynomial Control for Linear and Nonlinear Structures," by A.K. Agrawal and J.N. Yang, 12/11/95, (PB96-168737, A07, MF-A02).

NCEER-95-0020 "Retrofit of Non-Ductile Reinforced Concrete Frames Using Friction Dampers," by R.S. Rao, P. Gergely and R.N. White, 12/22/95, (PB97-133508, A10, MF-A02).

NCEER-95-0021 "Parametric Results for Seismic Response of Pile-Supported Bridge Bents," by G. Mylonakis, A. Nikolaou and G. Gazetas, 12/22/95, (PB97-100242, A12, MF-A03).

NCEER-95-0022 "Kinematic Bending Moments in Seismically Stressed Piles," by A. Nikolaou, G. Mylonakis and G. Gazetas, 12/23/95, (PB97-113914, MF-A03, A13).

NCEER-96-0001 "Dynamic Response of Unreinforced Masonry Buildings with Flexible Diaphragms," by A.C. Costley and D.P. Abrams," 10/10/96, (PB97-133573, MF-A03, A15).

NCEER-96-0002 "State of the Art Review: Foundations and Retaining Structures," by I. Po Lam, to be published.

NCEER-96-0003 "Ductility of Rectangular Reinforced Concrete Bridge Columns with Moderate Confinement," by N. Wehbe, M. Saiidi, D. Sanders and B. Douglas, 11/7/96, (PB97-133557, A06, MF-A02).

NCEER-96-0004 "Proceedings of the Long-Span Bridge Seismic Research Workshop," edited by I.G. Buckle and I.M. Friedland, to be published.

NCEER-96-0005 "Establish Representative Pier Types for Comprehensive Study: Eastern United States," by J. Kulicki and Z. Prucz, 5/28/96, (PB98-119217, A07, MF-A02).

NCEER-96-0006 "Establish Representative Pier Types for Comprehensive Study: Western United States," by R. Imbsen, R.A. Schamber and T.A. Osterkamp, 5/28/96, (PB98-118607, A07, MF-A02).

NCEER-96-0007 "Nonlinear Control Techniques for Dynamical Systems with Uncertain Parameters," by R.G. Ghanem and M.I. Bujakov, 5/27/96, (PB97-100259, A17, MF-A03).

NCEER-96-0008 "Seismic Evaluation of a 30-Year Old Non-Ductile Highway Bridge Pier and Its Retrofit," by J.B. Mander, B. Mahmoodzadegan, S. Bhadra and S.S. Chen, 5/31/96, (PB97-110902, MF-A03, A10).

NCEER-96-0009 "Seismic Performance of a Model Reinforced Concrete Bridge Pier Before and After Retrofit," by J.B. Mander, J.H. Kim and C.A. Ligozio, 5/31/96, (PB97-110910, MF-A02, A10).

NCEER-96-0010 "IDARC2D Version 4.0: A Computer Program for the Inelastic Damage Analysis of Buildings," by R.E. Valles, A.M. Reinhorn, S.K. Kunnath, C. Li and A. Madan, 6/3/96, (PB97-100234, A17, MF-A03).

NCEER-96-0011 "Estimation of the Economic Impact of Multiple Lifeline Disruption: Memphis Light, Gas and Water Division Case Study," by S.E. Chang, H.A. Seligson and R.T. Eguchi, 8/16/96, (PB97-133490, A11, MF-A03).

NCEER-96-0012 "Proceedings from the Sixth Japan-U.S. Workshop on Earthquake Resistant Design of Lifeline Facilities and Countermeasures Against Soil Liquefaction, Edited by M. Hamada and T. O'Rourke, 9/11/96, (PB97-133581, A99, MF-A06).

NCEER-96-0013 "Chemical Hazards, Mitigation and Preparedness in Areas of High Seismic Risk: A Methodology for Estimating the Risk of Post-Earthquake Hazardous Materials Release," by H.A. Seligson, R.T. Eguchi, K.J. Tierney and K. Richmond, 11/7/96, (PB97-133565, MF-A02, A08).

NCEER-96-0014 "Response of Steel Bridge Bearings to Reversed Cyclic Loading," by J.B. Mander, D-K. Kim, S.S. Chen and G.J. Premus, 11/13/96, (PB97-140735, A12, MF-A03).

NCEER-96-0015 "Highway Culvert Performance During Past Earthquakes," by T.L. Youd and C.J. Beckman, 11/25/96, (PB97-133532, A06, MF-A01).

NCEER-97-0001 "Evaluation, Prevention and Mitigation of Pounding Effects in Building Structures," by R.E. Valles and A.M. Reinhorn, 2/20/97, (PB97-159552, A14, MF-A03).

NCEER-97-0002 "Seismic Design Criteria for Bridges and Other Highway Structures," by C. Rojahn, R. Mayes, D.G. Anderson, J. Clark, J.H. Hom, R.V. Nutt and M.J. O'Rourke, 4/30/97, (PB97-194658, A06, MF-A03).

NCEER-97-0003 “Proceedings of the U.S.-Italian Workshop on Seismic Evaluation and Retrofit,” Edited by D.P. Abrams and G.M. Calvi, 3/19/97, (PB97-194666, A13, MF-A03).

NCEER-97-0004 "Investigation of Seismic Response of Buildings with Linear and Nonlinear Fluid Viscous Dampers," by A.A. Seleemah and M.C. Constantinou, 5/21/97, (PB98-109002, A15, MF-A03).

NCEER-97-0005 "Proceedings of the Workshop on Earthquake Engineering Frontiers in Transportation Facilities," edited by G.C. Lee and I.M. Friedland, 8/29/97, (PB98-128911, A25, MR-A04).

NCEER-97-0006 "Cumulative Seismic Damage of Reinforced Concrete Bridge Piers," by S.K. Kunnath, A. El-Bahy, A. Taylor and W. Stone, 9/2/97, (PB98-108814, A11, MF-A03).

NCEER-97-0007 "Structural Details to Accommodate Seismic Movements of Highway Bridges and Retaining Walls," by R.A. Imbsen, R.A. Schamber, E. Thorkildsen, A. Kartoum, B.T. Martin, T.N. Rosser and J.M. Kulicki, 9/3/97, (PB98-108996, A09, MF-A02).

NCEER-97-0008 "A Method for Earthquake Motion-Damage Relationships with Application to Reinforced Concrete Frames," by A. Singhal and A.S. Kiremidjian, 9/10/97, (PB98-108988, A13, MF-A03).

NCEER-97-0009 "Seismic Analysis and Design of Bridge Abutments Considering Sliding and Rotation," by K. Fishman and R. Richards, Jr., 9/15/97, (PB98-108897, A06, MF-A02).

NCEER-97-0010 "Proceedings of the FHWA/NCEER Workshop on the National Representation of Seismic Ground Motion for New and Existing Highway Facilities," edited by I.M. Friedland, M.S. Power and R.L. Mayes, 9/22/97, (PB98-128903, A21, MF-A04).

NCEER-97-0011 "Seismic Analysis for Design or Retrofit of Gravity Bridge Abutments," by K.L. Fishman, R. Richards, Jr. and R.C. Divito, 10/2/97, (PB98-128937, A08, MF-A02).

NCEER-97-0012 "Evaluation of Simplified Methods of Analysis for Yielding Structures," by P. Tsopelas, M.C. Constantinou, C.A. Kircher and A.S. Whittaker, 10/31/97, (PB98-128929, A10, MF-A03).

NCEER-97-0013 "Seismic Design of Bridge Columns Based on Control and Repairability of Damage," by C-T. Cheng and J.B. Mander, 12/8/97, (PB98-144249, A11, MF-A03).

NCEER-97-0014 "Seismic Resistance of Bridge Piers Based on Damage Avoidance Design," by J.B. Mander and C-T. Cheng, 12/10/97, (PB98-144223, A09, MF-A02).

NCEER-97-0015 “Seismic Response of Nominally Symmetric Systems with Strength Uncertainty,” by S. Balopoulou and M. Grigoriu, 12/23/97, (PB98-153422, A11, MF-A03).

NCEER-97-0016 “Evaluation of Seismic Retrofit Methods for Reinforced Concrete Bridge Columns,” by T.J. Wipf, F.W. Klaiber and F.M. Russo, 12/28/97, (PB98-144215, A12, MF-A03).

NCEER-97-0017 “Seismic Fragility of Existing Conventional Reinforced Concrete Highway Bridges,” by C.L. Mullen and A.S. Cakmak, 12/30/97, (PB98-153406, A08, MF-A02).

NCEER-97-0018 “Loss Asssessment of Memphis Buildings,” edited by D.P. Abrams and M. Shinozuka, 12/31/97, (PB98-144231, A13, MF-A03).

NCEER-97-0019 “Seismic Evaluation of Frames with Infill Walls Using Quasi-static Experiments,” by K.M. Mosalam, R.N. White and P. Gergely, 12/31/97, (PB98-153455, A07, MF-A02).

NCEER-97-0020 “Seismic Evaluation of Frames with Infill Walls Using Pseudo-dynamic Experiments,” by K.M. Mosalam, R.N. White and P. Gergely, 12/31/97, (PB98-153430, A07, MF-A02).

NCEER-97-0021 “Computational Strategies for Frames with Infill Walls: Discrete and Smeared Crack Analyses and Seismic Fragility,” by K.M. Mosalam, R.N. White and P. Gergely, 12/31/97, (PB98-153414, A10, MF-A02).

NCEER-97-0022 "Proceedings of the NCEER Workshop on Evaluation of Liquefaction Resistance of Soils," edited by T.L. Youd and I.M. Idriss, 12/31/97, (PB98-155617, A15, MF-A03).

MCEER-98-0001 "Extraction of Nonlinear Hysteretic Properties of Seismically Isolated Bridges from Quick-Release Field Tests," by Q. Chen, B.M. Douglas, E.M. Maragakis and I.G. Buckle, 5/26/98, (PB99-118838, A06, MF-A01).

MCEER-98-0002 "Methodologies for Evaluating the Importance of Highway Bridges," by A. Thomas, S. Eshenaur and J. Kulicki, 5/29/98, (PB99-118846, A10, MF-A02).

MCEER-98-0003 "Capacity Design of Bridge Piers and the Analysis of Overstrength," by J.B. Mander, A. Dutta and P. Goel, 6/1/98, (PB99-118853, A09, MF-A02).

MCEER-98-0004 "Evaluation of Bridge Damage Data from the Loma Prieta and Northridge, California Earthquakes," by N. Basoz and A. Kiremidjian, 6/2/98, (PB99-118861, A15, MF-A03).

MCEER-98-0005 "Screening Guide for Rapid Assessment of Liquefaction Hazard at Highway Bridge Sites," by T. L. Youd, 6/16/98, (PB99-118879, A06, not available on microfiche).

MCEER-98-0006 "Structural Steel and Steel/Concrete Interface Details for Bridges," by P. Ritchie, N. Kauhl and J. Kulicki, 7/13/98, (PB99-118945, A06, MF-A01).

MCEER-98-0007 "Capacity Design and Fatigue Analysis of Confined Concrete Columns," by A. Dutta and J.B. Mander, 7/14/98, (PB99-118960, A14, MF-A03).

MCEER-98-0008 "Proceedings of the Workshop on Performance Criteria for Telecommunication Services Under Earthquake Conditions," edited by A.J. Schiff, 7/15/98, (PB99-118952, A08, MF-A02).

MCEER-98-0009 "Fatigue Analysis of Unconfined Concrete Columns," by J.B. Mander, A. Dutta and J.H. Kim, 9/12/98, (PB99-123655, A10, MF-A02).

MCEER-98-0010 "Centrifuge Modeling of Cyclic Lateral Response of Pile-Cap Systems and Seat-Type Abutments in Dry Sands," by A.D. Gadre and R. Dobry, 10/2/98, (PB99-123606, A13, MF-A03).

MCEER-98-0011 "IDARC-BRIDGE: A Computational Platform for Seismic Damage Assessment of Bridge Structures," by A.M. Reinhorn, V. Simeonov, G. Mylonakis and Y. Reichman, 10/2/98, (PB99-162919, A15, MF-A03).

MCEER-98-0012 "Experimental Investigation of the Dynamic Response of Two Bridges Before and After Retrofitting with Elastomeric Bearings," by D.A. Wendichansky, S.S. Chen and J.B. Mander, 10/2/98, (PB99-162927, A15, MF-A03).

MCEER-98-0013 "Design Procedures for Hinge Restrainers and Hinge Sear Width for Multiple-Frame Bridges," by R. Des Roches and G.L. Fenves, 11/3/98, (PB99-140477, A13, MF-A03).

MCEER-98-0014 "Response Modification Factors for Seismically Isolated Bridges," by M.C. Constantinou and J.K. Quarshie, 11/3/98, (PB99-140485, A14, MF-A03).

MCEER-98-0015 "Proceedings of the U.S.-Italy Workshop on Seismic Protective Systems for Bridges," edited by I.M. Friedland and M.C. Constantinou, 11/3/98, (PB2000-101711, A22, MF-A04).

MCEER-98-0016 "Appropriate Seismic Reliability for Critical Equipment Systems: Recommendations Based on Regional Analysis of Financial and Life Loss," by K. Porter, C. Scawthorn, C. Taylor and N. Blais, 11/10/98, (PB99-157265, A08, MF-A02).

MCEER-98-0017 "Proceedings of the U.S. Japan Joint Seminar on Civil Infrastructure Systems Research," edited by M. Shinozuka and A. Rose, 11/12/98, (PB99-156713, A16, MF-A03).

MCEER-98-0018 "Modeling of Pile Footings and Drilled Shafts for Seismic Design," by I. PoLam, M. Kapuskar and D. Chaudhuri, 12/21/98, (PB99-157257, A09, MF-A02).

MCEER-99-0001 "Seismic Evaluation of a Masonry Infilled Reinforced Concrete Frame by Pseudodynamic Testing," by S.G. Buonopane and R.N. White, 2/16/99, (PB99-162851, A09, MF-A02).

MCEER-99-0002 "Response History Analysis of Structures with Seismic Isolation and Energy Dissipation Systems: Verification Examples for Program SAP2000," by J. Scheller and M.C. Constantinou, 2/22/99, (PB99-162869, A08, MF-A02).

MCEER-99-0003 "Experimental Study on the Seismic Design and Retrofit of Bridge Columns Including Axial Load Effects," by A. Dutta, T. Kokorina and J.B. Mander, 2/22/99, (PB99-162877, A09, MF-A02).

MCEER-99-0004 "Experimental Study of Bridge Elastomeric and Other Isolation and Energy Dissipation Systems with Emphasis on Uplift Prevention and High Velocity Near-source Seismic Excitation," by A. Kasalanati and M. C. Constantinou, 2/26/99, (PB99-162885, A12, MF-A03).

MCEER-99-0005 "Truss Modeling of Reinforced Concrete Shear-flexure Behavior," by J.H. Kim and J.B. Mander, 3/8/99, (PB99-163693, A12, MF-A03).

MCEER-99-0006 "Experimental Investigation and Computational Modeling of Seismic Response of a 1:4 Scale Model Steel Structure with a Load Balancing Supplemental Damping System," by G. Pekcan, J.B. Mander and S.S. Chen, 4/2/99, (PB99-162893, A11, MF-A03).

MCEER-99-0007 "Effect of Vertical Ground Motions on the Structural Response of Highway Bridges," by M.R. Button, C.J. Cronin and R.L. Mayes, 4/10/99, (PB2000-101411, A10, MF-A03).

MCEER-99-0008 "Seismic Reliability Assessment of Critical Facilities: A Handbook, Supporting Documentation, and Model Code Provisions," by G.S. Johnson, R.E. Sheppard, M.D. Quilici, S.J. Eder and C.R. Scawthorn, 4/12/99, (PB2000-101701, A18, MF-A04).

MCEER-99-0009 "Impact Assessment of Selected MCEER Highway Project Research on the Seismic Design of Highway Structures," by C. Rojahn, R. Mayes, D.G. Anderson, J.H. Clark, D'Appolonia Engineering, S. Gloyd and R.V. Nutt, 4/14/99, (PB99-162901, A10, MF-A02).

MCEER-99-0010 "Site Factors and Site Categories in Seismic Codes," by R. Dobry, R. Ramos and M.S. Power, 7/19/99, (PB2000-101705, A08, MF-A02).

MCEER-99-0011 "Restrainer Design Procedures for Multi-Span Simply-Supported Bridges," by M.J. Randall, M. Saiidi, E. Maragakis and T. Isakovic, 7/20/99, (PB2000-101702, A10, MF-A02).

MCEER-99-0012 "Property Modification Factors for Seismic Isolation Bearings," by M.C. Constantinou, P. Tsopelas, A. Kasalanati and E. Wolff, 7/20/99, (PB2000-103387, A11, MF-A03).

MCEER-99-0013 "Critical Seismic Issues for Existing Steel Bridges," by P. Ritchie, N. Kauhl and J. Kulicki, 7/20/99, (PB2000-101697, A09, MF-A02).

MCEER-99-0014 "Nonstructural Damage Database," by A. Kao, T.T. Soong and A. Vender, 7/24/99, (PB2000-101407, A06, MF-A01).

MCEER-99-0015 "Guide to Remedial Measures for Liquefaction Mitigation at Existing Highway Bridge Sites," by H.G. Cooke and J. K. Mitchell, 7/26/99, (PB2000-101703, A11, MF-A03).

MCEER-99-0016 "Proceedings of the MCEER Workshop on Ground Motion Methodologies for the Eastern United States," edited by N. Abrahamson and A. Becker, 8/11/99, (PB2000-103385, A07, MF-A02).

MCEER-99-0017 "Quindío, Colombia Earthquake of January 25, 1999: Reconnaissance Report," by A.P. Asfura and P.J. Flores, 10/4/99, (PB2000-106893, A06, MF-A01).

MCEER-99-0018 "Hysteretic Models for Cyclic Behavior of Deteriorating Inelastic Structures," by M.V. Sivaselvan and A.M. Reinhorn, 11/5/99, (PB2000-103386, A08, MF-A02).

MCEER-99-0019 "Proceedings of the 7th U.S.- Japan Workshop on Earthquake Resistant Design of Lifeline Facilities and Countermeasures Against Soil Liquefaction," edited by T.D. O'Rourke, J.P. Bardet and M. Hamada, 11/19/99, (PB2000-103354, A99, MF-A06).

MCEER-99-0020 "Development of Measurement Capability for Micro-Vibration Evaluations with Application to Chip Fabrication Facilities," by G.C. Lee, Z. Liang, J.W. Song, J.D. Shen and W.C. Liu, 12/1/99, (PB2000-105993, A08, MF-A02).

MCEER-99-0021 "Design and Retrofit Methodology for Building Structures with Supplemental Energy Dissipating Systems," by G. Pekcan, J.B. Mander and S.S. Chen, 12/31/99, (PB2000-105994, A11, MF-A03).

MCEER-00-0001 "The Marmara, Turkey Earthquake of August 17, 1999: Reconnaissance Report," edited by C. Scawthorn; with major contributions by M. Bruneau, R. Eguchi, T. Holzer, G. Johnson, J. Mander, J. Mitchell, W. Mitchell, A. Papageorgiou, C. Scaethorn, and G. Webb, 3/23/00, (PB2000-106200, A11, MF-A03).

MCEER-00-0002 "Proceedings of the MCEER Workshop for Seismic Hazard Mitigation of Health Care Facilities," edited by G.C. Lee, M. Ettouney, M. Grigoriu, J. Hauer and J. Nigg, 3/29/00, (PB2000-106892, A08, MF-A02).

MCEER-00-0003 "The Chi-Chi, Taiwan Earthquake of September 21, 1999: Reconnaissance Report," edited by G.C. Lee and C.H. Loh, with major contributions by G.C. Lee, M. Bruneau, I.G. Buckle, S.E. Chang, P.J. Flores, T.D. O'Rourke, M. Shinozuka, T.T. Soong, C-H. Loh, K-C. Chang, Z-J. Chen, J-S. Hwang, M-L. Lin, G-Y. Liu, K-C. Tsai, G.C. Yao and C-L. Yen, 4/30/00, (PB2001-100980, A10, MF-A02).

MCEER-00-0004 "Seismic Retrofit of End-Sway Frames of Steel Deck-Truss Bridges with a Supplemental Tendon System: Experimental and Analytical Investigation," by G. Pekcan, J.B. Mander and S.S. Chen, 7/1/00, (PB2001-100982, A10, MF-A02).

MCEER-00-0005 "Sliding Fragility of Unrestrained Equipment in Critical Facilities," by W.H. Chong and T.T. Soong, 7/5/00, (PB2001-100983, A08, MF-A02).

MCEER-00-0006 "Seismic Response of Reinforced Concrete Bridge Pier Walls in the Weak Direction," by N. Abo-Shadi, M. Saiidi and D. Sanders, 7/17/00, (PB2001-100981, A17, MF-A03).

MCEER-00-0007 "Low-Cycle Fatigue Behavior of Longitudinal Reinforcement in Reinforced Concrete Bridge Columns," by J. Brown and S.K. Kunnath, 7/23/00, (PB2001-104392, A08, MF-A02).

MCEER-00-0008 "Soil Structure Interaction of Bridges for Seismic Analysis," I. PoLam and H. Law, 9/25/00, (PB2001-105397, A08, MF-A02).

MCEER-00-0009 "Proceedings of the First MCEER Workshop on Mitigation of Earthquake Disaster by Advanced Technologies (MEDAT-1), edited by M. Shinozuka, D.J. Inman and T.D. O'Rourke, 11/10/00, (PB2001-105399, A14, MF-A03).

MCEER-00-0010 "Development and Evaluation of Simplified Procedures for Analysis and Design of Buildings with Passive Energy Dissipation Systems, Revision 01," by O.M. Ramirez, M.C. Constantinou, C.A. Kircher, A.S. Whittaker, M.W. Johnson, J.D. Gomez and C. Chrysostomou, 11/16/01, (PB2001-105523, A23, MF-A04).

MCEER-00-0011 "Dynamic Soil-Foundation-Structure Interaction Analyses of Large Caissons," by C-Y. Chang, C-M. Mok, Z-L. Wang, R. Settgast, F. Waggoner, M.A. Ketchum, H.M. Gonnermann and C-C. Chin, 12/30/00, (PB2001-104373, A07, MF-A02).

MCEER-00-0012 "Experimental Evaluation of Seismic Performance of Bridge Restrainers," by A.G. Vlassis, E.M. Maragakis and M. Saiid Saiidi, 12/30/00, (PB2001-104354, A09, MF-A02).

MCEER-00-0013 "Effect of Spatial Variation of Ground Motion on Highway Structures," by M. Shinozuka, V. Saxena and G. Deodatis, 12/31/00, (PB2001-108755, A13, MF-A03).

MCEER-00-0014 "A Risk-Based Methodology for Assessing the Seismic Performance of Highway Systems," by S.D. Werner, C.E. Taylor, J.E. Moore, II, J.S. Walton and S. Cho, 12/31/00, (PB2001-108756, A14, MF-A03).

MCEER-01-0001 "Experimental Investigation of P-Delta Effects to Collapse During Earthquakes," by D. Vian and M. Bruneau, 6/25/01, (PB2002-100534, A17, MF-A03).

MCEER-01-0002 "Proceedings of the Second MCEER Workshop on Mitigation of Earthquake Disaster by Advanced Technologies (MEDAT-2)," edited by M. Bruneau and D.J. Inman, 7/23/01, (PB2002-100434, A16, MF-A03).

MCEER-01-0003 "Sensitivity Analysis of Dynamic Systems Subjected to Seismic Loads," by C. Roth and M. Grigoriu, 9/18/01, (PB2003-100884, A12, MF-A03).

MCEER-01-0004 "Overcoming Obstacles to Implementing Earthquake Hazard Mitigation Policies: Stage 1 Report," by D.J. Alesch and W.J. Petak, 12/17/01, (PB2002-107949, A07, MF-A02).

MCEER-01-0005 "Updating Real-Time Earthquake Loss Estimates: Methods, Problems and Insights," by C.E. Taylor, S.E. Chang and R.T. Eguchi, 12/17/01, (PB2002-107948, A05, MF-A01).

MCEER-01-0006 "Experimental Investigation and Retrofit of Steel Pile Foundations and Pile Bents Under Cyclic Lateral Loadings," by A. Shama, J. Mander, B. Blabac and S. Chen, 12/31/01, (PB2002-107950, A13, MF-A03).

MCEER-02-0001 "Assessment of Performance of Bolu Viaduct in the 1999 Duzce Earthquake in Turkey" by P.C. Roussis, M.C. Constantinou, M. Erdik, E. Durukal and M. Dicleli, 5/8/02, (PB2003-100883, A08, MF-A02).

MCEER-02-0002 "Seismic Behavior of Rail Counterweight Systems of Elevators in Buildings," by M.P. Singh, Rildova and L.E. Suarez, 5/27/02. (PB2003-100882, A11, MF-A03).

MCEER-02-0003 "Development of Analysis and Design Procedures for Spread Footings," by G. Mylonakis, G. Gazetas, S. Nikolaou and A. Chauncey, 10/02/02, (PB2004-101636, A13, MF-A03, CD-A13).

MCEER-02-0004 "Bare-Earth Algorithms for Use with SAR and LIDAR Digital Elevation Models," by C.K. Huyck, R.T. Eguchi and B. Houshmand, 10/16/02, (PB2004-101637, A07, CD-A07).

MCEER-02-0005 "Review of Energy Dissipation of Compression Members in Concentrically Braced Frames," by K.Lee and M. Bruneau, 10/18/02, (PB2004-101638, A10, CD-A10).

MCEER-03-0001 "Experimental Investigation of Light-Gauge Steel Plate Shear Walls for the Seismic Retrofit of Buildings" by J. Berman and M. Bruneau, 5/2/03, (PB2004-101622, A10, MF-A03, CD-A10).

MCEER-03-0002 "Statistical Analysis of Fragility Curves," by M. Shinozuka, M.Q. Feng, H. Kim, T. Uzawa and T. Ueda, 6/16/03, (PB2004-101849, A09, CD-A09).

MCEER-03-0003 "Proceedings of the Eighth U.S.-Japan Workshop on Earthquake Resistant Design f Lifeline Facilities and Countermeasures Against Liquefaction," edited by M. Hamada, J.P. Bardet and T.D. O'Rourke, 6/30/03, (PB2004-104386, A99, CD-A99).

MCEER-03-0004 "Proceedings of the PRC-US Workshop on Seismic Analysis and Design of Special Bridges," edited by L.C. Fan and G.C. Lee, 7/15/03, (PB2004-104387, A14, CD-A14).

MCEER-03-0005 "Urban Disaster Recovery: A Framework and Simulation Model," by S.B. Miles and S.E. Chang, 7/25/03, (PB2004-104388, A07, CD-A07).

MCEER-03-0006 "Behavior of Underground Piping Joints Due to Static and Dynamic Loading," by R.D. Meis, M. Maragakis and R. Siddharthan, 11/17/03, (PB2005-102194, A13, MF-A03, CD-A00).

MCEER-04-0001 "Experimental Study of Seismic Isolation Systems with Emphasis on Secondary System Response and Verification of Accuracy of Dynamic Response History Analysis Methods," by E. Wolff and M. Constantinou, 1/16/04 (PB2005-102195, A99, MF-E08, CD-A00).

MCEER-04-0002 "Tension, Compression and Cyclic Testing of Engineered Cementitious Composite Materials," by K. Kesner and S.L. Billington, 3/1/04, (PB2005-102196, A08, CD-A08).

MCEER-04-0003 "Cyclic Testing of Braces Laterally Restrained by Steel Studs to Enhance Performance During Earthquakes," by O.C. Celik, J.W. Berman and M. Bruneau, 3/16/04, (PB2005-102197, A13, MF-A03, CD-A00).

MCEER-04-0004 "Methodologies for Post Earthquake Building Damage Detection Using SAR and Optical Remote Sensing: Application to the August 17, 1999 Marmara, Turkey Earthquake," by C.K. Huyck, B.J. Adams, S. Cho, R.T. Eguchi, B. Mansouri and B. Houshmand, 6/15/04, (PB2005-104888, A10, CD-A00).

MCEER-04-0005 "Nonlinear Structural Analysis Towards Collapse Simulation: A Dynamical Systems Approach," by M.V. Sivaselvan and A.M. Reinhorn, 6/16/04, (PB2005-104889, A11, MF-A03, CD-A00).

MCEER-04-0006 "Proceedings of the Second PRC-US Workshop on Seismic Analysis and Design of Special Bridges," edited by G.C. Lee and L.C. Fan, 6/25/04, (PB2005-104890, A16, CD-A00).

MCEER-04-0007 "Seismic Vulnerability Evaluation of Axially Loaded Steel Built-up Laced Members," by K. Lee and M. Bruneau, 6/30/04, (PB2005-104891, A16, CD-A00).

MCEER-04-0008 "Evaluation of Accuracy of Simplified Methods of Analysis and Design of Buildings with Damping Systems for Near-Fault and for Soft-Soil Seismic Motions," by E.A. Pavlou and M.C. Constantinou, 8/16/04, (PB2005-104892, A08, MF-A02, CD-A00).

MCEER-04-0009 "Assessment of Geotechnical Issues in Acute Care Facilities in California," by M. Lew, T.D. O'Rourke, R. Dobry and M. Koch, 9/15/04, (PB2005-104893, A08, CD-A00).

MCEER-04-0010 "Scissor-Jack-Damper Energy Dissipation System," by A.N. Sigaher-Boyle and M.C. Constantinou, 12/1/04 (PB2005-108221).

MCEER-04-0011 "Seismic Retrofit of Bridge Steel Truss Piers Using a Controlled Rocking Approach," by M. Pollino and M. Bruneau, 12/20/04 (PB2006-105795).

MCEER-05-0001 "Experimental and Analytical Studies of Structures Seismically Isolated with an Uplift-Restraint Isolation System," by P.C. Roussis and M.C. Constantinou, 1/10/05 (PB2005-108222).

MCEER-05-0002 "A Versatile Experimentation Model for Study of Structures Near Collapse Applied to Seismic Evaluation of Irregular Structures," by D. Kusumastuti, A.M. Reinhorn and A. Rutenberg, 3/31/05 (PB2006-101523).

MCEER-05-0003 "Proceedings of the Third PRC-US Workshop on Seismic Analysis and Design of Special Bridges," edited by L.C. Fan and G.C. Lee, 4/20/05, (PB2006-105796).

MCEER-05-0004 "Approaches for the Seismic Retrofit of Braced Steel Bridge Piers and Proof-of-Concept Testing of an Eccentrically Braced Frame with Tubular Link," by J.W. Berman and M. Bruneau, 4/21/05 (PB2006-101524).

MCEER-05-0005 "Simulation of Strong Ground Motions for Seismic Fragility Evaluation of Nonstructural Components in Hospitals," by A. Wanitkorkul and A. Filiatrault, 5/26/05 (PB2006-500027).

MCEER-05-0006 "Seismic Safety in California Hospitals: Assessing an Attempt to Accelerate the Replacement or Seismic Retrofit of Older Hospital Facilities," by D.J. Alesch, L.A. Arendt and W.J. Petak, 6/6/05 (PB2006-105794).

MCEER-05-0007 "Development of Seismic Strengthening and Retrofit Strategies for Critical Facilities Using Engineered Cementitious Composite Materials," by K. Kesner and S.L. Billington, 8/29/05 (PB2006-111701).

MCEER-05-0008 "Experimental and Analytical Studies of Base Isolation Systems for Seismic Protection of Power Transformers," by N. Murota, M.Q. Feng and G-Y. Liu, 9/30/05 (PB2006-111702).

MCEER-05-0009 "3D-BASIS-ME-MB: Computer Program for Nonlinear Dynamic Analysis of Seismically Isolated Structures," by P.C. Tsopelas, P.C. Roussis, M.C. Constantinou, R. Buchanan and A.M. Reinhorn, 10/3/05 (PB2006-111703).

MCEER-05-0010 "Steel Plate Shear Walls for Seismic Design and Retrofit of Building Structures," by D. Vian and M. Bruneau, 12/15/05 (PB2006-111704).

MCEER-05-0011 "The Performance-Based Design Paradigm," by M.J. Astrella and A. Whittaker, 12/15/05 (PB2006-111705).

MCEER-06-0001 "Seismic Fragility of Suspended Ceiling Systems," H. Badillo-Almaraz, A.S. Whittaker, A.M. Reinhorn and G.P. Cimellaro, 2/4/06 (PB2006-111706).

MCEER-06-0002 "Multi-Dimensional Fragility of Structures," by G.P. Cimellaro, A.M. Reinhorn and M. Bruneau, 3/1/06 (PB2007-106974, A09, MF-A02, CD A00).

MCEER-06-0003 "Built-Up Shear Links as Energy Dissipators for Seismic Protection of Bridges," by P. Dusicka, A.M. Itani and I.G. Buckle, 3/15/06 (PB2006-111708).

MCEER-06-0004 "Analytical Investigation of the Structural Fuse Concept," by R.E. Vargas and M. Bruneau, 3/16/06 (PB2006-111709).

MCEER-06-0005 "Experimental Investigation of the Structural Fuse Concept," by R.E. Vargas and M. Bruneau, 3/17/06 (PB2006-111710).

MCEER-06-0006 "Further Development of Tubular Eccentrically Braced Frame Links for the Seismic Retrofit of Braced Steel Truss Bridge Piers," by J.W. Berman and M. Bruneau, 3/27/06 (PB2007-105147).

MCEER-06-0007 "REDARS Validation Report," by S. Cho, C.K. Huyck, S. Ghosh and R.T. Eguchi, 8/8/06 (PB2007-106983).

MCEER-06-0008 "Review of Current NDE Technologies for Post-Earthquake Assessment of Retrofitted Bridge Columns," by J.W. Song, Z. Liang and G.C. Lee, 8/21/06 (PB2007-106984).

MCEER-06-0009 "Liquefaction Remediation in Silty Soils Using Dynamic Compaction and Stone Columns," by S. Thevanayagam, G.R. Martin, R. Nashed, T. Shenthan, T. Kanagalingam and N. Ecemis, 8/28/06 (PB2007-106985).

MCEER-06-0010 "Conceptual Design and Experimental Investigation of Polymer Matrix Composite Infill Panels for Seismic Retrofitting," by W. Jung, M. Chiewanichakorn and A.J. Aref, 9/21/06 (PB2007-106986).

MCEER-06-0011 "A Study of the Coupled Horizontal-Vertical Behavior of Elastomeric and Lead-Rubber Seismic Isolation Bearings," by G.P. Warn and A.S. Whittaker, 9/22/06 (PB2007-108679).

MCEER-06-0012 "Proceedings of the Fourth PRC-US Workshop on Seismic Analysis and Design of Special Bridges: Advancing Bridge Technologies in Research, Design, Construction and Preservation," Edited by L.C. Fan, G.C. Lee and L. Ziang, 10/12/06 (PB2007-109042).

MCEER-06-0013 "Cyclic Response and Low Cycle Fatigue Characteristics of Plate Steels," by P. Dusicka, A.M. Itani and I.G. Buckle, 11/1/06 06 (PB2007-106987).

MCEER-06-0014 "Proceedings of the Second US-Taiwan Bridge Engineering Workshop," edited by W.P. Yen, J. Shen, J-Y. Chen and M. Wang, 11/15/06 (PB2008-500041).

MCEER-06-0015 "User Manual and Technical Documentation for the REDARS^{TM} Import Wizard," by S. Cho, S. Ghosh, C.K. Huyck and S.D. Werner, 11/30/06 (PB2007-114766).

MCEER-06-0016 "Hazard Mitigation Strategy and Monitoring Technologies for Urban and Infrastructure Public Buildings: Proceedings of the China-US Workshops," edited by X.Y. Zhou, A.L. Zhang, G.C. Lee and M. Tong, 12/12/06 (PB2008-500018).

MCEER-07-0001 "Static and Kinetic Coefficients of Friction for Rigid Blocks," by C. Kafali, S. Fathali, M. Grigoriu and A.S. Whittaker, 3/20/07 (PB2007-114767).

MCEER-07-0002 "Hazard Mitigation Investment Decision Making: Organizational Response to Legislative Mandate," by L.A. Arendt, D.J. Alesch and W.J. Petak, 4/9/07 (PB2007-114768).

MCEER-07-0003 "Seismic Behavior of Bidirectional-Resistant Ductile End Diaphragms with Unbonded Braces in Straight or Skewed Steel Bridges," by O. Celik and M. Bruneau, 4/11/07 (PB2008-105141).

MCEER-07-0004 "Modeling Pile Behavior in Large Pile Groups Under Lateral Loading," by A.M. Dodds and G.R. Martin, 4/16/07(PB2008-105142).

MCEER-07-0005 "Experimental Investigation of Blast Performance of Seismically Resistant Concrete-Filled Steel Tube Bridge Piers," by S. Fujikura, M. Bruneau and D. Lopez-Garcia, 4/20/07 (PB2008-105143).

MCEER-07-0006 "Seismic Analysis of Conventional and Isolated Liquefied Natural Gas Tanks Using Mechanical Analogs," by I.P. Christovasilis and A.S. Whittaker, 5/1/07.

MCEER-07-0007 "Experimental Seismic Performance Evaluation of Isolation/Restraint Systems for Mechanical Equipment – Part 1: Heavy Equipment Study," by S. Fathali and A. Filiatrault, 6/6/07 (PB2008-105144).

MCEER-07-0008 "Seismic Vulnerability of Timber Bridges and Timber Substructures," by A.A. Sharma, J.B. Mander, I.M. Friedland and D.R. Allicock, 6/7/07 (PB2008-105145).

MCEER-07-0009 "Experimental and Analytical Study of the XY-Friction Pendulum (XY-FP) Bearing for Bridge Applications," by C.C. Marin-Artieda, A.S. Whittaker and M.C. Constantinou, 6/7/07 (PB2008-105191).

MCEER-07-0010 "Proceedings of the PRC-US Earthquake Engineering Forum for Young Researchers," Edited by G.C. Lee and X.Z. Qi, 6/8/07 (PB2008-500058).

MCEER-07-0011 "Design Recommendations for Perforated Steel Plate Shear Walls," by R. Purba and M. Bruneau, 6/18/07, (PB2008-105192).

MCEER-07-0012 "Performance of Seismic Isolation Hardware Under Service and Seismic Loading," by M.C. Constantinou, A.S. Whittaker, Y. Kalpakidis, D.M. Fenz and G.P. Warn, 8/27/07, (PB2008-105193).

MCEER-07-0013 "Experimental Evaluation of the Seismic Performance of Hospital Piping Subassemblies," by E.R. Goodwin, E. Maragakis and A.M. Itani, 9/4/07, (PB2008-105194).

MCEER-07-0014 "A Simulation Model of Urban Disaster Recovery and Resilience: Implementation for the 1994 Northridge Earthquake," by S. Miles and S.E. Chang, 9/7/07, (PB2008-106426).

MCEER-07-0015 "Statistical and Mechanistic Fragility Analysis of Concrete Bridges," by M. Shinozuka, S. Banerjee and S-H. Kim, 9/10/07, (PB2008-106427).

MCEER-07-0016 "Three-Dimensional Modeling of Inelastic Buckling in Frame Structures," by M. Schachter and AM. Reinhorn, 9/13/07, (PB2008-108125).

MCEER-07-0017 "Modeling of Seismic Wave Scattering on Pile Groups and Caissons," by I. Po Lam, H. Law and C.T. Yang, 9/17/07 (PB2008-108150).

MCEER-07-0018 "Bridge Foundations: Modeling Large Pile Groups and Caissons for Seismic Design," by I. Po Lam, H. Law and G.R. Martin (Coordinating Author), 12/1/07 (PB2008-111190).

MCEER-07-0019 "Principles and Performance of Roller Seismic Isolation Bearings for Highway Bridges," by G.C. Lee, Y.C. Ou, Z. Liang, T.C. Niu and J. Song, 12/10/07 (PB2009-110466).

MCEER-07-0020 "Centrifuge Modeling of Permeability and Pinning Reinforcement Effects on Pile Response to Lateral Spreading," by L.L Gonzalez-Lagos, T. Abdoun and R. Dobry, 12/10/07 (PB2008-111191).

MCEER-07-0021 "Damage to the Highway System from the Pisco, Perú Earthquake of August 15, 2007," by J.S. O'Connor, L. Mesa and M. Nykamp, 12/10/07, (PB2008-108126).

MCEER-07-0022 "Experimental Seismic Performance Evaluation of Isolation/Restraint Systems for Mechanical Equipment – Part 2: Light Equipment Study," by S. Fathali and A. Filiatrault, 12/13/07 (PB2008-111192).

MCEER-07-0023 "Fragility Considerations in Highway Bridge Design," by M. Shinozuka, S. Banerjee and S.H. Kim, 12/14/07 (PB2008-111193).

MCEER-07-0024 "Performance Estimates for Seismically Isolated Bridges," by G.P. Warn and A.S. Whittaker, 12/30/07 (PB2008-112230).

MCEER-08-0001 "Seismic Performance of Steel Girder Bridge Superstructures with Conventional Cross Frames," by L.P. Carden, A.M. Itani and I.G. Buckle, 1/7/08, (PB2008-112231).

MCEER-08-0002 "Seismic Performance of Steel Girder Bridge Superstructures with Ductile End Cross Frames with Seismic Isolators," by L.P. Carden, A.M. Itani and I.G. Buckle, 1/7/08 (PB2008-112232).

MCEER-08-0003 "Analytical and Experimental Investigation of a Controlled Rocking Approach for Seismic Protection of Bridge Steel Truss Piers," by M. Pollino and M. Bruneau, 1/21/08 (PB2008-112233).

MCEER-08-0004 "Linking Lifeline Infrastructure Performance and Community Disaster Resilience: Models and Multi-Stakeholder Processes," by S.E. Chang, C. Pasion, K. Tatebe and R. Ahmad, 3/3/08 (PB2008-112234).

MCEER-08-0005 "Modal Analysis of Generally Damped Linear Structures Subjected to Seismic Excitations," by J. Song, Y-L. Chu, Z. Liang and G.C. Lee, 3/4/08 (PB2009-102311).

MCEER-08-0006 "System Performance Under Multi-Hazard Environments," by C. Kafali and M. Grigoriu, 3/4/08 (PB2008-112235).

MCEER-08-0007 "Mechanical Behavior of Multi-Spherical Sliding Bearings," by D.M. Fenz and M.C. Constantinou, 3/6/08 (PB2008-112236).

MCEER-08-0008 "Post-Earthquake Restoration of the Los Angeles Water Supply System," by T.H.P. Tabucchi and R.A. Davidson, 3/7/08 (PB2008-112237).

MCEER-08-0009 "Fragility Analysis of Water Supply Systems," by A. Jacobson and M. Grigoriu, 3/10/08 (PB2009-105545).

MCEER-08-0010 "Experimental Investigation of Full-Scale Two-Story Steel Plate Shear Walls with Reduced Beam Section Connections," by B. Qu, M. Bruneau, C-H. Lin and K-C. Tsai, 3/17/08 (PB2009-106368).

MCEER-08-0011 "Seismic Evaluation and Rehabilitation of Critical Components of Electrical Power Systems," S. Ersoy, B. Feizi, A. Ashrafi and M. Ala Saadeghvaziri, 3/17/08 (PB2009-105546).

MCEER-08-0012 "Seismic Behavior and Design of Boundary Frame Members of Steel Plate Shear Walls," by B. Qu and M. Bruneau, 4/26/08 . (PB2009-106744).

MCEER-08-0013 "Development and Appraisal of a Numerical Cyclic Loading Protocol for Quantifying Building System Performance," by A. Filiatrault, A. Wanitkorkul and M. Constantinou, 4/27/08 (PB2009-107906).

MCEER-08-0014 "Structural and Nonstructural Earthquake Design: The Challenge of Integrating Specialty Areas in Designing Complex, Critical Facilities," by W.J. Petak and D.J. Alesch, 4/30/08 (PB2009-107907).

MCEER-08-0015 "Seismic Performance Evaluation of Water Systems," by Y. Wang and T.D. O'Rourke, 5/5/08 (PB2009-107908).

MCEER-08-0016 "Seismic Response Modeling of Water Supply Systems," by P. Shi and T.D. O'Rourke, 5/5/08 (PB2009-107910).

MCEER-08-0017 "Numerical and Experimental Studies of Self-Centering Post-Tensioned Steel Frames," by D. Wang and A. Filiatrault, 5/12/08 (PB2009-110479).

MCEER-08-0018 "Development, Implementation and Verification of Dynamic Analysis Models for Multi-Spherical Sliding Bearings," by D.M. Fenz and M.C. Constantinou, 8/15/08 (PB2009-107911).

MCEER-08-0019 "Performance Assessment of Conventional and Base Isolated Nuclear Power Plants for Earthquake Blast Loadings," by Y.N. Huang, A.S. Whittaker and N. Luco, 10/28/08 (PB2009-107912).

MCEER-08-0020 "Remote Sensing for Resilient Multi-Hazard Disaster Response – Volume I: Introduction to Damage Assessment Methodologies," by B.J. Adams and R.T. Eguchi, 11/17/08 (PB2010-102695).

MCEER-08-0021 "Remote Sensing for Resilient Multi-Hazard Disaster Response – Volume II: Counting the Number of Collapsed Buildings Using an Object-Oriented Analysis: Case Study of the 2003 Bam Earthquake," by L. Gusella, C.K. Huyck and B.J. Adams, 11/17/08 (PB2010-100925).

MCEER-08-0022 "Remote Sensing for Resilient Multi-Hazard Disaster Response – Volume III: Multi-Sensor Image Fusion Techniques for Robust Neighborhood-Scale Urban Damage Assessment," by B.J. Adams and A. McMillan, 11/17/08 (PB2010-100926).

MCEER-08-0023 "Remote Sensing for Resilient Multi-Hazard Disaster Response – Volume IV: A Study of Multi-Temporal and Multi-Resolution SAR Imagery for Post-Katrina Flood Monitoring in New Orleans," by A. McMillan, J.G. Morley, B.J. Adams and S. Chesworth, 11/17/08 (PB2010-100927).

MCEER-08-0024 "Remote Sensing for Resilient Multi-Hazard Disaster Response – Volume V: Integration of Remote Sensing Imagery and VIEWS^{TM} Field Data for Post-Hurricane Charley Building Damage Assessment," by J.A. Womble, K. Mehta and B.J. Adams, 11/17/08 (PB2009-115532).

MCEER-08-0025 "Building Inventory Compilation for Disaster Management: Application of Remote Sensing and Statistical Modeling," by P. Sarabandi, A.S. Kiremidjian, R.T. Eguchi and B. J. Adams, 11/20/08 (PB2009-110484).

MCEER-08-0026 "New Experimental Capabilities and Loading Protocols for Seismic Qualification and Fragility Assessment of Nonstructural Systems," by R. Retamales, G. Mosqueda, A. Filiatrault and A. Reinhorn, 11/24/08 (PB2009-110485).

MCEER-08-0027 "Effects of Heating and Load History on the Behavior of Lead-Rubber Bearings," by I.V. Kalpakidis and M.C. Constantinou, 12/1/08 (PB2009-115533).

MCEER-08-0028 "Experimental and Analytical Investigation of Blast Performance of Seismically Resistant Bridge Piers," by S.Fujikura and M. Bruneau, 12/8/08 (PB2009-115534).

MCEER-08-0029 "Evolutionary Methodology for Aseismic Decision Support," by Y. Hu and G. Dargush, 12/15/08.

MCEER-08-0030 "Development of a Steel Plate Shear Wall Bridge Pier System Conceived from a Multi-Hazard Perspective," by D. Keller and M. Bruneau, 12/19/08 (PB2010-102696).

MCEER-09-0001 "Modal Analysis of Arbitrarily Damped Three-Dimensional Linear Structures Subjected to Seismic Excitations," by Y.L. Chu, J. Song and G.C. Lee, 1/31/09 (PB2010-100922).

MCEER-09-0002 "Air-Blast Effects on Structural Shapes," by G. Ballantyne, A.S. Whittaker, A.J. Aref and G.F. Dargush, 2/2/09 (PB2010-102697).

MCEER-09-0003 "Water Supply Performance During Earthquakes and Extreme Events," by A.L. Bonneau and T.D. O'Rourke, 2/16/09 (PB2010-100923).

MCEER-09-0004 "Generalized Linear (Mixed) Models of Post-Earthquake Ignitions," by R.A. Davidson, 7/20/09 (PB2010-102698).

MCEER-09-0005 "Seismic Testing of a Full-Scale Two-Story Light-Frame Wood Building: NEESWood Benchmark Test," by I.P. Christovasilis, A. Filiatrault and A. Wanitkorkul, 7/22/09.

MCEER-09-0006 "IDARC2D Version 7.0: A Program for the Inelastic Damage Analysis of Structures," by A.M. Reinhorn, H. Roh, M. Sivaselvan, S.K. Kunnath, R.E. Valles, A. Madan, C. Li, R. Lobo and Y.J. Park, 7/28/09 (PB2010-103199).

MCEER-09-0007 "Enhancements to Hospital Resiliency: Improving Emergency Planning for and Response to Hurricanes," by D.B. Hess and L.A. Arendt, 7/30/09 (PB2010-100924).

MCEER-09-0008 "Assessment of Base-Isolated Nuclear Structures for Design and Beyond-Design Basis Earthquake Shaking," by Y.N. Huang, A.S. Whittaker, R.P. Kennedy and R.L. Mayes, 8/20/09 (PB2010-102699).

MCEER-09-0009 "Quantification of Disaster Resilience of Health Care Facilities," by G.P. Cimellaro, C. Fumo, A.M Reinhorn and M. Bruneau, 9/14/09.

MCEER-09-0010 "Performance-Based Assessment and Design of Squat Reinforced Concrete Shear Walls," by C.K. Gulec and A.S. Whittaker, 9/15/09 (PB2010-102700).

MCEER-09-0011 "Proceedings of the Fourth US-Taiwan Bridge Engineering Workshop," edited by W.P. Yen, J.J. Shen, T.M. Lee and R.B. Zheng, 10/27/09 (PB2010-500009).

MCEER-09-0012 "Proceedings of the Special International Workshop on Seismic Connection Details for Segmental Bridge Construction," edited by W. Phillip Yen and George C. Lee, 12/21/09.

MCEER-10-0001 "Direct Displacement Procedure for Performance-Based Seismic Design of Multistory Woodframe Structures," by W. Pang and D. Rosowsky, 4/26/10.

MCEER-10-0002 "Simplified Direct Displacement Design of Six-Story NEESWood Capstone Building and Pre-Test Seismic Performance Assessment," by W. Pang, D. Rosowsky, J. van de Lindt and S. Pei, 5/28/10.

MCEER-10-0003 "Integration of Seismic Protection Systems in Performance-Based Seismic Design of Woodframed Structures," by J.K. Shinde and M.D. Symans, 6/18/10.

MCEER-10-0004 "Modeling and Seismic Evaluation of Nonstructural Components: Testing Frame for Experimental Evaluation of Suspended Ceiling Systems," by A.M. Reinhorn, K.P. Ryu and G. Maddaloni, 6/30/10.

MCEER-10-0005 "Analytical Development and Experimental Validation of a Structural-Fuse Bridge Pier Concept," by S. El-Bahey and M. Bruneau, 10/1/10.

MCEER-10-0006 "A Framework for Defining and Measuring Resilience at the Community Scale: The PEOPLES Resilience Framework," by C.S. Renschler, A.E. Frazier, L.A. Arendt, G.P. Cimellaro, A.M. Reinhorn and M. Bruneau, 10/8/10.

MCEER-10-0007 "Impact of Horizontal Boundary Elements Design on Seismic Behavior of Steel Plate Shear Walls," by R. Purba and M. Bruneau, 11/14/10.

MCEER-10-0008 "Seismic Testing of a Full-Scale Mid-Rise Building: The NEESWood Capstone Test," by S. Pei, J.W. van de Lindt, S.E. Pryor, H. Shimizu, H. Isoda and D.R. Rammer, 12/1/10.

MCEER-10-0009 "Modeling the Effects of Detonations of High Explosives to Inform Blast-Resistant Design," by P. Sherkar, A.S. Whittaker and A.J. Aref, 12/1/10.

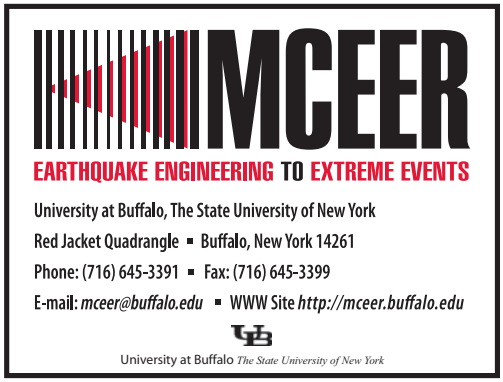

ISSN 1520-295X